

FLUID FLOW AND CONCENTRATION DISTRIBUTION IN A
RADIAL FLOW PLASMA ETCH REACTOR

by

VIKRAM SINGH, B.Tech.

A THESIS

IN

CHEMICAL ENGINEERING

Submitted to the Graduate Faculty
of Texas Tech University in
Partial Fulfillment of
the Requirements for
the Degree of

MASTER OF SCIENCE

IN

CHEMICAL ENGINEERING

December, 1990

805
73
1990
No. 145
Cop. 2

ACKNOWLEDGMENTS

I am deeply indebted to Dr. R. Russell Rhinehart, Chairman of my advisory committee, for his valuable advice, direction and financial support. I also express a sincere appreciation to Dr. J.B. Riggs and Dr. R.S. Narayan, my other committee members, for their suggestion and criticism throughout the course of this work.

Special thanks are extended to Texas Instruments, FSI Corporation and Microscience Incorporated for their equipment, material and technical assistance. Financial support for this work was provided through a State of Texas Advanced Technology Program Grant (4377) and an Engineering Foundation, Research Initiation Grant (RI-A-87-10).

I am grateful to my other co-workers, Tony and Vince, for all their help. Appreciation is extended to Dawn Eastman for her clerical assistance throughout my Masters program. Most of all I wish to take this opportunity to thank all my family members for their constant encouragement and moral support from so far away.

TABLE OF CONTENTS

ACKNOWLEDGMENTS	i
LIST OF TABLES	vi
LIST OF FIGURES	vii
CHAPTER 1 INTRODUCTION AND OVERVIEW	
CHAPTER 2 MODELING SURVEY	
2.1 Plasma Phase Reactions	
2.2 Mathematical Models	1
CHAPTER 3 EXPERIMENTAL SETUP AND PROCEDURE	1
3.1 Plasma Reactor System	1
3.2 Optical Emission Detection System	2
3.3 Langmuir Probe System	2
3.4 Film Thickness Measurement System	2
3.5 Experimental Procedure	3
CHAPTER 4 MEASUREMENT PRINCIPLES	3
4.1 Langmuir Probe Theory	3
4.1.1 Plane Probe	3
4.1.2 Cylindrical Probe	3
4.2 Argon Actinometry	4
CHAPTER 5 PLASMA AND SURFACE KINETIC MODEL	4
5.1 CF ₄ Plasma Kinetic Model	5
5.2 Surface Reaction Kinetic Model	6
CHAPTER 6 MODEL DEVELOPMENT	6
6.1 Fluid Flow Model	6
6.1.1 Differential Momentum Balance ..	6

	6.1.2	Assumptions	7
	6.1.3	Analysis of Momentum Balance Equation	7
	6.1.4	Boundary Conditions	8
	6.1.5	Nondimensionalization	8
	6.1.6	Method of Solution	8
	6.2	Species Distribution Model	9
	6.2.1	Differential Material Balance ..	9
	6.2.2	Assumptions	9
	6.2.3	Analysis of Material Balance Equation	9
	6.2.4	Boundary Conditions	10
	6.2.5	Nondimensionalization	10
	6.2.6	Method of Solution	10
CHAPTER 7		EXPERIMENTAL RESULTS	11
	7.1	Electron Density and Temperature	11
	7.1.1	Effect of Position	11
	7.1.2	Effect of Power	11
	7.1.3	Effect of Pressure	11
	7.2	Unloaded Reactor Runs	11
	7.2.1	Effect of Power	12
	7.2.2	Effect of Pressure	12
	7.2.3.	Effect of Flowrate	12
	7.3	Loaded Reactor Runs	12
	7.3.1	Process Disturbances	12
	7.3.2	Design of Experiments	12
	7.3.3	Process Parameters	12

CHAPTER 8	MODEL RESULTS VALIDATION	13
8.1	Electron Density Model Results	13
8.2	Fluid Flow Model Results	13
8.2.1	Effect of Boundary Conditions .	13
8.2.2	Effect of Pressure	13
8.2.3	Effect of Flowrate	13
8.3	Unloaded Reactor Runs	13
8.3.1	Effect of Power	14
8.3.2	Effect of Pressure	14
8.3.3	Effect of Flowrate	14
8.4	Loaded Reactor Runs	148
CHAPTER 9	CRITIQUE AND DISCUSSIONS	154
CHAPTER 10	CONCLUSIONS AND RECOMMENDATIONS	157
BIBLIOGRAPHY	160
APPENDIX A	MAJOR SPECIES IN A CF_4 PLASMA ETCH OF SILICON DIOXIDE	164
APPENDIX B	TEMPERATURE CHANGE OF GAS IN THE PLASMA REACTOR	173
APPENDIX C	PHYSICAL PROPERTY ESTIMATION OF THE GAS PHASE	178
APPENDIX D	FLOW REGIME AND TYPE OF FLOW	183
APPENDIX E	PARABOLIC FLOW VELOCITY PROFILE	186
APPENDIX F	COMPUTER CODE	188
APPENDIX G	ELECTRON DENSITY AND TEMPERATURE DISTRIBUTION DATA	200
APPENDIX H	EMPIRICAL MODEL FOR ELECTRON DENSITY DISTRIBUTION	225
APPENDIX I	UNLOADED REACTOR RUNS DATA	228

APPENDIX J	LOADED REACTOR RUNS DATA	23
APPENDIX K	MODEL VALIDATION RUNS	27

LIST OF TABLES

Table 1:	Reaction Scheme for a CF_4 Plasma--Proposed by Edelson and Flamm(4)	5
Table 2:	Reaction Scheme for a CF_4 Plasma--Proposed by Ryan and Plumb(6)	5
Table 3:	Operating Conditions for Loaded Runs	13
Table 4:	Percentage Dissociation at Various Powers	17
Table 5:	Leonard-Jones Potential	18
Table 6:	Model Constants at 200 mTorr Pressure and at Various Powers	22

LIST OF FIGURES

Figure 1:	Schematic Diagram of Smolinsky and Flamm's(3) Experimental Setup	11
Figure 2:	Schematic of Plasma Reactor System	19
Figure 3:	Plasma Reactor and Electrical Cabinet(13)	20
Figure 4:	Schematic Diagram of the Plasma System(13)	21
Figure 5:	Interior of the Depositionar Assembly(13)	25
Figure 6:	Film Thickness Measuring Device-NanoSpec(14) ..	29
Figure 7:	Plane Probe Ideal I-V Characteristic Curve	35
Figure 8:	I-V Characteristic Curve for Cylindrical Probe.	38
Figure 9:	Semilog Plot of I-V Curve	40
Figure 10:	Transverse Section of the Reactor Across the Optic Fiber Head	46
Figure 11:	Simplified View of a rf Glow Discharge Process(12)	50
Figure 12:	Etch Rate vs. F Concentration for Different Electrodes(16)	53
Figure 13:	Etch Rate vs. F Concentration for Different Feed Gases(1)	55
Figure 14:	Differential Momentum Balance Element	69
Figure 15:	Time Dependence of Fluorine Intensity	75
Figure 16:	Geometrical Representation of the Plasma Reactor	81
Figure 17:	Finite Difference Grid for Velocity Profile ...	87
Figure 18:	Differential Material Balance Element	93
Figure 19:	Reactor Bottom Plate Showing the Wafer Location	103
Figure 20:	Sector Over Which the Concentration Profile was Computed	110

Figure 21: Transverse Section of the Reactor Showing the Points where the Electron Characteristics were Investigated	115
Figure 22: Typical Optical Emission Spectrometer Output	.120
Figure 23: Operating Conditions for Loaded Reactor Runs	.130
Figure 24: Location of Wafer on the Finite Difference Grid	150
Figure 25: Three-Dimensional Plot of F Concentration on the Bottom Plate for the Wafer Placed Near the Inlet	151
Figure 26: Three-Dimensional Plot of F Concentration on the Top Plate for the Wafer Placed Near the Inlet	152
Figure 27: Operating Conditions for Sample Runs.....	170

CHAPTER 1

INTRODUCTION AND OVERVIEW

Electronic material processing involves the fabrication of microstructures which have unique and useful electronic and optical properties. This fabrication of microelectronic components involves a variety of complex physical transport and chemical processes in succession, such as film deposition, patterning, etching and doping operations. Film deposition and etching is normally done by plasma processes. The considerable interest in plasma etching and deposition is driven by the ability to remove and grow films respectively, at low process temperature and with considerable anisotropy. Plasma etching, alternately known as dry processing, has almost completely replaced aqueous (wet) etching since it provides almost unidirectional control of the shape of the microscopic etch profiles and is a very clean process requiring minimal waste disposal.

Present day microelectronics devices offer extensive circuit integration with as many as sixteen million components per circuit(1). This has caused material processing technology to become a manufacturing constraint. Thus it has become necessary to understand the actual underlying principles involved in the various semiconductor processing steps.

Plasma etching is one of the most important and probably least understood processes in the entire spectrum of semiconductor fabrication. Although phenomenological understanding of the plasma etching process has gained a great deal of attention recently, on the industrial scale, design and operation of this process is essentially empirical. This is because the multitude of complex processes which occur in the plasma environment make it very difficult to develop a model that can accurately predict or explain the observed results.

Plasma etching processes are conducted in a plasma reactor which is a continuous feed reactor, in which the feed gas is partially ionized by the electric field between the two electrodes. The ionized gas in the plasma consists of mostly neutral parent gas molecules along with a small amount of ions. In a plasma reactor the following sequence of steps typically occur:

1. Reactive species are generated from the parent feed molecules by the collision with high energy electrons emitted and accelerated in the radio frequency field in the plasma reactor.
2. These species are transported onto the surface of the material being etched both by diffusion and bulk transport flux.
3. Once on the surface the reactive species react and etch the surface with the formation of

volatile by-products, which are desorbed from the wafer surface.

4. The by-product is carried out of the reaction chamber by diffusion and bulk transport.

A radio frequency (rf) plasma with a standard 13.56 MHz frequency is used on most industrial scale reactors for the generation of reactive species. However, recently experimental procedures have been developed around other types of energy sources such as microwave and laser. In our reactor the standard 13.56 MHz rf plasma was used. The plasma phase reactions are a complex set of electron impact dissociation reactions coupled with another set of third body and wall association reactions. Various reaction schemes are available in literature and are dealt with in more detail in subsequent chapter. Also the exact mechanism of surface reaction is not understood; but, various reaction schemes have been proposed in the literature, and a comparison between them has been complicated by the dominance of different etching species and phenomena at different operating conditions and reactor geometry.

However, parallel work(31) conducted in this field was found to show good agreement with the experimental data and was used in this study to obtain the etch profile and explain the nonuniformity of etching in the plasma etching process.

The nonuniformity of etching is probably one of the biggest drawbacks of the plasma etching process. Both

intra- and inter-wafer nonuniformities have been observed in practice. The major cause of inter-wafer nonuniformities is the difference in the reactive species concentration across the reactor. The inter-wafer nonuniformities are caused by the concentration gradient in the reactive species that exists over the wafer surface. The reactive species are replenished by diffusion more readily on the sides of the wafer than at the center. This results in a higher wafer etch rate at the edges of the wafer than at the center, resulting in a dome-like etched wafer surface. Light interference patterns on this surface results in a ring-like appearance of the wafer surface. This is traditionally referred to as the bullseye effect because of the obvious similarity in appearance.

The modeling of the plasma etching process is greatly complicated by the physical and chemical coupling between charged particles, kinetics of neutral species and interactions between plasma and the surface. However, it is imperative for further development of etching technology, to sideline the fully empirical approach and employ more sophisticated methods based on a phenomenological understanding of the plasma etching process. Additionally, phenomenological models can predict process behaviors over a wide range of operating conditions and hence can be used for the design and control of plasma reactors. By contrast empirical models are highly unreliable outside the range of

operating conditions over which they are parameterized. Although extensive work has been conducted in various fields of plasma etching separately, a detailed model that incorporates the complexity of all these coupled sub-processes together has not been developed.

In this work, a three-dimensional, steady state mathematical model was developed to predict the reactive species concentration profiles throughout a radial flow reactor for a CF_4 etch of SiO_2 . Electron impact reactions with the parent molecule (CF_4 in our case), are responsible for the generation of reactive species in the plasma reactor. Experimental observations by various researchers show that F species created in a CF_4 plasma is the dominant etching species for Si and SiO_2 (1,2,4,6). In order to quantify the amount and effect of process parameters on the concentration of F species, it was found essential to develop a model for electron density distribution as well. Since electron density distribution is both a strong and extremely complicated function of reactor geometry, a parametric empirical model was developed, to allow this work to focus on chemical transport and reaction phenomena.

The model also uses an etch reaction kinetic model(31) to predict the etch rate distribution across the wafer surface. This way it was possible to test the effect of various combinations of operating conditions on the etch rate uniformity. Modeling results show that the background

fluid flow profile can be decoupled from diffusion and reaction effects and can be obtained by numerically solving the θ -symmetric momentum balance equation in the radial flow reactor. In the range of experimental operating conditions used, the flow was found to be both laminar and in the continuum regime. The velocity profile was used in conjunction with the material balance on each species to evaluate the concentration distribution of radicals and source gas in three-dimensions. The etch rate at each point was calculated from the concentration distribution of radicals over the wafer surface using a surface etch reaction kinetic expression as a boundary condition.

The model outputs were compared to experimental data generated at our plasma reactor. Unloaded and loaded reactor runs were separately used to compare the plasma and surface reaction kinetics, respectively. The model was able to predict similar trends as those obtained by experimentation.

The CF_4 etch of SiO_2 was selected for this study because this etching system is fundamental to one of the most commonly used systems in the industry. The oxide masking has evolved as a key step in the manufacture of silicon integrated circuits. Also freon is one of the key fluorocarbon gases used for etching oxide films. It is because of this reason that extensive research work has been conducted in this field over the past few years. This way

it is possible for us to compare our model to models suggested by various researchers and we found that our model was equal to those of other researchers and in certain instances even superior in predicting additional plasma features. These features include: (1) reactive species concentration profile and etch rate distribution with changing power, pressure and flowrate, (2) effect of radial, axial and tangential diffusion on the etch rates, and (3) relative dominance of diffusion flux over convective flux.

The development of a phenomenological plasma model that is able to predict similar trends as those found in real time experiments, is the primary goal of this thesis. In the future, this model will be used for on-line process model-based control of plasma etch reactor in order to improve semiconductor manufacturing efficiency.

A review of work done by various researchers along similar line is presented in Chapter 2. Our experimental setup and the principles behind the measuring instruments used are discussed in detail in Chapters 3 and 4, respectively. The plasma and surface kinetic models developed are presented in Chapter 5. Chapter 6 discusses the details of the model developed to study the reactive species and etch rate distribution in the plasma reactor. Experimental results obtained using the electrostatic probe and optical spectrometer for both unloaded and loaded reactor situations are presented and discussed in Chapter 7.

Comparison of model output to experimental data is presented in Chapter 8. Critique of the present work and an outline of the work to be undertaken in the future work is discussed in Chapters 9 and 10.

CHAPTER 2

MODELING SURVEY

Various key features that need to be considered in the modeling of plasma etching system were overviewd in Chapter 1. This chapter presents a detailed literature review of these features. In section one of this chapter various plasma phase reaction schemes available in literature have been highlighted, while in section two models developed by various researchers incorporating the plasma phase reactions in a transport and diffusion model to a system similar to ours have been discussed.

2.1 Plasma Phase Reactions

Earlier work in modeling of a CF_4 etch of SiO_2/Si , was based on simplified plasma kinetics. One of the reasons for this was that sufficient knowledge of plasma reactions was not available. However, in all the works using a fluorine based gas to etch Si or SiO_2 , it was universally accepted that F free radicals are the dominant etching species. Kao and Stenger(2) used a simplified kinetic expression, that accounted for only the dissociation of CF_4 and recombination of F free radicals. They used experimental data to solve for their rate constants. Hence, their rate constants were essentially fit parameters which gave a mechanistic but not necessarily phenomenological structure to their plasma reactor model.

The first detailed experimental work in the field of plasma chemistry was reported by Smolinsky and Flamm(3) for a wide range of operating conditions, both in the presence and absence of silicon. A schematic of their experimental equipment is presented in Figure 1. Smolinsky and Flamm passed both pure CF_4 and $\text{CF}_4\text{-O}_2$ mixture through a 1.9 cm diameter alumina flow tube. A range of gas pressures and flow rates were used and the gas was excited over a 5 cm length of the tube by a 49 Watt, 13.56 MHz discharge. Sampling of the effluent was done by a mass spectrometer located 15 cm downstream from where the discharge commenced. In some experiments single crystal Si was placed downstream of the discharge.

Edelson and Flamm(4) developed a model to simulate both a CF_4 plasma alone and a CF_4 plasma during a Si etch by compiling a set of reactions reported separately in literature. They used the experimental data reported by Smolinsky and Flamm to validate their model. In their model, processes occurring at the gas-surface interface were very important even in the absence of Si. For example, according to Edelson and Flamm the gas phase concentration of F atom is controlled by reactions of this species with absorbed CF_3 . In general they stressed the importance of wall reactions on the overall species concentration in the plasma. They reported the presence of certain charged species such as C_2F_6^+ , F^- , CF_3^+ along with their rate

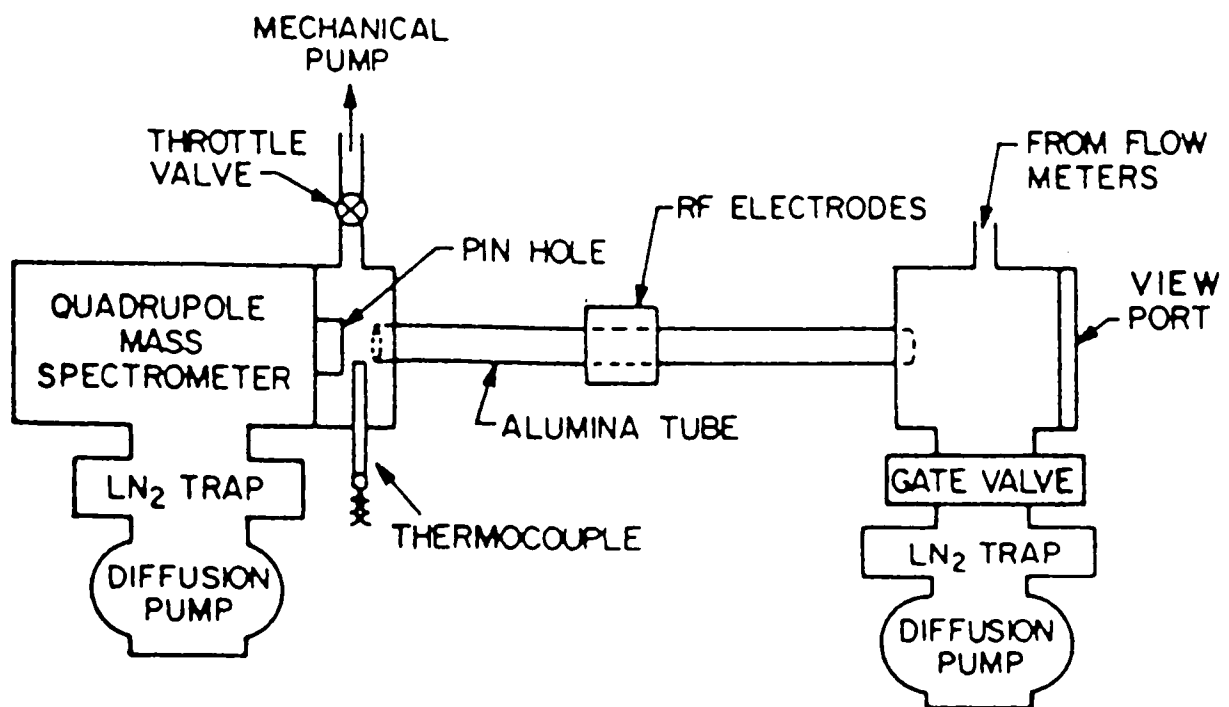


Figure 1: Schematic Diagram of Smolinsky and Flamm's(3) Experimental Setup.

constants. They used this reaction scheme in a one-dimensional plug flow reactor model, in which a packet of gas was traced through the plasma, allowing the simulation to be performed as an initial value problem. They reported that their model predictions were within an order of magnitude to the experimental results. However, the trend predicted by their model was significantly different from the experimental trend. Therefore their model is of little use for design and control of plasma reactors.

Plumb and Ryan(5,6) reinforced their own experimental data with the earlier Smolinsky and Flamm's data and suggested a reaction scheme for CF_4 plasmas. They suggested a direct dissociation of CF_4 to CF_2 , as the main source of production of F species, as against Edelson and Flamm who had suggested the formation of CF_2 from the electron impact reaction of CF_3 . The reaction scheme postulated by Plumb and Ryan also suggests that the F atom recombination rate in the plasma is about eighty times faster than that suggested by Edelson and Flamm.

Another important difference between the reaction schemes suggested by the two pairs of researchers is that, while Edelson and Flamm report kinetic rate constant values for electron impact reactions, the values reported by Plumb and Ryan for electron impact reactions are the product of rate constants and electron density. This limits the usage of Plumb and Ryan's kinetic data to only one particular

pressure and power since both these operating parameters are found to affect electron density.

These two widely accepted, but inherently different plasma phase reaction schemes, were each validated experimentally against a similar set of conditions. Both sets of researchers show that the scheme suggested by themselves does a fairly good job of predicting the experimental data. This clearly indicates the complexity of the plasma kinetics. Because of the presence of a number of species both charged and neutral, it is difficult to pinpoint the reactions responsible for generating these species. Another important point that needs to be considered here is that the geometry of the reactor and the entire experimental setup can affect the species concentration by affecting the conditions for the extent of occurrence of certain plasma reactions. This concept is discussed in more detail in Chapter 5.

2.2 Mathematical Models

In recent years there has been much interest in developing models of the plasma etching process. In developing such models there are a number of important phenomena which need to be considered. Such phenomena include glow discharge chemistry, electron density and energy distribution, ion transport, heat and mass transfer, and heterogenous reaction kinetics. Even if all the complicated phenomena taking place in the plasma are known,

the computational power of present state-of-the-art computer will not allow one to include details of all the above phenomena in a single model.

Earlier phenomenological models for CF_4 plasma reactions were developed by Kao and Stenger(2) and Dalvie, Jensen and Graves(7) independently. The models were developed for a CF_4 plasma etch of Si in a radial flow parallel plate plasma reactor. Simplified plasma and heterogenous kinetics were incorporated in the model along with a dispersion model for predicting flow profile and species concentration distribution. The models developed in both the instances were compared to experimental etch rate data and even though similar trends were predicted, the overall comparison was poor. The models did a poor job of predicting the etch rate distribution across the wafer surface. Also the models were used to predict the etch rates only at one set of operating conditions with varying wafer positions. This limited a complete validity of these models for a detailed study of the plasma process.

In the past few years, detailed mathematical models incorporating complicated plasma kinetics and detailed treatment of transport and diffusion have been developed for various plasmas. Kobayashi, Nakazato and Hiratsuka(8) modeled the etch of aluminum by a gas mixture of Cl_2 , CCl_4 , and BCl_3 in a parallel plate showerhead plasma reactor. They treated the gas flow as an axisymmetric laminar flow in

two dimensions. The concentration distribution of the radicals and the source gas molecules in the plasma were calculated by solving continuity equations for each component. The etch rate was computed based on reactive species concentration and surface kinetics and was compared to the experimental data. The calculation and the experiments show a good agreement towards the center of the wafer but on the edge there was a significant offset between the two.

Dalvie and Jensen(9) in their later article presented a detailed model for CF_4/O_2 etch of Si and compared their predicted results to experimental data. The model includes detailed treatment of transport (including diffusion) and chemical kinetics. Their reactor was a stainless steel cylindrical shell with the lower grounded electrode made of aluminum, while the charged electrode was a Teflon tube through which the source gas entered the chamber. In general the plasma reactor can be described as a showerhead radial flow reactor. The reaction scheme suggested by Plumb and Ryan was used along with certain modifications to account for the species recombination on the wall. Species concentration distribution was computed by solving mass balance equations for both loaded and unloaded cases. Experimental measurements of spatial variation in active species concentration was made by spatially resolved actinometry. Spatial variation in etch rate was also

measured. However, as pointed out earlier the reaction scheme suggested by Plumb and Ryan only accounts for constant pressure and power cases, because they present kinetics parameters as a product of electron density and kinetic rate constant. Hence Dalvie and Jensen, in their work, only used their model to observe the effect of flowrate and feed composition changes in the etch parameters. For these restricted set of operating conditions, their model was able to predict similar trends of F concentration as those obtained from their experiments. However, the Si etch rate prediction compared poorly to their experimental data, and this could probably be the result of insufficiencies in their surface kinetic model.

Similar kinds of phenomenological models, but for different etch systems have also been investigated by other researchers. Economou, Park and Williams(10) in their work developed a model to predict the etch rates using O_2 to etch the wafer surface, in a single wafer parallel plate reactor. Similarly Venkatesan, Edgar and Trachtenberg(11) studied the etching of silicon using NH_3 .

Due to the difference of reactor geometry and range of operating conditions used by different workers it is not possible to judge the superiority or thoroughness of any particular model reported in literature. However, because none of the researchers have done any measurements on the electron temperature or density, their models are restricted

to only one set of pressure and power operating conditions. Also, most of the researchers have used a laboratory scale reactor and hence their models will most probably be poor in predicting the etch rate uniformity and optimum etch time in a commercial reactor. One scale-up problem is that the residence time in a commercial reactor is significantly larger than in a small-scale reactor. Another problem is the influence of reactor geometry on the electron distribution. A third problem is the change in surface-to-volume ratio. For a longer residence time reactor, the affect of diffusion flux over convective flux is significant and hence more uniform etching can be expected.

The equipment used for our experiments is a commercial sized reactor. It makes plasma measurements difficult but the model developed for this system would be anticipated to be of greater practical significance. The experimental setup for this work is discussed in the next chapter.

CHAPTER 3

EXPERIMENTAL SETUP AND PROCEDURE

This chapter summarizes the equipment setup that is used to: (1) etch SiO_2 with CF_4 , (2) collect optical plasma emission data, (3) collect charged (ions and electron) species characterization data and, (4) evaluate SiO_2 wafer etch rate data. The experimental setup includes the plasma reactor system, optical emission detection system, Langmuir probe for charged species characterization and a NanoSpec/AFT to evaluate the etch rate by measuring the SiO_2 depth on Si wafer. A schematic of the equipment setup is presented in Figure 2.

The plasma reactor equipment was donated by Texas Instruments, Incorporated, Lubbock, Texas in three parts; the reactor, an electrical cabinet, and a vacuum pump (Figure 3). The entire optical emission detection system was purchased from EG&G Princeton Applied Research (PARC). Plane and cylindrical Langmuir probes and the power supply were bought from Microscience Incorporated. The NanoSpec/AFT used to determine the SiO_2 depth on Si was loaned to us by FSI Corporation, Lubbock, Texas.

3.1 Plasma Reactor System

This section outlines the operation and geometry of the plasma reactor, a Texas Instruments Depositioner Assembly Model A-24-D. Detailed information on the operation of this

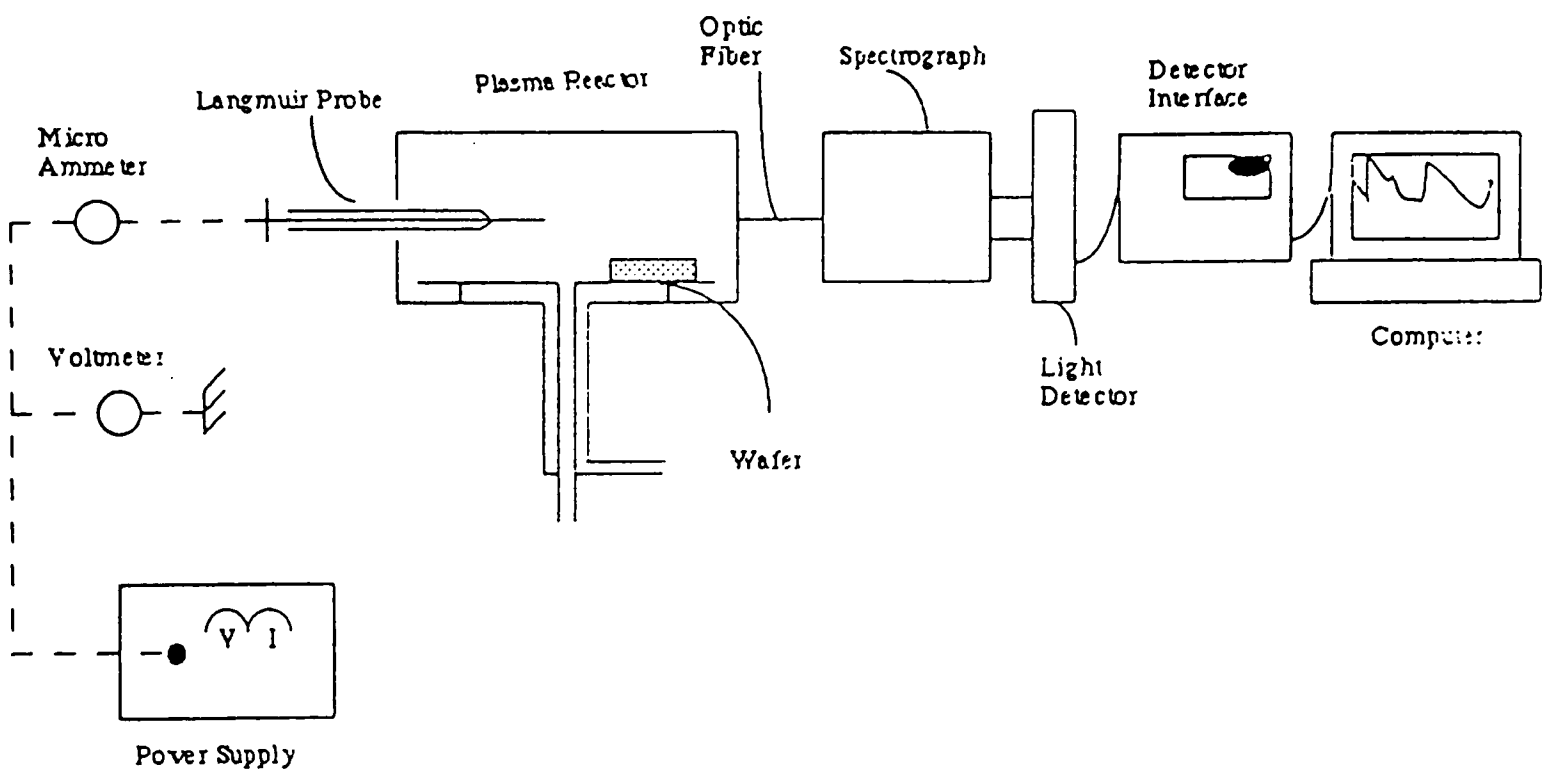
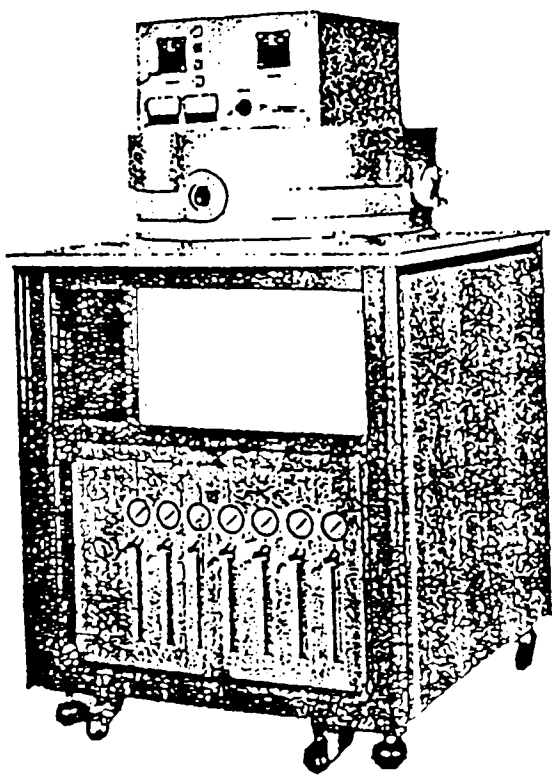
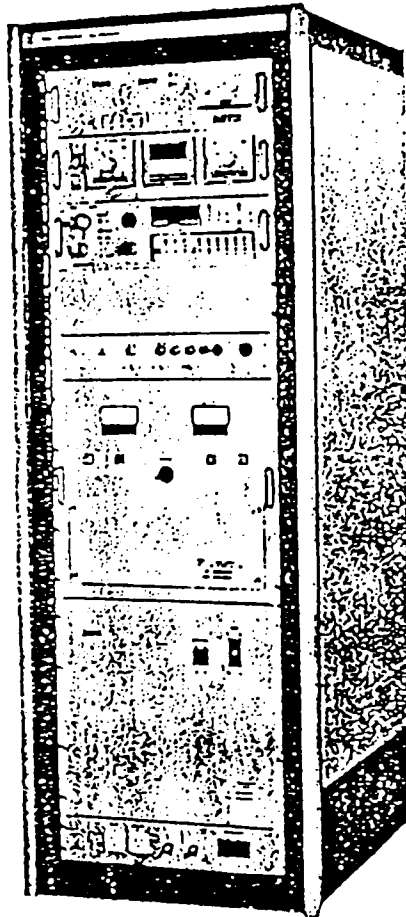


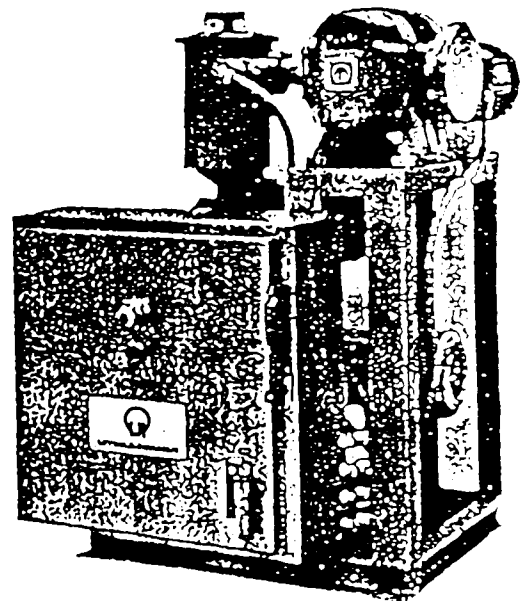
Figure 2: Schematic of Plasma Reactor System.



DEPOSITIONER ASSEMBLY



ELECTRICAL CABINET



VACUUM PUMP

Figure 3: Plasma Reactor and Electrical Cabinet(13).

system can be found in John T. Keating Master's Thesis(12) and in reference 13. This section presents features and operating characteristics of the plasma reactor system which are significant to this study.

The reactor (Figure 4) provides a controlled environment in which rf plasma processes take place. The cylindrical design of the reactor chamber allows for a radially inward flow of the reactant gases and consequently permits high volume processing of substrate. Exit for the gases is located at the center of the reactor bottom plate which is connected to a vacuum pump by way of a solenoid valve. The reactor chamber is of aluminum construction and measures 24" in diameter. The reactor bottom plate is 22" in diameter with a 2" diameter exit at the center. The distance between the top and bottom plates of the reactor is 2.5". The reactor cover can be lowered and raised using compressed air as the driving force. The interior of the reactor contains the top rf power plate and bottom grounded plate. The bottom plate has an internal heating element and a thermistor for temperature control. The wafers sit on the bottom plate (also known as the heater plate), where they are heated by conduction. There are three circular windows on the sides of the reactor. For our setup we used one window to gather the optical emission data, another to insert the Langmuir probe and the third to visually observe the rf glow discharge inside the reactor.

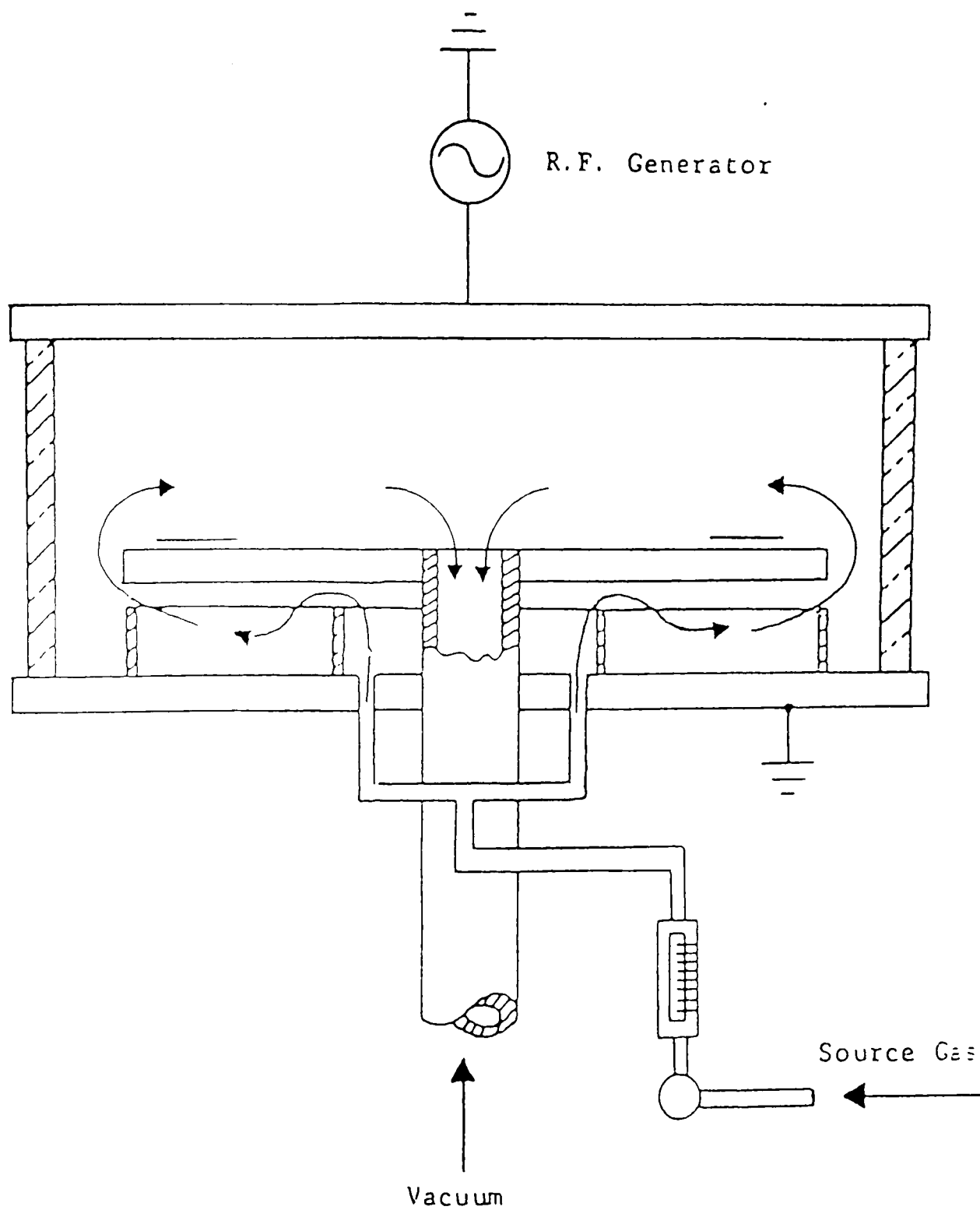


Figure 4: Schematic Diagram of the Plasma System(13).

For this work the effect on plasma species and subsequent etch rates of the following three operating parameters were conducted: CF_4 flowrate, rf power and reactor pressure.

1. Gas flowrate into the plasma reactor is controlled by the mass flow controllers when the interlocks on the solenoid valves are opened. The flow is manually adjusted with digital dials located on the reactor panel. The flowrates for different gases used in the etching process were calibrated to standard conditions using a temperature corrected soap-film meter.
2. The rf generator is housed in the electrical cabinet (Figure 3). The top plate in the reactor is the charged plate and the power applied across this plate can be adjusted manually. The incident and reflected power are displayed both on the electrical cabinet and on the matching box located on the top of the reactor assembly. The matching box has provisions to automatically minimize the reflected power, which may otherwise severely damage the rf generator. For the operating conditions used by us the matching box was able to minimize the reflected power to almost zero.
3. Reactor pressure is displayed on the electrical cabinet. The accuracy of this pressure gauge was

checked using a McLeod gauge and it was found to display pressure in centiTorr within $\pm 5\%$ of the McLeod gauge reading. This pressure in the reactor can be controlled by adjusting the size of the orifice on the three vacuum valves located at the exit pipe line. Figure 5 is a picture of the interior of the Plasma Depositinor Assembly. The inlet manifold and exit pipe with the three vacuum valves are illustrated in this picture.

3.2 Optical Emission Detection System

This section summarizes the setup and operation of equipment used for analyzing light emission from the plasma reactor system. Details of the various components and, the software OMAIID used to gather light emission data can be found in reference 12. The major components of the light detection step are (see Figure 2); a light collecting optic fiber, spectrograph, light detector, detector interface and host computer. The optic fiber head is installed through a slit at one the windows of the reactor through an opaque shield. The fiber head is approximately 1 cm above the lower electrode plate, which is the region of most intense emission. The light collected by the fiber is sent to a spectrograph which separates the different wavelengths of light. The detector uses spatially separated diodes to sense the intensity of the diffraction dispersed wavelengths

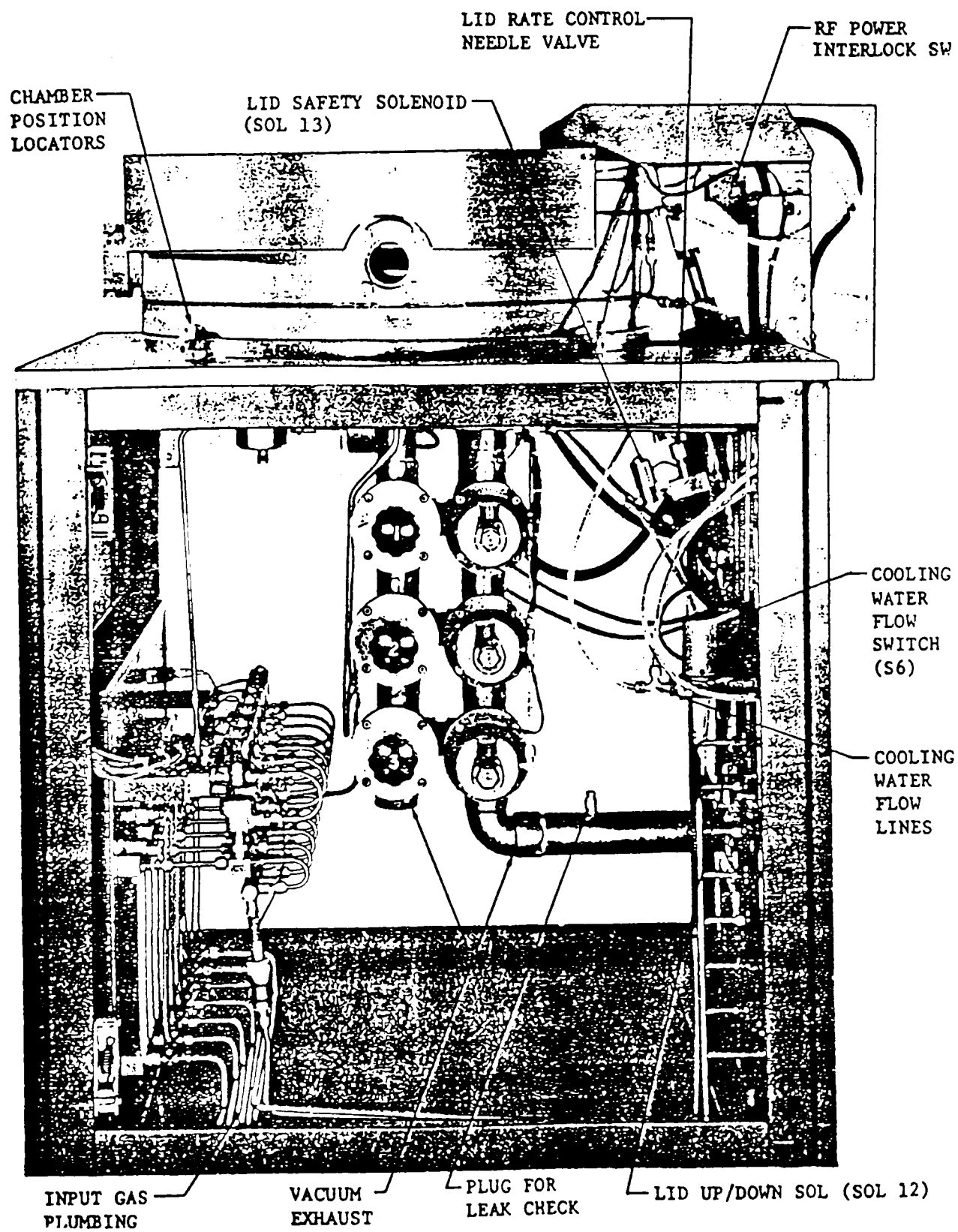


Figure 5: Interior of the Depositionar Assembly(13).

of light. Intensity readings are sent to the computer, via the detector interface, where they are displayed in a useful manner.

The spectrograph is an EG&G PARC Model 1229 spectrograph. The grating installed in the spectrograph diffracts the light into its component wavelengths and this is reflected out of the exit assembly. The grating was factory mounted and focused, and its useful spectral range is between 180 and 750 nm.

The light detector is a EG&G PARC Model 1452A detector. This is directly mounted on the exit slit of the spectrograph. The detector has an array of 512 silicon photodiodes and senses the light coming from the spectrograph. The detector senses the intensity of light and sends an analog signal to its controller which is mounted in the detector interface. The detector interface is an EG&G PARC Model 1461 Detector Interface. The detector interface along with its controller and detector are referred to as an Optical Multichannel Analyzer (OMA). The OMA system is run through a software in the host computer. The computer has an IEEE-488 General Purpose Instruction Bus (GPIB) that it uses to communicate with the detector interface. Further details and operating instructions on this software can be found in reference 12.

3.3 Langmuir Probe System

Due to the complexity of the physical and chemical environment in a process plasma, a large array of process monitors, historically termed "plasma diagnostics," are required to characterize the plasma, or to properly monitor important control parameters. Important parameters that characterize plasma are the electron (n_e), ion (n_i) and neutral (n_0) densities, and respective temperature (or energies) of the species. One of the earliest and still widely used plasma analysis technique is the electrostatic probe, first described and analyzed by Langmuir and thus the name. Langmuir probes are used for localized measurements of plasma electron and ion density (n_e, n_i) and temperature (T_e, T_i). Details of probe measuring principles used to characterize the plasma are presented in Chapter 4. In this chapter the experimental setup to be used to obtain probe data is discussed.

The cylindrical probe (see Figure 2) that was used in this study for evaluation of electron density and temperature comprises of a metallic wire of approximately .02" diameter inserted through a glass tube. The glass tube was hermetically sealed towards one end leaving approximately .5" of probe wire projecting out into the plasma. The glass tube with the probe wire was inserted into the plasma through an O-ring in a bore in one of the two remaining windows of the reactor. This helps maintains

the vacuum in the reactor under regular operating conditions. Figure 2 shows the probe circuit which was used to sweep the probe potential, using the power supply, while simultaneously measuring the probe current, which is of the order of micro amps. The probe along with power supply were bought from Microscience Incorporated. The principles behind the usage of the Langmuir probe are discussed in Chapter 4.

3.4 Film Thickness Measurement System

Model #010-0174 NanoSpec/AFT (automatic film thickness) gauge (see Figure 6), which is a computerized system for film thickness measurement for selected small areas was used to compute etch rate. The film thickness was measured at various points on the wafer both before and after etching and the difference divided by the etch time was used to compute the etch rate. In order to study the uniformity of etching a set of representative points both along and across the direction of flow were selected.

NanoSpec gauge includes; a microspectrophotometer head that employs a wavelength range of 480-800 nm, a grating monochromator and a wide range PMT (photo-multiplier tube). Linear wavelength and photo-intensity are displayed. A modified Olympus BHM microscope with incident illumination and a regulated tungsten lamp is used to focus on the point on the wafer where etch rates are desired. It is equipped with a variable field iris diaphragm, turret mounted 10X and

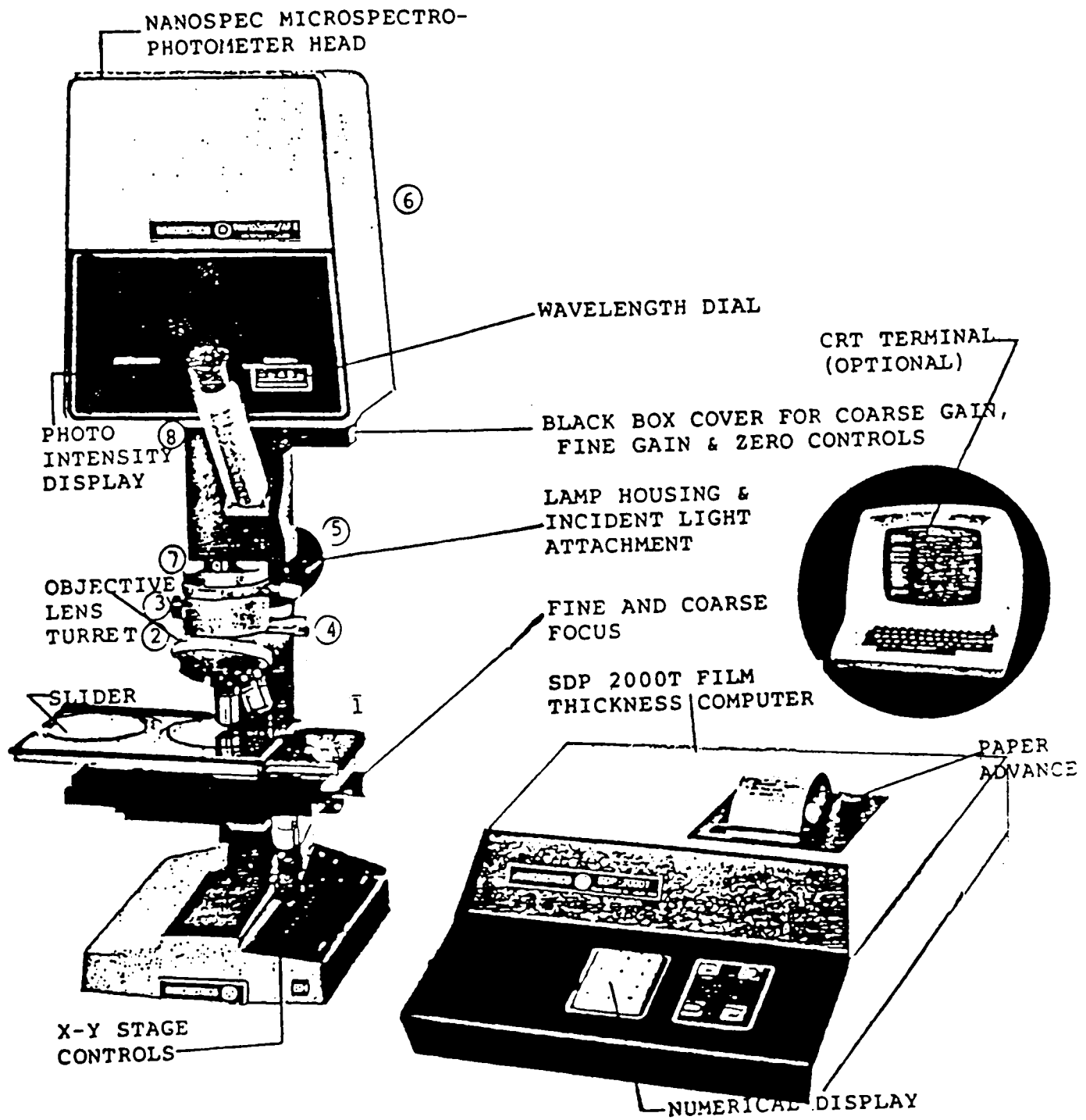


Figure 6: Film Thickness Measuring Device-NanoSpec(14).

40X objectives and a $.35\pm$ mm diameter measuring aperture. The 40X objective which measures an area of 9 microns square, was used in our experiments since it is recommended(14) for our film type (SiO_2 on Si). The computer has a stored software that computes the film thickness (in Angstroms) and prints it in the built-in printer.

A wafer is placed on the slider (Figure 6) and the 40X objective is focused at the point of interest. The type of film (SiO_2 on Si in our case) is manually input to the computer. Also in order to keep track of the experiment and wafer number being studied a sample identification number can be assigned to the experiment when the measure button is pressed, the microspectrophotometer head scans from 480 to 800 nm computing the ratio spectrum, point by point, to a bare silicon reference. The resulting curve is analyzed by the computer and upon the completion of a curve-matching program the film thickness is printed in angstroms. The wafers used in this study were donated by TI. These Si wafers were flat disks about 5" in diameter with a thermally grown film of SiO_2 of about 5000 A thickness.

3.5 Experimental Procedure

The experimental procedure that was followed during the course of the work is discussed in this section. Because of the multitude of plasma properties that need to be measured and the manual nature of the measuring equipment it was

found essential to have two operators during any experimental run. The experimental procedure followed is summarized below:

1. The NanoSpec was turned on and left on for half an hour so that it generates stable data(14). After this warming-up period the silicon dioxide film thickness at various points on the wafer was measured.
2. The wafer was set at one of the several specified locations in the reactor and the reactor was brought to all the desired operating conditions except the rf power. The reactor system was allowed to purge with the required gas mixture for a period of half hour. During this period the desired gas flowrates and bottom plate temperature are stabilized.
3. Power was turned on in the reactor and the vacuum valves were manually adjusted to maintain the pressure, since the sudden dissociation of feed gas leads to a surge in pressure. Simultaneously the light emission data was collected at equal time intervals of about half a minute.
4. Once the system pressure has stabilized (in about a minute), the electron and charged particles characteristics I-V values were obtained using the

Langmuir probe. All this time the light emission data was collected and stored.

5. After the desired etch time (usually 20 minutes) the power was turned off and the system was purged and pressurized with nitrogen. The wafer was then removed for film thickness measurements.

This whole process was repeated for various set of operating conditions.

CHAPTER 4

MEASUREMENT PRINCIPLES

In Chapter 3 the measuring system used to characterize the plasma and to obtain etch data was presented. In this chapter analysis of the data obtained from the Langmuir probe and the optical emission system are discussed.

4.1 Langmuir Probe Theory

A Langmuir probe is commonly used to obtain the densities and energies of the charged species present in the plasma. In a CF_4 plasma the major negative charge species are the electrons, while the ions are the dominant positive charge carriers. In this section, a discussion on plane probe used to characterize the positive ions and a cylindrical probe used to estimate the electron densities and temperatures is presented.

Positive ions are generated in the same manner as fluorine atoms, either via an electron impact reaction or a series of electron impact reactions. The dominant ion in CF_4 and CF_4/O_2 plasmas is CF_3^+ (39). Diffusion within the plasma transports chemical species to the reactor walls. Since electrons are lighter and more mobile than positive ions the plasma is weakly positively charged. The positive ions are accelerated along the electric field linearly across the sheath and hit the lower electrode surface. It has been well established that bombarding ions play a

significant role in the etching of SiO_2 . Electrons, on the other hand, are responsible for the dissociation of the parent feed gas molecule (CF_4), which creates enough reactive species to chemically react on the wafer surface and etch it. The probe circuitry used to generate the current-voltage (I-V) characteristics of the plasma was discussed in Chapter 3.

4.1.1 Plane Probe

The plane probe is a tungsten disk immersed in the plasma and grounded to the reactor vessel wall, which is the same as the lower electrode. By applying a potential to the probe it attracts electrons, positive ions, or both depending on the magnitude and sign of the potential. As the potential to the probe is varied (in both the negative and positive regimes) the current will also vary. An ideal characteristic I-V curve for a single plane probe is shown in Figure 7.

When the potential on the probe is driven sufficiently negative, with respect to the vessel wall, it will repel all electrons. The resulting current is due solely to positive ions. As the probe voltage is made more negative the current will become almost constant, because it will be diffusion limited. This current is termed the "ion saturation current"⁽¹⁾ and is illustrated in Figure 7 as the asymptotic limit in region A. As the probe potential is made more positive the probe will collect both ions and

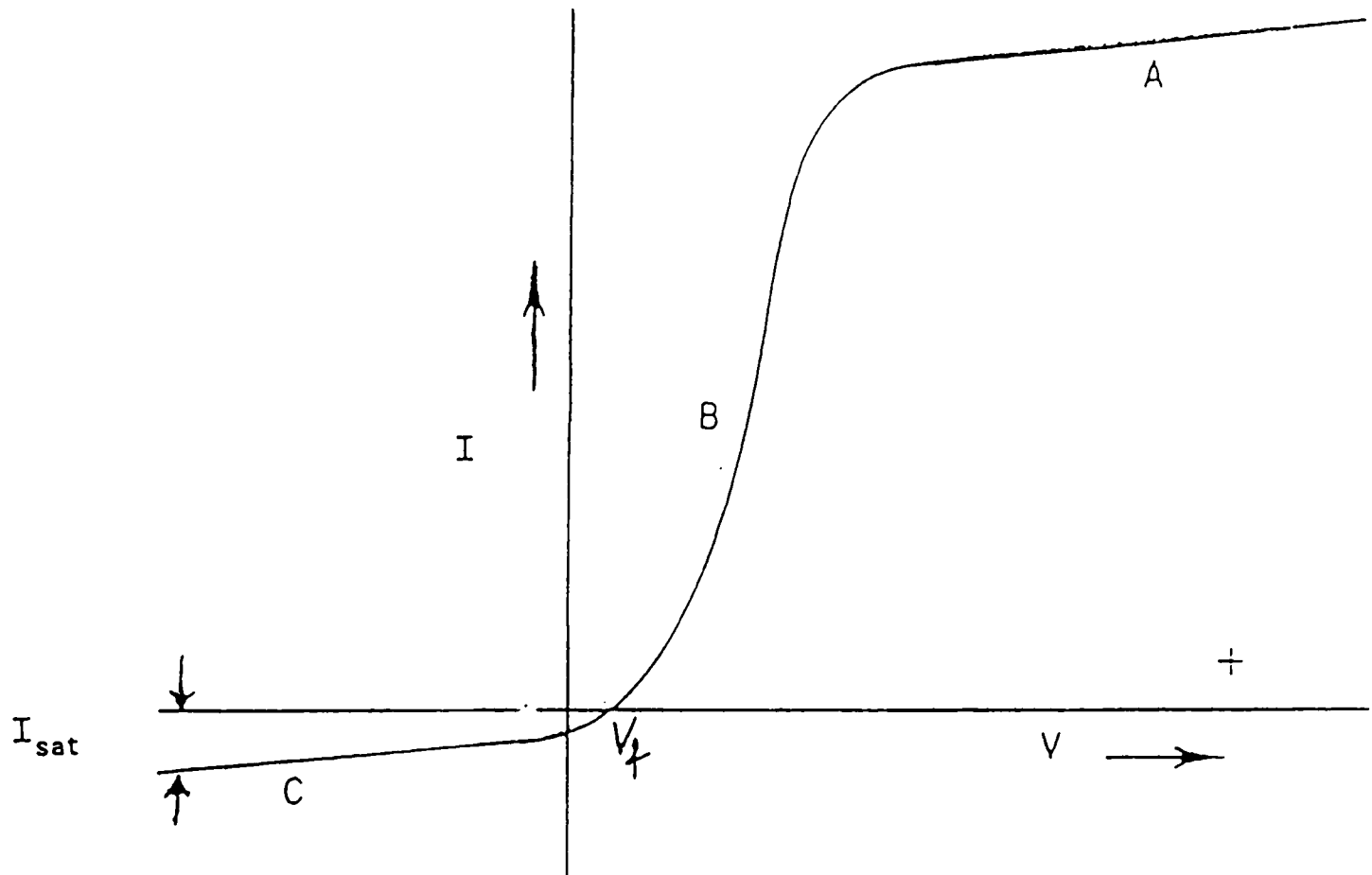


Figure 7: Plane Probe Ideal I-V Characteristic Curve.

electrons and will show an exponential rise in current as the probe starts to collect mainly electrons, this phenomena is seen as region B in Figure 7. At large positive potentials the probe current will saturate and this is known as the electron saturation current and is illustrated as the asymptotic limit in region C of Figure 7. The electron saturation current is much larger than the ion saturation current because of the higher mobility of electrons. The saturated region on the I-V curve for highly positive potential represented the electron saturation phenomena. Further details on this aspect is presented under cylindrical probe sub-section.

The plane probe was used for ion characterization because it has an easily distinguishable saturation region in the ionic part of the I-V characteristics. The ion saturation current density is a direct measure of the ion flux to the probe and is represented by(40):

$$I_{\text{Flux}} = \frac{I_{\text{sat}}}{A_p}. \quad (4.1)$$

Here A_p is the probe area and I_{sat} is the ion saturation current.

Equation (4.1) was used to monitor the ion flux to the probe during experimental etch runs since the ions are believed to participate in the reaction mechanism for a CF_4 and CF_4/O_2 plasma etch of SiO_2 .

4.1.2 Cylindrical Probe

The cylindrical probe is used to measure the plasma potential, electron temperature and the electron density. As the potential on the probe is increased from a large negative potential to a positive potential, the current drawn by the probe will start to include the high energy electrons. As the potential is increased it will reach a value where the current collected by the probe is zero. This is where the current due to electrons is equal to the current due to the ions and the net result is zero. The voltage at which this phenomena occurs is known as the floating potential, V_f (Figure 7).

Increasing the probe voltage in the positive direction, one will notice an exponential increase in the current collected by the probe, and as the potential is made relatively large the current will saturate and this is known as the electron saturation region. The electron saturation region is signalled by the appearance of a kink in the I-V characteristic curve of the probe (Figure 8). A clear saturation region is not obtained but a slight knee appears in the region of electron saturation. This is caused by polymer deposition from the plasma on the probe surface. This can be reduced by applying a negative potential, that results in ion-bombardment on the probe surface thereby removing the polymer deposition. However, this procedure for maintaining a clean probe has its side effects, in that

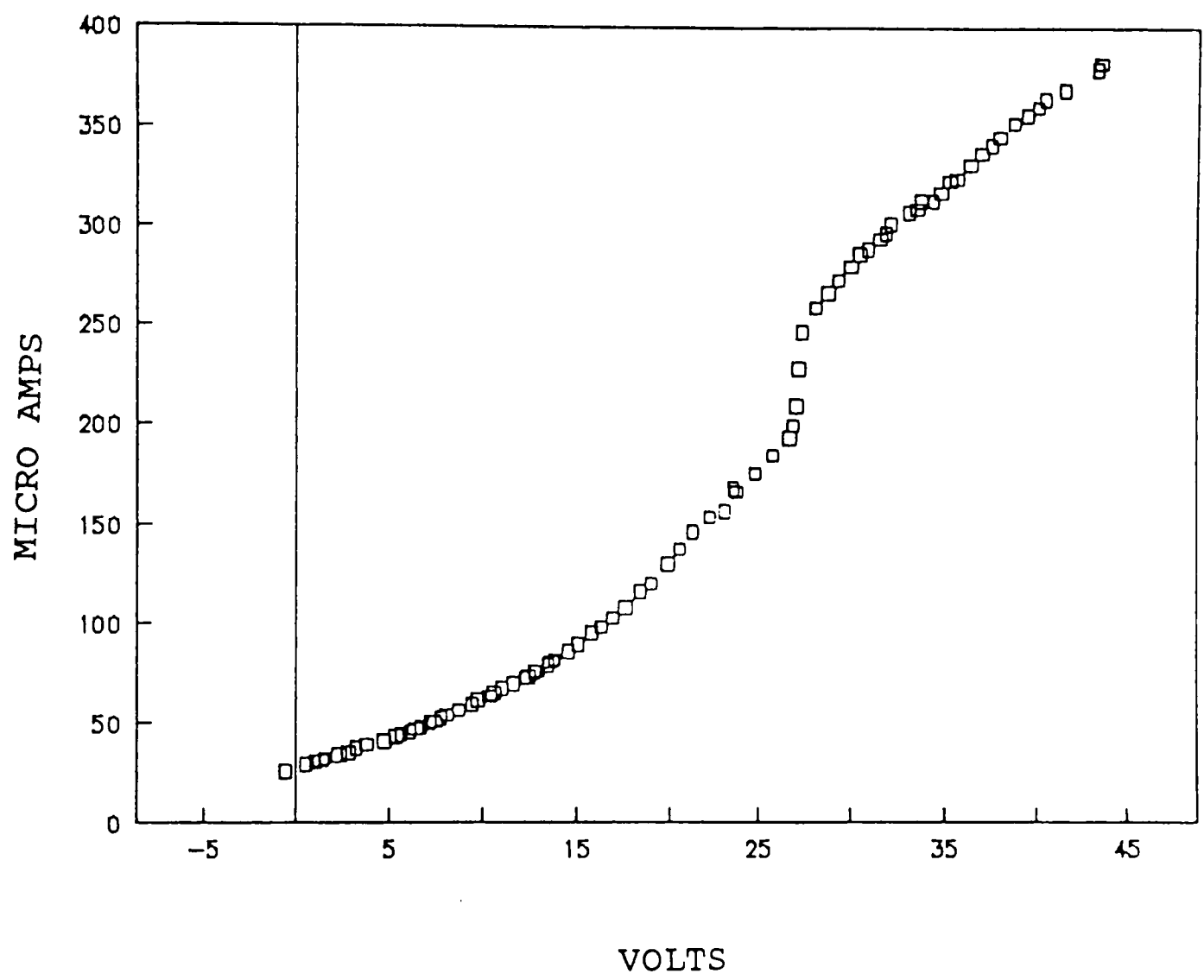


Figure 8: I-V Characteristic Curve for Cylindrical Probe.

the probe wire itself is slowly etched. This brings about a noticeable decrease of the wire diameter over extended period of time, thus affecting the effective probe area.

A semi-log plot of the probe current versus the potential applied to the probe will allow one to extract the electron temperature and the electron density. The electron temperature (T_e) can be found using the following equation(40):

$$T_e = 5040 \times (dv). \quad (4.2)$$

Here dv is the voltage difference for an order of magnitude change in the probe current; this can be seen in Figure 8. The electron density can be determined from the same graph and using the following equation:

$$n_e = \left(\frac{4.03 \times 10^{13} \times I_{sat,e}}{A_p \times T_e^5} \right). \quad (4.3)$$

Here $I_{sat,e}$ is the electron saturation current in amps, A_p is the area of the probe in cm^2 and T_e is the electron temperature in Kelvin. The electron saturation current is extracted from the semi-log plot shown in Figure 9, by drawing a tangent line to the electron saturation region. The electron saturation current is the point of intersection of this tangent line and the y-axis. The electron temperature is found from Equation (4.2).

Once the electron density and temperature are known, we can use their value in our plasma kinetic model to obtain

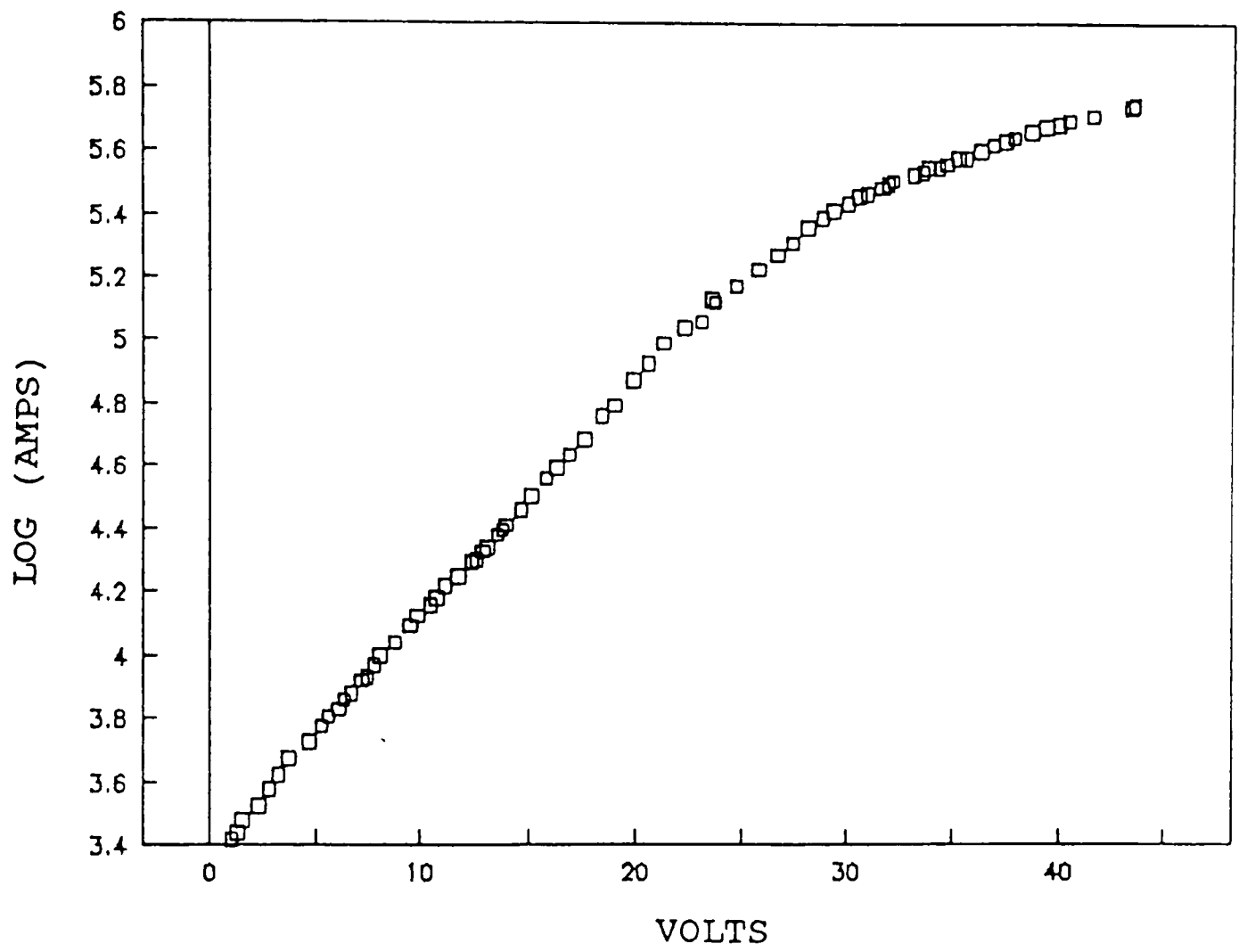


Figure 9: Semilog Plot of I-V Curve.

the extent of electron impact dissociations in the plasma. The electron densities and temperatures obtained with different operating conditions and radial positions in the plasma are presented in Chapter 6.

4.2 Argon Actinometry

A simple non-intrusive method for determining the relative concentration of excited species in a plasma is spectroscopic diagnostics. An excited species is one which has an electron elevated into a higher energy orbital, which is usually unstable. When the electron returns back to its original, stable orbital, or relaxes, it emits a characteristic wavelength of light. The excitations of the atomic or molecular species of interest are dependent on the density of the excited species, which are dependent on electron impact, the emission intensities can be related to the electron density and energy(41). Therefore, the emission intensities alone will not provide a measure of the emissive species concentration.

Coburn and Chen(33), deliberately introduced a small amount of argon (less than 5%) to a CF_4 plasma system which has an excited state at an energy above the ground state close to that of the species of interest so both species sample the same range of the electron energy distribution. A measure of the reactive species concentrations is obtained by taking the ratio of both emission intensities. The

following derivation will show this effect. The excitation reactions for fluorine and argon can be represented by:



Here F^* and Ar^* are the excited states of fluorine and argon, respectively, e^- is an electron and the K 's are the reaction rate constants. The relaxation reactions are:



Here hv is a photon emission and the K 's are the relaxation constants for fluorine and argon, respectively.

The intensities can be written as:

$$I_f = K_{F^*}[F^*] , \quad (4.4)$$

$$I_{Ar} = K_{Ar^*}[Ar^*] . \quad (4.5)$$

Here I_f and I_{Ar} are the emissive intensities of fluorine and argon, respectively. At equilibrium the following equations

can be written:

$$[F^*] = \left(\frac{K_F}{K_{F^*}} \right) \times [F] \times [e^-] , \quad (4.6)$$

$$[Ar^*] = \left(\frac{K_{Ar}}{K_{Ar^*}} \right) \times [Ar] \times [e^-] . \quad (4.7)$$

Combining Equations (4.4) to (4.7) and taking the ratio of intensities gives:

$$\frac{I_F}{I_{Ar}} = \left(\frac{K_F}{K_{Ar}} \right) \times \left(\frac{[F]}{[Ar]} \right) . \quad (4.8)$$

Here K_F and K_{Ar} are the optical excitation rates for fluorine and argon in the discharge, respectively.

The fluorine emission line at 703.7 nm and the oxygen emission line at 884.6, corresponding to 14.5 eV and about 11 eV, respectively, are calibrated to the argon emission line at 750.4 nm, corresponding to an excited state at 13.5 eV(43).

Upon start-up of the reactor the dissociation of CF_4 dilutes the argon. Once steady state is reached and since argon is inert in the plasma, hence unreactive, the argon concentration remains constant. Therefore one obtains a measure of the relative concentration of F atoms in the ground state, [F].

Coburn and Chen(33) found that argon concentrations of less than 5% had to be used in order to maintain the electron energy distribution. The validity of this

technique has been investigated by the use of downstream chemical titration(44) or laser induced fluorescence(45) to monitor variations in F and O atoms concentrations directly. The technique of Ar actinometry was found to perform well and thus was used throughout our experiments.

However, experimentally we can only obtain the intensity of light emission by various species, averaged throughout the reactor. This is because the optic fiber head is located at one point in the reactor and reads an average intensity throughout the reactor. It was observed using point light source (Mercury calibration lamps) that the fiber was able to pick up light emissions from all but a very small portion of the reactor, near the fiber head. However, because this portion was so small, so the light emission from the entire reactor was used for computing the average intensity emission.

In order to experimentally validate the developed plasma model we have to compute the intensity ratios as suggested by Coburn and Chen from the spatial variation of F and Ar concentration predicted by our model.

Using Equation (4.8) and model-predicted values for F and Ar concentration it is possible to compute the intensity ratio of F and Ar at various points in the reactor. However, the emission intensities diminish as they travel over a distance. The inverse square law, popularly used for light emissions, was used to compute the possible average

intensity ratio at the optic fiber from the individual intensity ratio. By this assumption all the emission emanating from an excited atom was assumed to reach the optic fiber without absorption along the way. This may be acceptable to our system due to the low pressure in the reactor, hence:

$$I_2 = I_1 \times \frac{D_1^2}{D_2^2} . \quad (4.9)$$

Here I's represent the intensities and D's represent the distance of the two points 1 and 2 from the center of the atom emitting light.

Figure 10 is a transverse section of the reactor across the optic fiber head. It is required to compute the distance of the emitting particles from the fiber. From Figure 10 we can see that this distance (X) can be easily computed in terms of reactor radius (R), radial distance of the emitting point from the reactor center (r), and the angle (θ) this point makes with the line passing through the fiber head and the center of the reactor, to be:

$$X = \sqrt{(R^2 + r^2 - 2Rr\cos(\theta))} . \quad (4.10)$$

For a particle located in a plane different from the one across the optic fiber, the distance of the light emitting

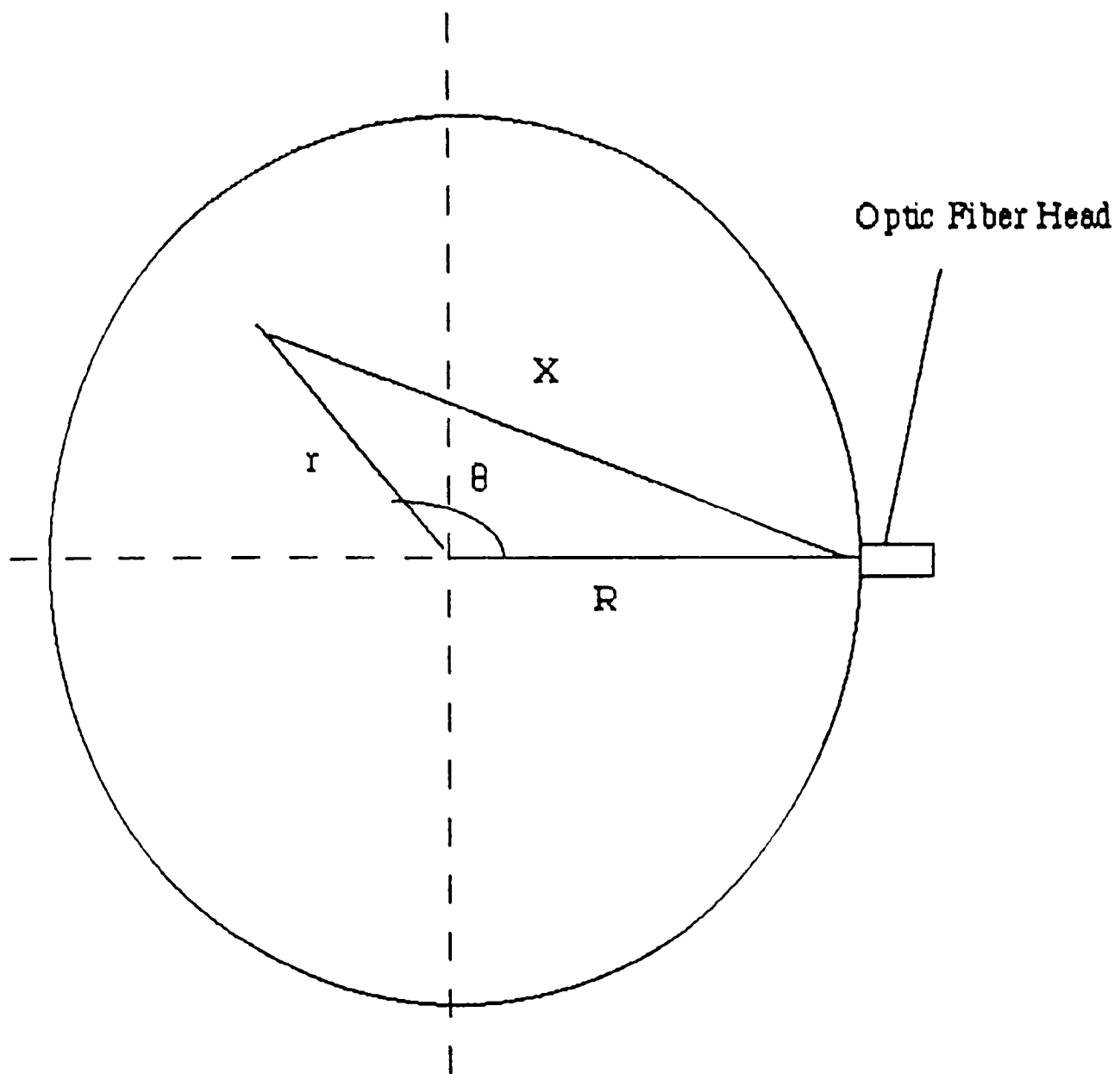


Figure 10: Transverse Section of the Reactor Across the Optic Fiber Head.

particle from the fiber head is:

$$D = \sqrt{(Z^2 + X^2)} . \quad (4.11)$$

Here Z is the distance of the plane containing the particle from the central plane.

Combining Equations (4.4), (4.6), (4.9), (4.10) and (4.11) we obtain the overall intensity of F as a function of the spatial concentration distribution of F, to be:

$$I_F = 2 \sum \left(\frac{K_F [e^-] [F]_i r_F^2}{(z_i^2 + R^2 + r_i^2 - 2Rr_i \cos(\theta_i))^{.5}} \right) . \quad (4.12)$$

Here subscript 'i' designated a particular point on one side of the central plane in the reactor and r_f is the atomic radius of the fluorine atom.

Similarly we can obtain the overall intensity of Ar as:

$$I_{Ar} = 2 \sum \left(\frac{K_F [e^-] [Ar]_i r_{Ar}^2}{(z_i^2 + R^2 + r_i^2 - 2Rr_i \cos(\theta_i))^{.5}} \right) . \quad (4.13)$$

Here r_{Ar} represents the atomic radius of Ar. The atomic radius of F and Ar used in the inverse square law relation represent the point of the maximum intensity. The ratio of F to Ar intensity can be obtained by dividing Equation

(4.12) by Equation (4.13), to give:

$$\frac{I_F}{I_{Ar}} = \sum \left[\frac{K_F}{K_{Ar}} \right] \left[\frac{[F]_i}{[Ar]_i} \right] \left[\frac{r_F^2}{r_{Ar}^2} \right] . \quad (4.14)$$

This equation can be used to convert the model-predicted concentration distribution of F and inert Ar in a CF₄ plasma to the intensity ratio of these species, which can be compared to the experimental results for model validation purposes.

However, in Equation (4.14) the value of the ratio of the constants K_F and K_{Ar} is still not known. A range of values for the ratio of these constants have been suggested in literature. From 0.68 by Mogab(42) to 26 used by Dalvie and Jensen(9), in their model validation step. What is probably more important in assigning a value to this unknown is keeping its value constant for all validation tests for the model against experimental runs and watching if similar trends between model and process are obtained. In our experimental setup a constant value of 0.04 for the product of the ratio of constants and the ratio of the atomic radii was found to give consistently good results. Details of the model outputs are presented in Chapter 8.

CHAPTER 5

PLASMA AND SURFACE KINETIC MODEL

In this chapter the plasma kinetics and surface reaction kinetics which are employed in the model development for this work are discussed. Section one of this chapter presents an overview of plasma reactions suggested in literature along with the reasons for deriving the simplified kinetics used in this work. The surface kinetic model developed from the wafer-plasma reactions is summarized in section two.

Before going into the details of the overall plasma kinetics, it is important to understand the very concept of plasma and its initiation. A plasma is a collection of positively and negatively charged and neutral particles. Simplistically, charge neutrality of the plasma requires that the number density of the positive charge be equal to that of the negative ones. Plasma constitutes the "fourth state" of matter. While solid, liquid and gaseous states dominate our earthly experiences plasma is by far the most common form of matter, constituting about 99% of the universe(15). It is also the most energetic state.

There are three important regions in the plasma, a dark space or sheath by each electrode and a glowing region, "plasma like," between them. Figure 11 illustrates the three regions in a simplified view of the rf discharge. The glow region is relatively neutral, because the concentration

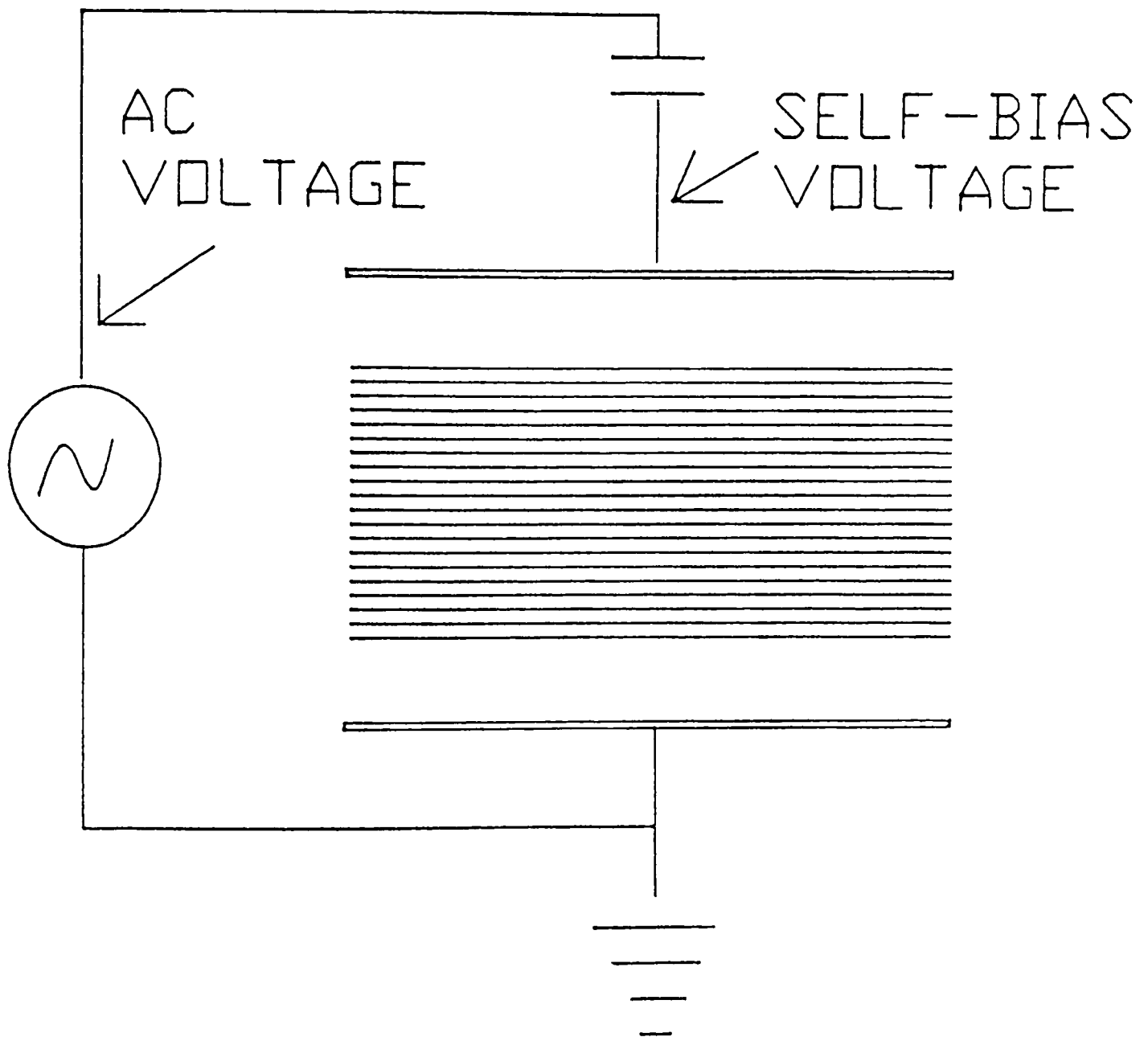


Figure 11: Simplified View of a rf Glow Discharge Process(12).

of the negative species (mostly electrons) is essentially equal to the positive ions. The sheath areas are ion clouds of charge opposite to that of their adjacent electrodes. These areas contain the main electric fields of the system.

The essence of rf plasma as applied to film deposition and etching lies in a self-sustaining discharge between the cathode and anode. The polarity of the electrode plates in a rf plasma changes per cycle and thus prevents the glow from being extinguished by the wafer covered (insulated) lower electrode. When a high frequency voltage is applied between the electrodes, current flows forming a plasma which emits a characteristic glow. The electrons emitted from the electrode plates strike the gas phase species and either cause them to dissociate or excite the electrons in the outer orbital of these species. The characteristic glow is observed as the excited electrons in the outer orbital of the gas phase relax to lower energy orbital. Reactive radicals are generated by this electric discharge. Semiconductor wafers or other substrate material on the electrode surfaces are exposed to reactive neutral and charged species. Some of these species combine with the substrate and form volatile products that volatilize, etching the substrate.

In our CF_4 plasma system a multitude of positive and negative species are produced. The positive charge is mostly in the form of singly ionized neutrals, mostly

CF_3^+ (39). The majority of negative charged particles are free electrons, being lighter than other species in the plasma they are more mobile. As they collide with parent gas molecules, they gain higher energies than neutrals and other ions in the plasma. The energy of electrons can reach 5 to 20 eV which is equivalent to tens of thousands of degrees above the gas temperature(1). This elevated electron temperature permits electron-molecule collisions to excite high temperature type reactions, which forms reactive free radicals, in a low temperature neutral gas.

The most abundant products from a CF_4 discharge are F, F_2 , CF_2 , C_2F_6 and CF_3 (3,9), but a number of other species like C_2F_4 , CF (30,28) have also been detected and reported in the literature. However, there is increasing evidence in the literature(1,2,4,25) that F, which is the most abundant reactive species in a CF_4 plasma is chiefly responsible for the etching of SiO_2 wafers. D'Agostino et al.(16) obtained data, Figure 12, which indicates that the etch rate of silicon dioxide is proportional to the F concentration. Oxygen addition to the feed gas (CF_4), results in an enhancement of the F radical concentration. This has been modeled by Plumb and Ryan(5). But higher oxygen concentration reduces the etch rate and this could be because of the increased amount of oxygen on the wafer surface. This blocks off the F atom from reaching the wafer surface. Mogab et al.(17) have also reported etch rate data

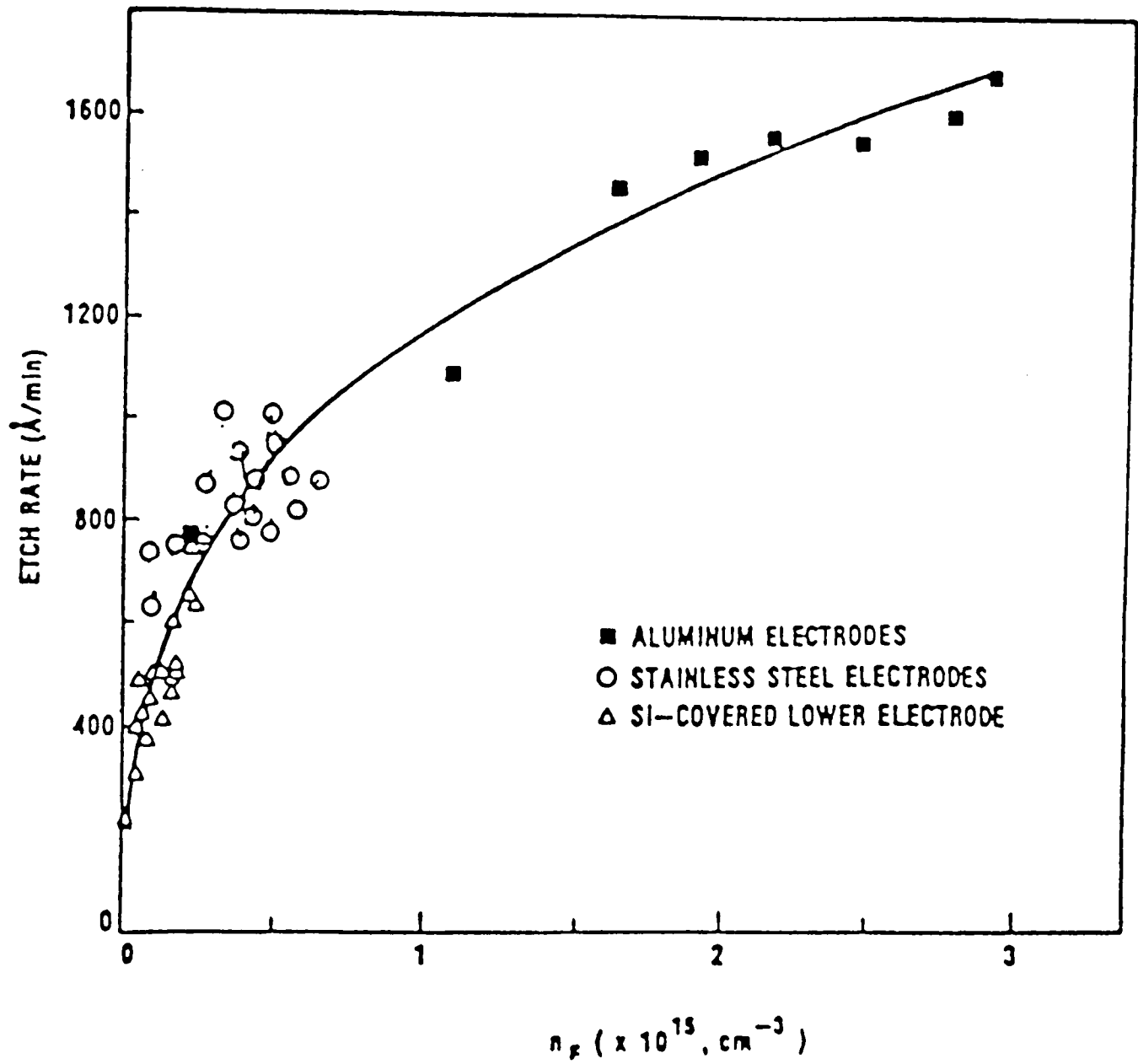


Figure 12: Etch Rate vs. F Concentration for Different Electrodes(16).

against increasing F concentration. The etch rate was a strong function of F concentration. Some other data indicating that F atoms are the dominant etchants of SiO₂ (Figure 13) was obtained by Manos and Flamm(1). Their data show the etch rate of silicon dioxide as a function of F atom concentration for three gases mixtures. All these three gases generate F in the plasma. Their data support both the multi step F etch mechanism (rate vs. F concentration) as well as simultaneous etching by some other mechanism (positive intercept).

There are a multitude of other species present in the plasma that could be etching the SiO₂ wafer along with F. However, it is not possible to detect and quantify the concentration of these other species in the plasma using an optical emission spectrometer that is available to us. A mass spectrometer is minimally required for this service. Taking into account the constraints put forth by the data gathering system and realizing the fact that F is the dominant etching species the modeling in this work was based around F concentration.

The etching reaction is also believed to be assisted by ion bombardment on the wafer surface, which weakens the SiO₂ bonds, and helps hasten the reaction of F with SiO₂ to form volatile product SiF₄. Further details on the surface reaction mechanism are outlined in next section of this chapter.

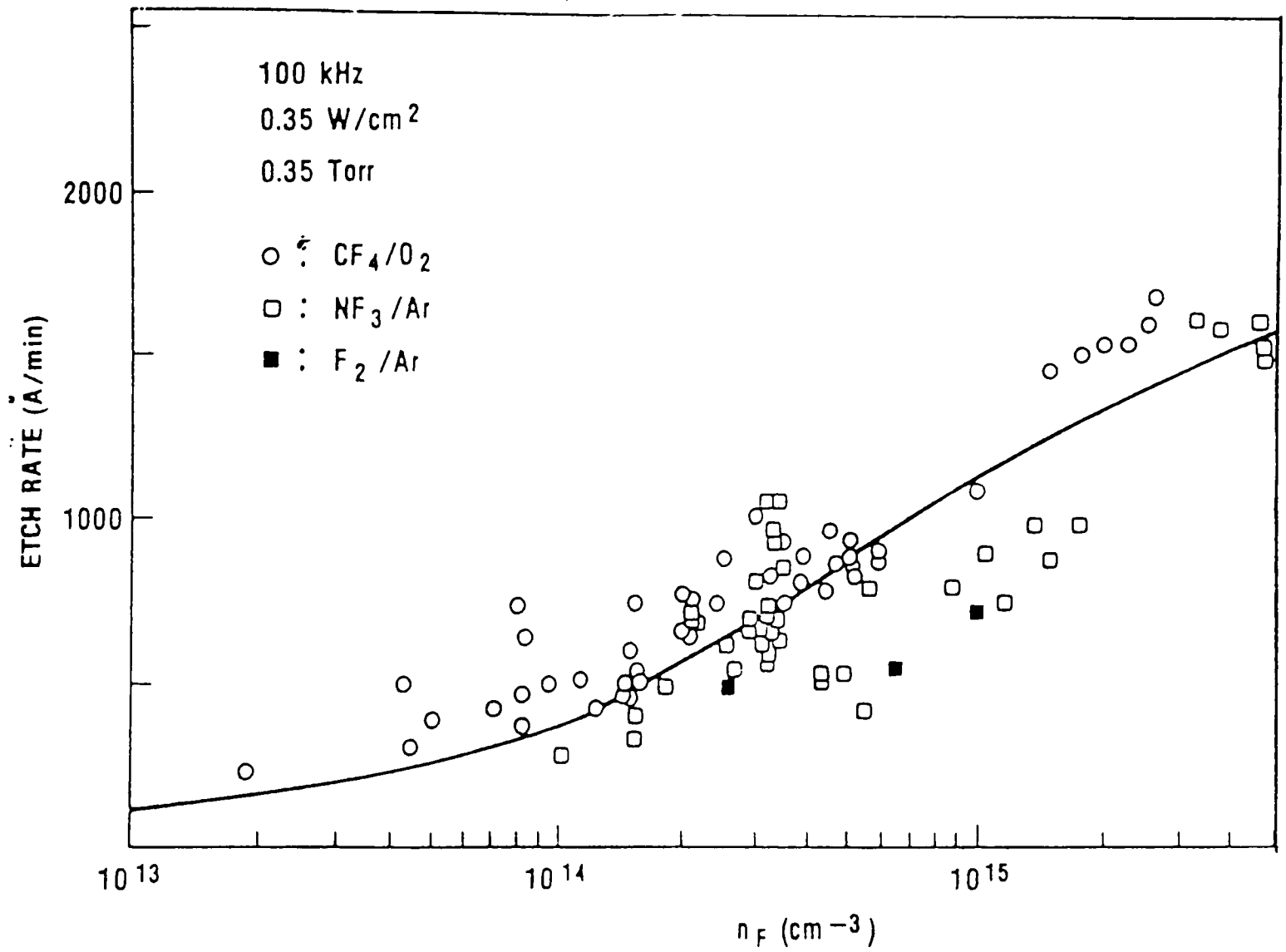


Figure 13: Etch Rate vs. F Concentration for Different Feed Gases(1).

5.1 CF₄ Plasma Kinetic Model

As pointed out in Chapter 2, there have been several works published on plasma kinetics. However, the works of Edelson and Flamm and Plumb and Ryan present detailed treatment of a CF₄ plasma and are of primary use here. Moreover, it was also pointed out in Chapter 2 that the equipment setup used to generate the kinetic data was entirely different from our setup. Figure 1 shows Smolinsky and Flamm's experimental setup from which both these pairs of researchers developed their kinetic models. The mass spectrometer used by Smolinsky and Flamm to detect and identify the species present in the plasma was housed 15 cm downstream of the rf powered reaction chamber. The reaction chamber is a cube of 5 cm dimensions. This setup would result in a very small residence time for feed gas in the reaction chamber, even for a moderately low flowrate. Hence the percentage dissociation of CF₄ would to be very small. The tube through which the reaction products flow into the mass spectrometer offers a significant residence time and reaction area for these highly reactive products to recombine. The residence time of the reactants coming out of the reaction chamber is about three times more than that in the reaction chamber. This raises the question whether the concentration or the very nature of all the species detected downstream are of any significance in the plasma where the actual etching process takes place.

However, in our experimental setup (Figure 4) the feed gas (CF_4) enters the reactor chamber, dissociates, and produces reactive species (mostly F) before exiting through the center of the reactor. Hence, directly using the reaction scheme developed for a totally different setup may not be a true representation of our system. In our modeling work an attempt is made to use simplified plasma kinetics derived out of the reaction schemes in literature to predict the trends obtained by experimentation. Table 1 illustrates the reaction scheme proposed by Edelson and Flamm, and Table 2 illustrates Plumb and Ryan's reaction scheme. The complexity of these schemes is readily noticeable. Plumb and Ryan's kinetic scheme accounts for eight species participating in sixteen reactions, whereas Edelson and Flamm's scheme is even more complicated.

Another facet of the two schemes that was pointed out earlier was that while Edelson and Flamm reported kinetic rate constants for the electron dissociation reaction, Plumb and Ryan reported the product of electron density and kinetic rate constant for the same reactions. But, since Plumb and Ryan do not indicate the electron density that they found to exist in their system, so there is no way of computing their rate constants. Moreover, using the electron density from our setup to compute their rate constants is not justified either, since it electron density is a very strong function of reactor geometry. Hence

Table 1: Reaction Scheme for a CF₄ Plasma--Proposed by Edelson and Flamm(4).

Rxn No.	Reactions	Rate Expression	Rate constant (cgs units)
(5)	$e^- + CF_4 \rightarrow CF_3 + F + e^-$	Parameter	1.00×10^{-10}
(6)	$CF_3 + F + M \rightarrow CF_4 + M$	Parameter	3.50×10^{-32}
(7)	$2CF_3 \rightarrow C_2F_6^*$	$2.002 \times 10^{-14} - 3.462 \times 10^{-13}$	5.92×10^{-32}
(8)	$C_2F_6^* \rightarrow 2CF_3$	$2.367 T^{1.5} - 4.093 \times 10^{12} x$ $(T/500)^{3.3196}$	1.30×10^4
(9)	$C_2F_6^* + M \rightarrow C_2F_6 + M$	$9.6 \times 10^{12} T^{0.5}$	1.70×10^{-10}
(10)	$e^- + C_2F_6 \rightarrow 2CF_3 + e^-$	Parameter	5.00×10^{-9}
(11)	$F + F + M \rightarrow F_2 + M$	$7.3 \times 10^{-32} T^{-1.0334}$	1.92×10^{-34}
(12)	$e^- + F_2 \rightarrow F + F + e^-$	$1.0 \times 10^{-9} T_e^{1.5} x$ $(2 + 2.7/T_e) e^{(-2.7/T_e)}$	1.65×10^{-8}
(13)	$e^- + F_2 \rightarrow F + F^-$	$T_e < 0.67$ $T_e > 0.672.92 \times 10^{-10}$	6.0×10^{-9}
(14)	$e^- + F^- \rightarrow F + 2e^-$	$1.2 \times 10^{-10} T_e^{1.5} x$ $(2 + 3.45/T_e) e^{(-3.45/T_e)}$	1.81×10^{-9}
(15)	$CF_3^+ + F^- \rightarrow CF_3 + F$	Estimated	4.00×10^{-7}
(16)	$F + F^- \rightarrow F_2 + e^-$	$1.4 \times 10^{-10} e^{-1.9/T_i}$	9.73×10^{-32}
(17)	$F^- + M \rightarrow F + M + e^-$	$1.1 \times 10^{-10} x$ $e^{-42940/(1.16 \times 10^4 T_i)}$	0.0
(18)	$CF_3 + F_2 \rightarrow CF_4 + F$	Estimated	3.32×10^{-12}
(19)	$CF_3 + F^- \rightarrow CF_4 + e^-$	Estimated	5.00×10^{-10}
(20)	$e^- + CF_3^+ \rightarrow CF_3$	$3.95 \times 10^{-9} T_e^{-0.5} T_i^{-1}$	4.53×10^{-8}

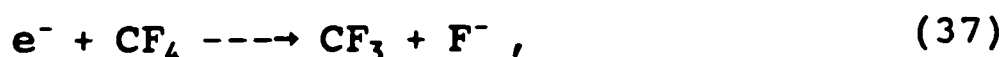
Table 2: Reaction Scheme for a CF_4 Plasma--Proposed by Plumb and Ryan(6).

Rxn. No.	Reaction	Rate Coefficient at .5 torr (cgs units)
(21)	$CF_4 + e^- \rightarrow CF_3 + F + e^-$	6.0
(22)	$CF_4 + e^- \rightarrow CF_2 + 2F + e^-$	14.0
(23)	$CF_3 + e^- \rightarrow CF_2 + F + e^-$	20.0
(24)	$CF_2 + e^- \rightarrow CF + F$	20.0
(25)	$CF_3 + CF_3 + M \rightarrow C_2F_6 + M$	8.0×10^{-12}
(26)	$CF_3 + F + M \rightarrow CF_4$	1.3×10^{-11}
(27)	$CF_2 + CF_2 \rightarrow C_2F_4$	5.0×10^{-14}
(28)	$CF_2 + F + M \rightarrow CF_3$	4.2×10^{-13}
(29)	$CF + F + M \rightarrow CF_2$	5.0×10^{-15}
(30)	$C_2F_6 + e^- \rightarrow CF_3 + CF_3$	20.0
(31)	$C_2F_4 + e^- \rightarrow CF_2 + CF_2$	20.0
(32)	$F + C_2F_4 \rightarrow CF_3 + CF_2$	4.0×10^{-11}
(33)	$CF_2 + CF_3 + M \rightarrow C_2F_5 + M$	8.8×10^{-13}
(34)	$C_2F_5 + F \rightarrow CF_3 + CF_3$	1.0×10^{-11}
(35)	$CF + CF_2 \rightarrow C_2F_3$	1.0×10^{-12}
(36)	$C_2F_3 + F \rightarrow C_2F_4$	1.0×10^{-12}

Edelson and Flamm's model was employed after further modifications in our modeling work.

The gas phase reactions compiled by Edelson and Flamm along with their rate constants were presented in Table 1. They compiled the reaction set from various sources and validated it against the experimentally generated data of Smolinsky and Flamm.

The overall plasma phase reactions proposed by Edelson and Flamm are based on the ion impact reaction of CF_4 and subsequent recombination of the reactive species formed. When impacted by energetic electrons, CF_4 tends to dissociate since it does not have any excited states(18). It takes a relatively high energy electron to dissociate CF_4 , and Mogab et al.(17) proposed a dissociative attachment route employed by Edelson and Flamm for the dissociation of CF_4 . The reactions they proposed are as follows:



Reaction (38) is an extremely fast reaction and hence reaction (37) becomes the rate limiting step. Since it is difficult to detect any traces of F^- , the rate constant for the above two reactions is reported by Edelson and Flamm for

a single step overall reaction:



This reaction produces small amounts of CF_3 and F species. According to Edelson and Flamm these two species take part in a number of side reactions.

The reactions involving CF_3 show that there is no significant association or dissociation of this species any further. The rate constant for reaction (8) is approximately 2.0×10^{15} times greater than reaction (7) and 8.0×10^{13} times greater than reaction (9). Hence whatever minimal amount of CF_3 combines to form $C_2F_6^*$, dissociates readily to CF_3 . Thus the concentration of C_2F_6 is negligible compared to the concentration of CF_3 and hence the side reactions involving CF_3 can be neglected for modeling purposes.

Similarly, studying the F species recombination reactions we can clearly see from reaction (11), from Table 1 that the rate constant for recombination of F is of the order of 2.0×10^{-34} and also this reaction takes place only on the wall. This would mean that very small amounts of F are removed by recombination, hence for all practical purposes the recombination of F can be neglected.

Of the sixteen reactions proposed by Edelson and Flamm we are now left with only two reactions:



Here again the recombination rate proposed by Edelson and Flamm (reaction (3)) is slow compared to the rate of dissociation of CF_4 (reaction (5)). The CF_4 recombination rate is about 4.0×10^{-22} times slower than the dissociation reaction and also it occurs only on the wall of the reaction chamber. This leaves us with only one reaction of significance from the plasma reaction scheme proposed by Edelson and Flamm. They also proposed that the electron-impact dissociation reactions are first-order with respect to CF_4 . Hence the rate expression for reaction(5) can be expressed as:

$$r_{CF_4} = - k_1 \times [CF_4][e^-] . \quad (5.16)$$

The value of k_1 used in this modeling work was different from that proposed by Edelson and Flamm. This value of the plasma kinetic rate constant is 1.1×10^{-11} cm/sec.

The simplified plasma kinetics developed above was used to model the reactive species concentration distribution in the plasma reactor.

5.2 Surface Reaction Kinetic Model

In a parallel research work(31) conducted at Texas Tech University, a phenomenological kinetic model was derived from a proposed sequence of elementary chemical reactions to predict the etch rate of SiO₂ in a CF₄ and CF₄/O₂ plasmas. The kinetic model developed was parameterized using the experimental data available in literature(1) and also through our own data generated at our experimental setup. The kinetic model was found to be in good agreement with the data used. Details of this work will be addressed to in reference 31. In this section the final form of the kinetic expression is reported.

In developing the kinetic model it was assumed that an ion assisted chemical reaction is responsible for the etching of SiO₂ surface. The high energy ions are responsible for weakening the SiO₂ bonds while the F atoms react with the surface forming a volatile product, which desorbs. The final kinetic model developed that accounts for these two phenomena is:

$$\text{Etch Rate} = \frac{K_1 \times [F] \times [\text{ION}] + K_2 \times [F]}{[\text{ION}] + K_3 \times [F]} \quad (5.17)$$

The values of the rate constant K₁, K₂ and K₃ were adapted from reference 31. The surface kinetic model was parameterized using the average F concentration in the reactor. This average F concentration can be expected to be generally higher than the F concentration on the wafer

surface, which should be used for parameterization purposes. Hence all the rate constants used here were reduced from those presented in reference 31. The values of these rate constants are:

$$K_1 = 4.34 \times 10^8 \text{ A cm}^3 / \text{min g-mole},$$

$$K_2 = 95.45 \text{ A /min g-mole},$$

$$K_3 = 0.74 \text{ l /g-mole}.$$

The ion density used in the surface kinetic equation was obtained experimentally. It was observed here that during experimental that ion density value does not change much (1.0×10^{11} to 1.0×10^{12} ion/cm³), hence a constant intermediate of 0.5×10^{12} ion/cm³ was used for ion density.

CHAPTER 6

MODEL DEVELOPMENT

The three-dimensional mathematical model developed to model the F concentration distribution in the reactor is presented in this chapter. In order to gain a phenomenological insight into the plasma etching process it is important to obtain the etch rate distribution profile in the reactor, for which we have to solve the concentration distribution equation for F. Fluorine is the main reactive species for CF_4 etch of SiO_2 . However, in order to solve the concentration distribution equation it is important to know the background flow profile in the reactor. Knowing the reactive species distribution in the reactor it is possible to access the factors that influence the uniformity of etching and these factors can be subsequently manipulated to eliminate undesired phenomena like the bullseye effect. The fluid flow and the concentration distribution model which are needed to model the plasma reactor are presented in this chapter.

The modeling of a plasma system requires various coupled phenomena to be considered. However, one advantage offered by a CF_4 plasma is that because of the small dissociation of CF_4 , less than 10%(1,5), there is an insignificant change in the volume of the overall gaseous system. This feature, along with the fact that the gas temperature and pressure stay almost constant in the plasma

reactor, can be used to decouple the momentum balance equation from the material (or species) balance equation. Appendix A presents simple calculations to support the fact that the dominant species in the plasma is CF_4 . The gas flowing through the reactor retains the physical properties of the feed gas because of negligible change in the gas composition and temperature. Two sources that contribute to changes in gas temperature are the heat of reaction from the dissociation of CF_4 and the heat transfer from the heater plate to the gaseous system. Since the overall dissociation of CF_4 is small, the heat of generated in this dissociation reaction is diluted by the gas phase and thus has an insignificant affect on the overall gas temperature. Elementary calculations show that the heat transfer from the heater plate to the bulk gas phase is very small. This results in a very small rise in the gas temperature and hence has been neglected in our modeling work. These calculations are presented in Appendix B.

Before details of the mathematical model are discussed, it is important to develop guidelines for the estimate of the important physical properties of the gas phase. The physical properties that need to be estimated are: density of the gas phase, viscosity of the gas phase and the diffusion coefficient of various species. Typically, for plasma etching runs our reactor was operated at low pressures, between the range of 200 to 400 mTorr (2.6×10^{-4}

to 5.3×10^{-4} atm). Taking into account the low pressures of the reacting gaseous systems and considering the fact that all gases exhibit near ideal properties at low pressures, the ideal gas law was used in the estimation of gas properties. Details of estimation methods used to compute the gas property are presented and discussed in Appendix C.

6.1 Fluid Flow Model

In order to model the plasma reactor so as to predict the species concentration distribution, it is momentous to obtain the flow profile. Velocity profile is an important variable in the material balance equation and hence has to be solved first. In order to obtain the velocity profile, the momentum balance equations needs to be solved. However, before we go into the details of the momentum balance equations it is imperative to get a feel of the type of flow that typically exists our plasma reactor. Two aspects of flow that help characterize it are--regime of flow (slip or nonslip) and type of flow (laminar or turbulent). The flow regime characterizes the boundary conditions whereas flow type outlines the solution procedure that has to be followed in order to solve the momentum balance equations. Typical operating conditions in our reactor were selected and preliminary calculations were conducted which show that the flow is laminar and exhibits no slip at the boundary. Details of these calculations are presented in Appendix D.

The first step in obtaining the velocity profile was the formulation of the differential momentum balance on a cylindrical element. The final momentum balance equation developed is simplified based on various assumptions summarized later. The final equation was developed by nondimensionalizing the simplified momentum balance equation. The solution methodology developed to solve the final equation along with the boundary conditions is discussed towards the end of this section.

6.1.1 Differential Momentum Balance

The differential element along with the various momentum transport forces is presented in Figure 14. The general momentum balance on a differential element for time Δt is given as:

$$\begin{array}{ccccccc} & & & \text{Sum} & & & \\ & & & \text{of} & & & \\ & & & \text{Forces} & & & \\ & & & \text{Acting} & = & & \\ & & & \text{on} & & & \\ & & & \text{the} & & & \\ & & & \text{System} & & & \\ \text{Rate} & & \text{Rate} & & \text{Rate} & & \\ \text{of} & & \text{of} & & \text{of} & & \\ \text{momentum} & - & \text{Momentum} & - & \text{Momentum} & & \\ \text{in} & & \text{out} & & \text{Accumulation} & & \\ & & & & & & \\ & & & & & & \text{(6.18)} \end{array}$$

Advection and diffusion contribute to the rate of momentum flow into and out of the element. Body forces, or the forces acting on the system, could be gravity, electromagnetic forces, and momentum generated due to change in volume and pressure. However, there is a negligible dissociation of CF_4 and negligible change in feed gas temperature, thus the change in volume of the reacting mixture can be neglected. Also bulk of the CF_4 plasma is

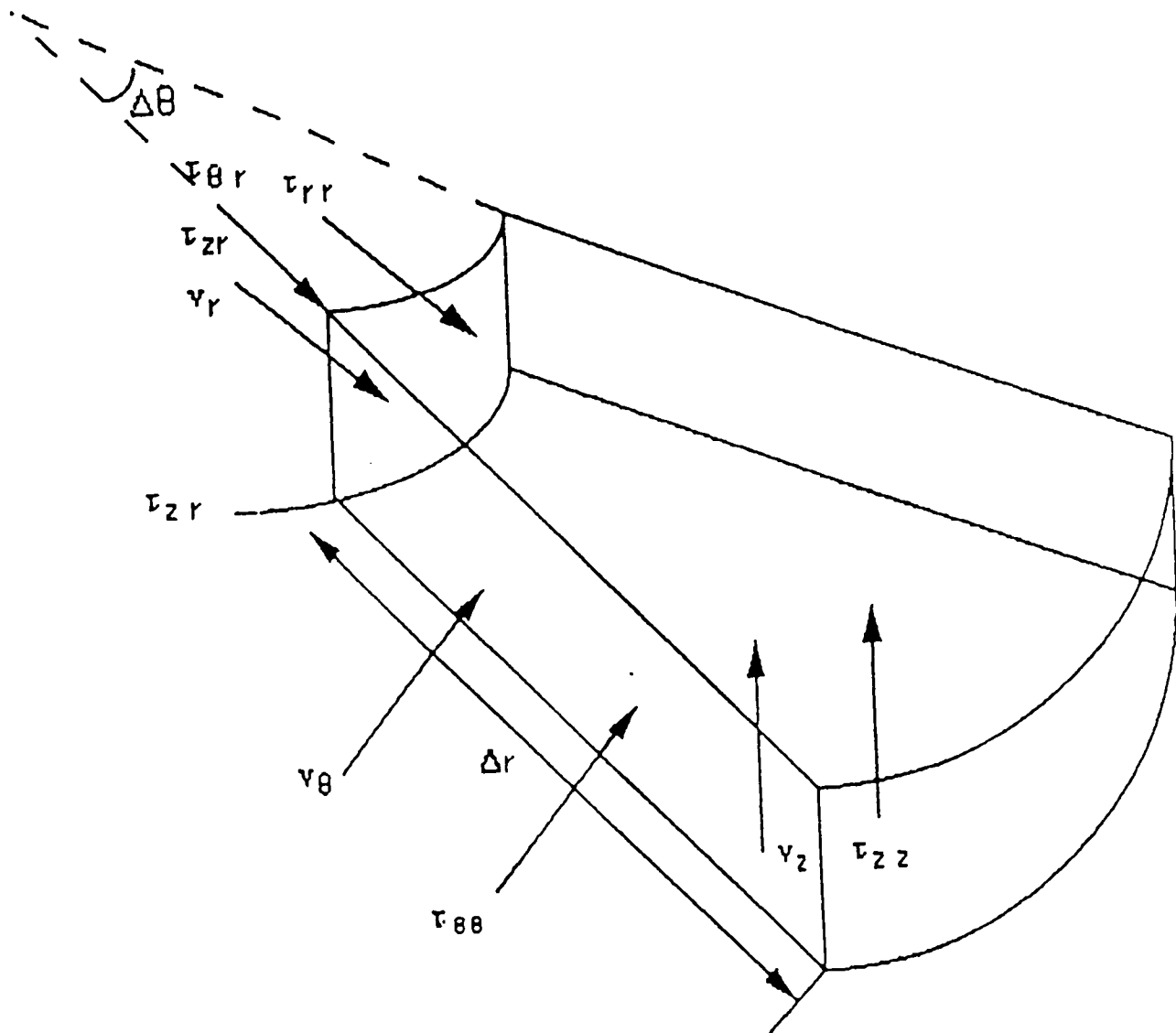


Figure 14: Differential Momentum Balance Element.

neutral in nature, hence the net electromagnetic force acting on it is zero. Thus gravity force and momentum generated due to pressure drop are the body forces that are left to be accounted for in the momentum balance equation.

Equation (6.18) is the momentum balance equation for un-steady state systems. The fluid can move through all six faces (Figure 14) of the differential element in any arbitrary direction. It should also be emphasized that Equation (6.18) is a vector equation with components in each of the three co-ordinate directions r, θ and z . However, for simplicity only the r -component of each momentum force is considered here and the θ - and z -component are handled analogously.

First of all the rate of flow of the r -component of momentum into the volume element is considered. Momentum flows into and out of the cylindrical differential element by two mechanisms: by advection (bulk fluid flow) and by molecular transfer (velocity gradient).

The rate at which the r -component of momentum enters the face at r by advection is $\rho v_r v_r |_{r} r \Delta \theta \Delta z \Delta t$ and the rate at which it leaves at $r + \Delta r$ is $\rho v_r v_r |_{r + \Delta r} (r + \Delta r) \Delta \theta \Delta z \Delta t$. Similar expressions may be written for the other three faces and net advective r -momentum flow into the differential volume for

time Δt is:

$$\begin{aligned}
 & \rho \underline{v}_r \underline{v}_r |_{r} r \Delta \theta \Delta z \Delta t - \rho \underline{v}_r \underline{v}_r |_{r+\Delta r} (r+\Delta r) \Delta \theta \Delta z \Delta t \\
 & + \rho \underline{v}_\theta \underline{v}_r |_{\theta} \Delta r \Delta z \Delta t - \rho \underline{v}_\theta \underline{v}_r |_{\theta+\Delta \theta} \Delta r \Delta z \Delta t \quad (6.19) \\
 & + \rho \underline{v}_z \underline{v}_r |_{z} r \Delta \theta \Delta r \Delta t - \rho \underline{v}_z \underline{v}_r |_{z+\Delta z} r \Delta \theta \Delta r \Delta t.
 \end{aligned}$$

Here ρ represents the density of the gas mixture and v 's are the velocities in r -, θ - and z -directions. Similarly the rate at which the r -component of momentum enters the face at r by net molecular transport is $\underline{\tau}_{rr} |_{r} r \Delta \theta \Delta z \Delta t$, and the rate at which it leaves at $r+\Delta r$ is $\underline{\tau}_{rr} |_{r+\Delta r} r \Delta \theta \Delta z \Delta t$. Similarly other molecular transport momentum can be summed up and for the r -component momentum we get:

$$\begin{aligned}
 & \underline{\tau}_{rr} |_{r} r \Delta \theta \Delta z \Delta t - \underline{\tau}_{rr} |_{r+\Delta r} (r+\Delta r) \Delta \theta \Delta z \Delta t \\
 & + \underline{\tau}_{zr} |_{z} r \Delta \theta \Delta r \Delta t - \underline{\tau}_{zr} |_{z+\Delta z} r \Delta \theta \Delta r \Delta t \quad (6.20) \\
 & + \underline{\tau}_{\theta r} |_{\theta} \Delta z \Delta r \Delta t - \underline{\tau}_{\theta r} |_{\theta+\Delta \theta} \Delta z \Delta r \Delta t.
 \end{aligned}$$

Here $\underline{\tau}_{rr}$ is the normal stress on the r -face and $\underline{\tau}_{zr}$ and $\underline{\tau}_{\theta r}$ are the r -directed tangential stresses on the z -face and θ -face, respectively, resulting from the viscous forces.

The body forces arising from the fluid pressure p and the gravitational forces per unit mass g can be expressed in r -direction as:

$$\begin{aligned}
 & p |_{r} r \Delta \theta \Delta z \Delta t - p |_{r+\Delta r} (r+\Delta r) \Delta \theta \Delta z \Delta t \quad (6.21) \\
 & + \rho g_r r \Delta \theta \Delta r \Delta z \Delta t.
 \end{aligned}$$

Finally, the rate of accumulation of r-momentum for time Δt within the cylindrical element is:

$$\rho \underline{v}_r |_{t+\Delta t} r \Delta \theta \Delta r \Delta z - \rho \underline{v}_r |_t r \Delta \theta \Delta r \Delta z . \quad (6.22)$$

The individual momentum expressions were substituted in Equation (6.18) and on dividing by $r \Delta r \Delta \theta \Delta z \Delta t$, and taking the limit as Δr , $\Delta \theta$, Δz and Δt approach zero, we obtain the r-component of the momentum balance equation:

$$\begin{aligned} & - \left(\frac{1}{r} \frac{\partial}{\partial r} (r \underline{v}_r^2 \rho) + \frac{1}{r} \frac{\partial}{\partial \theta} (\underline{v}_\theta \underline{v}_r \rho) + \frac{\partial}{\partial z} (\underline{v}_z \underline{v}_r \rho) \right) \quad (6.23) \\ & - \left(\frac{1}{r} \frac{\partial}{\partial r} (r \underline{\tau}_{rr}) + \frac{1}{r} \frac{\partial}{\partial \theta} (\underline{\tau}_{\theta r}) + \frac{\partial}{\partial z} (\underline{\tau}_{zr}) \right) - \frac{\partial p}{\partial r} + \rho g_r = \frac{\partial}{\partial t} (\rho \underline{v}_r) . \end{aligned}$$

Equation (6.23) can be expanded and rearranged as:

$$\begin{aligned} & - (\underline{v}_r \frac{\partial}{\partial r} (\underline{v}_r \rho) + \frac{1}{r} \underline{v}_\theta \frac{\partial}{\partial \theta} (\underline{v}_r \rho) + \underline{v}_z \frac{\partial}{\partial z} (\underline{v}_r \rho)) \\ & - \left(\frac{1}{r} (\underline{v}_r \rho) \frac{\partial}{\partial r} (r \underline{v}_r \rho) + \frac{1}{r} (\underline{v}_r \rho) \frac{\partial}{\partial \theta} \underline{v}_\theta \right) \quad (6.24) \\ & + (\underline{v}_r \rho) \frac{\partial}{\partial z} \underline{v}_z - \left(\frac{1}{r} \frac{\partial}{\partial r} (r \underline{\tau}_{rr}) + \frac{1}{r} \frac{\partial}{\partial \theta} (\underline{\tau}_{\theta r}) + \frac{\partial}{\partial z} (\underline{\tau}_{zr}) \right) \\ & - \frac{\partial p}{\partial r} + \rho g_r = \frac{\partial}{\partial t} (\rho \underline{v}_r) . \end{aligned}$$

Now the like terms can be combined using the ∇ operator to give:

$$- \underline{v} \cdot \underline{\nabla} (\rho \underline{v}_r) - \underline{v}_r \rho (\underline{\nabla} \cdot \underline{v}) - \underline{\nabla} \cdot \underline{\tau}_{ir} \quad (6.25)$$

$$\rho g_r \frac{\partial p}{\partial r} = \frac{\partial}{\partial t} (\rho \underline{v}_r) .$$

The θ - and z -component of the momentum balance equations may be obtained similarly. For θ -direction we have:

$$\begin{aligned}
 & - \underline{v} \cdot \underline{\nabla}(\rho \underline{v}_\theta) - \underline{v}_\theta \rho (\underline{\nabla} \cdot \underline{v}) - \underline{\nabla} \cdot \underline{\tau}_{i\theta} + \rho \underline{g}_\theta \\
 & - \frac{1}{r} \frac{\partial}{\partial \theta} p = \frac{\partial}{\partial t} (\rho \underline{v}_\theta) .
 \end{aligned} \tag{6.26}$$

For z -direction we have:

$$\begin{aligned}
 & - \underline{v} \cdot \underline{\nabla}(\rho \underline{v}_z) - \underline{v}_z \rho (\underline{\nabla} \cdot \underline{v}) - \underline{\nabla} \cdot \underline{\tau}_{iz} + \rho \underline{g}_z \\
 & - \frac{\partial}{\partial z} p = \frac{\partial}{\partial t} (\rho \underline{v}_z) .
 \end{aligned} \tag{6.27}$$

The tensor $\underline{\tau}_{ir}$ represents $\underline{\tau}_{rr}$, $\underline{\tau}_{\theta r}$ and $\underline{\tau}_{zr}$, and similarly for the other two sets of stresses we have the tensor $\underline{\tau}_{i\theta}$ and $\underline{\tau}_{iz}$. All these nine components can be represented as $\underline{\Gamma}$ (stress tensor) and we can write the combined momentum balance equations as:

$$- \underline{v} \cdot \underline{\nabla}(\rho \underline{v}) - \underline{v} \rho (\underline{\nabla} \cdot \underline{v}) - \underline{\nabla} \cdot \underline{\Gamma} + \rho \underline{g} - \underline{\nabla} p = \frac{\partial}{\partial t} (\rho \underline{v}) . \tag{6.28}$$

6.1.2 Assumptions

Various assumptions have been stated earlier in this chapter. Here we summarize all the earlier mentioned assumptions along with certain additional presuppositions that have been used to solve the momentum balance equation in the next section.

1. The major assumption that the gas phase is homogenous with mostly CF_4 , discussed in Appendix

A, leads to various other presuppositions that are stated below:

The volume, temperature and pressure changes in the gas phase are negligible as it flows across the plasma reactor. This further implies that the physical properties of gas such as density (ρ), viscosity (μ) and diffusion coefficients stay constant.

2. Because of the low operating pressure in the plasma reactor the gas phase is treated as ideal.
3. Consistent with the ideal gas state, gas phase is assumed to be Newtonian.
4. The etching process is assumed to be at steady state. During experimentation it was observed that the steady state condition is achieved relatively quickly (2 minutes) as compared to the total etch time (20 minutes). Figure 15 illustrates a typical plot of the ratio of intensity of F to Ar with etch time. Details on this plot were discussed in Chapter 4, and it was indicated that this plot represents F concentration versus time. The F concentration is seen to build up initially and later stabilize to its steady state value. This happens when the rate of production of F is balanced by its rate of consumption on the wafer surface. Hence the

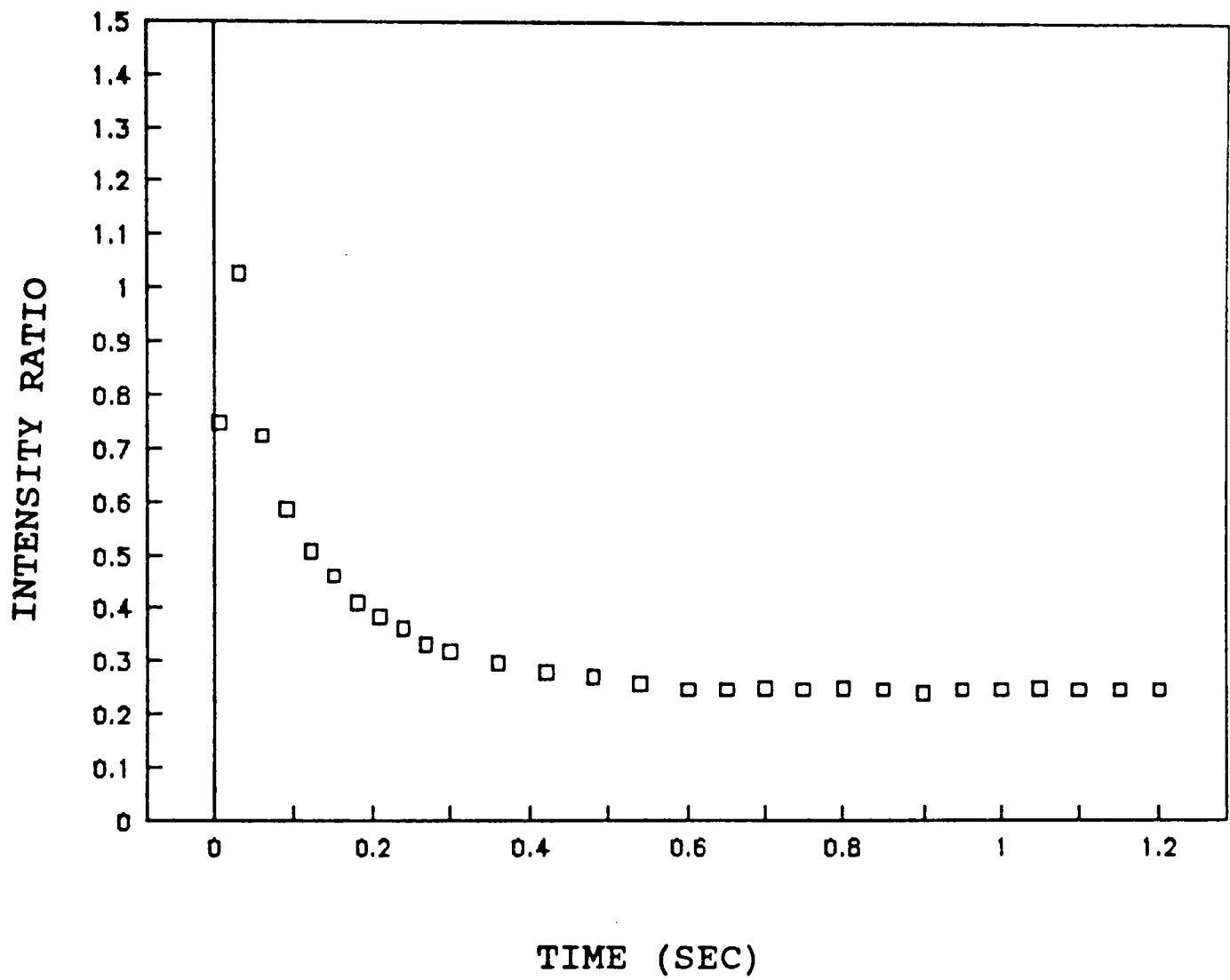


Figure 15: Time Dependence of Fluorine Intensity.

assumption of steady state condition in solving momentum and material balance equations is fairly justified.

5. The flow in the reactor was assumed to be in r-direction only (one dimension). It is easy to see based on the highly laminar nature of the flow (Appendix D) that the flow is axisymmetric, meaning that there is no tangential velocity (v_θ) in the reactor. Axial velocity (v_z) becomes prominent only at the inlet and exit of the reactor, due to the end effects. However, for now it will be assumed that the inlet and exit lengths are negligible as compared to the overall flow path length. This assumption will be justified later, in Chapter 9 by constraining the inlet and exit flow to both parabolic and flat profile and by observing the distance over which the flow fluid develops.

6.1.3 Analysis of Momentum Balance Equation

The r-component momentum balance which describes the flow for our plasma reactor can be simplified by using the various assumptions stated earlier. First of all we restate

the r-component momentum balance equation:

$$\begin{aligned}
 & - \underline{\underline{V}} \cdot \underline{\underline{\nabla}}(\rho \underline{\underline{v}}_r) - \underline{\underline{v}}_r \rho (\underline{\underline{\nabla}} \cdot \underline{\underline{V}}) - \underline{\underline{\nabla}} \cdot \underline{\underline{\tau}}_{ir} \\
 & + \rho \underline{\underline{g}}_r - \frac{\partial}{\partial r} p = \frac{\partial}{\partial t} (\rho \underline{\underline{v}}_r).
 \end{aligned} \tag{6.25}$$

The simplification of this equation is conducted as follows:

1. The etching process is assumed to be at steady state, hence the net accumulation is zero. This simplifies Equation (6.25) to:

$$\begin{aligned}
 & - \underline{\underline{V}} \cdot \underline{\underline{\nabla}}(\rho \underline{\underline{v}}_r) - \underline{\underline{v}}_r \rho (\underline{\underline{\nabla}} \cdot \underline{\underline{V}}) - \underline{\underline{\nabla}} \cdot \underline{\underline{\tau}}_{ir} \\
 & + \rho \underline{\underline{g}}_r - \frac{\partial}{\partial r} p = 0.
 \end{aligned} \tag{6.29}$$

2. The body forces acting in r-direction is only due to pressure and not gravity, hence Equation (6.29) is further simplified to:

$$- \underline{\underline{V}} \cdot \underline{\underline{\nabla}}(\rho \underline{\underline{v}}_r) - \underline{\underline{v}}_r \rho (\underline{\underline{\nabla}} \cdot \underline{\underline{V}}) - \underline{\underline{\nabla}} \cdot \underline{\underline{\tau}}_{ir} - \frac{\partial}{\partial r} p = 0. \tag{6.30}$$

3. The physical property of the gas phase in the plasma reactor is assumed constant. For a fluid with constant density (incompressible fluid) the equation of continuity states that the gradient of velocity vector is zero or:

$$\underline{\underline{\nabla}} \cdot \underline{\underline{V}} = 0. \tag{6.31}$$

This fact further simplifies the momentum balance equation to:

$$-\underline{v} \cdot \nabla(\rho \underline{v}_r) - \nabla \cdot \underline{\tau}_{ir} - \frac{\partial}{\partial r} p = 0. \quad (6.32)$$

4. Now we need to develop a constitutive relation for various stresses. The gas phase is treated as Newtonian and incompressible hence the stresses can be expressed as(21):

$$\tau_{rr} = -\mu_{mix} \left(\frac{\partial}{\partial r} \underline{v}_r \right), \quad (6.33)$$

Across θ - and z - direction we have:

$$\tau_{\theta r} = -\mu_{mix} \left(r \frac{\partial}{\partial r} \left(\frac{v_\theta}{r} \right) + \frac{1}{r} \frac{\partial}{\partial \theta} \underline{v}_r \right), \quad (6.34)$$

$$\tau_{zr} = -\mu_{mix} \left(\frac{\partial}{\partial r} \underline{v}_r + \frac{\partial}{\partial z} \underline{v}_r \right). \quad (6.35)$$

Equation (6.32) can be expanded and simplified by substituting Equations (6.33), (6.34) and (6.35) into it and setting the tangential (v_θ) and axial velocities (v_z) to zero. Also due to axisymmetric and 1-dimensional nature of the flow we have:

$$\frac{\partial}{\partial \theta} \underline{v}_r = 0. \quad (6.36)$$

Hence we have:

$$\begin{aligned}
 & - \rho v_r \frac{\partial}{\partial r} v_r + \frac{\mu_{\text{mix}}}{r} \frac{\partial}{\partial r} \left(r \frac{\partial}{\partial r} v_r \right) \\
 & + \mu_{\text{mix}} \frac{\partial}{\partial z} \left(\frac{\partial}{\partial z} v_r \right) - \frac{\partial}{\partial r} p = 0.
 \end{aligned} \tag{6.37}$$

Expanding Equation (6.37) further we have:

$$\begin{aligned}
 & - \rho v_r \frac{\partial}{\partial r} v_r + \frac{\mu_{\text{mix}}}{r} \frac{\partial}{\partial r} v_r \\
 & + \mu_{\text{mix}} \frac{\partial^2}{\partial r^2} v_r + \mu_{\text{mix}} \frac{\partial}{\partial z^2} v_r - \frac{\partial}{\partial r} p = 0.
 \end{aligned} \tag{6.38}$$

This Equation (6.38) is the final simplified momentum balance equation in r-direction. However, we can see from this equation that there are two unknowns to be solved: radial velocity (v_r) and pressure (p). Hence we need another equation in order to solve for the two unknowns. The second equation can be obtained from the principles of conservation of mass:

$$m = \sum v_r \rho A. \tag{6.39}$$

In this equation m is the mass flow rate, and A is the area of cross section of flow. Equations (6.38) and (6.39) can be solved simultaneously with the appropriate boundary conditions to give the radial velocity (v_r) and pressure (p) distribution in the reactor. The boundary conditions developed to solve the two momentum balance governing equations are discussed in the next section.

6.1.4 Boundary Conditions

The two equations that have to be solved in order to predict the fluid flow pattern in the reactor are restated below:

$$- \rho v_r \frac{\partial}{\partial r} v_r + \frac{\mu_{\text{mix}}}{r} \frac{\partial}{\partial r} v_r + \mu_{\text{mix}} \frac{\partial^2}{\partial r^2} v_r \quad (6.38)$$

$$+ \mu_{\text{mix}} \frac{\partial^2}{\partial z^2} v_r - \frac{\partial}{\partial r} p = 0,$$

$$m = \sum v_r \rho A . \quad (6.39)$$

It can be observed from these two equations that the highest order of differential with respect to v_r is 2 for both r- and z-directions. But for p the highest order of differential is 1 with respect to r . Hence two boundary conditions are needed for v_r with both r- and z-directions, whereas only 1 boundary condition is needed for p with respect to r . Boundary conditions for both v_r and p are discussed below:

1. The boundary condition on radial velocity (v_r) with axial direction (z) is based on no slip at the wall. This can be expressed as:

$$v_r |_{\text{bottom plate}} = 0 , \quad (6.40)$$

$$v_r |_{\text{top plate}} = 0 . \quad (6.41)$$

With respect to radial direction two types of boundary conditions were investigated in order to check the influence of entrance and exit effects. Both parabolic and flat flow profiles were constrained at the inlet and exit. The governing equations for flat profile are:

$$v_r|_{\text{inlet}} = \langle v_r \rangle|_{\text{inlet}} , \quad (6.42)$$

$$v_r|_{\text{exit}} = \langle v_r \rangle|_{\text{exit}} . \quad (6.43)$$

Here $\langle v_r \rangle$ represents the average velocity across a specific axial plane. Similarly for parabolic profile the governing equations are (Appendix E):

$$v_r|_{\text{inlet}} = 6 \times \langle v_r \rangle \times \left[\left(\frac{z}{H} \right) - \left(\frac{z}{H} \right)^2 \right] , \quad (6.44)$$

$$v_r|_{\text{exit}} = 6 \times \langle v_r \rangle|_{\text{exit}} \times \left[\left(\frac{z}{H} \right) - \left(\frac{z}{H} \right)^2 \right] . \quad (6.45)$$

Here z is the distance from the center of the two electrode plates and H is the total distance between these two plates.

2. The operating pressure was measured at the exit of the reactor. Hence the boundary condition on pressure can be expressed as:

$$p|_{\text{exit}} = \text{operating pressure} . \quad (6.46)$$

In order to further simplify and generalize the governing equations for fluid flow calculations, the momentum and the mass conservation equation along with the

boundary conditions were nondimensionalized. The procedure followed to nondimensionalize these equations is outlined in the next section.

6.1.5 Nondimensionalization

A simplified geometrical representation indicating various dimensions and axes in the plasma reactor is presented in Figure 16. The two flow governing equations and the boundary conditions on v_r and p are nondimensionalized in this section.

The nondimensionalized variables are differentiated from the state variables by superscripting them with an asterisk. Various dimensionless variables used to nondimensionalize the fluid flow equation and the boundary conditions are:

1. Dimensionless radial distance:

$$r^* = \frac{r}{R} . \quad (6.47)$$

2. Dimensionless axial distance:

$$z^* = \frac{z}{H} . \quad (6.48)$$

3. Dimensionless radial velocity:

$$v_r^* = \frac{v_r}{V_0} . \quad (6.49)$$

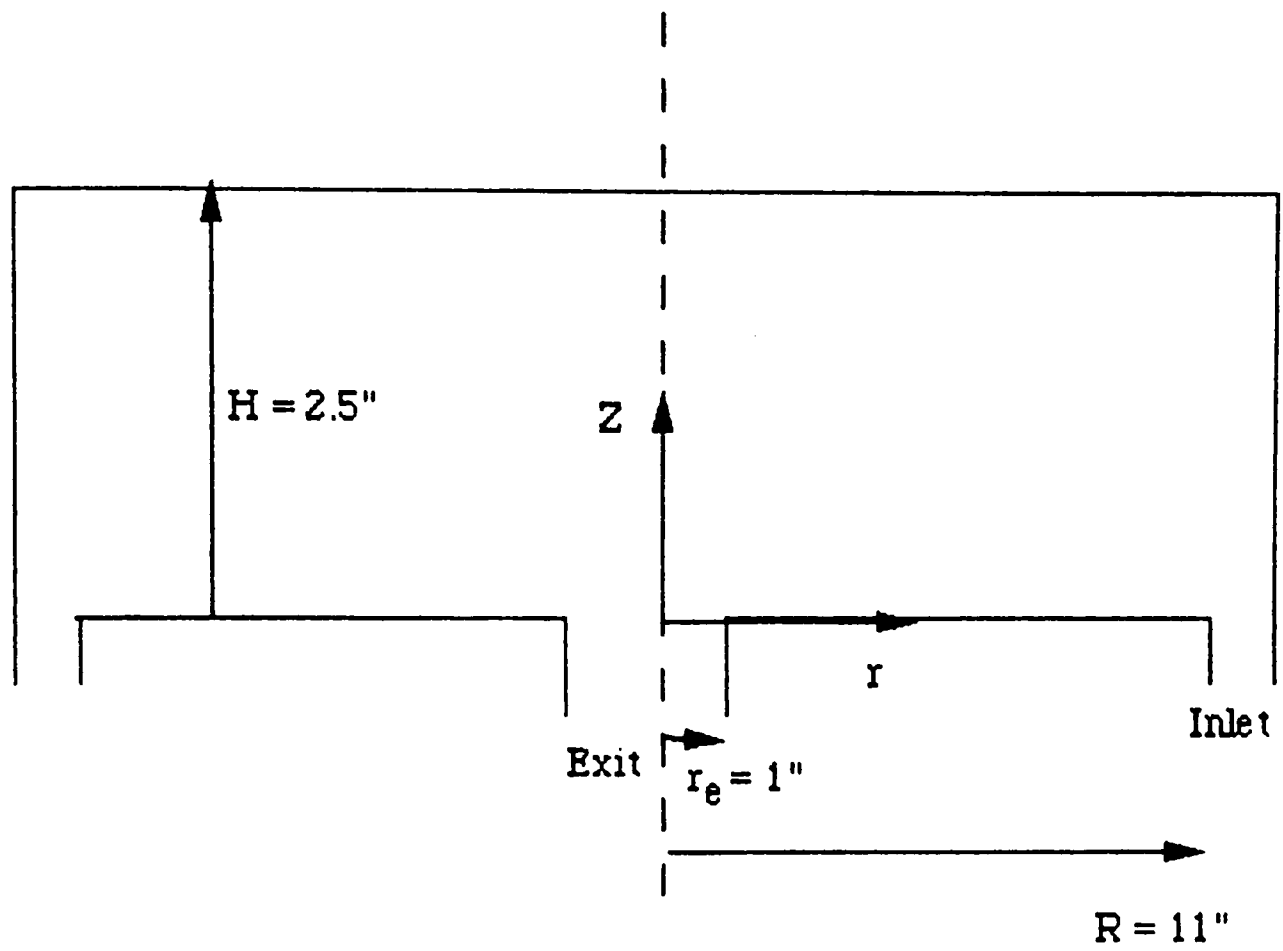


Figure 16: Geometrical Representation of the Plasma Reactor.

4. Geometric factor:

$$G = \frac{H}{R} . \quad (6.50)$$

5. Reynolds number based on the distance between the electrode plates is:

$$R_e = \frac{H \times V_0 \times \rho}{\mu_{mix}} . \quad (6.51)$$

6. Dimensionless pressure:

$$p^* = \frac{p}{\rho \times V_0^2} . \quad (6.52)$$

From Figure 16 we can observe that the radial velocity increases with decreasing radial distance in the reactor because of decreasing area of cross section of flow. The velocity at the exit is maximum and this velocity ($\langle v \rangle|_{exit}$) was used as the characteristic velocity (v_0) in this nondimensionalization procedure.

First we discuss the nondimensionalization procedure on the r-component momentum balance equation. With the introduction of the above mentioned variables in Equation (6.38) we get:

$$\begin{aligned} & - \rho \frac{v_0^2}{R} v_r^* \frac{\partial}{\partial r^*} v_r^* + \mu_{mix} \frac{v_0}{R^2} \frac{1}{r^*} \frac{\partial}{\partial r^*} v_r^* \quad (6.53) \\ & + \mu_{mix} \frac{v_0}{R^2} \frac{\partial^2}{\partial r^{*2}} v_r^* + \mu_{mix} \frac{v_0}{H^2} \frac{\partial^2}{\partial z^{*2}} v_r^* - \frac{\rho^2 v_0^2}{R} \frac{\partial}{\partial r^*} p^* = 0 . \end{aligned}$$

Multiplying this equation by $(R \times r^* / v_0^* \rho)$ we get:

$$\begin{aligned}
 & - r^* \underline{v}_r^* \frac{\partial}{\partial r^*} \underline{v}_r^* + \left(\frac{G}{R_e}\right) \frac{\partial}{\partial r^*} \underline{v}_r^* + \left(\frac{G}{R_e}\right) r^* \frac{\partial^2}{\partial r^{*2}} \underline{v}_r^* & (6.54) \\
 & + \left(\frac{1}{R_e G}\right) r^* \frac{\partial^2}{\partial z^{*2}} \underline{v}_r^* - r^* \frac{\partial}{\partial r^*} p^* = 0.
 \end{aligned}$$

Equation (6.54) is the final nondimensionalized r-component momentum balance equation.

The boundary conditions can be nondimensionalized in a similar manner and the final form is given below:

1. Boundary condition on \underline{v}_r^* with respect to z^* is:

$$\underline{v}_r^* \Big|_{z^*=0} = 0, \quad (6.55)$$

$$\underline{v}_r^* \Big|_{z^*=1} = 0. \quad (6.56)$$

2. Boundary condition on v_r^* with respect to r^* for plug flow condition is:

$$\underline{v}_r^* \Big|_{r^*=1} = \langle v_r^* \rangle \Big|_{r^*=1}, \quad (6.57)$$

$$\underline{v}_r^* \Big|_{r^*=r_e^*} = 1. \quad (6.58)$$

3. Boundary condition on \underline{v}_r^* with respect to r^* for parabolic flow condition is:

$$\underline{v}_r^*|_{r^*=1} = 6(\underline{v}_r^*)|_{r^*=1}(z^* - z^{*2}), \quad (6.59)$$

$$\underline{v}_r^*|_{r^*=r_e^*} = G(\underline{v}_r^*)|_{r^*=r_e^*}(z^* - z^{*2}). \quad (6.60)$$

4. Boundary condition on p^* with respect to r^* is,

$$p^*|_{r^*=r_e^*} = \left(\frac{\text{operating pressure}}{\rho \underline{v}_0^2} \right). \quad (6.61)$$

6.1.6 Method of Solution

The governing momentum balance and mass conservation equations were solved numerically using successive over relaxation (SOR) method. This method was found suitable for the solution of this boundary value (BVP) problem using finite difference method in two dimensions(22). The finite difference grid specified to solve for velocity profile and pressure gradient is illustrated in Figure 17. This grid encompasses one edge of the bottom plate to other and extends up to the top plate. Equal node spacing was incorporated in this grid and the number of grid points were set based on the accuracy of numerical solution for concentration distribution at the central plane in the reactor. It was found that 42 grids in radial direction and 21 grids in axial direction were sufficient in predicting

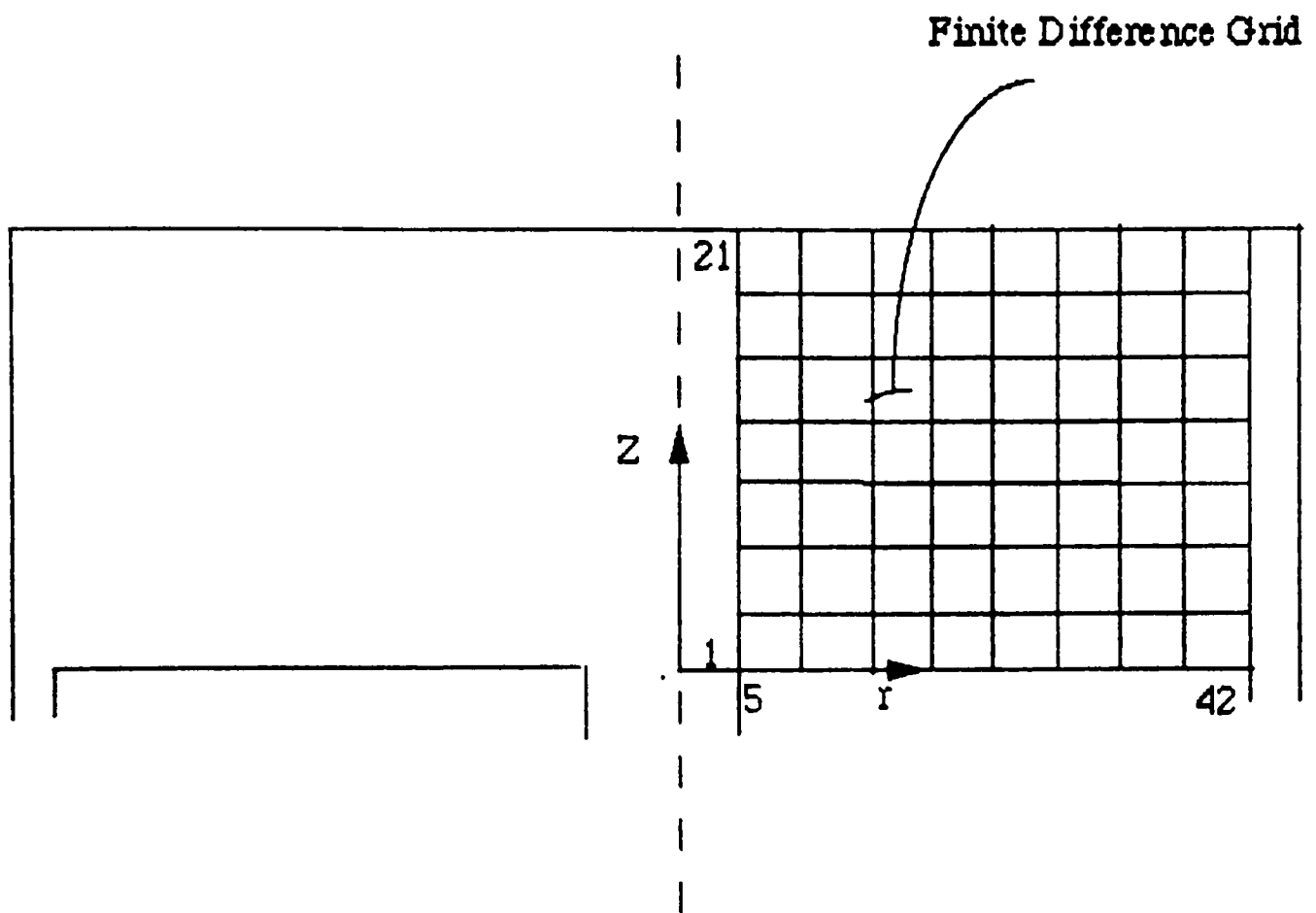


Figure 17: Finite Difference Grid for Velocity Profile.

the velocity and concentration profile within 2% of that with 84 by 42 grid points.

In order to employ the SOR method to solve the BVP a recursive relation has to be first developed. This relation is developed by first substituting the finite difference approximations for the derivatives into the governing equations and then algebraically solving for the central point. In our case since all the boundary conditions are simple algebraic equations so they can be used as such.

Second order central difference approximation was substituted in the nondimensionalized momentum balance equation. The recursive relation developed for the nondimensionalized r-component balance equation is presented below.

The velocity component at various node points are defined in two dimensions (r- and z-directions), whereas the pressure is only unidirectional (r-direction). The pressure across each axial plane is assumed uniform, because there is no axial component of the velocity vector.

For the r-component momentum balance equation the final expression for velocity at a central point is:

$$\begin{aligned}
 V^*(I,J) = & - \left[\left(\frac{G}{R_e} \right) \left(\frac{V^*(I,J+1) - V^*(I,J-1)}{2\Delta R} \right) \right. \\
 & - \left(\frac{Gr^*}{R_e} \right) \left(\frac{V^*(I,J+1) + V^*(I,J-1)}{\Delta R^2} \right) \\
 & \left. - \left(\frac{r^*}{R_e G} \right) \left(\frac{V^*(I+1,J) + V^*(I-1,J)}{\Delta Z^*} \right) + r^* \left(\frac{P^*(I,J+1) - P^*(I,J-1)}{2\Delta R} \right) \right] \\
 & / \left[\left(-r^* \left(\frac{V^*(I,J+1) - V^*(I,J-1)}{2\Delta R} \right) - \left(\frac{G}{R_e} \right) \left(2 \frac{r^*}{\Delta R^2} \right) - \left(\frac{2r^*}{R_e G \Delta Z^2} \right) \right] .
 \end{aligned} \tag{6.62}$$

The solution method developed to solve for the velocity profile from the r-component momentum balance was based on the general numerical marching procedure presented by S.V. Patankar and Spalding(23). This marching was modified for our system and is discussed below:

1. Initial pressure drop between various axial planes was guessed.
2. Using the boundary condition, that the exit pressure equals pressure in the reactor and using the guessed pressure drop, pressure at various axial cross section planes was computed.
3. Dimensionless velocity at various nodes was obtained from the SOR method solution of Equation (6.62). A Successive Relaxation Factor (SRF) of

1.55 and relative error limit of 1×10^{-5} were used for optimum balance between the accuracy of results versus the computational time.

4. During the first step of solution the estimated and actual mass flowrates were compared at the axial planes next to the exit axial plane. After convergence was achieved on this plane the plane on the right of it was considered, and so on. Hence this solution method is referred to as the marching procedure. The error limit in the comparison between actual and estimated mass flowrate was established by the difference between the mass flowrates at the exit or inlet boundaries. It could be recalled that the boundary velocity profiles are ideal flow profiles.
5. If the difference between the actual and estimated mass flowrates was found to be over the specified error limit then the pressure drop was corrected by optimization. The correct value of pressure drop starting from the guess value was bound by the step size doubling technique(22). This bounding of the correct pressure drop was done by observing the sign of the error of the actual and predicted mass flowrates, at consecutive computations. An initial step size of 0.1 was

found acceptable for almost all cases studied. Once the required value of pressure drop was bound, modified fibonacci method (golden section method) was used to arrive at the correct value. Modified Fibonacci Method is a highly efficient one-dimensional search method and once initiated it reduces the region of uncertainty by 38.2 % per cycle(22). This method for the solution of the momentum balance equation may appear very tedious at first because for each cycle of the modified fibonacci method the velocity profile has to be computed at all the grid points using the SOR method. However, due to the small pressure drop in our system rapid convergence is achieved at all the axial planes, after the solution for the first axial grid is obtained.

6. Once convergence was achieved at one particular axial plane the program marches on to the plane immediately right of it and once again the above 2 to 5 steps are repeated. The pressure drop across the plane just left of the plane is used as the starting guess for this plane and similarly for other axial planes.

The computer code developed to model the entire plasma reactor is presented in Appendix F. This program first computes the velocity profile which are stored in data file

and subsequently used in the solution procedure for concentration distribution of plasma species and etch rates in the reactor, discussed in the next section. Typically about 4 CPU of computing time was taken for each velocity profile simulation run. The velocity profile simulation results are discussed in the Chapter 9.

6.2 Species Distribution Model

This section discusses the development of a model that will be used to compute the concentration distribution of plasma species: CF_4 , F , and CF_3 , and the etch rate distribution profile across the wafer. The differential material balance equation developed here along with the plasma kinetic expression (Chapter 5) were solved using the Dankwerts boundary conditions to predict the plasma species concentration distribution. The surface reactions were incorporated as the etch rate boundary conditions at the wafer sites, to predict the etch rate distribution profile.

6.2.1 Differential Material Balance

This section deals with the development of the differential material balance on the i^{th} component about a cylindrical element (Figure 18). The general material

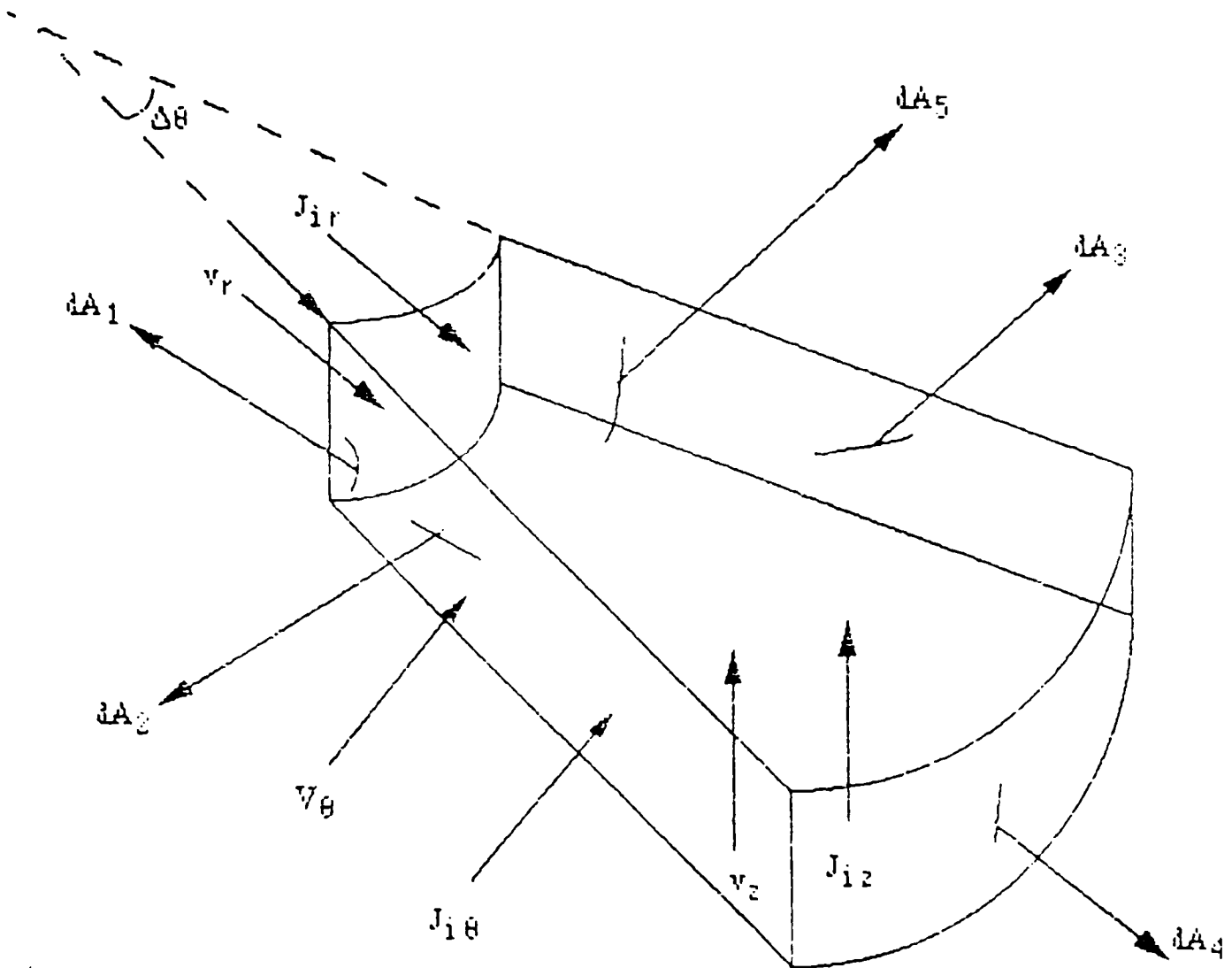


Figure 18: Differential Material Balance Element.

balance equation on the i^{th} component can be written as:

$$\begin{aligned} & \begin{array}{c} \text{Rate} \\ \text{of} \\ \text{(Mass)} \\ \text{In} \end{array} - \begin{array}{c} \text{Rate} \\ \text{of} \\ \text{(Mass)} \\ \text{Out} \end{array} + \begin{array}{c} \text{Rate} \\ \text{of} \\ \text{Mass} \\ \text{Produced} \end{array} - \begin{array}{c} \text{Rate} \\ \text{of} \\ \text{Mass} \\ \text{Depleted} \end{array} \quad (6.63) \end{aligned}$$

$$= (\text{Rate of Mass Accumulation}) .$$

Rate of material entering and leaving the cylindrical element is by two mechanism: bulk and diffusion flux. The transport of component 'i' by diffusion may be assumed to be superimposed on the general movement of the fluid.

The rate of mass in for time Δt through the face dA_1 at r is $\underline{v}_r|_r r \Delta \theta \Delta z \Delta t C_i + \underline{J}_{i,r}|_r r \Delta \theta \Delta z \Delta t$, and the rate of mass out through the face dA_4 at $r+\Delta r$ is $\underline{v}_r|_{r+\Delta r} (r+\Delta r) \Delta \theta \Delta z \Delta t C_i + \underline{J}_{i,r}|_{r+\Delta r} (r+\Delta r) \Delta \theta \Delta z \Delta t$. Here $\underline{J}_{i,r}$ represents the diffusion flux of i^{th} component in r -direction. Similar expressions can be written for the other two pairs of faces. The rate of production and/or depletion of the i^{th} component in time Δt through the j^{th} reaction is $r \Delta \theta \Delta r \Delta z \Delta t \sum r_{ij}$. Here r_{ij} represents the production or depletion of the i^{th} component by reaction number j . The rate of mass accumulation over time Δt can be obtained as the difference between the mass content of the volume element over the differential time Δt . The rate of mass accumulation is:

$$r \Delta \theta \Delta r \Delta z C_i|_{t+\Delta t} - r \Delta \theta \Delta r \Delta z C_i|_t. \quad (6.64)$$

After substituting for the individual terms the material balance equation (Equation (6.63)) becomes:

$$\begin{aligned}
& (\underline{v}_r|_r C_i + \underline{J}_{ir}|_r) r \Delta \theta \Delta z \Delta t - (\underline{v}_r|_{r+\Delta r} C_i + \underline{J}_{ir}|_{r+\Delta r}) r \Delta \theta \Delta z \Delta t \\
& \quad + (\underline{v}_\theta|_\theta C_i + \underline{J}_{i\theta}|_\theta) \Delta r \Delta z \Delta t \\
& \quad - (\underline{v}_\theta|_{\theta+\Delta \theta} C_i + \underline{J}_{i\theta}|_{\theta+\Delta \theta}) \Delta r \Delta z \Delta t \tag{6.65} \\
& \quad + (\underline{v}_z|_z C_i + \underline{J}_{iz}|_z) r \Delta \theta \Delta r \Delta t - (\underline{v}_z|_{z+\Delta z} C_i + \underline{J}_{iz}|_{z+\Delta z}) r \Delta \theta \Delta r \Delta t \\
& \quad + r \Delta \theta \Delta r \Delta z \Delta t \sum r_{ij} = r \Delta \theta \Delta r \Delta z (C_i|_{t+\Delta t} - C_i|_t).
\end{aligned}$$

Dividing Equation (6.65) by $r \Delta r \Delta \theta \Delta t$ and taking the limit as these dimensions approach zero we get:

$$-\frac{1}{r} \frac{\partial}{\partial r} (r \underline{v}_r C_i) - \frac{1}{r} \frac{\partial}{\partial r} (r \underline{J}_{ir}) - \frac{1}{r} \frac{\partial}{\partial \theta} (C_i \underline{v}_\theta) \tag{6.66}$$

$$\frac{1}{r} \frac{\partial}{\partial \theta} (\underline{J}_{i\theta}) - \frac{\partial}{\partial z} (\underline{v}_z C_i) - \frac{\partial}{\partial z} (\underline{J}_{iz}) + \sum r_{ij} = \frac{\partial}{\partial t} C_i.$$

Or in terms of ∇ operator we have:

$$-\nabla \cdot (\underline{v} C_i) - \nabla \cdot \underline{J}_i + \sum r_{ij} = \frac{\partial}{\partial t} C_i. \tag{6.67}$$

The generalized material balance equation, developed above can be simplified to meet the requirements of our plasma reactor. The simplifying assumption used, are presented in the next section.

6.2.2 Assumptions

The assumptions discussed in the section on fluid flow model are used along with certain additional presumptions to

simplify the material balance equation discussed in the earlier section. The additional assumptions used are discussed as follows.

The expression for the mass flux J_i , in a multicomponent system generally consists of three contributions associated with the mechanical driving forces and an additional contribution associated with the thermal driving force(21):

$$\underline{J}_i = \underline{J}_i^{(C_i)} + \underline{J}_i^{(p)} + \underline{J}_i^{(g)} + \underline{J}_i^{(T)}. \quad (6.68)$$

In Equation (6.68) the mass flux is shown to be the sums of terms describing ordinary (concentration) diffusion, pressure diffusion, forced diffusion and thermal diffusion respectively. The pressure drop across the reactor is very small (Chapter 9) to result in any significant pressure mass flux across the reactor. The forced diffusion resulting from electromagnetic and gravity forces also are not of significance in our system. This is because the plasma species (CF_4 , CF_3 and F) are essentially neutral and the flow is almost entirely in horizontal direction. Thermal diffusion component for our plasma system can be neglected too, because there is a small change in gas temperature as it flows across the reactor (Appendix B).

The diffusion flux of any significance left to be considered is that resulting from concentration gradient of all the species present. The diffusion flux resulting from

concentration gradient has been represented by the Fick's Law as:

$$\underline{J}_i = - D_{i\text{-mix}} \nabla C_i . \quad (6.69)$$

It has been reported in literature(32) that for ideal gases and dilute liquids, the diffusion coefficient $D_{i\text{-mix}}$ is almost constant for a given pressure, temperature and pair of substances. Also, diffusivity is almost independent of concentration. In our system where there is predominately CF_4 , we can assume that F and CF_3 diffuse in CF_4 instead of a gas mixture. The estimation method for diffusion coefficient for various species diffusing in CF_4 has been presented in Appendix C.

The plasma phase is almost uniform because of the predominance of CF_4 , hence the value of diffusion coefficient can be assumed constant in all directions. The simplification of the material balance equation from the assumptions listed above and in earlier section (6.1.2) is discussed in the next section.

6.2.3 Analysis of Material Balance Equation

The differential material balance equation developed in section 6.2.1 can be analyzed based on assumptions stated in section 6.1.2 and the earlier section (6.1.2) and a discussion on this is presented in this section.

1. The plasma etching process can be assumed to be at steady state, hence the transient term is zero.

2. The fluid flow profile develops in one-dimension (r) over a very short length in the reactor, hence the axial (v_z) can be neglected. The tangential velocity (v_θ) can be neglected too, due to the axisymmetric nature of the flow. The simplified form of the final material balance equation can be represented as:

$$-\frac{1}{r} \frac{\partial}{\partial r} (rv_r C_i) - \nabla \cdot \underline{J}_i + \sum r_{ij} = 0. \quad (6.70)$$

3. The diffusion flux can be represented in the three directions as:

$$\underline{J}_i = \underline{J}_{ir} + \underline{J}_{i\theta} + \underline{J}_{iz}. \quad (6.71)$$

Substituting Fick's Law in Equation (6.71) we get:

$$\underline{J}_i = -D_i \frac{\partial}{\partial r} C_i - D_i \frac{1}{r} \frac{\partial}{\partial \theta} C_i - D_i \frac{\partial}{\partial z} C_i. \quad (6.72)$$

Equation (6.72) can be substituted in Equation (6.70) to give the final material balance equation as:

$$-\frac{1}{r} \frac{\partial}{\partial r} (rv_r C_i) + D_i \nabla^2 C_i + \sum r_{ij} = 0. \quad (6.73)$$

4. The plasma phase kinetic reaction incorporated for our system was developed in Chapter 5 as:



Whereas for the products the rate expression for the electron impact dissociation reaction is:

$$R_F = R_{CF_3} = k_1[CF_4][e^-]. \quad (5.16)$$

We can now include the plasma kinetics in the material balance expression (Equation (6.73)) to get the final expression for various components.

For CF_4 we have:

$$\begin{aligned} & - \frac{1}{r} \frac{\partial}{\partial r} (r v_r C_{CF_4}) + D_{CF_4-CF_4} \left[\frac{1}{r} \frac{\partial}{\partial r} \left(r \frac{\partial}{\partial r} C_{CF_4} \right. \right. \\ & \left. \left. + \frac{1}{r^2} \frac{\partial^2}{\partial \theta^2} C_{CF_4} + \frac{\partial^2}{\partial z^2} C_{CF_4} \right] - k_1[CF_4][e^-] = 0. \end{aligned} \quad (6.74)$$

For CF_3 we have:

$$\begin{aligned} & - \frac{1}{r} \frac{\partial}{\partial r} (r v_r C_{CF_3}) + D_{CF_3-CF_4} \left[\frac{1}{r} \frac{\partial}{\partial r} \left(r \frac{\partial}{\partial r} C_{CF_3} \right) \right. \\ & \left. + \frac{1}{r^2} \frac{\partial^2}{\partial \theta^2} C_{CF_3} + \frac{\partial^2}{\partial z^2} C_{CF_3} \right] + k_1[CF_4][e^-] = 0. \end{aligned} \quad (6.75)$$

For F we have:

$$\begin{aligned} & - \frac{1}{r} \frac{\partial}{\partial r} (r v_r C_F) + D_{F-CF_4} \left[\frac{1}{r} \frac{\partial}{\partial r} \left(r \frac{\partial}{\partial r} C_F \right) \right. \\ & \left. + \frac{1}{r^2} \frac{\partial^2}{\partial \theta^2} C_F + \frac{\partial^2}{\partial z^2} C_F \right] + k_1[CF_4][e^-] = 0. \end{aligned} \quad (6.76)$$

The three-component material balance equations were solved with the appropriate boundary conditions to predict the concentration profile in the plasma reactor. The

boundary condition used to solve the material balance equation are presented in the next sub-section.

6.2.4 Boundary Conditions

By observing the highest order on the dependent variable (concentration) with the three independent variables (r , θ and z) from Equations (6.74) to (6.76), we can determine the number of boundary conditions required on concentration. The highest order on concentration with each one of the three independent variables is 2, hence two boundary conditions are required for r -, θ - and z -directions.

1. The r -direction boundary conditions were obtained from Dankwerts Boundary Conditions at the inlet and zero concentration gradient at the exit. Dankwerts Boundary Condition at the inlet is expressed as:

$$-D_{i-CF_4} \frac{\partial C_i}{\partial r} \Big|_{r=R} = v_r \Big|_{r=R} (C_i \Big|_{r=R} - C_i^0); \quad (6.77)$$

$$i = CF_4, CF_3, F .$$

It can be noticed here that the inlet concentration (C_i^0) of CF_3 and F are zero, hence the last term in the above expression is zero for these species. This expression states that the inlet concentration of any species (superscript 0) is transported by both diffusion and convection

fluxes. This results in a more uniform distribution of reactive species than assuming zero reactive species (F, CF₃) concentration at the inlet section. This was found consistent with the experimental results on etch rate distribution.

The exit boundary condition in the plasma reactor was based on zero concentration gradient:

$$\frac{\partial}{\partial r} C_i |_{r=r_e} = 0; \quad i = \text{CF}_4, \text{CF}_3, \text{F}. \quad (6.78)$$

2. The surface or wall boundary condition were also based on zero concentration gradient:

$$\frac{\partial}{\partial z} C_i |_{z=0} = 0; \quad i = \text{CF}_4, \text{CF}_3, \text{F}, \quad (6.79)$$

$$\frac{\partial}{\partial z} C_i |_{z=H} = 0; \quad i = \text{CF}_4, \text{CF}_3, \text{F}. \quad (6.80)$$

This was based on our assumption of no recombination reactions on the wall.

3. In order to employ the zero concentration gradient boundary condition on the plasma species along the tangential direction, it is necessary to take a large enough section of the reactor so that the influence of the wafer reactions is not significant in that region. It was observed that if one sector of the reactor was considered for computations, with the wafer placed halfway

(Figure 19) on one edge of the sector then the affect of diffusion flux emanating due to the wafer reactions to the other edge of the sector was negligible. Figure 19 is a top view of the bottom electrode plate showing the sector over which modeling was undertaken and the wafer location on this section of the reactor. This positioning of wafer is consistent with the experimental runs discussed in Chapter 7. Due to this position of the wafer the concentration gradient across plane 1 or $\theta=0$ is zero. Also because of the distance in wafer location and the direction of flow the concentration gradient across plane 2 or $\theta=\pi$ is zero. Hence the boundary conditions on concentration with respect to θ -direction are:

$$\frac{\partial}{\partial \theta} C_i |_{\theta=0} = 0; \quad i=CF_4, CF_3, F. \quad (6.81)$$

$$\frac{\partial}{\partial \theta} C_i |_{\theta=\frac{\pi}{2}} = 0; \quad i=CF_4, CF_3, F. \quad (6.82)$$

4. The etch rate boundary condition is developed from the surface reaction kinetic model discussed in Chapter 5. The wafer reaction kinetic model is

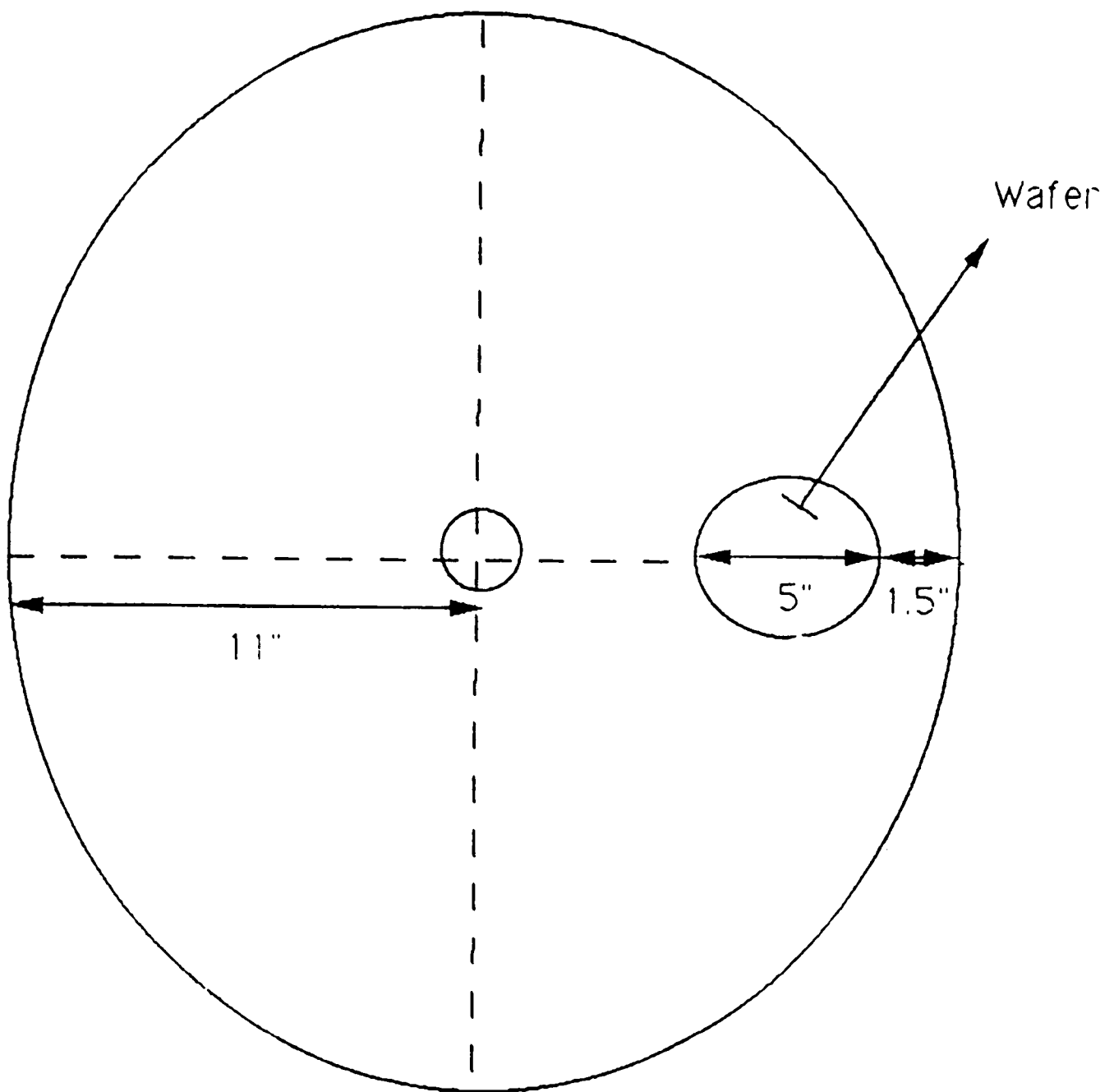


Figure 19: Reactor Bottom Showing the Wafer Location.

first restated as:

$$R_{\text{SiO}_2} = \frac{K_1[\text{F}][\text{ION}] + K_2[\text{F}]}{[\text{ION}] + K_3[\text{F}]} . \quad (6.83)$$

This kinetic model was developed based on the overall reaction of SiO_2 with F as:



The SiF_4 formed is volatile and desorbs from the surface, thereby etching the surface. Hence for each mole of SiO_2 etched 4 moles of F are consumed. Thus we can write the etch rate expression in terms of F depletion as:

$$R_f = 4 \left(\frac{K_1[\text{F}][\text{ION}] + K_2[\text{F}]}{[\text{ION}] + K_3[\text{F}]} \right) . \quad (6.84)$$

The etch rate boundary condition was developed based on steady state assumption, wherein the rate of diffusion of F species on the surface equals its reaction on the surface, hence:

$$- D_{\text{F-CF}_4} \frac{\partial}{\partial z} C_f \Big|_{z=0} = -4 \left(\frac{K_1[\text{F}][\text{ION}] + K_2[\text{F}]}{[\text{ION}] + K_3[\text{F}]} \right) . \quad (6.85)$$

This surface boundary condition was used to predict the F concentration on the wafer surface. The final material balance and boundary conditions developed were generalized using dimensionless

variables and a discussion on this is presented in the next sub-section.

6.2.5 Nondimensionalization

A simplified geometrical representation of the plasma reactor indicating various dimensions and axes in the plasma reactor was presented in Figure 16. The material balance equation were solved in one sector of the reactor in three-dimensions. The governing material and boundary conditions were nondimensionalized and the dimensionless variables used are presented below:

1. Dimensionless radial distance:

$$r^* = \frac{r}{R}. \quad (6.86)$$

2. Dimensionless axial distance:

$$z^* = \frac{z}{H}. \quad (6.87)$$

3. Dimensionless tangential distance:

$$\theta^* = \theta. \quad (6.88)$$

4. Dimensionless radial velocity:

$$v_r^* = \frac{v_r}{V_0} \quad (6.89)$$

5. Dimensionless concentration:

$$C_i^* = \frac{C_i}{CF_4^0}. \quad (6.90)$$

6. Geometric factor:

$$G = \frac{H}{R}. \quad (6.91)$$

7. Peclet Number:

$$P_{e_i} = R \frac{V_{\max}}{D_{i-CF_4}}. \quad (6.92)$$

8. Damkohler Number:

$$D_{a_i} = \frac{k_1[e^-]R}{V_0}. \quad (6.93)$$

The generalized material balance Equation (6.73) can be expanded as:

$$\begin{aligned} & -\frac{v_r}{r} C_i - C_i \frac{\partial}{\partial r} \frac{v_r}{r} - \frac{v_r}{r} \frac{\partial}{\partial r} C_i + D_{i-CF_4} \left(\frac{1}{r} \frac{\partial}{\partial r} C_i \right. \\ & \left. + \frac{\partial^2}{\partial r^2} C_i + \frac{1}{r^2} \frac{\partial^2}{\partial \theta^2} C_i + \frac{\partial^2}{\partial z^2} C_i \right) + \sum r_{ij} = 0. \end{aligned} \quad (6.94)$$

This equation can be nondimensionalized by introducing the above mentioned dimensionless numbers to give the final form

for material balance for CF_4 as:

$$\begin{aligned}
 & -v_r^* \frac{C_{CF_4}^*}{r^*} - C_{CF_4}^* \frac{\partial}{\partial r^*} v_r^* - v_r^* \frac{\partial}{\partial r^*} C_{CF_4}^* \\
 & + \frac{1}{Pe_{CF_4}} \left(\frac{1}{r^*} \frac{\partial}{\partial r^*} C_{CF_4}^* + \frac{\partial^2}{\partial r^{*2}} C_{CF_4}^* \right) \quad (6.95)
 \end{aligned}$$

$$\frac{1}{r^{*2}} \frac{\partial}{\partial \theta^{*2}} C_{CF_4}^* + \left(\frac{1}{G^2} \right) \frac{\partial^2}{\partial z^{*2}} C_{CF_4}^* - Da_1 C_{CF_4}^* = 0.$$

Similarly, we can obtain the dimensionless equations for CF_3 and F.

The boundary conditions can be nondimensionalized in a similar manner and here we present the final forms of the boundary condition equations:

1. The r-direction boundary condition at the inlet is:

$$C_i^* \Big|_{r^*=1} = X - \left(\frac{1}{Pe_i} \right) \frac{1}{v_r^*} \frac{\partial}{\partial r^*} C_i^* \Big|_{r^*=1}. \quad (6.96)$$

Where $X=1$ for $i=CF_4$ and $X=0$ for $i=CF_3$ and F.

At the exit we have:

$$\frac{\partial}{\partial r^*} C_i^* = 0. \quad (6.97)$$

2. For the θ -direction the nondimensionalized boundary conditions are:

$$\frac{\partial}{\partial \theta^*} C_i^* \Big|_{\theta^*=0} = 0, \quad (6.98)$$

$$\frac{\partial}{\partial \theta^*} C_i^* \Big|_{\theta^*=\frac{\pi}{2}} = 0. \quad (6.99)$$

3. For z-direction the nondimensionalized boundary conditions are:

$$\frac{\partial}{\partial z^*} C_i^* \Big|_{z^*=0} = 0, \quad (6.100)$$

$$\frac{\partial}{\partial z^*} C_i^* \Big|_{z^*=1} = 0. \quad (6.101)$$

4. The etch rate boundary condition of F species can be nondimensionalized in a similar manner and is represented as:

$$\frac{\partial}{\partial z^*} C_F^* \Big|_{z^*=\text{wafer}} = X, \quad (6.102)$$

$$X = \left(\frac{4H}{D_{F-CF_4} C_{CF_4}^0} \right) \left(\frac{K_1 [ION] F^* C_{CF_4}^0 + K_2 F^* C_{CF_4}^0}{[ION] + K_3 F^* C_{CF_4}^0} \right) \quad (6.103)$$

The solution procedure developed to obtain the concentration profile is discussed in next sub-section.

6.2.6 Method of Solution

The governing material balance equations developed were solved numerically using the successive over relaxation

(SOR) method(22). The velocity profile solved by the fluid flow model was used in conjunction with the developed boundary conditions to predict the concentration profiles of the three components: CF_4 , CF_3 , F in three-dimension in one sector of the reactor. Both the situations involving wafer presence (loaded) and absence (unloaded) in the reactor were investigated.

Due to the irreversible nature of the plasma kinetics considered it was possible to solve for the species concentration distribution individually. CF_4 concentration was solved for first and then F concentration, CF_3 concentration was obtained by difference.

The finite difference grid specified to solve for concentration distribution equation is illustrated in Figure 20. The grid encompasses one sector of the reactor and extends up in three-dimensions. Equal grid spacing was incorporated in this grid and the number of grid points in various directions were based on the optimum balance between the numerical error and the computational time. It was found that 42 grids in radial direction, 21 grids in axial direction and 25 grids in the tangential direction were able to predict the concentration profile without significant error. The error was estimated by doubling the number of grid points.

In order to solve the material balance equations using SOR method it is important to develop a recursive method for

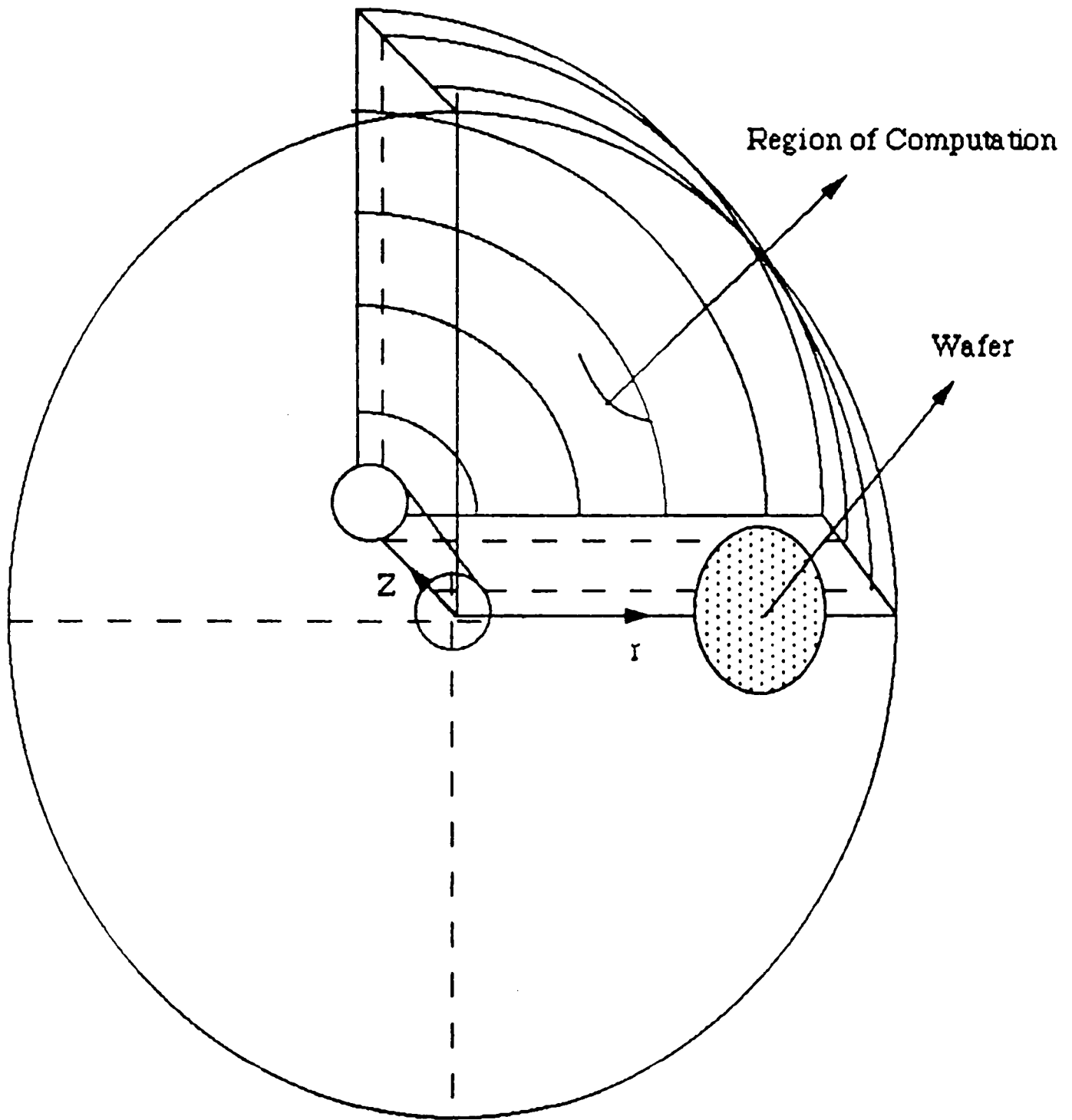


Figure 20: Sector Over Which the Concentration Profile was Computed.

the governing equations and the boundary conditions. The recursive relation were developed by substituting second order finite difference form in these equations and solving for the central point.

The recursive relation developed for boundary conditions were based on substituting second order forward or backward difference relation depending on whether the boundary condition was at the exit or inlet respectively.

1. The recursive relation for r-direction boundary conditions at the inlet for CF_4 are:

$$C_{CF_4}^* |_{inlet} \quad (6.104)$$

$$= \frac{-X V^*(I, J) + 4C_{CF_4}^*(I, N-1, K) - C_{CF_4}^*(I, N-2, K)}{3 - X V^*(I, N)},$$

where:

$$X = \frac{RV_0 2 \Delta R}{Di - CF_4}$$

Similarly we can obtain the boundary conditions for CF_3 and F, there the value of X is zero.

At the exit the recursive relation is:

$$C_i^*(I, NO, K) \quad (6.105)$$

$$= \left(\frac{1}{3}\right) (4 C_i^*(I, NO+1, K) - C_i^*(I, NO+2, K)).$$

3. The recursive relation for the θ -direction boundary conditions are:

$$C_i^*(I, J, 1) = \left(\frac{1}{3}\right) (4 C_i^*(I, J, 2) - C_i^*(I, J, 3)) \quad (6.106)$$

$$C_i^*(I, J, L) = \left(\frac{1}{3}\right) (4 C_i^*(I, J, L-1) - C_i^*(I, J, L-2)). \quad (6.107)$$

3. The recursive relation for the z -direction boundary conditions are:

$$C_i^*(1, J, K) = \left(\frac{1}{3}\right) (4 C_i^*(2, J, K) - C_i^*(3, J, K)). \quad (6.108)$$

$$C_i^*(M, J, K) = \left(\frac{1}{3}\right) (4 C_i^*(M-1, J, K) - C_i^*(M-2, J, K)). \quad (6.109)$$

4. A recursive relation was also developed for the etch rate boundary condition for F .

The solution method developed to solve the above illustrated three-dimensional boundary value problem was based on the method illustrated in reference 22. Initial concentrations of CF_4 and F were guessed at all the points in the grid. CF_4 concentration was solved at various grid points using the SOR method. A SRF factor of 2 and a relative error limit of 1×10^{-4} were found to predict accurate results without taking too much computational time. Once convergence on CF_4 was achieved then a similar procedure was employed for F . Typically 26 CPU of computing time was required for each concentration profile run.

CHAPTER 7

EXPERIMENTAL RESULTS

In this chapter the results obtained during the course of experimentation are illustrated and discussed. This chapter is sub-divided into three sections; the first section discusses the cylindrical Langmuir probe results for electron density and temperature, the second section discusses the optical emission data obtained during runs without SiO₂ wafers (unloaded) and the third section presents the etch rate data during loaded runs.

7.1 Electron Density and Temperature

The variation of electron density and temperature with radial position, power and pressure are discussed in this section.

7.1.1 Effect of Position

Spatial variation in electron density and temperature are essentially due to the nature of electron interactions with the reactor wall. Electrons impact with the reactor wall and are either absorbed or are reflected back. However, the rate of absorption of electrons far exceeds their reflection, and hence a significant decrease in electron density is observed near the reactor wall(24). The radial variation of electron density and temperature was studied at various points in the reactor. These points

where the electron characteristics were investigated are illustrated in Figure 21.

The electron density distribution with radial position obtained using the Langmuir probe at constant pressure and at five different powers is presented in Appendix G, page 206. It can be seen from this plot that at all different powers the electron density variation with radial position is of a similar form. Near the inlet the electron density is the minimum, because electrons are readily absorbed on the side walls of the reactor, but as we progress towards the center the electron density increases and again drops down at the center of the reactor.

The electrons present in the plasma are from two sources; one source of electrons are the primary electrons emitted from the top charged electrode and the other source of electrons are the secondary electrons produced as a result of the primary electrons striking the reactor walls(46,47). The electron density near the reactor exit is low because there is less reactor surface for the production of the secondary electrons as compared to a point half way through the reactor radius. Another reason for the low electron density at the reactor center is that the electrons are swept out of the exit pipe. The electron density at the center of the reactor is in general higher as compared to the electron density at the inlet section. This radial distribution of electron density at five different powers

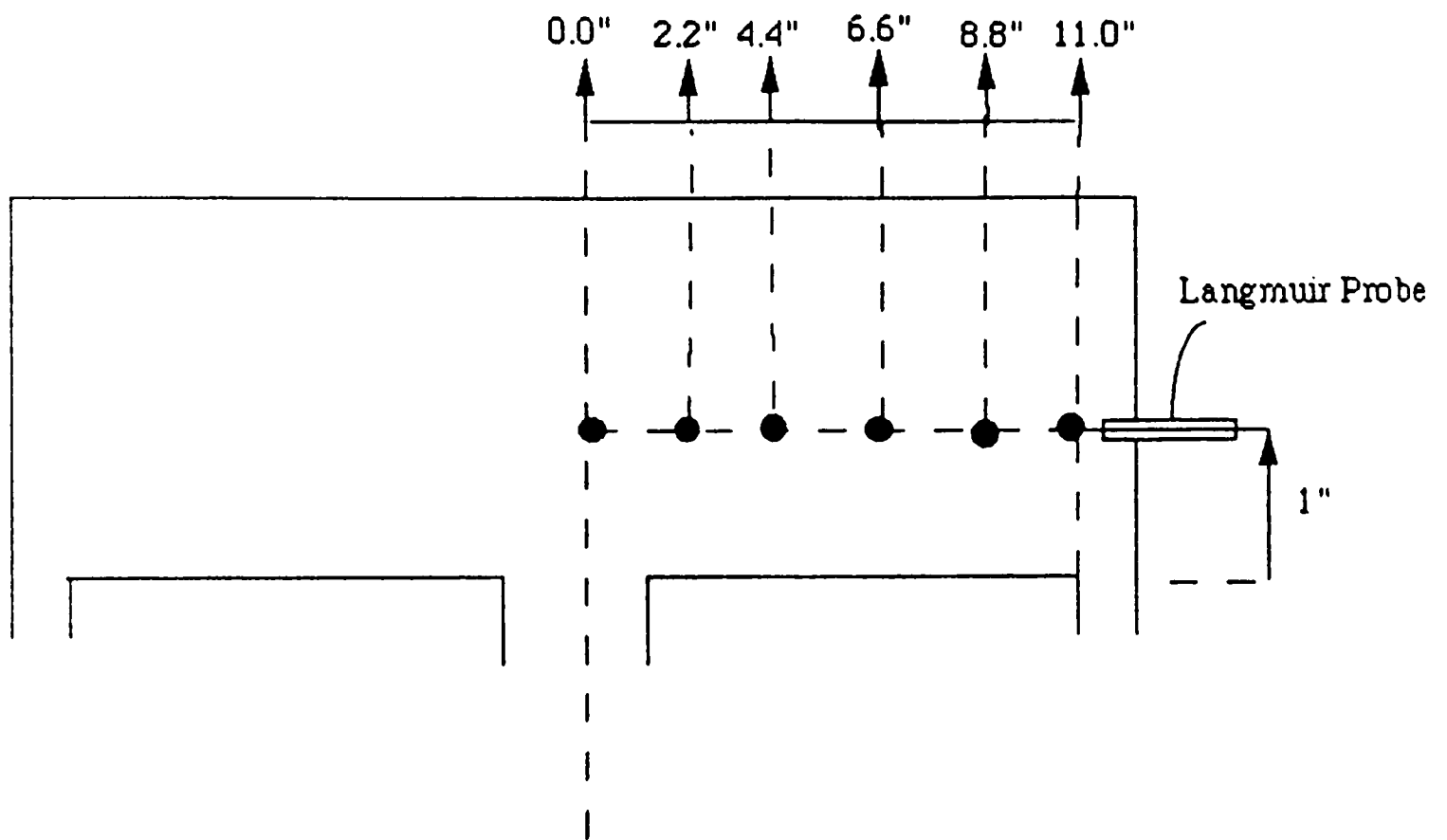


Figure 21: Transverse Section of the Reactor
 Showing the Points where the Electron
 Characteristics were Investigated.

(100, 200, 300, 400 and 500 watts) and at 200 mTorr pressure is presented individually in Appendix G from pages 207 to 211.

Appendix G, page 212, presents the electron temperature (in eV) distribution with radial position at constant pressure (200 mTorr) and at five different powers (100, 200, 300 and 400 watts). Once again we can observe a trend similar to the density distribution in the behavior of the electron temperature distribution. At the inlet section the electron temperature is low but steadily increases towards the middle of the reactor radius and then drops down slightly at the exit. The energetic (high temperature) electrons are more mobile and are more easily absorbed at the reactor walls and are also more readily swept out of the reactor exit. This is the reason why we obtain this form of the electron energy (temperature) distribution function.

7.1.2 Effect of Power

The variation of electron density and temperature with increasing power in the reactor is illustrated in Appendix G from pages 213 to 220. The electron densities are presented at various pressures (200, 300, 350, 400, 450, 500 and 600 mTorr) at the midway (6.6") through the reactor radius. At this radial position the electron density is near its maximum for any operating condition in the reactor. The electron density increases almost linearly with increasing power. This is basically because increasing power results

in increasing the charge carriers across the electrode plate, which happen to be electrons for our case. Appendix G, pages 213 to 219, shows the same trend in electron density with increasing power.

Appendix G, page 220, illustrates the change in electron temperature at a radial position of 6.6" (Figure 21) from the center, in the reactor for different pressures with increasing power. Here again we can see that the electron temperature increases with increasing power. At higher powers more energetic electrons are emitted from the electrode and as they collide with each other and with the gas molecules they gain higher energies or temperature.

7.1.3 Effect of Pressure

The influence on electron density and temperature of increasing pressure at various powers and constant radial position of 6.6" from the center of the reactor is shown in Appendix G, pages 221 to 224. With increasing pressure the number of gas molecules in the reactor also increase and hence the probability of an electron being captured by the gas molecule increases. This results in a decrease in the electron density. Appendix G, pages 221 to 223, shows the influence of increasing pressure on the electron density. In all these plots the electron density is seen to decrease with increasing pressure at constant power and radial position. This decrease in electron density is comparatively more steep at lower pressures than at higher

pressures, thereby representing some kind of a steady state on the electron capturing capacity of the gas molecules. Also the decrease in electron density with increasing pressure is comparatively smaller as compared to that observed with decreasing power. Thus suggesting that power has a larger influence on electron density than pressure within the ranges studied.

Electron temperature or energy is also seen to decrease with increasing pressure. This has been represented at four different powers (300, 400, 600 and 700 watts) and at a radial position of 6.6" from the center, in Appendix G, page 224. The mean free path of electrons are reduced with increasing pressure because of increased number of gas molecules. The electrons collide with the gas molecules more frequently and hence lose more of their energies resulting in lower temperatures.

The influence of radial position, power and pressure on electron density and temperature was presented and discussed in this section. An empirical model was developed to predict the electron density distribution in the reactor around the maximum electron density occurring at 6.6" from the center of the reactor. Details of the model are presented in Appendix H.

7.2 Unloaded Reactor Runs

Variation in F concentration with changing power, pressure and flowrate in the plasma reactor is illustrated

and discussed in this section. The F concentration was monitored in the plasma reactor by using the emission results of F and Ar species obtained from the Optical Spectrometer. This strategy referred to as Argon Actinometry was discussed in Chapter 4. In this technique about 5% argon is continuously injected in the plasma reactor and the ratio of near equal energy peaks of F and Ar are used to estimate the concentration ratios of these two species:

$$\frac{I_F}{I_{Ar}} = K \frac{[F]}{[Ar]}. \quad (7.110)$$

The intensities are obtained using the optical spectrometer. A typical output from the spectrometer is presented in Figure 22. The F and Ar intensities used to estimate the concentration ratio are indicated in this figure. The height of the peaks over the background noise were used to estimate the intensities.

Unloaded reactor runs were used in this study to check the validity of plasma kinetics employed in the model. A detailed discussion on the model validation is presented in the next chapter. The experimental runs discussed in this section were conducted without any wafer in the plasma reactor, and hence the wafer surface kinetics was eliminated. Thus it is possible to study the effect of process parameters (power, pressure and flowrate) on the plasma phase reactions through these experiments.

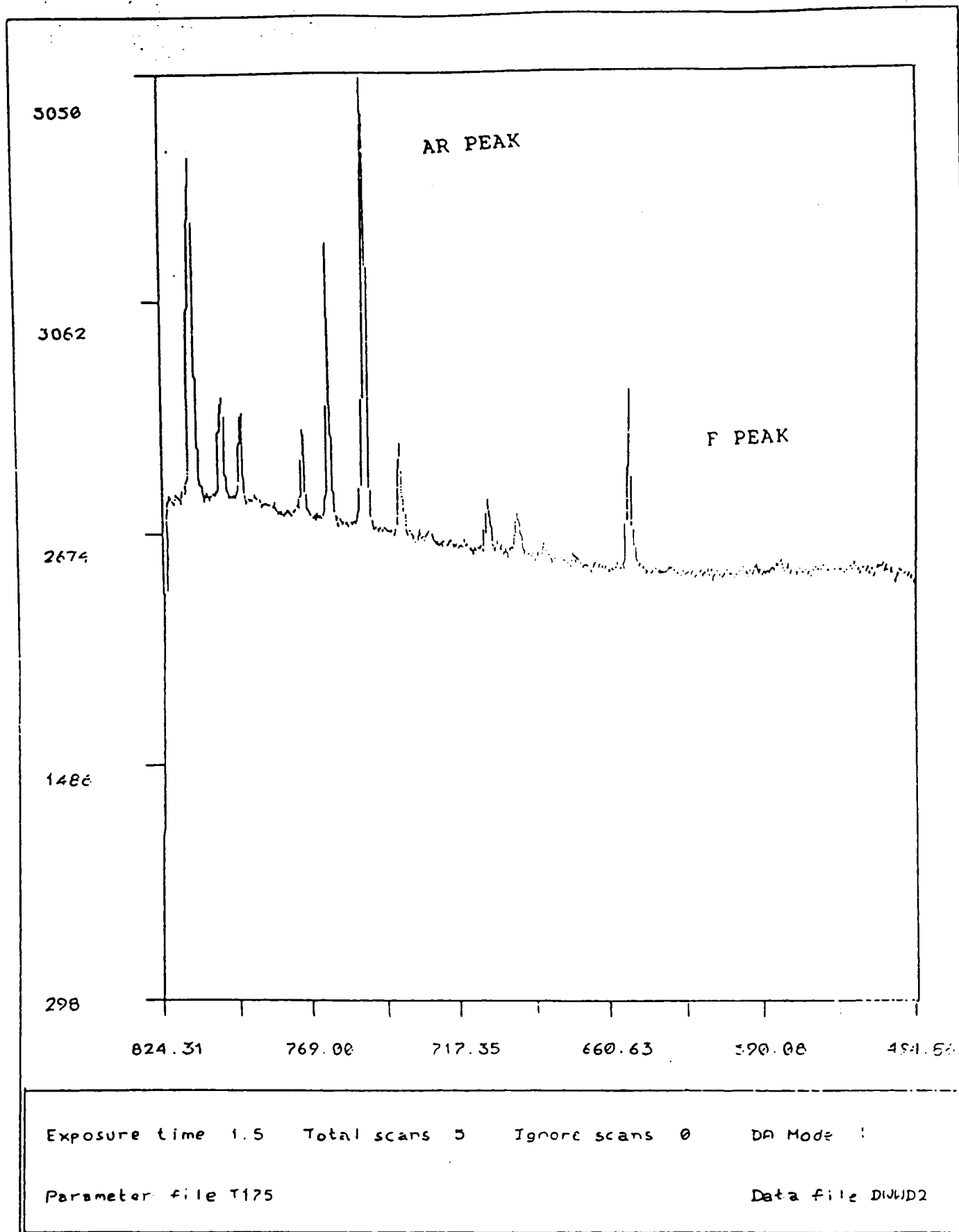


Figure 22: Typical Optical Emission Spectrometer Output.

7.2.1 Effect of Power

Power has a direct effect on the electron density and temperature existing in the plasma reactor. When the power is increased greater number of highly energetic electrons are produced, resulting in a higher number of collisions with CF_4 molecules. These electron impact reactions with the parent feed gas (CF_4) results in its dissociation, which produces F. The change in the intensity of F to intensity of Ar with reactor power is presented in Appendix I, pages 228 to 233. Argon is inert in a CF_4 plasma, hence its concentration stays constant with changing power, thus the plot I_F/I_{Ar} against power essentially represents the changing F concentration in the plasma reactor. Appendix I, pages 228 to 233, represents the intensity ratio of F to Ar with changing power at different pressures (from 150 to 500 mTorr) and at a constant flowrate of 92.21 sccm (90 sccm CF_4 and 2.21 sccm Ar). It can be seen from all these plots that the F concentration increases with increasing power. The trend of I_F/I_{Ar} plot against increasing power at various pressures is almost linear and similar. This indicates that the effect of increasing power on F production is by a single mechanism. The most probable mechanism is the increased number of electron impact reaction. Also the intensity ratio is higher at lower pressures than at higher pressures. This behavior is explained in next sub-section.

Appendix I, pages 232 to 233, illustrates the reproductivity of the unloaded reactor runs with increasing power at two different pressures (200 and 350 mTorr). Appendix I, page 232, shows a plot at 200 mTorr and we can observe from this plot that even though similar trends are shown by the two different experimental runs but the values of intensity ratios are different. A similar behavior is observed in Appendix I, page 233. This is because of the leak rates in the plasma reactor change every time the reactor is opened. The air leaking into the reactor contains O_2 which has been observed to enhance the dissociation of CF_4 to F. The effect of O_2 addition with the feed gas on the etch rate is presented in the next section. All the experimental runs were conducted at one time, so it can be assumed that the leak rate is fairly uniform for all the cases. However, for loaded reactor runs it was imperative to open and shut the reactor in order to load a fresh wafer, thus it can be expected that the leak rates and hence the F concentration was different for the same set of operating conditions. This behavior is further discussed in the next chapter.

7.2.2 Effect of Pressure

Appendix I, pages 234 to 236, shows the influence of changing pressure on the intensity ratio (I_F/I_{Ar}) at various powers (300, 400, 500 and 600 watts) and at a constant flowrate of 92.21 sccm. The intensity ratio of F to Ar was

found to decrease slightly with increasing pressure. As we had observed in the earlier section, the electron density was found to decrease with increasing pressure. This was because with increasing pressure the number of feed gas molecules (CF_4) increase thereby increasing the probability of electron being captured by the gas molecules. Hence increasing pressure, increases the probability of a CF_4 molecule being impacted by electrons. Thus the rate of dissociation of CF_4 would also increase, resulting in an increased formation of F species. However, at the same time the Argon concentration also goes up and judging by the nature of the plots, it can be concluded that the increase in F concentration with increasing pressure is not as high as the increase in Ar concentration. This is the reason why the ratio of intensities of F to Ar is found to decrease with increasing pressure. However, it will be shown in the next section that the etch rate of SiO_2 wafer increases with increasing pressure, thereby confirming our belief that F concentration does increase with increasing pressure.

7.2.3 Effect of Flowrate

The effect of flowrate on intensity ratio (I_F/I_{Ar}) at various sets of pressure and power is presented in Appendix I, pages 237 to 238. Appendix I, page 237, shows the change in I_F/I_{Ar} with flowrate at 350 mTorr pressure and 400 watts. As long as pressure is maintained constant the concentration of Ar in the reactor stays constant, hence a decrease in the

trend in the plot indicates that F concentration decreases with increasing flowrate. As the flowrate is increased in the reactor the residence time of the gas in the reactor decreases. This means that the time available for the dissociation of the same concentration of gas at 350 mTorr pressure and 400 watts power decreases, hence the dissociation of CF_4 to F decreases. A similar trend can be seen in Appendix I, page 238. Here the effect of changing flowrate at 200 mTorr and at three different powers (300, 400 and 600 watts) are presented.

7.3 Loaded Reactor Runs

The experimental runs conducted with the reactor loaded with a single SiO_2 wafer, with changing: power, pressure, flowrate, oxygen percentage in the feed, bottom plate temperature and wafer position, in the reactor are presented and discussed in this section. The etch rate distribution across the wafer was obtained using the film thickness measuring strategy discussed in Chapter 3. Equidistance points on the wafer were selected, both along and across the direction of flow. The wafer was placed close to the reactor window through which the optical emission data was obtained. This was done so that the effect of wafer-surface reaction on the F species concentration could be monitored. The reactor position where the wafer was placed for all the loaded experimental runs was shown in Figure 19. The effect

of changing wafer position on the etch rate distribution was also conducted.

Loaded reactor runs were conducted to parameterize the surface kinetic model developed(31) and to validate the fluid flow and species distribution model developed in this study. The species distribution model uses the background flow profile to predict the F species concentration across the wafer. F species were shown to be the dominant reactive species in the surface kinetic model developed(31), hence a concentration profile of this species would predict the etch rate distribution across the wafer. The effect of various process parameters such as power, pressure and flowrate on the etch rate distribution on the wafer surface is of prime concern for this study. The plasma reactor model developed, accounts for changes in the above mentioned process variables. However, it was found that the etch rate across the wafer was effected by other process disturbances such as: etch time, leak rate into the reactor and bottom plate temperature. The influence of these parameters on the loaded reactor runs is discussed first.

7.3.1 Process Disturbances

Etch time is an important design variable in the loaded reactor runs. The etch rate which is a very strong function of F concentration is not constant throughout an experimental run but changes almost in the same way as does the F concentration. Initially as the power is turned on

the F concentration shoots up and finally comes down to a steady state value as the pressure in the reactor stabilizes (Figure 15). Hence in order for the loaded reactor runs to be of any use for the validation of the steady state species distribution model developed, it is important to etch the wafer long enough so that steady state etching dominates but at the same time overetching (etching of the substrate) does not take place. Appendix J, pages 239 to 240, illustrates the etch rate data obtained at 500 watts power, 300 mTorr pressure and 90 sccm flowrate (CF_4) in the plasma reactor. This condition represents the intermediate operating conditions in the plasma reactor. Etch rate data is presented both along and across the direction of flow. The etch rates are maximum for the shortest etch time situation of 7 minutes. This is because for this short time an etch time the influence of initial surge in F concentration (Figure 15) is maximum but this effect decreases as the etch time is increased (Appendix J, pages 239 to 240). This can be observed for the other three experimental runs at 14 and 20 minutes. The etch rates are close to each other as the etch time is increased from 14 to 20 minutes. This indicates a decrease in the influence of the initial surge, at this etch time of 20 minutes, which was selected as the etch time for the remaining runs. Another important aspect that can be observed from the etch rate data is the uniformity of etching. The etch rates are comparatively

lower at the left hand section which represents the side of wafer closer to the inlet than at the right hand side section. This is because the F concentration builds up in the reactor from the inlet to the exit as more and more CF_4 dissociates. Also it can be seen that the etch rate distribution across the direction of flow is almost uniform (Appendix J, page 240). An etch time of 20 minutes was selected for the rest of the experimental runs to study the effect of various process variables and disturbances on the etch rate distribution.

It was pointed out in the last section that oxygen in the air leaking into the reactor can have a significant effect on the overall etching process. Oxygen is found to enhance the production of F from CF_4 , thereby effecting the etch rate. To study the effect of oxygen on the etch rate distribution, pure oxygen was fed into the reactor at 0, 4, 8 and 20% of the CF_4 and Ar feed. The effect of adding oxygen on the etch rate distribution is presented in Appendix J, from pages 241 to 242, for a reactor power of 500 watts, pressure 300 mTorr and flowrate 90 SCCM. Here again a similar trend in the etch rate distribution as the one obtained earlier can be seen but the most important thing to be noticed is the tremendous increase in etch rate with increasing oxygen percent in the feed. The main purpose of presenting this etch rate data in this study is to demonstrate the sensitivity of the etch process to air leaks

into the system. However, in real system the influence of air leak is small due to the small air leak rate compounded with the small percentage of oxygen in air.

The last disturbance variable whose influence on the etch rate distribution was studied was the temperature of the bottom heater plate. It was demonstrated earlier in Chapter 6 that the conduction of heat from the bottom plate to the gas phase is very small to be able to influence the production of F species in the gas phases. But Appendix J, pages 243 to 244, shows that the etch rate data is significantly effected by the temperature of the bottom plate. The influence of changing temperature on the etch rate data is mainly on the surface kinetics than on the plasma kinetics. Hence it is important that the bottom plate be maintained at a constant temperature for an unbiased study on the influence of process parameters such as power, pressure and flowrate on etch rate. A constant temperature of 65 degrees centigrade was maintained throughout the remaining loaded reactor runs.

7.3.2 Design of Experiments

Various process disturbances that effect the experimental results were identified in the earlier section. An attempt was made to reduce the effect of these disturbances essentially by; using a sufficiently long etch time of 20 minutes and by maintaining the temperature to a constant value of 65 degree centigrade during the course of

each experimental run. Air leak to the reactor was minimized by greasing the O-ring at the reactor opening every time the reactor was opened.

As pointed out earlier the influence of power, pressure and flowrate and wafer position on the etch rate data and distribution were of prime importance in this study. These process parameters are highly interactive to the etch process and in order to study the influence of all parameters individually and interactively conditions that encompass the entire spectrum of operating conditions possible for our reactor were identified. Figure 23 presents a cuboid with its three axes as the fore mentioned process parameters. The conditions marked by bold dots were the identified operating conditions for this study. It can be seen that both the extremes and intermediate operating conditions were selected. The operating conditions at various points in this figure are presented in Table 3.

7.3.3 Process Parameters

The effect of varying power, pressure, flowrate and radial position on the etch rate data and its distribution is presented and discussed in this section.

Increasing power was found to enhance the dissociation of CF_4 and hence the production of reactive species mostly F. Hence it can be expected that with increasing power the etch rate will also go up, and this was observed in all the cases investigated, presented in Appendix J from pages 245

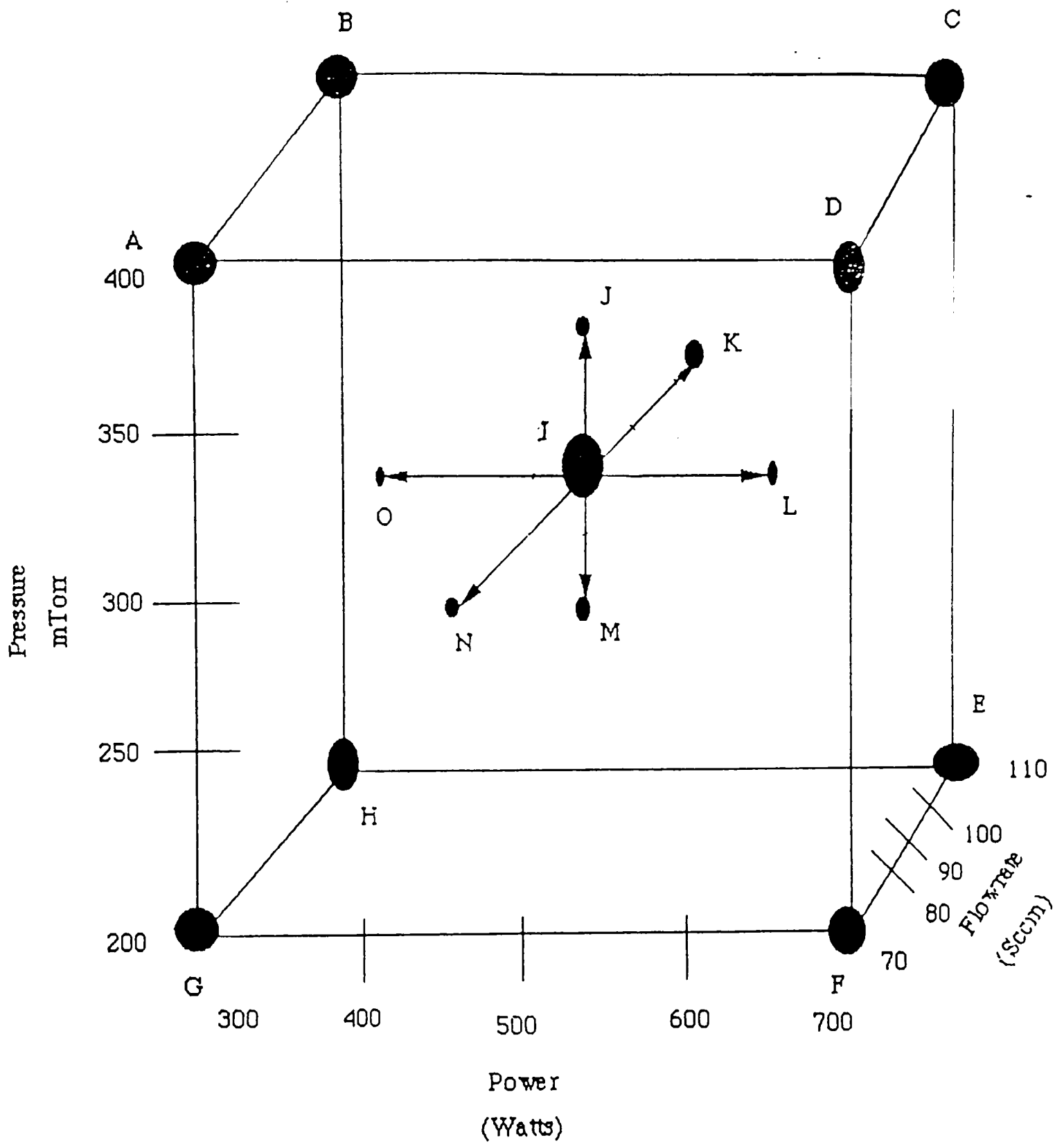


Figure 23: Operating Conditions for Loaded Reactor Runs.

Table 3: Operating Conditions for Loaded Runs.

Point (From Figure 23) -----	Power (Watt) -----	Pressure (mTorr) -----	Flowrate (Sccm) -----
A	300	400	70
B	300	400	110
C	700	400	110
D	700	400	70
E	700	200	110
F	700	200	70
G	300	200	70
H	300	200	110
I	500	300	90
J	500	350	90
K	500	300	100
L	600	300	90
M	500	250	90
N	500	300	80
O	400	300	90

to 254. Etch rate distribution both along and across the direction of flow at various sets of pressure and flowrate and at changing powers were investigated. The etch rates at higher power was found to be in general higher, but as Appendix J, page 245, shows the uniformity of etching at higher powers was poor. The etch rate were lower near the inlet of the reactor as compared to the exit. This is because the CF_4 feed coming in starts to dissociate near the inlet and the F produced, starts building up towards the exit. This change in F concentration is more drastic at higher powers than at lower and so the etch rate uniformities are also poor.

With increasing pressures, it was observed in the earlier section that the ratio of intensities of F to Ar decreases. However, this was essentially because the proportional increase in Ar concentration was much higher than the increase in F concentration. Another effect of increasing pressure is an increase in the ion density which also results in increasing etch rates. Thus it can be expected that increased pressure helps increase the etch rate as well. This can be observed in Appendix J from pages 255 to 264.

Increasing flowrate reduces the residence time of the feed CF_4 in the reactor hence less dissociation takes place, thereby reducing the etch rate. This trend can be observed

in Appendix J from pages 265 to 274. The uniformity of etching was found to become poorer with increasing flowrate.

The effect of changing the radial position in the etch rate and its distribution is presented in Appendix J from pages 275 to 276. The etch rate is not effected much but the uniformity of etching is found to improve.

CHAPTER 8

MODEL RESULTS VALIDATION

In this chapter a discussion on the validation of various models developed during the course of this research work is presented. The models validated in this chapter include: (1) empirical parametric electron density distribution model, (2) fluid flow model, (3) reactive species concentration distribution model for unloaded reactor runs and (4) reactive species concentration and etch rate distribution model for loaded reactor runs. All but the fluid flow model results were validated against experimental data. Since experimental data was not available for the validation of the fluid flow model, hence its validation was based on expected trends in pressure and velocity profiles for changing operating conditions.

8.1 Electron Density Model Results

The empirical model developed for the prediction of radial variation in electron density is presented in Appendix H. This model was parameterized against radial electron density distribution data available at five different powers (100, 200, 300, 400 and 500 watts) and at 200 mTorr pressure. The experimental data used to parameterize this model was presented in Chapter 7. Appendix K, pages 277 to 280, illustrates the comparison of electron density distribution predicted by the model and that obtained

experimentally using the Langmuir probe. These plots show that the model is able to predict a trend in the radial distribution of electron density, which is similar to that obtained experimentally. The model predictions are seen to be randomly greater or smaller than the experimental data irrespective of the power or the radial position. The difference between the experimental and predicted data was computed and is presented in Appendix K, page 281, as a function of radial position and power. Appendix K, page 281, clearly indicates the random nature of error between the predicted and experimental data. The model cannot be statistically rejected at the 95% confidence level using either the Wilcoxon Signed Rank Runs or slope test(48).

8.2 Fluid Flow Model Results

In this section the validity of the fluid flow model developed for the parallel plate radial flow reactor is presented. Since experimental validation of the fluid flow and pressure distribution model is not possible with our experimental setup, a qualitative model validation based on expected trends was conducted. The velocity and pressure profiles predicted by the model for changing flowrate and pressure were used to validate the model. The entrance and exit lengths were investigated by constraining the inlet and exit profiles to parabolic and flat profiles separately. The distance over which the flow developed was used to characterize the end effects. Appendix K, page 282, depicts

the velocity profile for parabolic inlet and outlet boundary conditions at 300 mTorr pressure and 90 sccm total flowrate in the plasma reactor. This operating condition was selected because it represents an intermediate operating condition in our reactor. These conditions were used as the base case for the study of the influence of changing boundary condition, pressure and flowrate. The x-z plane over which the velocity profile was computed was rotated to the horizontal position and the dimensionless axial distance, radial distance and velocities were plotted in three-dimensions. The velocity profile in the reactor was found to be near parabolic. The dimensionless velocity component can be seen to increase from the inlet to the exit. This can be expected since the cross section area of flow decreases from the inlet to the exit (center) of the reactor. Appendix K, page 283, presents the pressure distribution (in pascal) in the reactor with changing radial distance. The exit pressure was constrained to the operating pressure in the reactor. For this reason the model predicts an increasing pressure towards the inlet. Also the pressure drop is higher towards the exit than at the inlet, because the velocity of fluid increases rapidly towards the exit. But the overall pressure drop is small.

8.2.1 Effect of Boundary Conditions

Flat and parabolic velocity profile boundary conditions were constrained on the inlet and exit sections of the

reactor. This was done in order to study the end effects. One of the assumptions in the development of our fluid flow model was that the flow is uni-directional (r-direction). This assumption was the direct result of the presupposition that the flow develops over a very short length at the entrance and also that the exit length is negligible compared to the overall flow path length. Hence the axial velocity (v_z) which is essentially due to the end effects was considered negligible for our modeling purposes. In order to study the end effects in the reactor the inlet and exit velocity profiles were individually constrained to a flat profile, and the overall velocity profile obtained for these cases was compared to the base case velocity profile. Appendix K, page 284, presents the velocity profile for the plug flow exit boundary condition. We can see from this plot that the influence of constraining the exit to flat profile is felt only in a very small region about 0.3" out of the total flow path length of 10". The pressure distribution (Appendix K, page 285) is almost undisturbed from the earlier base case situation. The effect of changing the profile on the entrance length to plug flow, is presented in Appendix K, page 286. The inlet was constrained to plug flow and it can be seen from this plot that the entrance effect has an influence only over a small distance. About 3 x-z planes after the inlet section are influenced, this is about 0.8" out of 10" of total flow path

length. The pressure distribution (Appendix K, page 287) in the reactor is also the same as in parabolic profile case except at the inlet section where it shows a small surge.

Taking into account the short end lengths for our operating conditions, our assumption that axial velocity can be neglected in the flow modeling is fairly well justified.

8.2.2 Effect of Pressure

The effect of changing pressure on the flow profile is presented in Appendix K from pages 288 to 289. The original base case of 300 mTorr pressure and 90 sccm flowrate were used to study the effect of reducing the pressure to 200 mTorr while keeping the flowrate constant. The dimensionless velocity profile was observed to be the same form as that obtained earlier, however, the actual velocity increases with decreasing pressure. This is because decreasing pressure results in increased volumetric flowrate across the reactor. The pressure distribution (Appendix K, page 288 to 289) shows a similar trend but is lower throughout the reactor.

8.2.3 Effect of Flowrate

The effect of increasing the flowrate from the base case of 90 sccm to 120 sccm, while keeping the pressure constant is presented in Appendix K from pages 290 to 292. The dimensionless velocity (Appendix K, page 292) stays the same, but there is a significant change in the pressure drop

across the reactor. When the flowrate across the reactor is increased it would be expected that the pressure drop would increase too. However, in our case we have constrained the exit pressure to the operating pressure hence increasing flowrate pushes the inlet pressure to a higher value, thereby increasing the pressure drop across the reactor (Appendix K, page 292). The pressure at the outlet was set equal to the operating pressure because the pressure measuring device is located at the outlet, hence this constraint on pressure, models a real time situation.

Based on the above three validation steps we can conclude that the fluid flow model developed is a good representation of the actual phenomena taking place.

8.3 Unloaded Reactor Runs

Unloaded reactor runs were conducted in order to study the influence of changing power, pressure and flowrate operating parameters on the reactive fluorine species concentration. The species distribution model developed incorporates the plasma kinetics model, to predict the F concentration. The plasma kinetic model developed for our system was discussed in Chapter 5. Since in these experimental runs the reactor was not loaded with SiO₂ wafers, hence the effect of wafer-surface kinetics on the F concentration was eliminated. Thus the validity of the plasma kinetic model was tested using the unloaded reactor runs. The empirical electron density distribution model

discussed earlier was used in the plasma kinetic model to predict the F concentration in the reactor. The F intensity obtained experimentally was compared to its model-predicted concentration values, using argon actinometry technique discussed in Chapter 4. The ratio of F to Ar intensities obtained experimentally was compared to the ratio of these intensities predicted by the model. Argon actinometry was used to convert model-predicted spatial F and Ar concentrations to overall intensities. Here we present the final form of the expression developed in Chapter 4:

$$\frac{I_F}{I_{Ar}} = \sum \left[\frac{K_F}{K_{Ar}} \right] \left[\frac{[F]_i}{[Ar]_i} \right] \left[\frac{r_F^2}{r_{Ar}^2} \right] . \quad (4.14)$$

Here I's represent the overall intensities based on the spatial distribution of the ground state concentration of F and Ar. K's are the constants and r's are the radius of F and Ar atoms. All the constants in Equation (4.14) can be lumped together to give:

$$\frac{I_F}{I_{Ar}} = K \sum \left[\frac{[F]_i}{[Ar]_i} \right] . \quad (8.110)$$

A constant value was assigned to K in all the unloaded reactor runs and the intensity ratios predicted by the model were compared to the intensity ratios obtained experimentally. It was observed that for a value of 0.04 for K, excellent comparison between model-predicted and experimentally obtained intensity ratios was obtained. The

individual comparisons of model-predicted results to experimental data for changing power, pressure and flowrate are presented in the subsequent sections.

8.3.1 Effect of Power

Electron density and temperature were found to increase when the reactor power is increased. The electrons thus produced, strike the parent CF_4 gas molecules more frequently and with higher vigor to cause it to dissociate more. This results in an increase in F concentration. The experimental data for electron density variation with increasing power, at 200 mTorr pressure and at 6.6" radial position in the reactor is presented in Appendix K, page 293. The electron densities obtained experimentally at four different powers are illustrated here. The experimental values of the electron density with changing power were fit to a polynomial function. The electron density variation with power obtained from the polynomial curve fit is presented as the continuous upper curve in Appendix K, page 294. This polynomial function used to predict the electron density at a radial position of 6.6" is of the following form:

$$[EL] |_{power} = -6.292 \times 10^8 + 2.127 \times 10^6 \times po \quad (8.111)$$
$$+ 3.595 \times 10^4 \times po^2 .$$

Here p_0 represents the power in watts. The electron density values from 150 to 700 watts obtained from this polynomial function were used in the species distribution model to predict the intensity ratio of F to Ar. Appendix K, page 295, presents a comparison of experimentally obtained intensity ratios against the model-predicted intensity ratios. The trend predicted by the model for increasing power is very poor, especially at higher powers.

One reason for the poor comparison between the experimental and model-predicted values could be the insufficiency of our plasma kinetic model with changing power. Another possible reason could be the experimental error in the electron density data with power. Especially at higher powers where the electron density measurements are more susceptible to experimental error(49,50) because of the rapid contamination of the Langmuir probe. The influence of a possible error in the measurement of electron density with changing power was investigated in this study, in order to account for the poor model prediction.

Going back to Appendix K, page 293, we can see that there are only four data points available to fit a polynomial for electron density variation with changing power. The empirical radial electron density distribution model discussed in section 8.1 of this chapter was used to obtain a range between which the actual electron density values may be assumed to lie. This electron density

distribution model was developed by parameterizing the experimental electron density data available at five different powers (100, 200, 300, 400 and 500 watts) and at 200 mTorr pressure. It should be noticed here that the operating pressure was same for both the experimental run which was used to parameterize the empirical electron density distribution model and for this unloaded reaction run. The difference between the model-predicted and experimentally obtained data from Appendix K, pages 277 to 280, at 100, 300, 400 and 500 watts and at 6.6" radial position, were used to set the possible range of occurrence of electron density values for this unloaded reactor run condition. The upper and lower limits of possible occurrence on these experimental data points are illustrated in Appendix K, page 293. A straight line fit through the range of electron density values for the four different experimental data points is presented as the lower curve in Appendix K, page 294. The new polynomial function parameterized against these extreme data points is:

$$[EL] |_{p_0} = -2.889 \times 10^9 + 2.318 \times 10^7 \times p_0 . \quad (8.112)$$

The electron density from 150 to 700 watts obtained from this linear fit were used in the species distribution model to predict the intensity ratios of F to Ar. Appendix K, page 296, presents a comparison of experimentally obtained intensity ratios against the model-predicted intensity

ratios for the new electron density distribution function with changing power. The model is now able to predict a trend very similar to that obtained experimentally. The drastic change in the model predictions to changing electron density variation with power clearly indicates the sensitivity of model outputs to electron density.

The model intensity ratio outputs were also compared to experimental intensity data of F and Ar at 350 mTorr pressure and with changing power. Appendix K, page 297, presents the three electron density values experimental obtained at 350 mTorr and at 6.6" radial position, with increasing power.

The possible range of occurrence of these experimental values at each pressure was obtained as before from the electron density distribution data presented in Section 8.1. The pressure at which the electron density distribution model was parameterized in Section 8.1 was 200 mTorr which is not equal to the pressure for this unloaded reactor run (350 mTorr), but changing pressure does not have a very strong influence on the electron density (Chapter 7), hence its values was used here. The possible range of the electron density values is presented in Appendix K, page 297. The output from the polynomial curve fit of the experimental electron density data points is presented in Appendix K, page 298, along with the linear fit through the extreme ranges of the possible limits in experimental

values. The polynomial function of the experimental data is:

$$[\text{EL}]|_{\text{power}} = -1.112 \times 10^{10} + 4.917 \times 10^7 \times p_0 - 3.467 \times 10^4 \times p_0^2 \quad (8.113)$$

The linear curve fit function is:

$$[\text{EL}]|_{\text{power}} = -4.434 \times 10^9 + 1.74 \times 10^7 \times p_0 \quad (8.114)$$

Appendix K, page 299, shows the comparison between the intensity ratio of F and Ar based on both experimental data and model-predicted data using the polynomial curve fit of the electron density experimental data shown in Appendix K, page 297. The comparison was found to be poor again at higher powers. Appendix K, page 300, presents the comparison of model-predicted and experimental data for the same conditions except here the linear fit model for electron density distribution with power was used. The species distribution model is able to predict the same trend as that obtained experimentally.

In this section the experimental validation of the species distribution model for changing reactor power was conducted. The model-predicted intensity ratios of F and Ar were compared to the experimental data. It was observed here that the plasma kinetic model which is used by the species distribution model to predict the intensity ratio is very sensitive to electron density variations. Also the

comparison at higher powers is not good, suggesting either an unaccounted kinetic phenomenon at higher powers or errors in electron density measurement. However, within the range of experimental error in electron density values the species distribution model predicts trend in F concentration similar to that obtained experimentally.

8.3.2 Effect of Pressure

Here we present the comparison of model-predicted intensity ratio against experimental data with changing pressure at two different powers (300 and 600 watts).

With increasing pressure the intensity ratio of F to Ar were found to decrease essentially because the proportional increase in Ar concentration with increasing pressure is higher than the increase in F concentration. The electron density was found to decrease with increasing pressure too. Appendix K, page 301, presents the electron density variation with changing pressure from 100 to 500 mTorr and at 300 watts at 6.6" radial position. The polynomial curve fit of the experimental data is also presented on this page and its form is:

$$[EL] |_{\text{pressure}} = 4.226 \times 10^9 - 1.390 \times 10^7 \times pr \quad (8.115)$$
$$+ 1.047 \times 10^4 \times pr^2 .$$

The value of electron density from 150 to 400 Mtorr pressure obtained from this polynomial curve fit were used in the

species distribution model to predict the intensity ratio of F to Ar.

The model-predicted values are presented along with the experimental values in Appendix K, page 302. The model shows the same trend in the intensity ratio as that obtained experimentally. But on the whole the model-predicted intensity ratios are smaller than the experimentally obtaining intensity ratios. This could be because of air leaking into the reactor which is found to enhance the F concentration (Chapter 7).

Appendix K, page 303, presents the electron density variation with pressure at 600 watts and at 6.6" radial position in the reactor. The comparison of model outputs with experimental data at these conditions is presented in Appendix K, page 304. Here again the model does an excellent job of predicting the experimental trend with changing pressure.

8.3.3 Effect of Flowrate

Changing flowrate is not found to effect the electron density as long as the pressure and power are maintained constant. However, flowrate does effect the production of the reactive F species as it effects the residence time of feed gas in the reactor. It would be expected that increasing flowrate reduces the F concentration in the reactor since the feed gas has less time in the reactor to dissociate. Appendix K, page 305, illustrates the

comparison of model-predicted intensity ratios of F and Ar with changing flowrate to the experimental intensity ratio data. The comparison of model outputs with experimental data is good.

8.4 Loaded Reactor Runs

The model-predicted reaction species (F) concentrations were compared to experimental data for unloaded reactor cases in the earlier section. The model was able to predict trends vary similar to those obtained experimentally for all but the high power operating conditions cases. The comparison between the experimental data and the model outputs for unloaded reactor case suggested that the plasma kinetic expression used in conjunction with the electron density distribution function is sufficient to model the influence of operating parameters on the overall F concentration.

In this section we present a comparison between the experimental and model-predicted data for loaded reactor runs. These results will help check the validity of the surface kinetic expression(31) and the reactive species concentration distribution predicted by the species distribution model. The etch rate distribution data over the wafer surface, both along and across the direction of flow was used to validate the reactive species concentration distribution and the surface kinetic expression.

The surface kinetic expression used in this study along with the values of the kinetic parameters was presented in Chapter 5. Both F species and ions in the plasma were accounted by the surface kinetic expression for etching purposes. Fluorine concentration predicted by the model and ion density obtained experimentally were used in the species distribution model to study the influence of operating parameters on both the inter- and intra-wafer etch rate distribution.

For the loaded reactor runs studied here the wafer was placed both near the inlet and exit of the reactor and the etch rate predicted by the model was compared to the experimental etch rate data. Figure 24 shows the location of the wafers on the finite difference grids at the bottom plate. The three-dimensional plot of the F concentration for the wafer located near the inlet, on both the bottom and top plate is presented in Figures 25 and 26 respectively. Figure 25 shows the decrease in F concentration over the wafer surface, indicating that F is being consumed during etching. Figures 25 and 26 both show the gradient in F concentration in all the three directions. Diffusion plays an important role in replenishing the F atoms from all the directions over the wafer surface.

Appendix K, pages 306 and 307, illustrates the comparison between the experimental and model-predicted etch rate data both along and across the direction of flow for

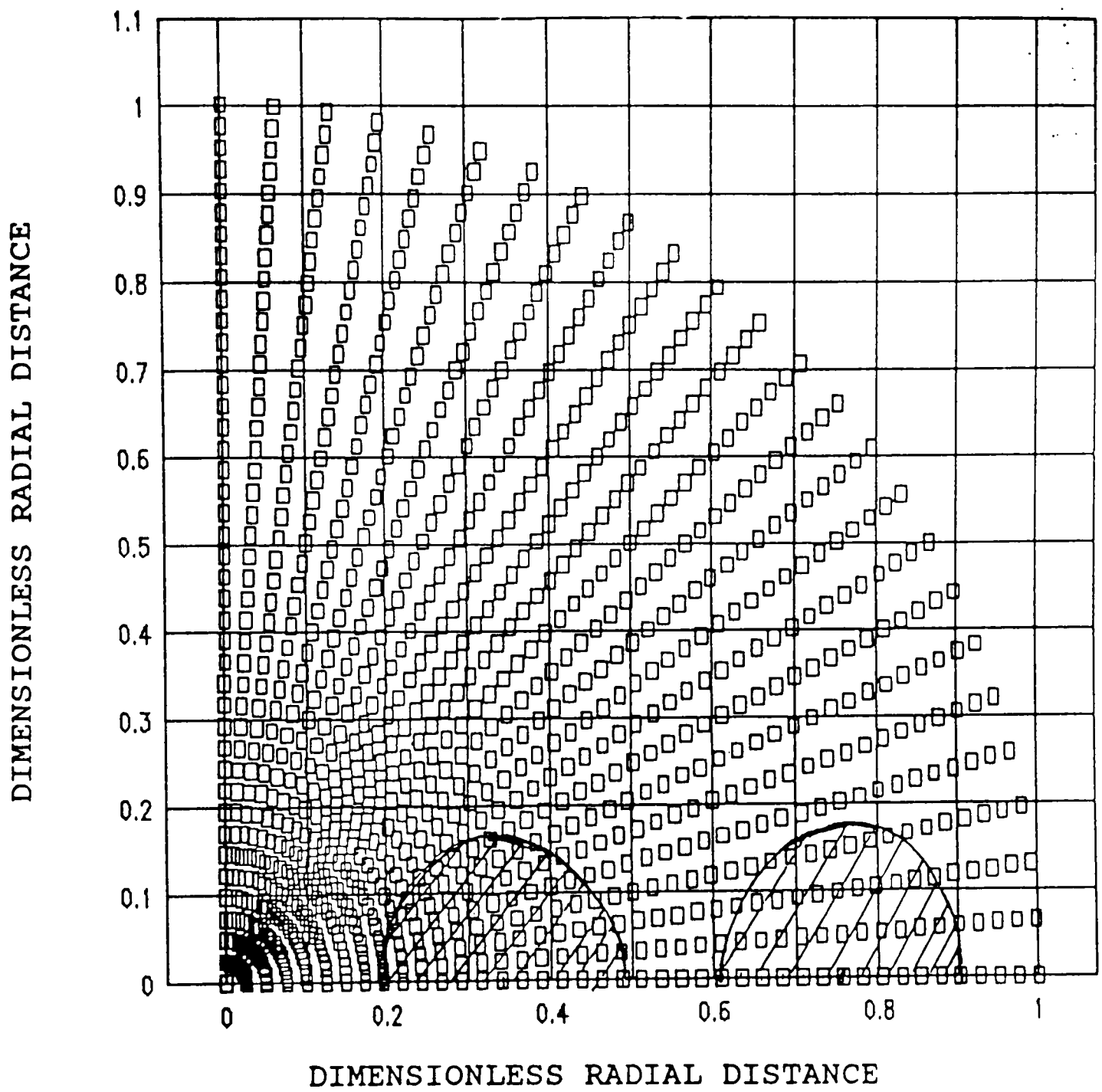


Figure 24: Location of Wafer on the Finite Difference Grid.

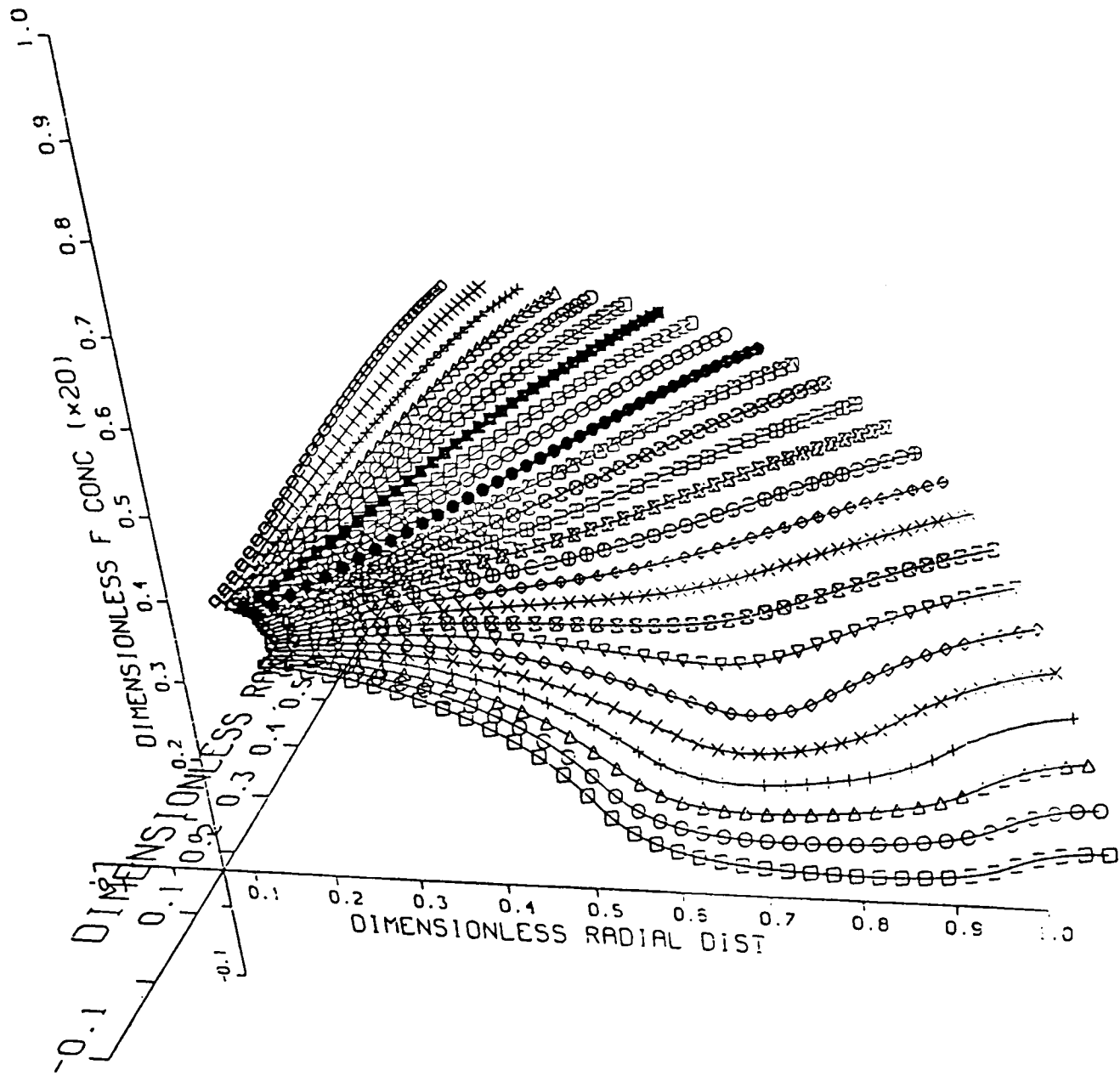


Figure 25: Three-Dimensional Plot of F. Concentration on the Bottom Plate for the Wafer Placed Near the Inlet.

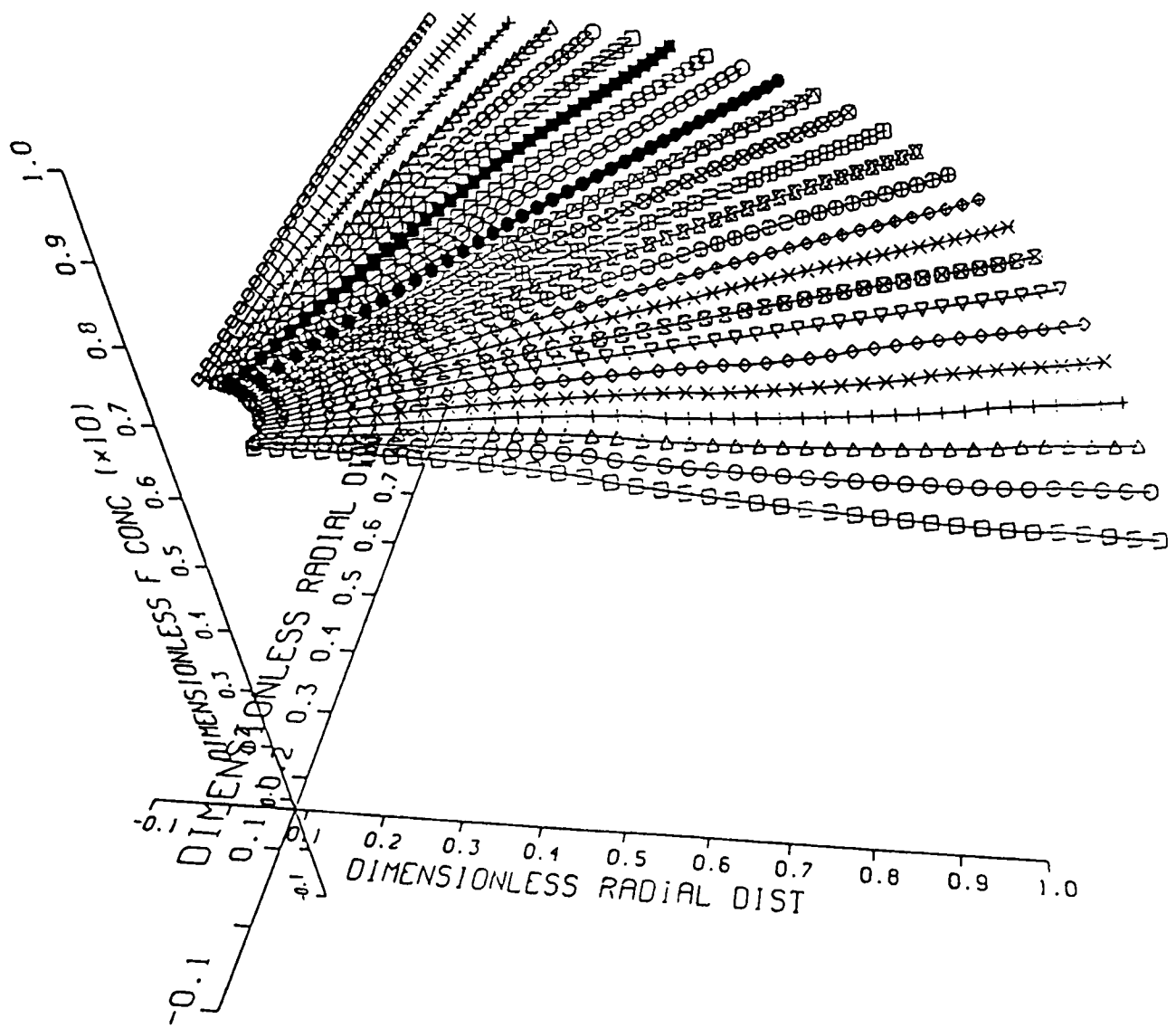


Figure 26: Three-Dimensional plot of F Concentration on the Top Plate for the Wafer Placed Near the Inlet.

the wafer located near the inlet. The model-predicted values are very close to the experimentally obtained values. However, at higher power, such as the one studied here (500 Watts), the etch rates predicted by the model at the region of the wafer close to the inlet compare poorly with the experimental data. One of the possible reasons for this could be that at higher powers ions play an important role in the etching process, by physically removing the SiO_2 molecules from the wafer surface. Also it can be expected that radial ion density distribution is vary similar to radial electron density distribution (Chapter 7), which is found to increase significantly from the inlet to the exit. This trend would be very similar to the etch rate profile obtained for higher powers. However, ion density distribution measurements were not taken, but a constant ion density value was used in the model, thereby suggesting the need for more extensive ion density measurements.

Appendix K, pages 308 and 309, shows the comparison between the experimental and model-predicted data for the wafer located near the exit. Both the model and experimental data show a fairly uniform etch rate distribution, thereby suggesting a uniform F and ion distribution at this wafer location.

CHAPTER 9

CRITIQUE AND DISCUSSIONS

In this work, results from the mathematical model developed for a CF_4 etch of SiO_2 were compared to experimental data. The mathematical model developed predicts the background fluid flow profile, reactive species (F) species and etch rate distribution over discrete wafer located in the reactor.

It was demonstrated that the background flow profile can be decoupled from diffusion and reaction effects, and can be obtained by numerically solving the θ -symmetric momentum balance equation. For the range of operating conditions used in this study the flow was found to be both laminar and in the continuum flow regime. The flow was assumed to be uni-directional (r-direction) since the influence of end effects were over a very small length as compared to the overall length of flow. Qualitative validation of the fluid flow model was conducted based on expected trends to changes in operating conditions and the model was found to behave well.

The velocity profile obtained from the fluid flow model was used in the species distribution model along with the electron density distribution and plasma and surface kinetic expression to model the reactive species and etch rate distribution across the reactor. The species distribution model solves the continuity equation for each species (CF_4 ,

CF_3 , F) in the reactor. Diffusion and bulk transport terms were included along with the plasma kinetic expression in the model. Simplified plasma kinetics based on dissociation of the parent feed gas molecules (CF_4) to CF_3 and F was used in conjunction with empirically developed electron density distribution expression.

The surface kinetic expression which accounts for the plasma-wafer reaction was used as a boundary condition. This interface kinetic expression was developed in a separate study and accounts for both F and ion assisted etching(31). The overall F concentration obtained by argon actinometry was used to parameterize the surface kinetic expression. Hence the kinetic parameters used in this study were scaled down from their original value, to account for the lower F concentration over the wafer surface. The ion density used in this expression was obtained experimentally and a constant value was used for all operating conditions. This assumption was justified since the ion density does not change much with changing operating conditions.

The concentration and etch rate distribution results from the model were validated experimentally using optical emission data and etch rate data. Argon actinometry was used with an arbitrary value assigned to the proportionality constant that is used to convert the intensity ratios to concentration ratios. Special stress was given to the

comparison of the trend predicted by the model and the experimental data, for a wide range of operating conditions.

The etch rate distribution value predicted by the model were compared to experimental data to account for the inter- and intra-wafer nonuniformities. It was observed that the model results were in general able to predict the trends obtained experimentally. Only at higher powers were the model-predicted results found to fall short of predicting the experimental results. This was attributed to the need for more extensive ion and electron density measurements. Most of all it was demonstrated through this work that if the charged species distributions are accounted for then a simplified plasma kinetic model can be used to model the plasma processes.

CHAPTER 10

CONCLUSIONS AND RECOMMENDATIONS

A three-dimensional mathematical model was developed to demonstrate the influence of process parameters on the uniformity of etching throughout a radial flow plasma reactor for a CF_4 etch of SiO_2 . The model use an empirical electron density distribution expression which was parameterized to account for variations in power, pressure and radial position in the reactor. The model also uses a phenomenologically developed etch reaction kinetic expression. The model predicts both the spatial fluorine concentration across the reactor and etch rate distribution across the wafer surface. The model results are compared to experimental data for a wide range of operating conditions. Model predictions were found to be in good agreement. The influence of operating parameters (power, pressure and flowrate) on both etch rate and uniformity is demonstrated. Such results indicate etch operating conditions that minimize computer chip yield sensitivity to process disturbances. The model developed in this work can be employed for various other related studies.

The model can be successfully employed for "parametric studies." The model developed accounts for all the major plasma reactor factors that influence the etch process, thus using the model it is possible to explore the influence of various operating variables on the etch characteristics.

Also using the model a "recipe" of operating conditions can be identified for the best etch uniformities. However, operating conditions that predict best etch are dependent to a certain extent on the reactor geometry. But the model developed predicts the background flow profile as well as the reactor species distribution, hence it can be successfully and easily modified for any other reactor geometry and/or etch system.

In conjunction with the above discussed possible line of study, the model can be also used to develop reactor design guidelines. The major aspects to be considered in a plasma reactor from etching stand-point are uniformity of etching as well as the rate of etching. Model simulations can be used to study the influence of operating parameters on the two desired aspects for various commercially available plasma reactors. Based on these studies plasma reactor guidelines that are conducive to faster and more uniform etching can be devised.

The steady state reactor species and etch rate distribution model can be coupled with a transient stochastic etch model to identify the operating conditions that would improve etch uniformity as well as optimize the etch process. Operating inputs to the model include power, pressure, and flowrate. Another important operating parameter to be considered in the future would be the affect of oxygen addition to the plasma system. Hence using the

model we anticipate that it will be possible to control the process on-line through the manipulation of the operating parameters discussed above, so as to achieve maximum etch uniformity in the shortest time.

BIBLIOGRAPHY

1. Manos D.M. and D.L. Flamm: "Plasma Etching: An Introduction," Plasma-Materials Interaction, Academic Press, 1989.
2. Kao A.S. and H.G. Stenger: "Analysis of Nonuniformities in the Plasma Etching of Silicon with CF_4/O_2 ," Submitted to the Journal of the Electrochemical Society, May 1989.
3. Smolinsky G. and D.L. Flamm: "The Plasma Oxidation of CF_4 in a Tubular-alumina Fast-flow Reactor," J. Appl. Phys., Vol. 50, No. 7, July 1979.
4. Edelson D. and D.L. Flamm: "Computer Simulation of a CF_4 Plasma Etching Silicon," J. Appl. Phys., Vol. 56, No. 5, September 1984.
5. Plumb I.C. and K.R. Ryan: "A Model of the Chemical Processes Occurring in CF_4/O_2 Discharges Used in Plasma Etching," Plas. Chem. and Plas. Proc., Vol. 6, No. 3, February 1986.
6. Plumb I.C. and K.R. Ryan: "A Model for the Etching of Si in CF_4 Plasma: Comparison with Experimental Measurements," Plas. Chem. and Plas. Proc., Vol. 6, No.3, February 1986.
7. Dalvie M., Jensen K.F. and D.B. Graves: "Modeling of Reaction for Plasma Processing I. Silicon Etching By CF_4 in a Radial Flow Reactor," Chem. Engg. Sci., Vol. 41, No. 4, August 1986.
8. Kobayashi J., Nakazato N. and K. Hiratsuka: "Numerical Simulation for Gas Flow and Mass Transfer in a Dry Etching Chamber," J. Electrochem. Soc., Vol. 136, No. 6, June 1989.
9. Dalvie M. and K.F. Jensen: "Combined Experimental and Modeling Study of Spatial Effects in Plasma Etching: CF_4/O_2 Etching of Silicon," J. Electrochem. Soc., Vol. 137, No. 4, April 1990.
10. Economou D.J., Park S.K. and G.D. Williams: "Uniformity of Etching in Parallel Plate Plasma Reactor," J. Electrochem. Soc., Vol. 136, No. 1, January 1989.

11. Venkatesan S.P., Edgar T.F. and I. Trachtenberg: "On the Dynamics of an Isothermal Radial-Flow Plasma Etcher," J. Electrochem. Soc., Vol. 136, No. 9, September 1989.
12. Keating J.T.: "Reactor Start Up and Reaction Kinetic Models for a Carbontetrafluoride Plasma Silicon Dioxide Etch," Master's Thesis, Texas Tech University, 1989.
13. "Plasma Reactor System Model A-24-D," Reference Manual, TI, 1980.
14. "NanoSpec/AFT #010-0174," Instruction Manual, Nanometrics Incorporation, July 1980.
15. H.H. Lee: "Fundamentals of Microelectronics Processing," McGraw-Hill Publishing Company, 1990.
16. D'Agostino R., Cramarossa F., De Benedicts P. and G. Ferraw: "Spectroscopic Diagnostic of CF_4 - O_2 Plasmas During Si and SiO_2 Etching Process," J. Appl. Phys., Vol. 52, No. 3, 1981.
17. Mogab G.J., Adam A.C. and D.L. Flamm: "Plasma Etching of Si and SiO_2 - The Effect of Oxygen Addition to CF_4 Plasma," J. Appl. Phys., Vol. 49, No.7, 1987.
18. Wolfe S. and R.N. Tauber: "Silicon Processing for the VLSI Era," Lattice Press, 1986.
19. Zamaideh E., Najmabadi F. and R.W. Conn: "Generalized Fluid Equation for Parallel Transport in Collisional to Weakly Collisional Plasma," Phys. Fluids, Vol. 29, No. 2, February 1986.
20. Economou D.J. and R.C. Alkire: "A Mathematical Model for a Parallel Plate Plasma Etching Reactor," J. Electrochem. Soc.: Solid-State Science and Technology, Vol. 131, November 1988.
21. Bird R.B., Stewart W.E. and E.N. Lightfoot: "Transport Phenomena," John Wiley and Sons, 1960.
22. Riggs J.B.: "An Introduction to Numerical Methods for Chemical Engineers," Texas Tech University Press, 1988.
23. Patankar S.V. and D.B. Spalding: "A Calculation Procedure for Heat, Mass and Momentum Transfer in Three-Dimensional Parabolic Flows," J. Heat Mass Transfer, Vol. 15, August 1971.

24. B.C. Chapman: "Glow Discharge Processing-Sputtering and Plasma Etching," Wiley-Interscience Publication, 1980.
25. Lee Y.H. and M.M. Chen: "Silicon Etching Mechanism and Anisotropy in $CF_4 + O_2$ Plasmas," J. Appl. Phys., Vol. 64, No. 10, October 1983.
26. Flamm D.L., Donnelly V.M. and J.A. Mucha: "The Reaction of Fluorine Atoms with Silicon," J. Appl. Phys., Vol. 52, No. 5, May 1981.
27. Doken M. and I. Miyata: "Etching Uniformity of Silicon in $CF_4 + O_2$ Plasmas," J. Electrochem. Soc., Vol. 120, No. 12, December 1979.
28. Robey S.W. and G.S. Oehrleim: "Fluorination of the Silicon Dioxide Surface During Reactive Ion and Plasma Etching in Halocarbon Plasmas," Surface Science, Vol. 210, August 1989.
29. Kawata T., Shibano T., Murata K. and K. Nagami: "A Study of Si Plasma Etching in $CF_4 + O_2$ gas with a Planer-Type Reactor," J. Appl. Phys., Vol. 54, No. 5, May 1983.
30. Winters H.F., Coburn J.W. and E. Kay: "Plasma Etching-A 'pseudo-black-box' Approach," J. Appl. Phys., Vol. 48, No. 12, December 1977.
31. Varnas A.K. and R.R. Rhinehart: "Reactive Kinetics for CF_4 and CF_4/O_2 Plasma Etching of Silicon Dioxide," To be presented at the Chicago AIChE meeting, November 1990.
32. Benneth C.O. and J.E. Myers: "Momentum, Heat and Mass Transfer," Tata McGraw-Hill Publishing Company, 1962.
33. Coburn J.W. and M. Chen: "Optical Emission Spectroscopy of Reactive Plasmas: A Method for Correlating Emission Intensity of Reactive Particle Density," J. App. Phys., Vol. 51, No. 6, June 1980.
34. Perry R.H., Green D.W. and J.O. Malony: "Perry's Chemical Engineers Handbook," McGraw-Hill Book Company, 1984.
35. Reichenberg D. "The Viscosity of Pure Gases at Low Pressure," AIChE J., Vol. 19, Pg. 854, May 1973.
36. Reid R.C., Sherewood T.K. and J.M. Praustnity: "The Properties of Gases and Liquids," McGraw-Hill Book Company, 1977.

37. Hirschfelder J.O., Curtiss C.F. and R.B. Bird:
"Molecular Theory of Gases and Liquids," Wiley, 1954.
38. Kreith F. and W.Z. Black: "Basic Heat Transfer," Harper
and Row Publishers, 1980.
39. Mayer T.M., and R.A. Baker: "Simulation of Plasma-
Assisted Etching Processes by Ion-beam Techniques," J.
Vac. Sci. Tech., Vol. 21, No. 3, Sept/Oct 1982.
40. O. Popov: Personal Correspondence, Microscience Inc.,
1990.
41. Field D., Hydes A.J. and D.F. Klemperer: "Spectroscopic
Studies of Florescent Emissions in Plasma Etching of Si
and SiO₂ and the Measurement of Gas-Surface
Interactions," Vac., Vol. 34, Pg. 563, June 1984.
42. Mogab G.J.: "Spectroscopic Studies for Plasma Etching
Systems," J. Vac. Tech., Vol. 34, No. 5, October 1983.
43. Baltes H.P.: "Numerical Simulation of a CF₄/O₂ Plasma
and Correlation with Spectroscopic and Etch Rate Data,"
J. Electrochem. Soc., Vol. 36, Pg. 199, August 1989.
44. Donnelly V.M., Flamm D.L. and W.C. Dantremont-Smith:
"Anisotropic Etching of SiO₂ in Low-frequency CF₄/O₂ and
NH₃/Ar Plasmas," Vol. 55, No. 1, January 1984.
45. Walkup R.E., Saenger K.L. and G.S. Selwyn:
"Spectroscopic Analysis for Plasma Etching Process," J.
Chem. Phys., Vol. 84, Pg. 2668, January 1986.
46. Graves D.B. and K.F. Jensen: "A Continuum Model of Dc
and RF Discharges," IEEE Trans. on Plas. Sci., Vol. PS-
14, No. 2, April 1986.
47. Kline L.E.: "Electron and Chemical Kinetics in the Low-
Pressure RF Discharge Etching of Silicon in SF₆," IEEE
Trans. on Plas. Sci., Vol. PS-14, No. 2, April 1986.
48. Bethea R.M. and R.R. Rhinehart: "Applied Engineering
Statistics ," Marcel Dekka Inc., 1991.
49. Clements R.M.: "Plasma Diagnostic with Electric
Probes," J. Vac. Sci. Tech., Vol. 15, No. 2,
March/April 1978.
50. Steinbruchel Ch.: "Langmuir Probe Measurements on CHF₃
and CF₄ Plasmas: The Role of Ions in the Reactive
Sputter Etching of SiO₂ and Si," J. Electrochem. Soc.,
Vol. 130, No. 3, March 1983.

APPENDIX A

MAJOR SPECIES IN A CF_4

PLASMA ETCH OF SILICON DIOXIDE

In a CF_4 plasma etch of SiO_2 , various species are present in the gas phase apart from CF_4 . These gas phase species can be categorized as,

1. The products of the dissociation of CF_4 in the plasma phase.
2. The products of the reaction of plasma species with the SiO_2 wafer.
3. The inert gas (Ar) fed to the reactor along with CF_4 for analysis of emission data.
4. Impurities along with the feed gases and leaks to the reactor system are other sources that contribute to the presence of various species in the reactor.

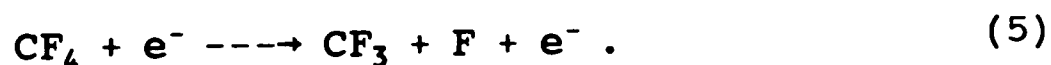
In this appendix an attempt is made to show that the major species in the plasma phase is CF_4 resulting in a near homogenous gas phase. The concentration of the other species categorized above are fairly small in the gas phase and this aspect has been discussed based on literature and our own sample calculations.

Sufficient evidence is available in literature to prove that the dissociation of CF_4 in the plasma is very small, less than 10%(1,4). Hence it is imperative that the products formed during the plasma phase electron impact

reactions are very small to significantly affect the uni-component nature of the plasma phase. Reactor geometry also has a strong influence on the overall dissociation of the feed gas molecules. Hence it is important to study the overall dissociation of the feed gas in our system. Simple calculations based on ideal gas law are presented subsequently for the estimation of the overall dissociation of CF_4 in the plasma reactor.

The start-up operation in our continuous flow plasma system involves first setting the flowrate and pressure in the reactor and letting the system purge for half hour (Chapter 3). Once steady state is achieved in the reactor the power is turned on, resulting in the dissociation of the feed CF_4 . This results in an increase in the pressure of the reactor gases initially but eventually the pressure comes down to its original value, due to the continuous nature of the plasma reactor system.

In the sample calculations discussed later it was assumed that the gas phase is ideal and all the dissociations occurring in the gas phase are of CF_4 going to CF_3 and F or:



Hence for every mole of CF_4 dissociated, two moles are formed. By ideal gas law the initial number of moles in the

reactor are:

$$N_1 = \frac{P_1 V}{RT} , \quad (\text{A.1})$$

and the final number of moles are:

$$N_2 = \frac{P_2 V}{RT} . \quad (\text{A.2})$$

Here N is the number of moles, P is the reactor pressure, V is the reactor volume, R is the gas constant and T is the temperature of the reactor gases. Subscripts 1 and 2 represent the initial and final conditions in the reactor, respectively. The increase in the number of moles in the plasma reactor as a result of dissociation is hence:

$$N_2 - N_1 = \frac{P_2 V}{RT} - \frac{P_1 V}{RT} . \quad (\text{A.3})$$

Lets assume that CF_4 is the only gas present in the reactor and X is the fraction of total number of moles of CF_4 that dissociate. Thus the total number of moles of CF_4 dissociated are XN_1 and the number of moles of products formed are $2XN_1$. Substituting this in Equation A.3 we get:

$$2XN_1 = N_2 - N_1 = (P_2 - P_1) \frac{V}{RT} . \quad (\text{A.4})$$

Substituting for N_1 in Equation (A.4) we get:

$$X = \frac{P_2 - P_1}{2P_1} . \quad (\text{A.5})$$

Hence if the maximum pressure reached in the reactor initially as the power is turned on is known then using its

values and the original pressure we can derive a rough estimate of the total fractional dissociation of feed CF_4 . Table 4 presents the percentage dissociation estimated based on the above method for different powers at 200 mTorr pressure for a pure CF_4 plasma. The maximum pressure in the reactor after the power is turned on, for various powers is also presented. It can be seen from this table that the range of dissociation for various powers is from 7.5% to 12.5%. However, it should be kept in mind that this dissociation rate is based on dissociation of CF_4 to CF_3 and F, but if CF_4 dissociates to CF_2 and 2F or if the CF_3 dissociates further then the percentage overall dissociation of CF_4 will decrease further. Hence these simple calculations show that the percentage dissociation of CF_4 in our plasma reactor are similar to the values reported in literature.

We have shown earlier in this appendix that the overall dissociation of CF_4 in our plasma reactor is small, here an attempt is made to show that the concentration of the etching products is also small compared to the overall CF_4 concentration. The ratio of the concentration of incoming feed gas to the concentration of the etching products concentration is compared to demonstrate the negligible amount of surface reactions products formed in the plasma reactor.

Table 4: Percentage Dissociation at Various Powers.

P_1 (mTorr)	Power	P_2 (atm)	Percentage Dissociation
200	150	210	2.5
200	200	220	5.0
200	250	230	7.5
200	300	230	7.5
200	350	240	10.0
200	400	240	10.0
200	450	240	10.0
200	500	250	12.5
200	550	250	12.5
200	600	250	12.5
200	650	250	12.5
200	700	250	12.5

The rate of influx of the feed gas (CF_4) concentration in the reactor is given as:

$$R_{\text{CF}_4} = Q_0 C_0 . \quad (\text{A.6})$$

Here Q_0 is the inlet gas flowrate in cm^3/sec and C_0 is the inlet concentration of CF_4 in $\text{g-moles}/\text{cm}_3$.

Enchant products are formed when the reaction phase species, mostly F (Chapter 5) react on the SiO_2 wafer surface. The rate of production of the enchant products is given by:

$$R_{\text{EP}} = R_{\text{ET}} A_{\text{ET}} . \quad (\text{A.7})$$

Here R_{ET} represents the etch rate in $\text{g-moles}/\text{cm}^3 \text{ sec}$ and A_{ET} represents the etch area in cm_2 .

The ratio of the production of etch products to the rate at which CF_4 enters the plasma reactor represents the dominance of the respective species. If this rate is smaller than one then CF_4 is the dominant species and vice versa.

The sample calculation conducted in this Appendix are based on the intermediated conditions existing in the reactor. For further details on operating conditions and etch rates refer to Chapter 7.

Figure 27 summarizes the value of various parameters used in the sample calculations. In all the experimental runs conducted the argon flowrate was maintained at 5% of the total flow. Using the typical data presented in Figure

1. Inlet Feed Flowrate (F_0) = 90 SCCM
2. Reactor Pressure (P) = 300 mTorr
3. Gas Temperature (T) = 298 K
4. Average Etch Rate (R_{ET}) = 50 A/min
5. Density of SiO_2 (ρ_{SiO_2}) = 2.75 g/cc(34)
6. Molecular Weight of SiO_2
(MW_{SiO_2}) = 60.08 g/g-moles
7. Gas Constant (R) = 82.06 atm cm³/K g-mole
8. Atmospheric Pressure (P_{atm}) = 760 Torr

Figure 27: Operating Conditions for Sample Run.

27 we can compute the values for the various terms.

Gas flowrate in the reactor is:

$$Q_0 = \left(\frac{F_0}{60}\right) \left(\frac{P_{atm}}{P}\right) . \quad (A.8)$$

$$Q_0 = 3800 \frac{\text{cm}^3}{\text{sec}} .$$

Assuming Ideal gas property of CF_4 and using 95% pure CF_4 in the feed we have:

$$C_o = \left(\frac{P}{P_{atm}}\right) \frac{\text{Fract.Purity}}{RT} \quad (A.9)$$

$$C_o = 1.53 \times 10^{-8} \text{ g-mole/cm}^3$$

Hence the rate of influx of CF_4 concentration in the reactor is:

$$R_{\text{CF}_4} = C_o Q_o \quad (A.6)$$

$$R_{\text{CF}_4} = 5.814 \times 10^{-5} \text{ g-moles/sec}$$

The etch rate in g-moles/cm^2 can be obtained as:

$$R_{\text{ET}} = ER \times 10^{-8} \left(\frac{1}{60}\right) \rho_{\text{SiO}_2} \left(\frac{1}{\text{MW}_{\text{SiO}_2}}\right) , \quad (A.10)$$

$$R_{\text{ET}} = 3.8 \times 10^{-10} \text{ g-moles/cm}^2 \text{ sec} .$$

For the 5" wafer used in our experimental study the etch area is:

$$A_{\text{ET}} = 126.68 \text{ cm}^2 .$$

Hence the rate of production of the enchant products is:

$$R_{EP} = R_{ET} \times A_{ET} , \quad (A.7)$$

$$R_{EP} = 4.83 \times 10^{-8} \text{ g-moles/sec} .$$

The ratio of R_{EP} and R_{CF_4} is computed to be:

$$\begin{aligned} \frac{R_{EP}}{R_{CF_4}} &= \frac{4.83 \times 10^{-8}}{5.814 \times 10^{-5}} , \\ &= 8.3 \times 10^{-4} . \end{aligned}$$

This ratio is much smaller than one hence any significant influence on the concentration of the overall plasma by the enchant product is not expected.

The last source contributing to the multi component species presence in the plasma phase is impurities entering the reactor system through the feed gas and air leaking to the reactor system. High purity (99.9%) CF_4 and Ar were used for plasma generation purposes. Also the leak of air to the reactor was minimized by sealing the O-ring at all the openings by vacuum grease.

APPENDIX B
TEMPERATURE CHANGE OF GAS
IN THE PLASMA REACTOR

Preliminary calculation done to show that the heat transfer from the reactor bottom heater plate to the gas flowing over it by forced convection is small is presented in this appendix. The heat transfer from the heater plate to the gas phase can be expressed as:

$$Q = A h (T_{\text{surf}} - \langle T \rangle) . \quad (\text{B.1})$$

Here A is the heat transfer area or the area of the bottom plate, h is the heat transfer coefficient, T_{surf} is the temperature of the bottom plate surface and $\langle T \rangle$ is the average temperature of the gas phase. The average temperature of the gas phase can be represented as:

$$\langle T \rangle = \frac{(T_{\text{in}} + T_{\text{out}})}{2} . \quad (\text{B.2})$$

Here T_{in} is the inlet temperature of the gas and T_{out} is the outlet temperature of the gas.

The heat transfer from the bottom plate to the gas results in an increase in the heat content of the gas:

$$Q = A h (T_{\text{surf}} - \langle T \rangle) = m C_p (T_{\text{out}} - T_{\text{in}}) . \quad (\text{B.3})$$

Here m is the mass flowrate of the gas and C_p is the specific heat capacity of the gas. The heat transfer coefficient was estimated from the forced convection heat transfer for external flow over a flat plate(38). This

expression for average Nusselt number is valid for laminar flow (Appendix D) and can be represented as:

$$\bar{N}_L = \frac{\bar{h}L}{k} = 0.664 \text{ Re}_L^{1/2} \text{ Pr}^{1/3}. \quad (\text{B.4})$$

Here Re_L is the Reynolds' number based on the free-velocity and on the length of the plate (L):

$$\text{Re}_L = \frac{\rho_{\text{CF}_4} L \langle V \rangle}{\mu}. \quad (\text{B.5})$$

Prandal Number (Pr) is expressed as:

$$\text{Pr} = \frac{\mu C_p}{k}. \quad (\text{B.6})$$

Here μ is the viscosity, k is the thermal conductivity and C_p is the specific heat of the gas phase. Specific heat of gas was estimated from the ideal gas heat capacity Equation(36):

$$C_p = A + B \times T + C \times T^2 + D \times T^3. \quad (\text{B.7})$$

Thermal Conductivity was estimated from the Misic and Thodos empirical estimation methods(36):

$$k = (10^{-6}) (14.52 T_r - 5.14)^{2/3} \frac{C_p}{\Gamma}. \quad (\text{B.8})$$

Where k is the low-pressure gas thermal conductivity in Cal/cm sec K, T_r is the reduced temperature and C_p is the heat capacity at constant pressure in Cal/g-moles K. Γ is

defined as:

$$\Gamma = \frac{T_c^{1/6} MW^{1/2}}{P_c^{2/3}} . \quad (B.9)$$

In order to estimate the temperature change of the gas flowing over the bottom heated plate, typical operating conditions in the reactor were selected (pressure=300 mTorr; gas flowrate=90 sccm; bottom plate temperature=65 °C; gas inlet temperature=25 °C).

At these conditions the density of the gas comprising of CF₄ can be estimated from the ideal gas law as:

$$\rho_{CF_4} = \frac{P MW_{CF_4}}{R T_{gas}} . \quad (B.10)$$

$$\rho_{CF_4} = 1.42 \times 10^{-6} \text{ gm/cm}^3 .$$

Radius of the bottom plate is 11" with 1" for the exit pipe at the center of the reactor. Hence the area of the bottom plate is:

$$A = 2432.2 \text{ cm}^2 .$$

Heat capacity of the gas phase at 298 K and at constant pressure was calculated from Equation (B.7) to be:

$$C_p = 14.594 \text{ Cal/g-mole K} .$$

The mass flowrate and the average velocity of gases at the operating conditions through the reaction are:

$$m = 5.4 \times 10^{-3} \text{ g/sec ,}$$

$$\langle V \rangle = 6.82 \text{ cm/sec .}$$

Thermal conductivity of CF_4 was estimated from Equations (B.9) and (B.8) and using the following physical constants:

Critical Temperature,

$$T_c = 227.6 \text{ K .}$$

Critical Pressure,

$$P_c = 36.9 \text{ atm .}$$

Molecular Weight,

$$MW = 88.005 \text{ g/g-mole .}$$

At a temperature of 298 K the reduced temperature of CF_4 gas is 1.3, and the corresponding thermal conductivity is:

$$k = 4.0 \times 10^{-5} \text{ Cal/cm sec K .}$$

Reynolds' number calculated from Equation (B.5) is:

$$Re_l = 1.64 \text{ .}$$

Prandal number calculated from Equation (B.6) is ,

$$Pr = 0.62 \text{ .}$$

Substituting the values of relevant parameters in Equation (B.5) we get the average heat transfer coefficient as:

$$h = 1.14 \times 10^{-6} \text{ Cal/cm}^2 \text{ sec K .}$$

From the heat balance Equation (B.3) and Equation (B.2) we get the temperature of the exiting gas as,

$$T_{\text{out}} = 298.43 \text{ K .}$$

The change in temperature for a gas flowing over a heated plate of 10" length at 65 °C is only 0.43 °C. Hence it is safe to assume that the heat transfer from the bottom plate to the gas phase is negligible.

APPENDIX C
PHYSICAL PROPERTY ESTIMATION
OF THE GAS PHASE

Physical properties of the gas phase are required before any detailed modeling of the plasma reactor can be conducted. In this appendix we discuss the estimation methods used in this study for gas density, viscosity and diffusion coefficient in the plasma reactor. The plasma phase was treated as a neutral gas phase in the estimation of the above mentioned physical properties. This assumption was fairly justified since the extent of dissociation of CF_4 is very small.

C.1 Gas Density

Density of the gas phase was estimated based on ideal gas law. Ideal gas law was used because the gases at low pressure, as that existing in the reactor (200-500 mTorr) are found to show ideal behavior. The gas was predominately CF_4 hence its density can be expressed as:

$$\rho_{\text{gas}} = \frac{P \text{ MW}_{CF_4}}{R T} \quad (\text{C.1})$$

Here P is the total pressure of the gas phase MW_{CF_4} is the molecular weight of CF_4 , R is the gas constant and T is the gas temperature.

At an intermediate operating condition: 300 mTorr pressure, 90 sccm flowrate and 298 K temperature, in the

reactor the gas density is:

$$\rho = 1.42 \times 10^{-6} \text{ g/cm}^3 .$$

C.2 Gas Viscosity

The viscosity of gas phase assumed to be comprising of pure CF_4 was estimated based on the corresponding-states relation suggested by Reichenberg(35). This method has been recommended for polar gases(36) such as CF_4 , at low pressures.

The corresponding state relation suggested by Reichenberg is:

$$\mu = \frac{a^* T_r}{[1 + 0.36 T_r (T_r - 1)]^{1/6}} . \quad (\text{C.2})$$

For organic compounds Reichenberg recommended for a^* :

$$a^* = \frac{\text{MW}^{1/2} T_c}{\sum n_i C_i} . \quad (\text{C.3})$$

Here MW is the molecular weight of the gas molecule, T_c is its critical temperature and n_i is the atomic groups of the i^{th} type with C_i as their group contribution. The values of these group contribution has been listed in reference 36.

For CF_4 the non-ring tetrahedron carbon group and four fluorine groups were used to estimate the values of the denominator in Equation (C.3). Critical temperature of CF_4 was also obtained from reference 36.

Hence for CF_4 we have:

$$\sum n_i C_i = 1 \times (-1.53) + 4 \times (4.46) .$$

$$\sum n_i C_i = 16.31 .$$

$$T_c = 227.6 \text{ K} .$$

$$MW_{CF_4} = 88.005 \text{ g/g-mole}$$

Thus at 298 K the viscosity of the gas in the plasma reactor can be obtained as follows:

$$a^* = 130.91 ,$$

$$T_r = 1.31 ,$$

$$\mu = 149.62 \text{ } \mu\text{P} .$$

C.3 Diffusion Coefficient of Gas Phase Species

In this section the estimation methods for predicting the diffusion coefficient of CF_4 in CF_4 (self-diffusion) and of CF_3 and F in CF_4 have been discussed.

C.3.1 $D_{CF_4-CF_4}$

The equation for low-pressure gas viscosity and diffusion have a common basis in the Chapman-Enskog theory and these two have been combined and expressed in reference 36 as:

$$D_{CF_4-CF_4} = 1.20 \frac{RT}{MW_{CF_4} P} \times \frac{\Omega_v}{\Omega_0} \times \mu_{CF_4} . \quad (C.4)$$

Here Ω_v/Ω_0 is approximately equal to 1.1 at ordinary temperature(36). Hence the final expression for self

diffusion of CF_4 is:

$$D_{CF_4-CF_4} = 1.32 \frac{RT}{MW_{CF_4} P} \times \mu_{CF_4} . \quad (C.5)$$

For a CF_4 plasma at 298 K and 300 mTorr pressure the self diffusion coefficient of CF_4 is:

$$D_{CF_4-CF_4} = 139.0 \text{ cm}^2/\text{sec} .$$

C.3.2 D_{F-CF_4}

Diffusion coefficient of F in CF_4 was estimated based on Chapman and Enskog's correlation along with Leonard-Jones Potential(36). The equation used was:

$$D_{F-CF_4} = 1.858 \times 10^{-3} T^{3/2} \frac{[(MW_F + MW_{CF_4}) / MW_F MW_{CF_4}]^{1/2}}{P \sigma_{F-CF_4}^2 \Omega_D} . \quad (C.6)$$

Here σ_{F-CF_4} represents the characteristic length of A for F and CF_4 interactions and Ω_D is the diffusion collision integral. Values of these two variables were estimated based on the Leonard-Jones Potential available in references 36 and 37. Table 5 lists the values of Leonard-Jones potential for F and CF_4 .

Table 5: Leonard-Jones Potential

	CF ₄	F
σ	4.662	3.0
ϵ	134.0	18.9985

APPENDIX D

FLOW REGIME AND TYPE OF FLOW

Knudsen number is used to characterize the flow regime(48). This dimensionless number is defined as the ratio of the mean free path (λ) of the gas molecule to the characteristic dimension of the vacuum system (d). For our system this number has been expressed as:

$$K_n = \frac{\lambda}{H} . \quad (D.1)$$

Here the distance (H) between the two electrodes is selected as the characteristic dimension. Furthermore the mean free path length (λ) for an ideal gas has been expressed as(24):

$$\lambda = \frac{1}{\sqrt{2} \pi d_0^2 n} . \quad (D.2)$$

Here n represents the number of gas molecules per unit volume and d_0 is the diameter of the gas molecule. Number of gas molecules per unit volume was calculated from the Avogadro's law. It was found stated earlier that the operating pressure in our reactor ranges from 200 mTorr to 500 mTorr and the reactor gas temperature is the same as its inlet temperature (298 K). Using the geometrical volume of the reactor as its actual volume the number of molecules of the gas (CF_4) are 2.0912×10^{17} to 3.0029×10^{17} per cm^3 . The range of number of molecules reported in literature is from 2.7×10^{14} to 2×10^{17} molecules per cm^3 . Thus our

value is well within the range of literature reported values.

Using the diameter of the CF_4 molecule as 2.82×10^{-8} cm(34), the Knudsen number can be computed for the two extreme operating pressures in the reactor.

For 200 mTorr:

$$K_n = 2.13 \times 10^{-4} ,$$

for 500 mTorr:

$$K_n = 1.48 \times 10^{-4} .$$

This low a value of Knudsen number indicates that the mean free path of the gas molecule is very small compared to the characteristic dimension of the reactor, hence the fluid is in continuum flow regime.

The range and operating conditions used in our experimental runs were discussed in the earlier chapters. Now we estimate the type of flow existing in the plasma reactor at typical operating condition. The distance between the plates (H) is used to compute the Reynolds' number:

$$R_e = \frac{H\langle V \rangle \rho}{\mu} . \quad (D.3)$$

Here $\langle v \rangle$ represents the average velocity across a axial plane, ρ is the density and μ is the viscosity of the gas phase. The data for calculating the Reynolds' number was presented in Appendix B. The Reynolds' number obtained at

the typical operating conditions in the reactor is:

$$R_e = 0.4 .$$

This indicated that the flow is laminar.

APPENDIX E

PARABOLIC FLOW VELOCITY PROFILE

The parabolic flow velocity profile can be represented as:

$$V_r(z) = C_2 \left[\frac{z}{H} - \frac{z^2}{H^2} \right] . \quad (\text{E.1})$$

Here $V_r(z)$ represents velocity of fluid flowing in r-direction perpendicular to the z-direction, C_2 is a constant and H is the total height of the z-plane.

For non-slip flow condition the boundary condition on the above equation is,

$$\text{at } z=0 \quad V_r(z) = 0 , \quad (\text{E.2})$$

$$\text{at } z=H \quad V_r(z) = 0 . \quad (\text{E.3})$$

The average velocity of fluid at any z-plane can be expressed as:

$$\langle V_r \rangle |_r = \frac{\int_0^{2\pi} \int_0^H R V_r(z) dz d\theta}{\int_0^{2\pi} \int_0^H R dz d\theta} . \quad (\text{E.4})$$

This equation can be solved by substituting for $V_r(z)$ to give:

$$\langle V_r \rangle |_r = C_2 1/6 . \quad (\text{E.5})$$

Hence C_2 is six times the average velocity at any z-plane at a distance r on the radial axis. The velocity profile at

any radial distance r can be expressed in terms of the average velocity at that plane as:

$$V_r(z) = 6 \langle V_r \rangle |_r \left[\frac{z}{H} - \frac{z^2}{H^2} \right] . \quad (\text{E.6})$$

APPENDIX F
COMPUTER CODE

C PLASMA.FOR
C VIKRAM SINGH

C THE SIMULATION OF A CF_4 PLASMA FOR SiO_2 ETCH IN A
RADIAL FLOW PLASMA REACTOR.

C This FORTRAN program PLASMA.FOR consists of two parts,
fluid flow section and the concentration distribution
section. The fluid flow section generates the velocity
profile which is used in the concentration distribution
section to model the species and etch rate distribution
in the reactor. The concentration profile of various
species calculated at discreet finite difference grid
points is stored in a data file to be later used in a
DISSPLA program, which plots the concentrations in
three dimensions.

C The code for PLASMA.FOR follows:

C MAIN PROGRAM

C The main program does the entire job of predicting the
velocity profile, concentration profile and etch rate
distribution. There are various sub-sections in this
program. The main program calls SUBROUTINE CONTOUR to
plot the contours at various levels.

C DOUBLE PRECISION

```
DOUBLE PRECISION VISC, REAVG, RE, EID, OP, ATMP, TAMB, FSTD
DOUBLE PRECISION CF4M, PGUESS, VGUESS, CONST, DR, DZ, RHO
DOUBLE PRECISION VELAVG, G, SRF, ERLIM, TOTAL, RA, VRCAL
DOUBLE PRECISION P(125, 125), VR(125, 125), TEST, ACON
DOUBLE PRECISION DPDR(120), DENO(120), CF4(70, 70, 70)
DOUBLE PRECISION F(70, 70, 70) CF3(70, 70, 70)
DOUBLE PRECISION AK1, AL1, AL2, AL3, DCF44, DCF43, DCF4F
DOUBLE PRECISION PECF3, PEF, DA1(50), C(70, 70, 70)
DOUBLE PRECISION DX(5, 1000), DY(5, 1000), CONTR(5, 100)
DOUBLE PRECISION ACF4(70), ACF3(70), AF(70), ET(1, 70, 70)
```

C OPEN INPUT AND OUTPUT FILES

```
OPEN (UNIT=8, FILE='CONC.PRN', STATUS='NEW')
OPEN (UNIT=9, FILE='VEL.PRN', STATUS='NEW')
OPEN (UNIT=7, FILE='TH.PRN', STATUS='NEW')
OPEN (UNIT=6, FILE='DEL.DAT', STATUS='OLD')
```


SIO2M=60.08

C MOLECULAR WEIGHT OF ARGON
ARM=39.948

C DENSITY OF SIO2
SIO2RH=2.75

C NUMBER OF GRIDS IN EITHER DIRECTIONS
N=42
NO=5
M=21
L=25

C KINETIC RATE CONSTANTS
C FOR PLASMA PHASE REACTIONS
AK1=1.1E-10

C FOR 'F' ETCHING REACTIONS
AL1=(7.897812E4/1.E3)*5.5E6
AL2=(1.735397E-2/1.E3)*5.5E6
AL3=(1.349056E-4/1.E3)*5.5E6

C VISCOSITY DATA
TCCF4=227.6
SIGNC=16.31

C DIFFUSIVITY DATA (CM²/SEC)
OMVOMD=1.1
SIGCF4=4.662
SIGNE=3.
ECF4KB=134.
ENEKB=110.
EONM=18.9985

C FRACTIONAL PURITY OF FEED CF4
FRPUR=FCF4F/FSTD

C FRACTION OF AR IN THE FEED
FRAR=FARF/FSTD

C ERROR CRITERIA FOR PRESSURE CORRECTION
PLIM=1.E-4

C FRACTION OF TOTAL CIRCUMFERENCE USED FOR COMPUTATION
FRC=0.25

C DATA FOR SPECTROSCOPIC STUDY
FRAD=6.875E-9
ARRAD=9.167E-9
ACON=1.
ACON1=.68

C IF YOU WANT TO SKIP VELOCITY PROFILE SECTION THEN ENTER
1 BELOW
ITUCK=2

C IF YOU WANT TO RUN FOR UNLOADED REACTOR ENTER 1 BELOW
ISKP=2

C INITIAL CALCULATIONS

TR=TREC/TCCF4
AX=(CF4M**.5)*TCCF4/SIGNC
VISC=(AX*TR/((1.+36*TR*(TR-1.))**.5/6.))*1.E-6
DCF44=(1.2*GASR*TREC*OMVOMD*VISC)/(CF4M*(OP/ATMP))
DCF441=1.4E4/(OP*101.3E3/760)
DCF43=DCF44*1.066
SIG=0.5*(SIGCF4+SIGNE)
EABKB=(ECF4KB*ENEKB)**.5
TSTAR=TREC/EABKB

OMED=(1.06036/TSTAR**0.15610)+(0.19300/EXP(.47635*TSTAR))+
*(1.03587/EXP(1.52996*TSTAR))+*(1.76474/EXP(3.89411*TSTAR))

DCF4F=1.8583E-3*(TREC**1.5)*(((1./CF4M)+(1./EONM))**.5)/
*((OP/ATMP) * (SIG**2) * OMED)
DCF4F1=(2.88E4)/(101.3E3*OP/760)

C DR=1./(FLOAT(N-1))
DZ=1./(FLOAT(M-1))
AL=2.*PI*R*FRC
DTH=AL/(FLOAT(L-1)*R)

C RHO=((OP/ATMP)/(GASR*TREC))*(FRPUR*CF4M+FRAR*ARM)
VOL=FSTD*ATMP*TREC/(OP*TAMB)
VELMAX=VOL/(PI*EID*H)
VELAVG=VOL/(2.*PI*(R/2.)*H)
VELMIN=VOL/(2.*PI*R*H)
REAVG=H*VELAVG*RHO/VISC
RE=H*VELMAX*RHO/VISC
FMASS=VOL*RHO
G=H/R
CF40=((OP/ATMP)*FRPUR)/(GASR*TREC)
ARO=((OP/ATMP)*FRAR)/(GASR*TREC)
NL=N-1
ML=M-1
LL=L-1

C ELECTRON DENSITY DISTRIBUTION

DRF1=R/(FLOAT(N-1))
DO 98 J=NO,N

```

      RP=FLOAT(J-1)*DRF1/100.
98    EL(J)=CEL*(.2025+10.109*RP-39.076*(RP**2)
      +30.786*(RP**3))
C
      IF (ITHF.EQ.0) GO TO 678
C    THIS NEXT LINE SKIPS VELOCITY PROFILE SECTION
      IF (ITUCK.EQ.1) GO TO 897

C    SET EXIT PRESSURE AS THE OP PRESSURE
PE=((OP/ATMP)*1.01325E5)/((RHO*1000.)*((VELMAX/100.)**2))

C    INITIAL GUESS AT EACH NODE POINT

      ITHF=0
      DO 10 J=NO,N
      DO 10 I=1,M
10    VR(I,J)=.5
      DO 5 I=1,M
5    P(I,NO)=PE

C          PRESSURE CORRECTION STARTS HERE

      WRITE(5,*) 'GUESS A LOGICAL NUMBER FOR PRESSURE
      CORRECTION'
      READ(5,*) F1
      F12=F1
      F19=F1

C
      DO 511 JK=NO+1,N-1
      DO 512 LP=1,100
      FAC=1./(10.**FLOAT(LP))
      WRITE(5,*) 'FAC',FAC
      FOLD=0.1
      FNEW=0.0
      DO 513 K=1,F12*20
      DPDR(JK)=F1-(FLOAT(K)*FAC)
      DO 514 LL=JK,N
514    DPDR(LL+1)=DPDR(LL)
      DO 515 JJ=NO,N
      DO 516 I=1,M
516    P(I,JJ+1)=P(I,JJ)+DR*DPDR(JJ+1)
515    CONTINUE
      WRITE(5,*) 'JK',JK
      WRITE(5,*) 'DPDR(JK)',DPDR(JK)

C    THIS SECTION CALCULATES VELOCITY

915  PRIGG=0.0
      SRF=1.55
      MAXITR=2000

```

```
ERLIM=1.E-5
ITER=0
ICOUNT=ICOUNT+1
```

C SET BOUNDRY POINTS FOR VELOCITY

```
DO 20 J=NO,N
VR(1,J)=0.0
20 VR(M,J)=0.0

DO 30 I=1,M
ZA=FLOAT(I-1)*DZ
VR(I,NO)=-VELMAX/VELMAX
30 VR(I,N)=-VELMIN/VELMAX
VR(I,NO)=-6.*1.*(ZA-(ZA*ZA))
30 VR(I,N)=-6.*( (VOL/(2.*PI*R*H)) / (VELMAX) ) * (ZA-(ZA*ZA))
```

C ITERATIVE CALCULATION FOR VELOCITY BEGINS HERE

```
100 ITER=ITER+1
PRIGG=TO+PRIGG
NUMERS=0
TOTAL=0.0
TO=0.0
```

C UPDATE INTERIOR POINTS

```
DO 40 J=NO+1,NL
DO 40 I=2,ML
RA=DR*FLOAT(J-1)
VRCAL1=-(G/RE)*(VR(I,J+1)-VR(I,J-1))/(2.*DR)
VRCAL2=-(G/RE)*RA*(VR(I,J+1)+VR(I,J-1))/(DR*DR)
VRCAL3=-(1./(RE*G))*RA*(VR(I+1,J)+VR(I-1,J))/(DZ*DZ)
VRCAL4=RA*(P(I,J+1)-P(I,J-1))/(2.*DR)
VRCAL5=-RA*(VR(I,J+1)-VR(I,J-1))/(2.*DR)
VRCAL6=-(G/RE)*RA*2./(DR*DR)
VRCAL7=-(1./(RE*G))*RA*2./(DZ*DZ)
```

```
VRCAL=(VRCAL1+VRCAL2+VRCAL3+VRCAL4)/(VRCAL5+VRCAL6+VRCAL7)
TEST=ABS((VRCAL-VR(I,J))/VRCAL)
TOTAL=TOTAL+TEST
TO=TOTAL
VR(I,J)=VR(I,J)+SRF*(VRCAL-VR(I,J))
40 IF(TEST.GT.ERLIM) NUMERS=NUMERS+1
IF(ITER.GT.MAXITR) GO TO 250
IF(NUMERS.NE.0) GO TO 100
250 CONTINUE
```

C PRESSURE CORRECTION CONTINUED

```
SUM=0.0
```

```

DENO(JK)=0.0
DO 913 I=1,M

SUM=RHO*2.*PI*DZ*H*R*(FLOAT(JK-1)*DR)*DABS(VR(I,JK))*VELMAX
913 DENO(JK)=SUM+DENO(JK)
WRITE(5,*)'DENO(JK)',DENO(JK),'JK',JK
FNEW=ABS(DENO(JK)-FMASS)
WRITE(5,*)'FNEW',FNEW,'FOLD',FOLD
IF(FNEW.LE.PLIM) GO TO 517
IF(FNEW.LT.FOLD) GO TO 518
GO TO 519
518 FOLD=FNEW
513 CONTINUE
519 F1=DPDR(JK)+2.*FAC
512 CONTINUE
517 IF(JK.GE.38) GO TO 992
F1=DPDR(JK)
GO TO 511
992 F1=F19
511 CONTINUE
FUNC=0.0
FU=0.0
DO 112 J=NO+1,N-1
FU=DABS(DENO(J)-FMASS)
112 FUNC=FUNC+FU
C
WRITE(5,*)'THE OPERATING CONDITIONS FOR THIS SIMULATION
RUN ARE'
WRITE(5,*)'THE OPERATING PRESSURE IN THE REACTOR
IS=',OP,'TORR'
WRITE(5,*)'FLOWRATE IN THE REACTOR IS=',FSTD*60,'SCCM'
WRITE(5,*)'TEMPERATURE IN THE REACTOR IS=',TAMB,'K'
WRITE(5,*)'TOTAL ERROR IN MASS FLOWRATE=',FUNC
C
DO 115 J=NO,N
DO 115 I=1,M
115 WRITE(6,*)VR(I,J)
GO TO 111

C THIS SECTION READS VELOCITY STORED FROM PREVIOUS RUNS

897 DO 121 J=NO,N
DO 121 I=1,M
121 READ(6,*)VR(I,J)

C CONSTANT CALCULATIONS FOR CONCENTRATION

678 PECF4=VELMAX*R/DCF44
PECF3=VELMAX*R/DCF43
PEF=VELMAX*R/DCF4F

C ORDER OF RXN W.R.T. ELECTRON IS ENTERED HERE
TR7=1.0

```

```

DO 9834 J=NO,N
9834 DA1(J)=AK1*(EL(J)**TR7)*R/VELMAX

```

C SET INITIAL GUESSES FOR CONCENTRATION

```

DO 199 I=1,M
DO 199 J=NO,N
DO 199 K=1,L
CF4(I,J,K)=1.E-1
F(I,J,K)=1.E-2
199 CF3(I,J,K)=0.003
IFLAG=0

```

C CALCULATION FOR CONCENTRATION BEGINS HERE

```

111 SRIGG=0.0
WRITE(5,*) 'ENTER THE SRF VALUE'
READ(5,*) SRF1
MAXIT1=5000
ITER1=0
ICONT1=ICONT1+1
ERLIM1=1.E-5
IFCO=-1
IF (IFLAG.NE.0) ERLIM1=5.E-5

```

C SET BOUNDARY POINTS

```

214 IFCO=1*IFCO
IF (IFLAG.EQ.0) GO TO 6
IF (IFLAG.EQ.1) GO TO 7
IF (IFLAG.EQ.2) GO TO 8
C **** THIS IS FOR CF4, ****
6 DO 212 K=1,L
DO 212 I=1,M
P12=(VELMAX*R*2.*DR/DCF44)
CF4(I,N,K)=(-P12*VR(I,N)+4.*CF4(I,N-1,K)-CF4(I,N-2,K))/
*(3.-P12*VR(I,N))
212 CF4(I,NO,K)=(1./3.)*(4.*CF4(I,NO+1,K)-CF4(I,NO+2,K))
DO 213 K=1,L
DO 213 J=NO,N
CF4(1,J,K)=(1./3.)*(4.*CF4(2,J,K)-CF4(3,J,K))
213 CF4(M,J,K)=(1./3.)*(4.*CF4(M-1,J,K)-CF4(M-2,J,K))
DO 219 J=NO,N
DO 219 I=1,M
CF4(I,J,1)=(1./3.)*(4.*CF4(I,J,2)-CF4(I,J,3))
219 CF4(I,J,L)=(1./3.)*(4.*CF4(I,J,L-1)-CF4(I,J,L-2))
GO TO 27
C **** THIS IS FOR CF3 ****
7 DO 411 I=1,M
DO 411 K=1,L

```

```

      P13=(VELMAX*R*2*DR/DCF43)
CF3(I,N,K)=(4.*CF3(I,N-1,K)-CF3(I,N-2,K))/(3.-P13*VR(I,N))
411  CF3(I,NO,K)=(1./3.)*(4.*CF3(I,NO+1,K)-CF3(I,NO+2,K))
      DO 412 J=NO,N
      DO 412 K=1,L
      CF3(1,J,K)=(1./3.)*(4.*CF3(2,J,K)-CF3(3,J,K))
412  CF3(M,J,K)=(1./3.)*(4.*CF3(M-1,J,K)-CF3(M-2,J,K))
      DO 415 J=NO,N
      DO 415 I=1,M
      CF3(I,J,1)=(1./3.)*(4.*CF3(I,J,2)-CF3(I,J,3))
415  CF3(I,J,L)=(1./3.)*(4.*CF3(I,J,L-1)-CF3(I,J,L-2))
      GO TO 27
C **** THIS IS FOR F *****
      DO 413 I=1,M
      DO 413 K=1,L
      P14=(VELMAX*R*2.*DR/DCF4F)
      F(I,N,K)=(4.*F(I,N-1,K)-F(I,N-2,K))/(3.-P14*VR(I,N))
C      F(I,N,K)=0.0
413  F(I,NO,K)=(1./3.)*(4.*F(I,NO+1,K)-F(I,NO+2,K))
      DO 414 J=NO,N
      DO 414 K=1,L
      F(1,J,K)=(1./3.)*(4.*F(2,J,K)-F(3,J,K))
414  F(M,J,K)=(1./3.)*(4.*F(M-1,J,K)-F(M-2,J,K))
      DO 416 J=NO,N
      DO 416 I=1,M
      F(I,J,1)=(1./3.)*(4.*F(I,J,2)-F(I,J,3))
416  F(I,J,L)=(1./3.)*(4.*F(I,J,L-1)-F(I,J,L-2))

      IF (ISKP.EQ.1) GO TO 27

C      ETCH RATE B/C
      P3=(8*1.E-8*SIO2RH*H*DZ/(DCF4F*CF40*60*SIO2M))
      K=1
      N01=10
      N1=27
      GO TO 810
803  IF (K.EQ.2) GO TO 804
      IF (K.EQ.3) GO TO 805
      IF (K.EQ.4) GO TO 806
      IF (K.EQ.5) GO TO 807
      IF (K.EQ.6) GO TO 808
      IF (K.EQ.7) GO TO 809
      IF (K.EQ.8) GO TO 811
      IF (K.EQ.9) GO TO 812
804  N01=10
      N1=27
      GO TO 810
805  N01=11
      N1=26
      GO TO 810
806  N01=11
      N1=26

```

```

      GO TO 810
807  N01=12
      N1=25
      GO TO 810
808  N01=12
      N1=24
      GO TO 810
809  N01=13
      N1=23
      GO TO 810
811  N01=14
      N1=22
      GO TO 810
812  N01=15
      N1=20
810  DO 8000 J=N01,N1
      8000
F(1,J,K)=((CE*F(3,J,K)-4.*CE*F(2,J,K))/(-3*CE-3*AL3*CF40*
*F(1,J,K)+4*AL3*CF40*F(2,J,K)-AL3*CF40*F(3,J,K)-AL1*P3*CE*CF
40
*-AL2*P3*CF40))
C    WRITE(5,*)'FLO',F(1,J,K)
      K=K+1
      IF (K.GT.9) GO TO 27
      GO TO 803

C    ITERATIVE CALCULATION FOR CONCENTRATION STARTS HERE

27   ITER1=ITER1+1
      SRIGG=TO1+SRIGG
      WRITE(5,*)IFLAG,ITER1,SRIGG,TOTAL1,NUMRS1
      WRITE(5,*)'ERROR=',TO2

C
      WRITE(5,*)'CF4',CF4(9,NO,2),CF4(9,10,2),CF4(9,25,2),CF4
(9,N,2)
C
      WRITE(5,*)'CF3',CF3(1,NO,2),CF3(1,10,2),CF3(1,25,2),CF3
(1,N,2)
C
      WRITE(5,*)'F',F(9,NO,2),F(9,10,2),F(9,25,2),F(9,35,2),F
(9,N,2)
      NUMRS1=0
      TOTAL1=0.0
      TO1=0.0
      TO2=0.0

C    UPDATE INTERIOR POINTS

      IF (IFLAG.EQ.0) GO TO 28
      IF (IFLAG.EQ.1) GO TO 28
      DO 215 K=2,LL

```

```

DO 215 J=NO+1,NL
DO 215 I=2,ML

C
  RA1=DR*FLOAT(J-1)
  IF (IFLAG.EQ.0)GO TO 1
  IF (IFLAG.EQ.1)GO TO 2
  IF (IFLAG.EQ.2)GO TO 3
C ***** THIS SECTION IS FOR CF4 *****
  1   C1=-VR(I,J)*(CF4(I,J+1,K)-CF4(I,J-1,K))/(2.*DR)

C2=(1./PECF4)*(1./RA1)*(CF4(I,J+1,K)-CF4(I,J-1,K))/(2.*DR)
  C3=(1./PECF4)*(CF4(I,J+1,K)+CF4(I,J-1,K))/(DR**2)

C4=(1./(PECF4*(G**2)))*(CF4(I+1,J,K)+CF4(I-1,J,K))/(DZ**2)
C5=(2./(PECF4*(DR**2)))+(2./((G**2)*PECF4*(DZ**2)))+DA1(J)
  *(2./(PECF4*(RA1**2)*(DTH**2)))

C51=((1./PECF4)*(1./(RA1**2))*(CF4(I,J,K+1)+CF4(I,J,K-1))
  *(DTH**2))
  CF4CAL=(C1+C2+C3+C4+C51)/C5
  TEST1=DABS((CF4CAL-CF4(I,J,K))/CF4CAL)
  TOTAL1=TOTAL1+TEST1
  TO1=TOTAL1
  CF4(I,J,K)=CF4(I,J,K)+SRF1*(CF4CAL-CF4(I,J,K))
  GO TO 215
C ***** THIS IS FOR CF3 *****
  2   C6=-VR(I,J)*(CF3(I,J+1,K)-CF3(I,J-1,K))/(2.*DR)

C7=(1./PECF3)*(1./RA1)*(CF3(I,J+1,K)-CF3(I,J-1,K))/(2.*DR)
C8=(1./PECF3)*(CF3(I,J+1,K)+CF3(I,J-1,K))/(DR**2)+DA1(J)
  **CF4(I,J,K)

C9=(1./(PECF3*(G**2)))*(CF3(I+1,J,K)+CF3(I-1,J,K))/(DZ**2)
  C10=(2./(PECF3*(DR**2)))+(2./((G**2)*PECF3*(DZ**2))
  *(2./(PECF3*(RA1**2)*(DTH**2)))

C91=(1./PECF3)*(1./(RA1**2))*(CF3(I,J,K+1)+CF3(I,J,K-1))
  *(DTH**2)
  CF3CAL=(C6+C7+C8+C9+C91)/C10
  TEST1=DABS((CF3CAL-CF3(I,J,K))/CF3CAL)
  TOTAL1=TOTAL1+TEST1
  TO1=TOTAL1
  CF3(I,J,K)=CF3(I,J,K)+SRF1*(CF3CAL-CF3(I,J,K))
  GO TO 215
C ***** THIS IS FOR F *****
  3   C11=-VR(I,J)*(F(I,J+1,K)-F(I,J-1,K))/(2.*DR)
  C12=(1./PEF)*(1./RA1)*(F(I,J+1,K)-F(I,J-1,K))/(2.*DR)
  C13=(1./PEF)*(F(I,J+1,K)+F(I,J-1,K))/(DR**2)+DA1(J)
  **CF4(I,J,K)
  C14=(1./((G**2)*PEF))*(F(I+1,J,K)+F(I-1,J,K))/(DZ**2)

```

C15=(2./ (PEF* (DR**2))) + (2./ ((G**2)*PEF*(DZ**2)))
 (2./ (PEF(RA1**2)*(DTH**2)))

C151=(1./PEF)*(1./ (RA1**2))*(F(I,J,K+1)+F(I,J,K-1))/(DTH**2)
 FCAL=(C11+C12+C13+C14+C151)/C15
 TO2=TO2+(C11+C12+C13+C14+C151-C15*F(I,J,K))
 TEST1=DABS((FCAL-F(I,J,K))/FCAL)
 TOTAL1=TOTAL1+TEST1
 TO1=TOTAL1
 F(I,J,K)=F(I,J,K)+SRF1*(FCAL-F(I,J,K))

C
 215 IF(TEST1.GT.ERLIM1) NUMRS1=NUMRS1+1
 IF(ITER1.GT.MAXIT1) GO TO 216
 IF(NUMRS1.NE.0) GO TO 214
 216 CONTINUE
 GO TO 237

C
 28 DO 217 K=LL,2,-1
 DO 217 J=NL,NO+1,-1
 DO 217 I=ML,2,-1

C
 RA1=DR*FLOAT(J-1)
 IF (IFLAG.EQ.0) GO TO 139
 IF (IFLAG.EQ.1) GO TO 299
 IF (IFLAG.EQ.2) GO TO 399

C ***** THIS SECTION IS FOR CF4 *****

139 C1=-VR(I,J)*(CF4(I,J+1,K)-CF4(I,J-1,K))/(2.*DR)

C2=(1./PECF4)*(1./RA1)*(CF4(I,J+1,K)-CF4(I,J-1,K))/(2.*DR)
 C3=(1./PECF4)*(CF4(I,J+1,K)+CF4(I,J-1,K))/(DR**2)

C4=(1./ (PECF4*(G**2)))*(CF4(I+1,J,K)+CF4(I-1,J,K))/(DZ**2)

C5=(2./ (PECF4*(DR**2))) + (2./ ((G**2)*PECF4*(DZ**2))) + DA1(J)
 (2./ (PECF4(RA1**2)*(DTH**2)))

C51=((1./PECF4)*(1./ (RA1**2))*(CF4(I,J,K+1)+CF4(I,J,K-1))
 *(DTH**2))
 CF4CAL=(C1+C2+C3+C4+C51)/C5
 TO2=TO2+(C1+C2+C3+C4+C51-C5*CF4(I,J,K))
 TEST1=DABS((CF4CAL-CF4(I,J,K))/CF4CAL)
 TOTAL1=TOTAL1+TEST1
 TO1=TOTAL1
 CF4(I,J,K)=CF4(I,J,K)+SRF1*(CF4CAL-CF4(I,J,K))
 GO TO 217

C ***** THIS IS FOR CF3 *****

299 C6=-VR(I,J)*(CF3(I,J+1,K)-CF3(I,J-1,K))/(2.*DR)

C7=(1./PECF3)*(1./RA1)*(CF3(I,J+1,K)-CF3(I,J-1,K))/(2.*DR)

C8=(1./PECF3)*(CF3(I,J+1,K)+CF3(I,J-1,K))/(DR**2)+DA1(J)
 **CF4(I,J,K)

```

C9=(1./ (PECF3*(G**2))) *(CF3(I+1,J,K)+CF3(I-1,J,K))/(DZ**2)
C10=(2./ (PECF3*(DR**2)))+2./ ((G**2)*PECF3*(DZ**2))
  *(2./ (PECF3*(RA1**2)*(DTH**2)))

C91=(1./PECF3)*(1./ (RA1**2)) *(CF3(I,J,K+1)+CF3(I,J,K-1))
  *(DTH**2)
CF3CAL=(C6+C7+C8+C9+C91)/C10
TEST1=DABS((CF3CAL-CF3(I,J,K))/CF3CAL)
TOTAL1=TOTAL1+TEST1
TO1=TOTAL1
CF3(I,J,K)=CF3(I,J,K)+SRF1*(CF3CAL-CF3(I,J,K))
GO TO 217

C ***** THIS IS FOR F *****
399 C11=-VR(I,J)*(F(I,J+1,K)-F(I,J-1,K))/(2.*DR)
C12=(1./PEF)*(1./RA1)*(F(I,J+1,K)-F(I,J-1,K))/(2.*DR)
C13=(1./PEF)*(F(I,J+1,K)+F(I,J-1,K))/(DR**2)+DA1(J)
  **CF4(I,J,K)
C14=(1./((G**2)*PEF))*(F(I+1,J,K)+F(I-1,J,K))/(DZ**2)
C15=(2./ (PEF*(DR**2)))+(2./ ((G**2)*PEF*(DZ**2)))
  *(2./ (PEF*(RA1**2)*(DTH**2)))

C151=(1./PEF)*(1./ (RA1**2)) *(F(I,J,K+1)+F(I,J,K-1))/(DTH**2)
FCAL=(C11+C12+C13+C14+C151)/C15
TEST1=DABS((FCAL-F(I,J,K))/FCAL)
TOTAL1=TOTAL1+TEST1
TO1=TOTAL1
F(I,J,K)=F(I,J,K)+SRF1*(FCAL-F(I,J,K))

C
217 IF(TEST1.GT.ERLIM1)NUMRS1=NUMRS1+1
  IF(ITER1.GT.MAXIT1) GO TO 226
  IF(NUMRS1.NE.0) GO TO 214
226 CONTINUE

C PRINT OUT THE FINAL RESULTS

237 WRITE(5,*) 'NO. OF ITERATION FOR
  IFLAG=',IFLAG,'=',ITER1
  IFLAG=IFLAG+2

C THIS SECTION COMPUTES THE PERCENTAGE DISS OF CF4

SUM99=0.0
DO 311 I=1,M
DO 311 K=1,L
311 SUM99=SUM99+CF4(I,NO,K)*CF40
SUM88=0.0
DO 312 I=1,M
DO 312 K=1,L
312 SUM88=SUM88+1.*CF40
PERC=((SUM88-SUM99)*100.)/SUM88
WRITE(5,*) 'PERCENTAGE DISS OF CF4 =',PERC

```

```

C      IF(IFLAG.GT.3) GO TO 1234
      GO TO 211
C 1234 IF (ISKP.EQ.1) GO TO 2234
      WRITE(5,*) 'ENTER THE VALUE OF I AT WHICH F CONC. IS
      PLOTTED'
      READ(5,*) I
      DO 4321 K=1,L
      DO 4321 J=NO,N
4321  WRITE(9,*) F(I,J,K)
      WRITE(5,*) 'IF YOU ENTER ZERO HERE THEN THE PROGRAM
PROCEEDS'
      READ(5,*) IDERG
      IF (IDERG.NE.0) GO TO 1234

C      SPECTROSCOPIC DATA MATCH

234  SUE=0.0
      IPUT=0
      DO 450 I=1,M
      DO 450 K=1,L
      DO 450 J=NO,N
      IPUT=IPUT+1
450  SUE=SUE+F(I,J,K)
      FDAR=((SUE/IPUT)*CF40)/AR0
      WRITE(5,*) 'THE RATIO OF F TO AR CONC.',FDAR
C      WRITE(8,*) 'THE RATIO OF F TO AR CONC.',FDAR
C

      M2=FLOAT(M)/2.
      L2=L*2
      SUMIA=0.0
      SUMIF=0.0
      DO 900 I=M2,M
      DO 900 K=1,L2
      DO 900 J=NO,NL
      TH=FLOAT(K-1)*DTH
      Z1=FLOAT(I-M2)*DZ*H
      RA1=FLOAT(J-1)*DR*R
901  IF(K.LT.L) KD=K
      ELSE KD=L

FI1=2.*((ACON*EL(J)*F(I,J,KD)*CF40*FRAD**2)/(Z1**2+RA1**2
+-2.*R*RA1*COS(TH)+R**2)**.5)
      SUMIF=SUMIF+FI1

ARI=2.*((ACON*EL(J)*AR0*ARRAD**2)/(Z1**2+RA1**2-2.*R*RA1*COS
(TH)
**+R**2)**.5)
      SUMIA=SUMIA+ARI
900  CONTINUE
      RATI=SUMIF/SUMIA
      WRITE(5,*) 'THE RATIO OF F TO AR INTENSITY',RATI

```

```

C      WRITE(8,*) 'THE RATIO OF F TO AR INTENSITY',RATI
C
      FDAR1=RATI*ACON1
      WRITE(5,*) 'THE RATIO OF F TO AR CONC IS',FDAR1
C
      DO 31 J=NO,N
31     WRITE(7,*)J,CF4(10,J,2),F(10,J,2)
      IF (ISKP.EQ.1) GO TO 8002

C      ETCH RATE CALCULATED IN THIS SECTION

      I=1
      WRITE(5,*) 'THIS SECTION IS FOR ETCH RATE'
      WRITE(8,*) 'THIS SECTION IS FOR ETCH RATE'
      DO 560 K=1,9
      DO 560 J=NO,N
      ET(I,J,K)=((AL1*CE*F(I,J,K)*CF40+AL2*F(I,J,K)*CF40)
+/(CE+AL3*F(I,J,K)*CF40))
      WRITE(5,*) 'I',I,'J',J,'K',K,'ETCH RATE',ET(I,J,K)
      WRITE(8,*)K,J,ET(I,J,K),F(I,J,K)
560    CONTINUE
C
      DON=1
      SUM66=0.0
      DO 673 J=12,26
      SUM66=SUM66+ET(1,J,1)
673    DON=DON+1
      DO 674 K=1,6
      SUM66=SUM66+ET(1,19,K)
674    DON=DON+1
      AVGET=SUM66/DON
      SUM77=0.0
      DO 675 J=12,16
675    SUM77=SUM77+(ET(1,J,1)-AVGET)**2
      DO 676 K=1,6
676    SUM77=SUM77+(ET(1,J,1)-AVGET)**2
      STDE=(SUM77/(DON-1))**.5
      WRITE(8,*) 'THE STANDARD DEVIATION IS=',STDE
      WRITE(5,*) 'THE STANDARD DEVIATION IS=',STDE

C      8001 WRITE(5,*) 'THE VALUE OF PLANE I AT WHICH CONTOUR IS
      DESIRED='
      READ(5,*)KPI

      IF (KPI.EQ.0) GO TO 8002
      KP=3
300    IF(KP.EQ.1) GO TO 301
      IF(KP.EQ.2) GO TO 302
      IF(KP.EQ.3) GO TO 303
301    CMAX=1.
      DCONT=(ACF4(N)-ACF4(NO))/15.
      CMIN=ACF4(NO)

```

```

DO 304 J=NO,N
DO 304 K=1,L
304 C(KPI,J,K)=CF4(KPI,J,K)
CALL CONTOUR(CMAX,DCONT,C,KPI,DR,DTH,L,N,KP,ITIM,DX,DY
+,CONTR,NO,CMIN)
KP=KP+1
ITIM1=ITIM
GO TO 300
302 CMAX=CF3(M,NO,L)
DCONT=(CF3(M,NO,L)-CF3(1,N,1))/15.
CMIN=CF3(1,N-1,1)
DO 305 J=NO,N
DO 305 K=1,L
305 C(KPI,J,K)=CF3(KPI,J,K)
CALL
CONTOUR(CMAX,DCONT,C,KPI,DR,DTH,L,N,KP,ITIM,DX,DY,CONTR
*,NO,CMIN)
KP=KP+1
ITIM2=ITIM
GO TO 300
303 CMAX=F(M,NO,1)
DCONT=(F(1,NO,1)-F(1,N,1))/15.
CMIN=F(1,N-1,1)
DO 306 J=NO,N
DO 306 K=1,L
306 C(KPI,J,K)=F(KPI,J,K)
CALL
CONTOUR(CMAX,DCONT,C,KPI,DR,DTH,L,N,KP,ITIM,DX,DY,CONTR
*,NO,CMIN)
ITIM3=ITIM

C PRINT OUT THE RESULTS FOR CONTOUR PLOTS

WRITE(7,*) 'CONTOUR PLOTTED AT I PLANE OF',KPI
DO 308 I=1,KP
IF (I.EQ.1) ITI=ITIM1
IF (I.EQ.2) ITI=ITIM2
IF (I.EQ.3) ITI=ITIM3
DO 308 J=1,ITI
WRITE(5,*) I,J,DX(I,J),DY(I,J)
308 WRITE(7,*) 'I',I,'J',J,DX(I,J),DY(I,J)
GO TO 8001

C
8002 STOP
END

C
SUBROUTINE
CONTOUR(CMAX,DCONT,C,KPI,DR,DTH,L,N,KP,ITIM,DX,DY,
*CONTR,NO,CMIN)

C
DOUBLE PRECISION
CONTR(5,100),CMAX,DCONT,C(70,70,70),DRR,DTH,TH

```

```

*,DYBDX,DX(5,1000),DY(5,1000),CMIN
C
  IFLAG=-1
  III=1
  I=1
10  IFLAG=IFLAG*(-1)
    CONTR(KP,III)=CMAX-(FLOAT(III-1)*DCONT)
    IF (CONTR(KP,III).LE.CMIN) GO TO 80
C
  WRITE(8,*)'CONTOUR PLOTS'
  WRITE(5,*)'SPECIES NO.',KP,'CONTR',CONTR(KP,III)
  WRITE(8,*)'SPECIES NO.',KP,'CONTR',CONTR(KP,III)
  WRITE(8,*)'PLOT AT I LEVEL OF=',KPI
C
  NOP=NO
  IF(IFLAG.LT.0) GO TO 20
  K=1
  GO TO 190
20  K=L
190 ISLAB=1
  NOP=NO
30  DO 40 J=NOP,N
    MKP=J
    IF (KP.NE.1) GO TO 70
    IF (C(KPI,J,K).GE.CONTR(KP,III)) GO TO 50
    GO TO 40
70  IF (KP.EQ.3) GO TO 90
    IF (C(KPI,J,K).LE.CONTR(KP,III)) GO TO 100
    GO TO 40
90  IF (ISLAB.EQ.1) GO TO 150
    IF (ISLAB.EQ.2) GO TO 160
    IF (ISLAB.EQ.3) GO TO 170
    IF (ISLAB.EQ.4) GO TO 130
150 IF (C(KPI,J,K).LE.CONTR(KP,III)) GO TO 100
    GO TO 40
160 IF (C(KPI,J,K).GE.CONTR(KP,III)) GO TO 100
    GO TO 40
170 IF (C(KPI,J,K).LE.CONTR(KP,III)) GO TO 100
40  CONTINUE
    IF (KP.EQ.3) GO TO 130
    GO TO 80
50  IF (MKP.EQ.NO) GO TO 80
    GO TO 110
100 IF (MKP.EQ.N-1) GO TO 80
110 DRR=FLOAT(MKP-1)*DR+(CONTR(KP,III)-C(KPI,MKP-1,K))
    **((FLOAT(MKP)-FLOAT(MKP-1))*DR)/
    *(C(KPI,MKP,K)-C(KPI,MKP-1,K))
    TH=DTH*FLOAT(K-1)
    DYBDX=TAN(TH)
    DX(KP,I)=ABS(DSQRT(DRR**2/(DYBDX**2+1)))
    DY(KP,I)=ABS((DYBDX*DX(KP,I)))
C

```

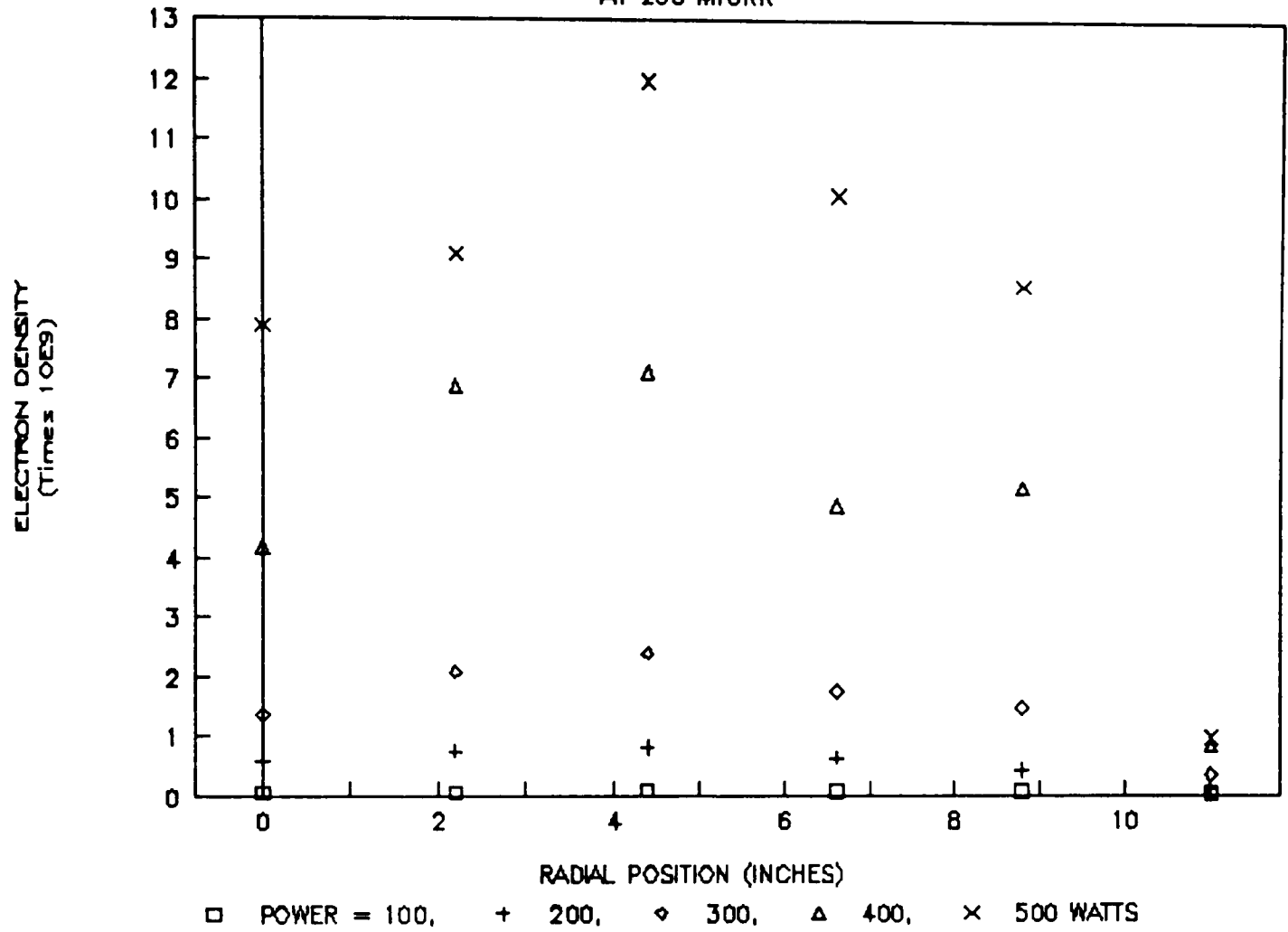
```

      I=I+1
C
      IF (KP.NE.3) GO TO 130
      IF (K.LE.8) GO TO 140
      GO TO 130
140   NOP=MKP+1
      ISLAB=ISLAB+1
      GO TO 30
130   IF (K.EQ.L) DX(KP,I)=0.0
      K=K+IFLAG
      IF(K.GT.L) GO TO 60
      IF(K.LT.1) GO TO 60
      ITIM=I
      GO TO 190
60    III=III+1
      GO TO 10
C
80    RETURN
      END

```

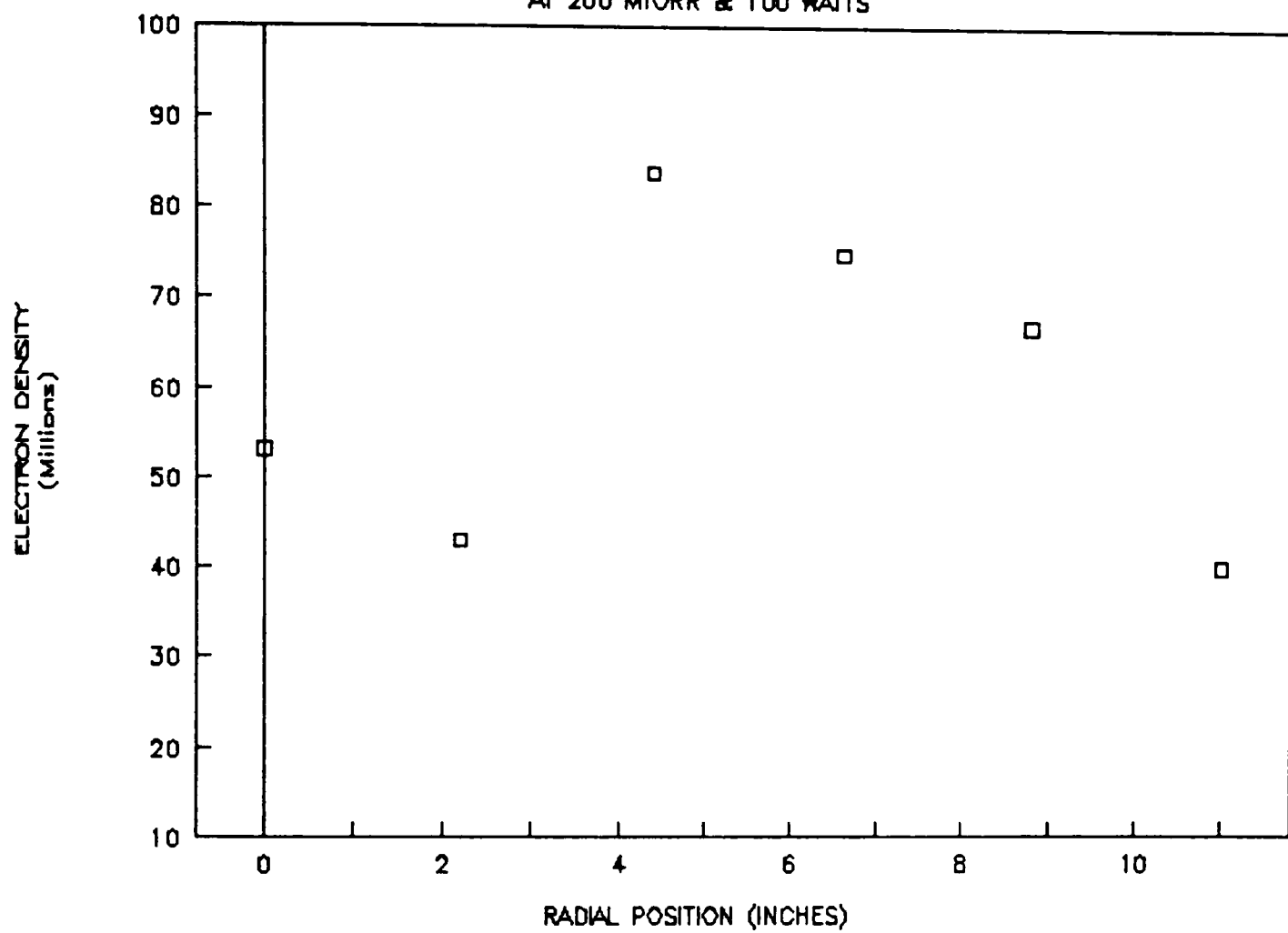
APPENDIX G
ELECTRON DENSITY AND TEMPERATURE
DISTRIBUTION DATA

ELECTRON DENSITY VS. RADIAL POSITION
AT 200 MTORR



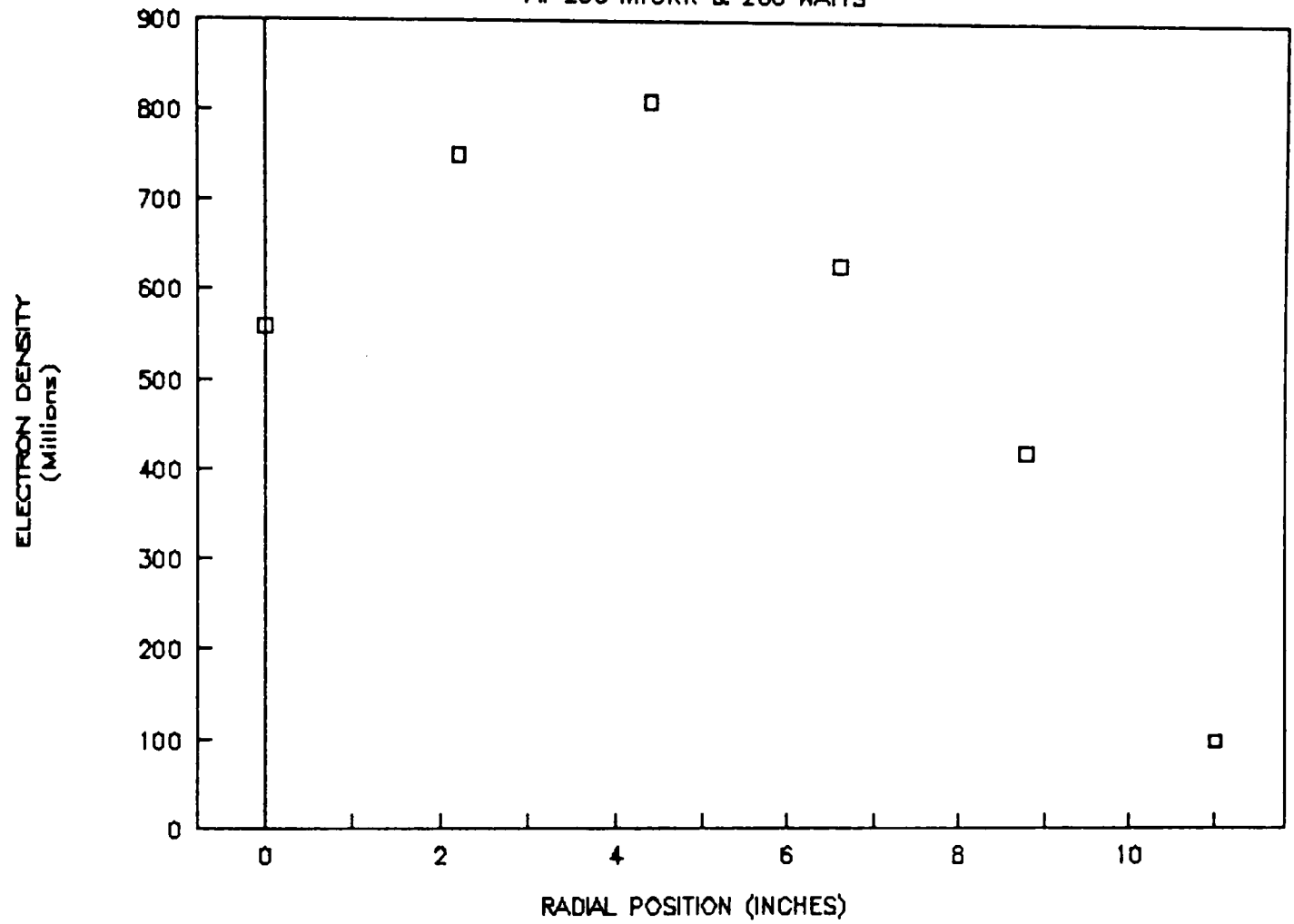
ELECTRON DENSITY VS. RADIAL POSITION

AT 200 MTORR & 100 WATTS



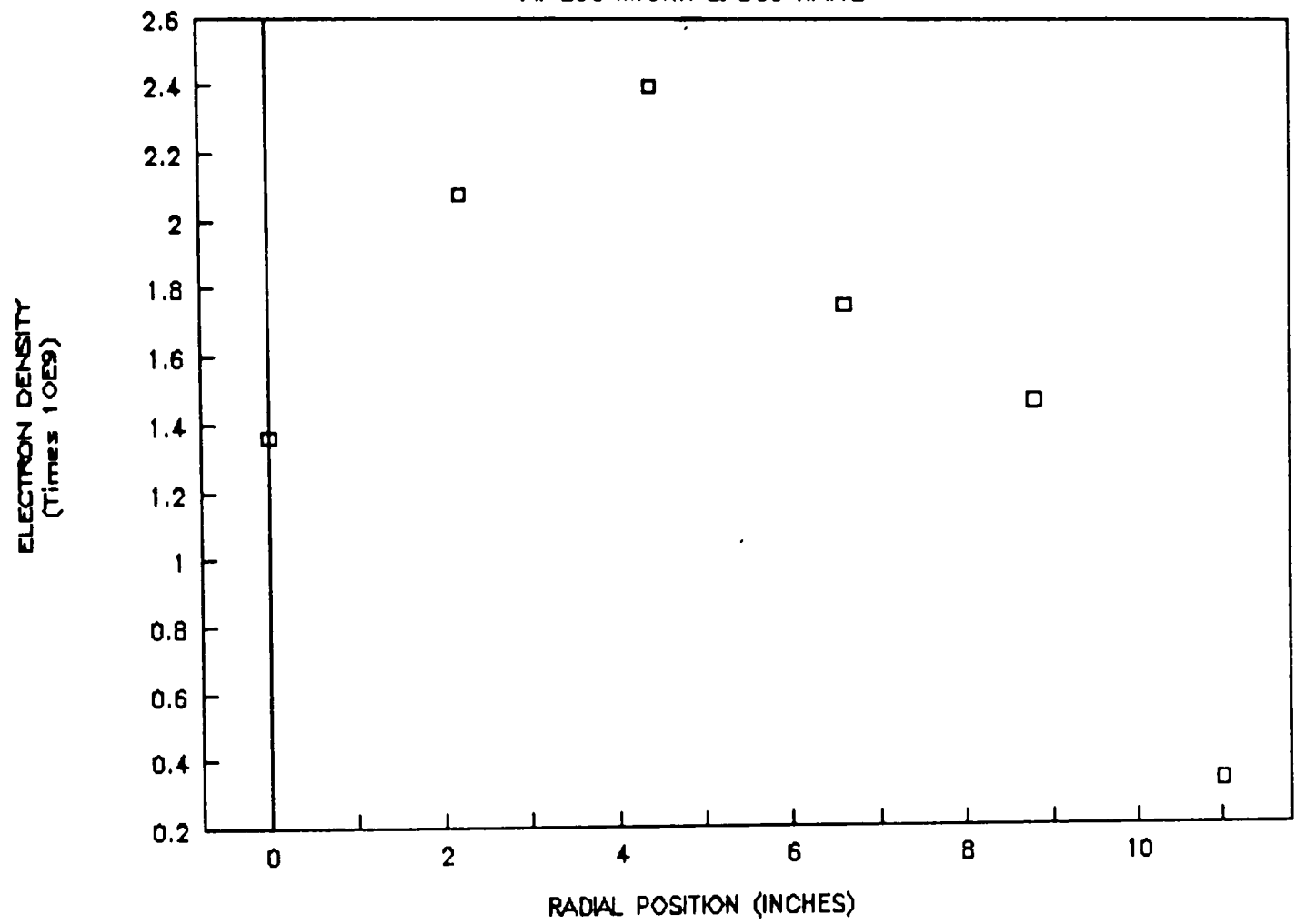
ELECTRON DENSITY VS. RADIAL POSITION

AT 200 MTORR & 200 WATTS



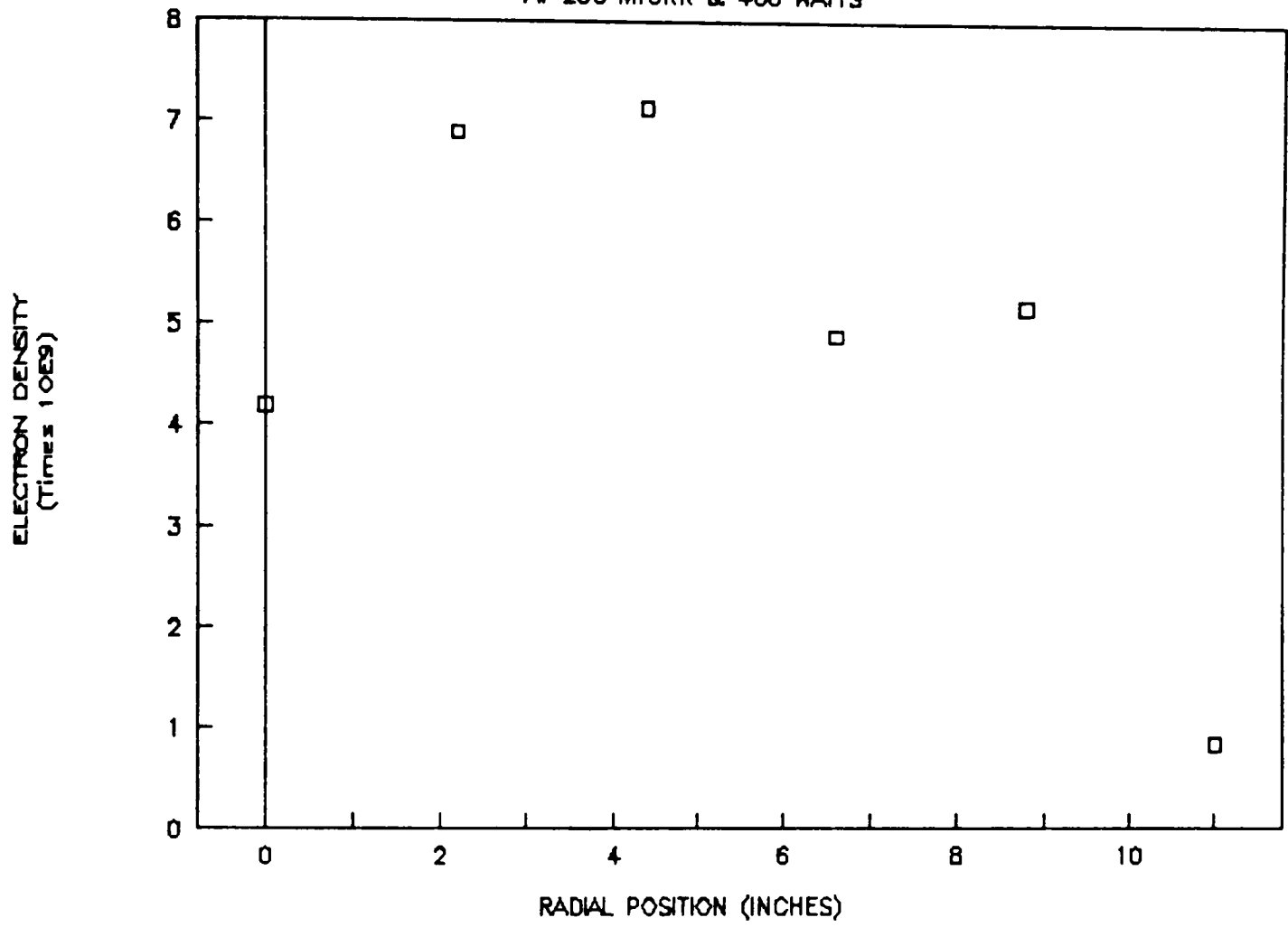
ELECTRON DENSITY VS. RADIAL POSITION

AT 200 MTORR & 300 WATTS



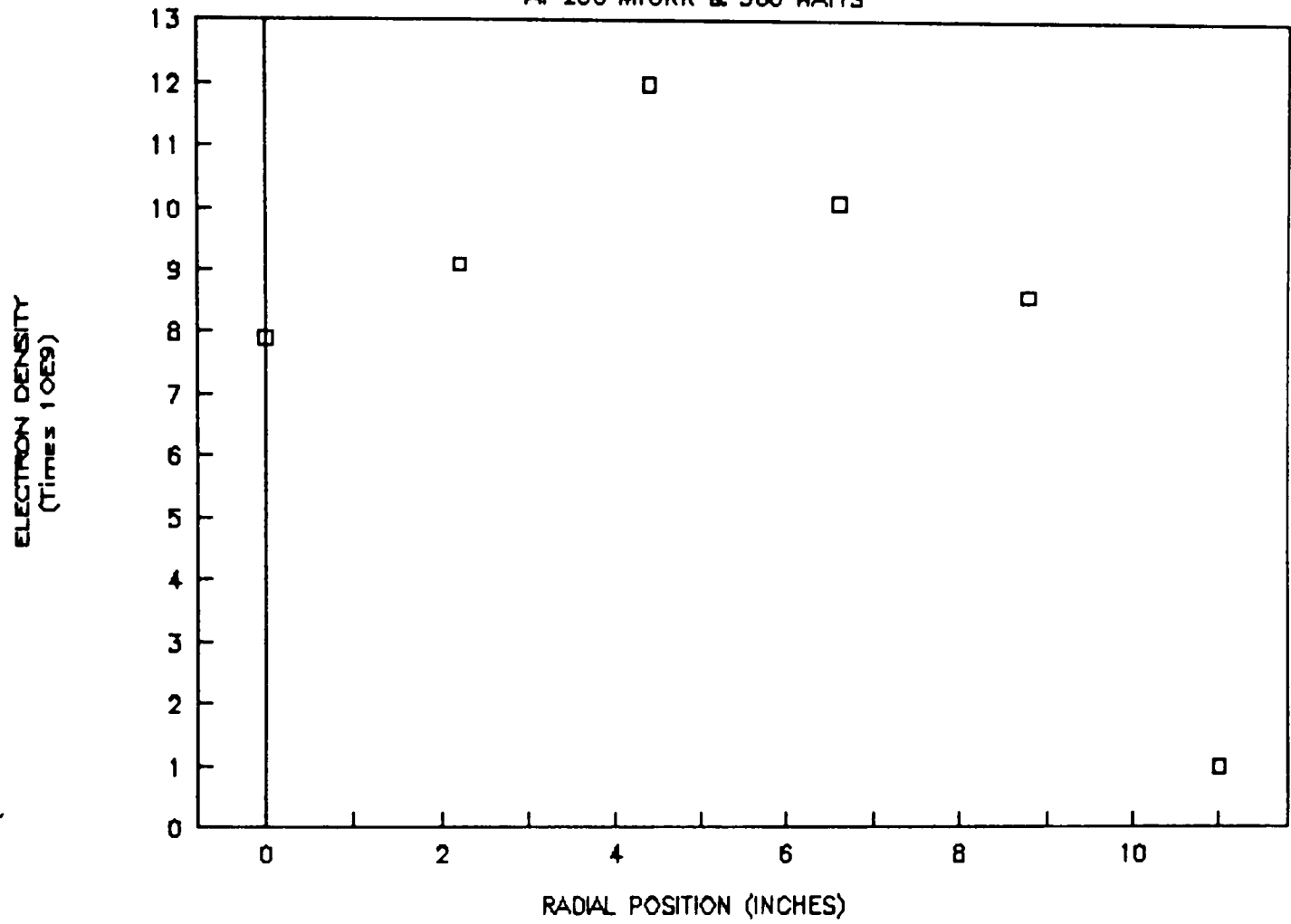
ELECTRON DENSITY VS. RADIAL POSITION

AT 200 MTORR & 400 WATTS

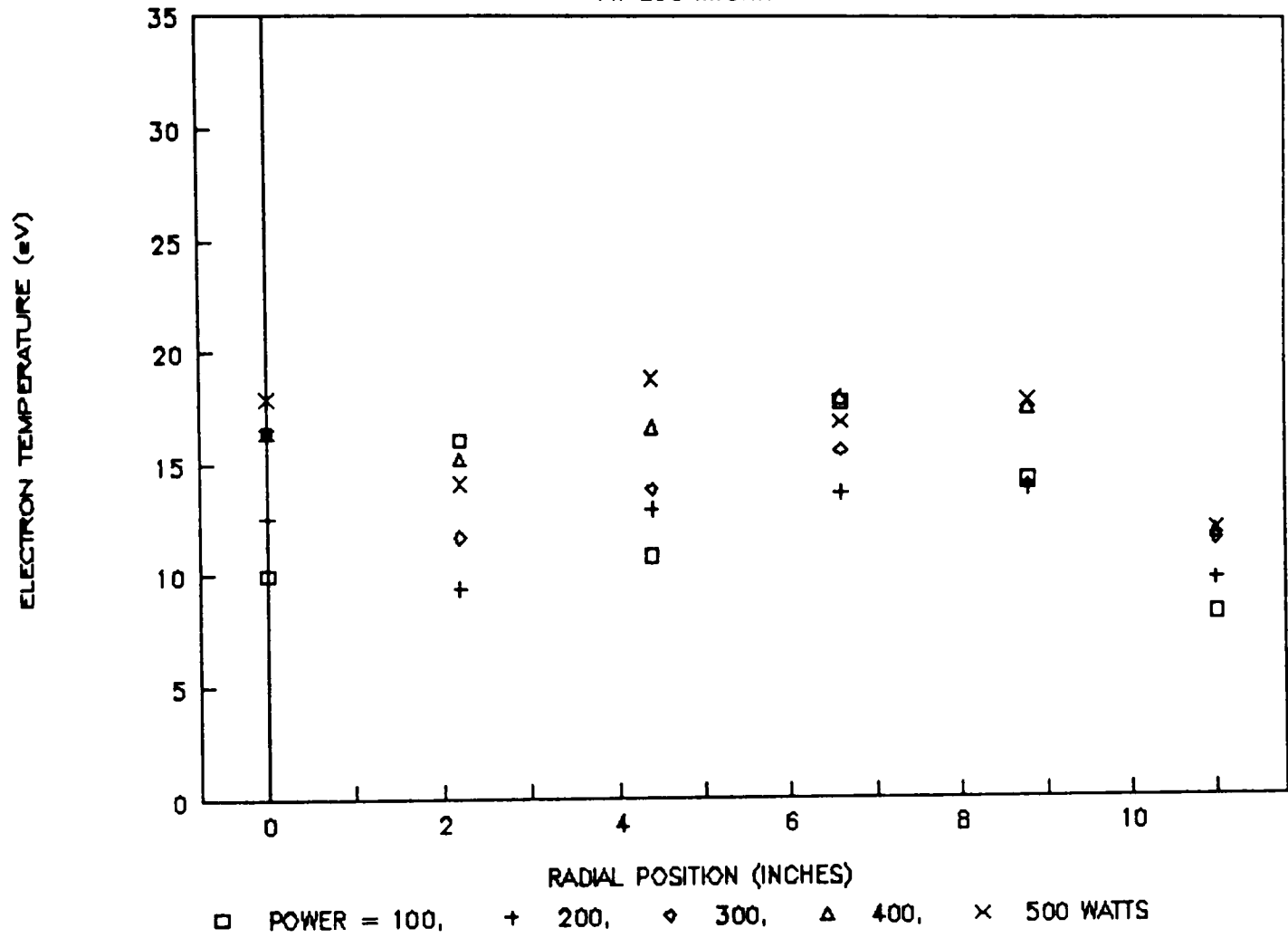


ELECTRON DENSITY VS. RADIAL POSITION

AT 200 MTORR & 500 WATTS

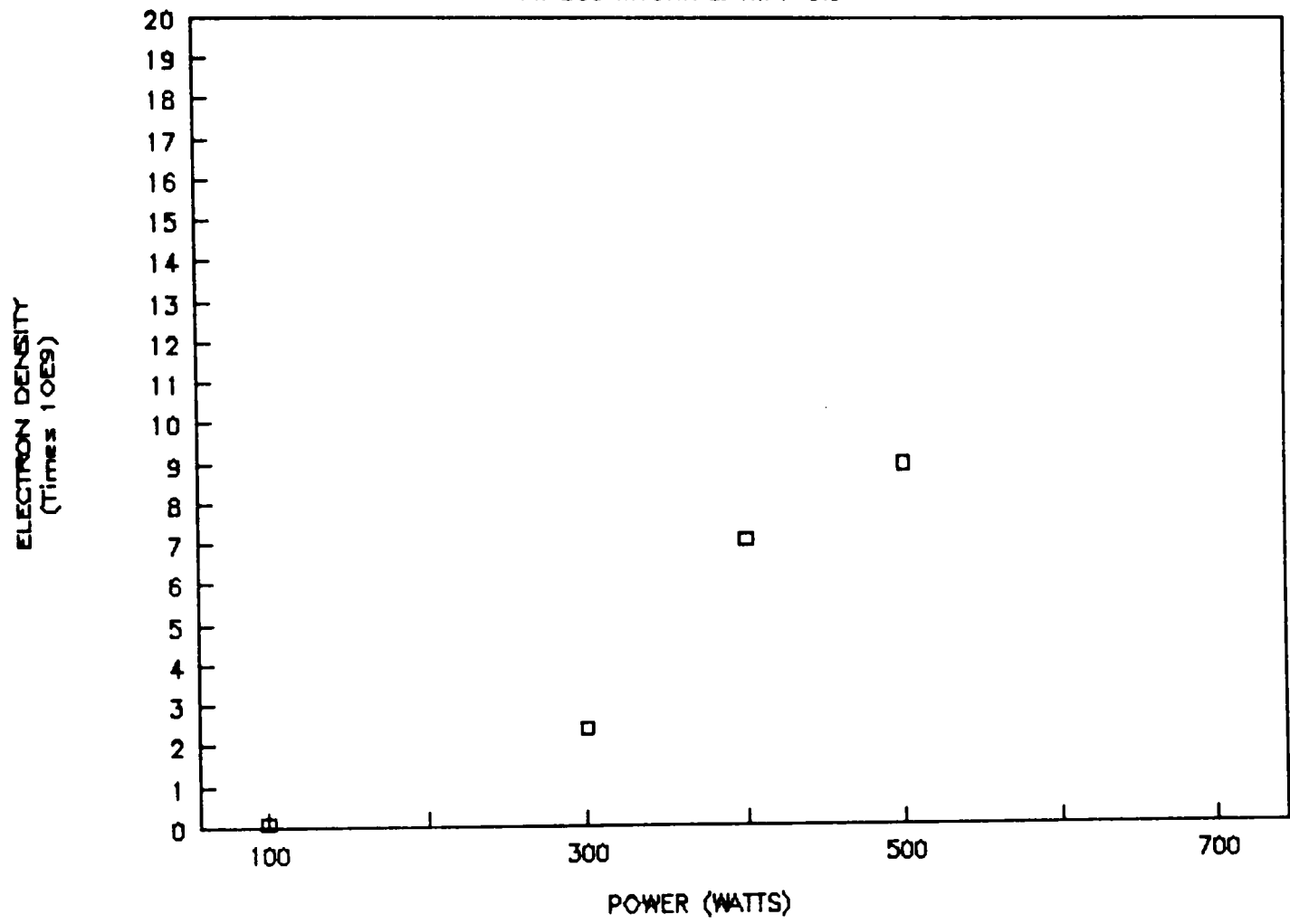


ELECTRON TEMP. VS. RADIAL POSITION AT 200 MTORR



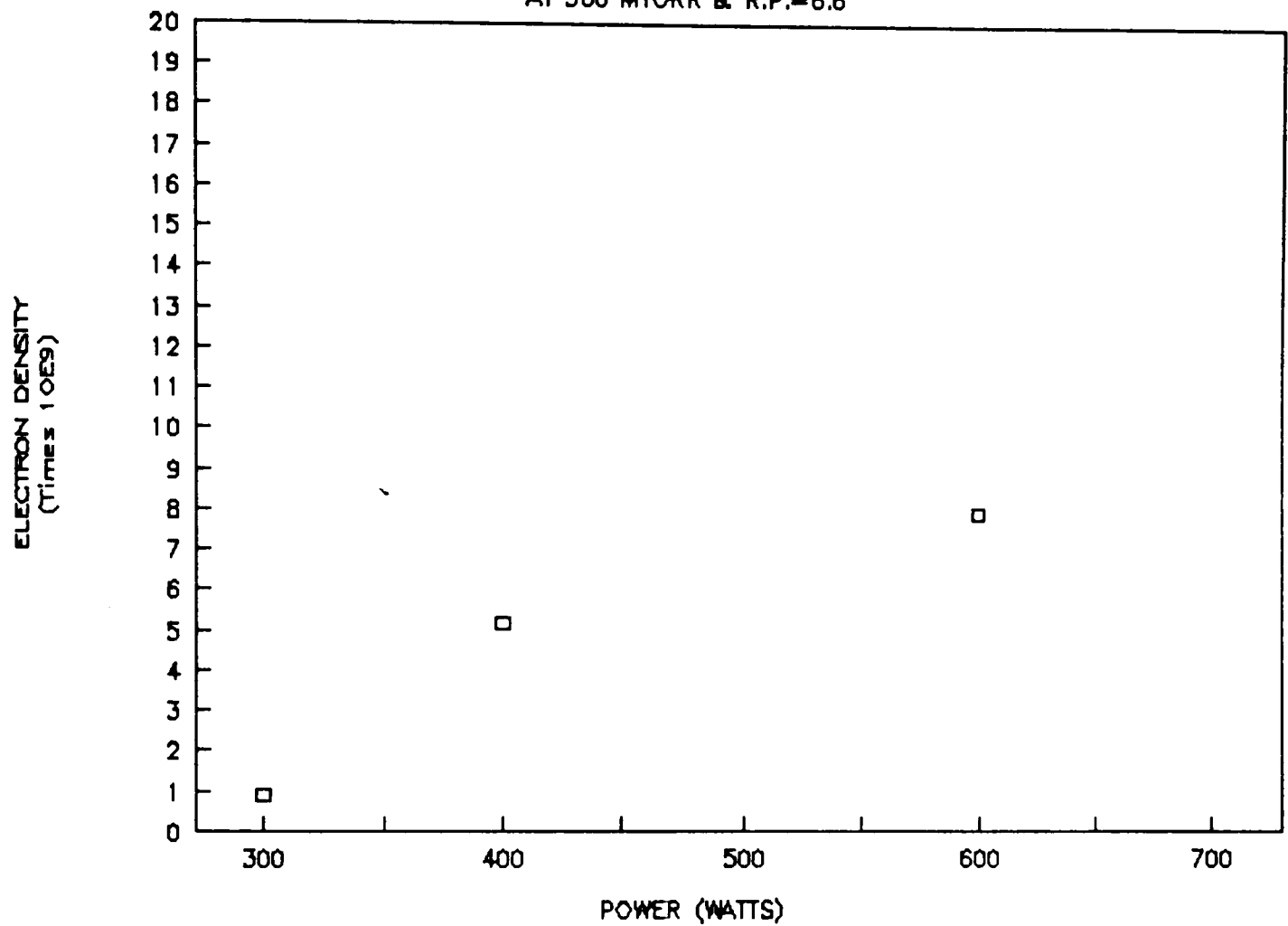
ELECTRON DENSITY VS. POWER

AT 200 MTORR & R.P.=6.6"



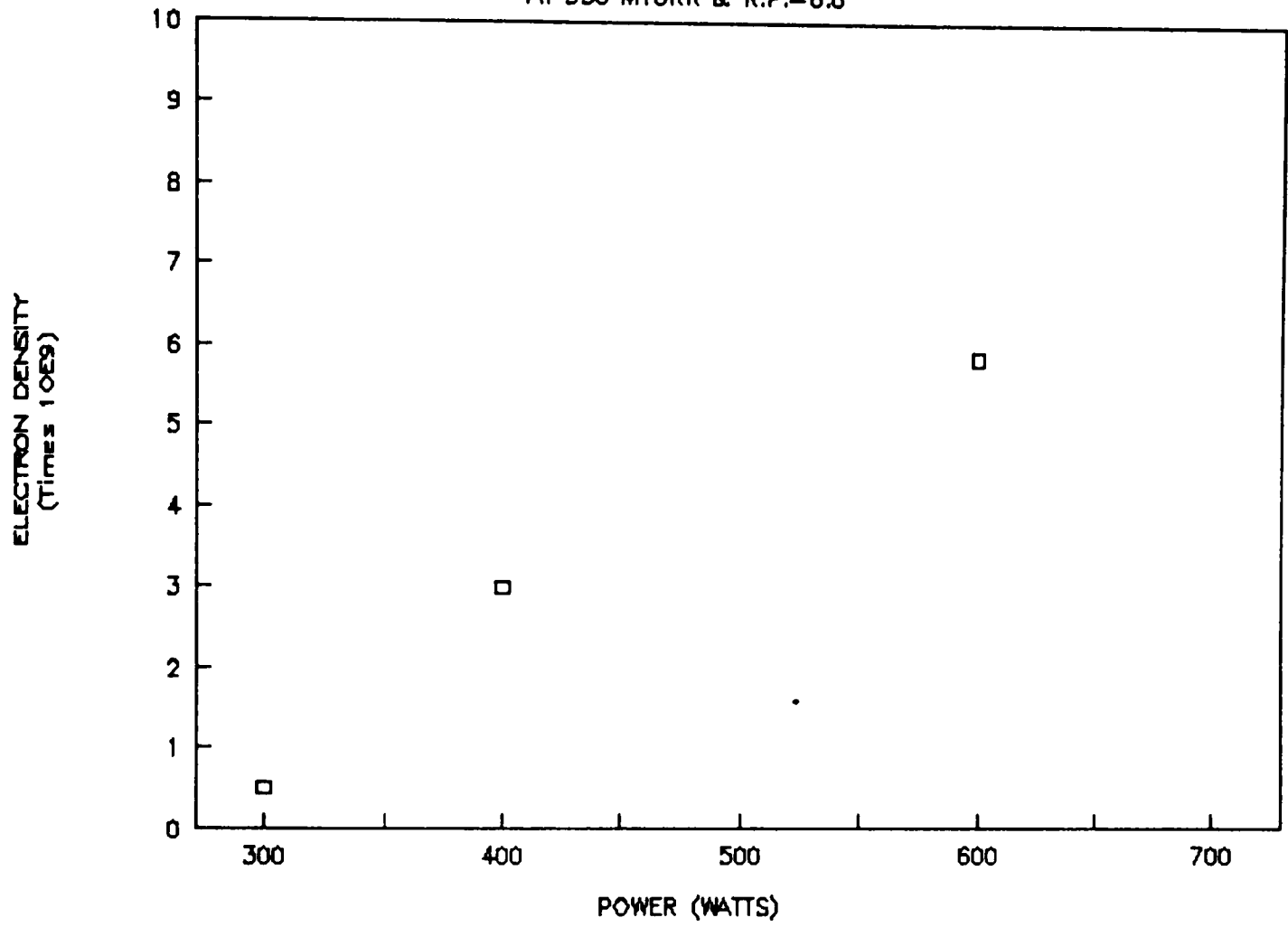
ELECTRON DENSITY VS. POWER

AT 300 MTORR & R.P.=6.6"



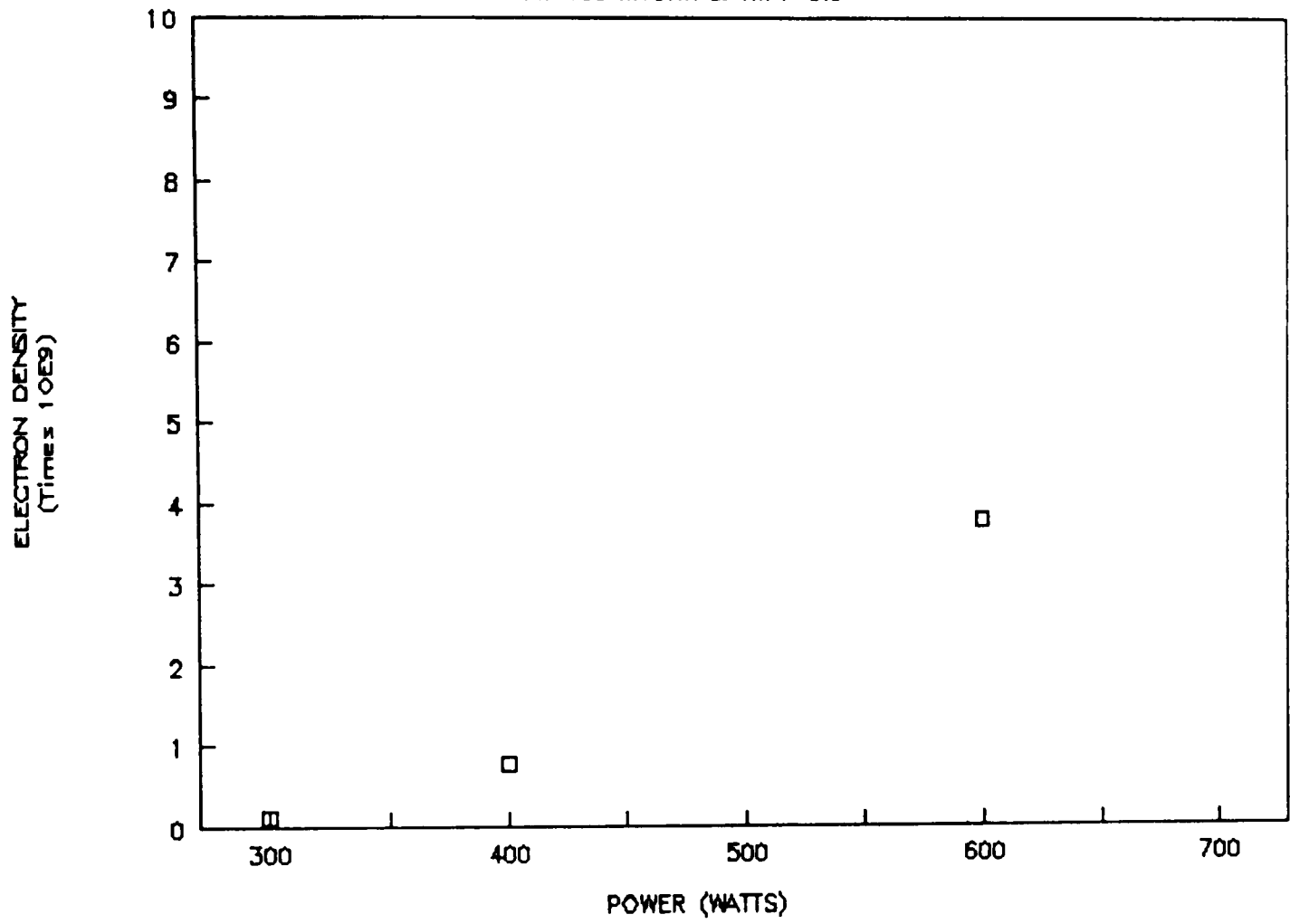
ELECTRON DENSITY VS. POWER

AT 350 MTORR & R.P.=6.6"



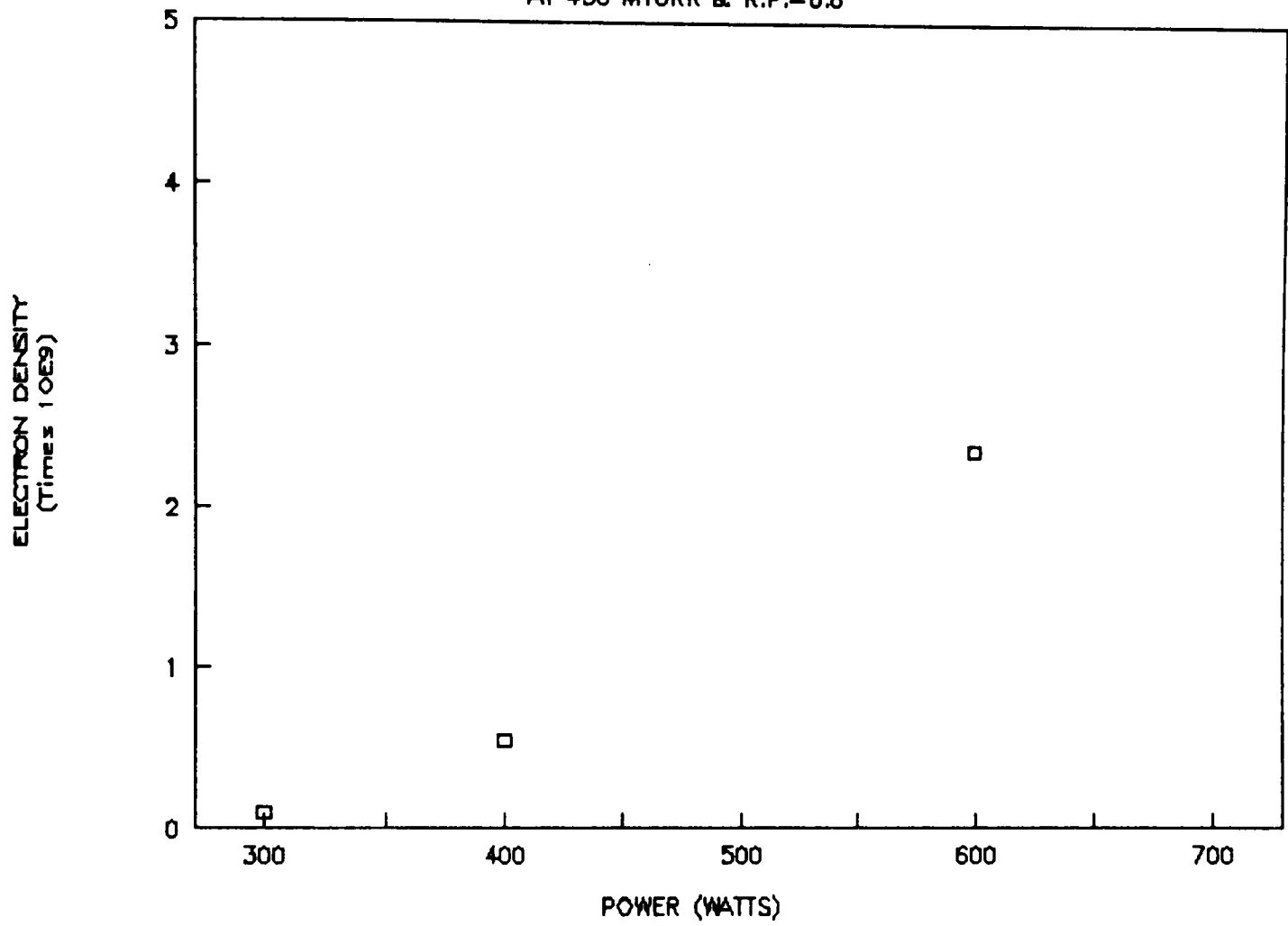
ELECTRON DENSITY VS. POWER

AT 400 MTORR & R.P.=6.6"



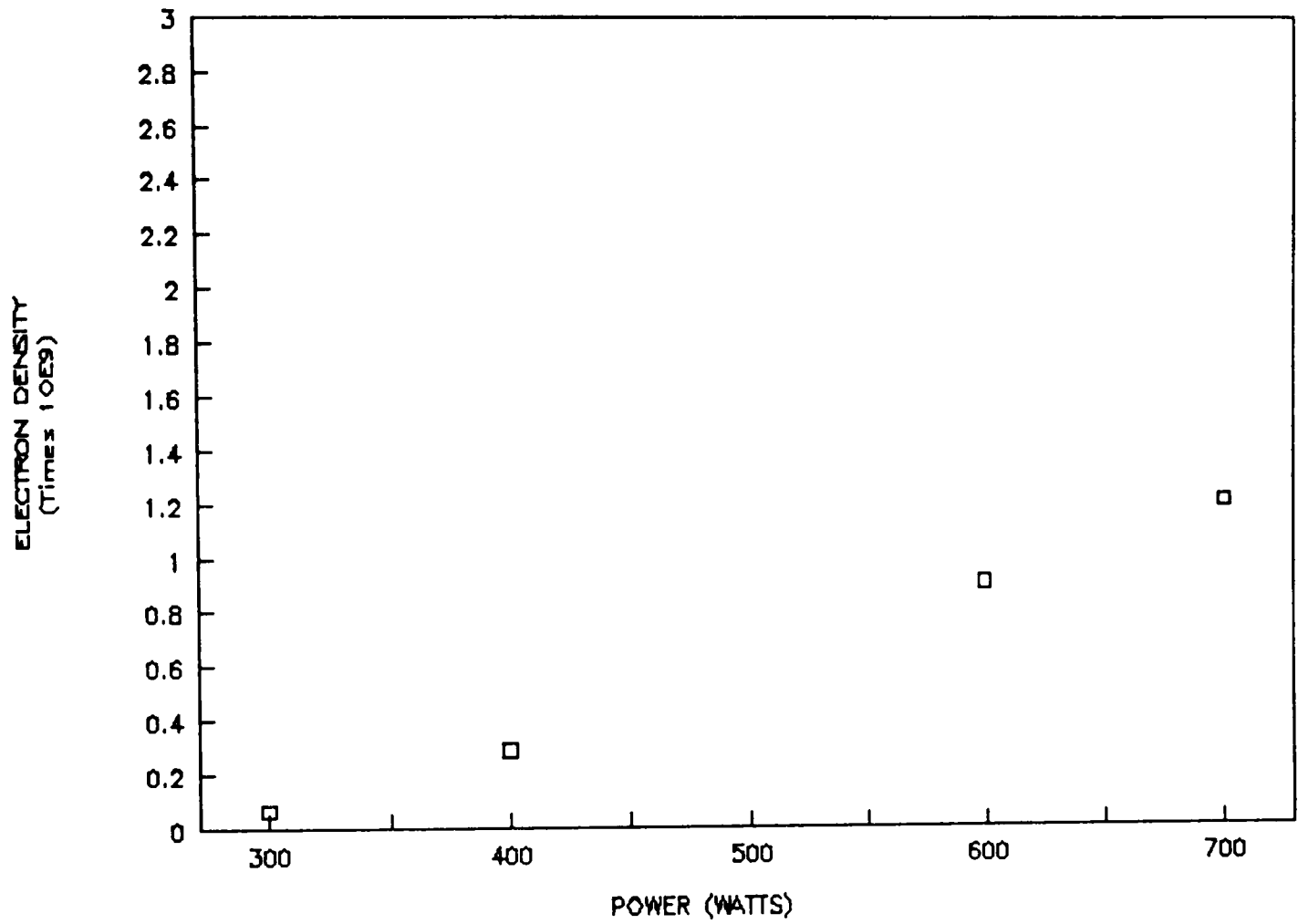
ELECTRON DENSITY VS. POWER

AT 450 MTORR & R.P.=6.6"



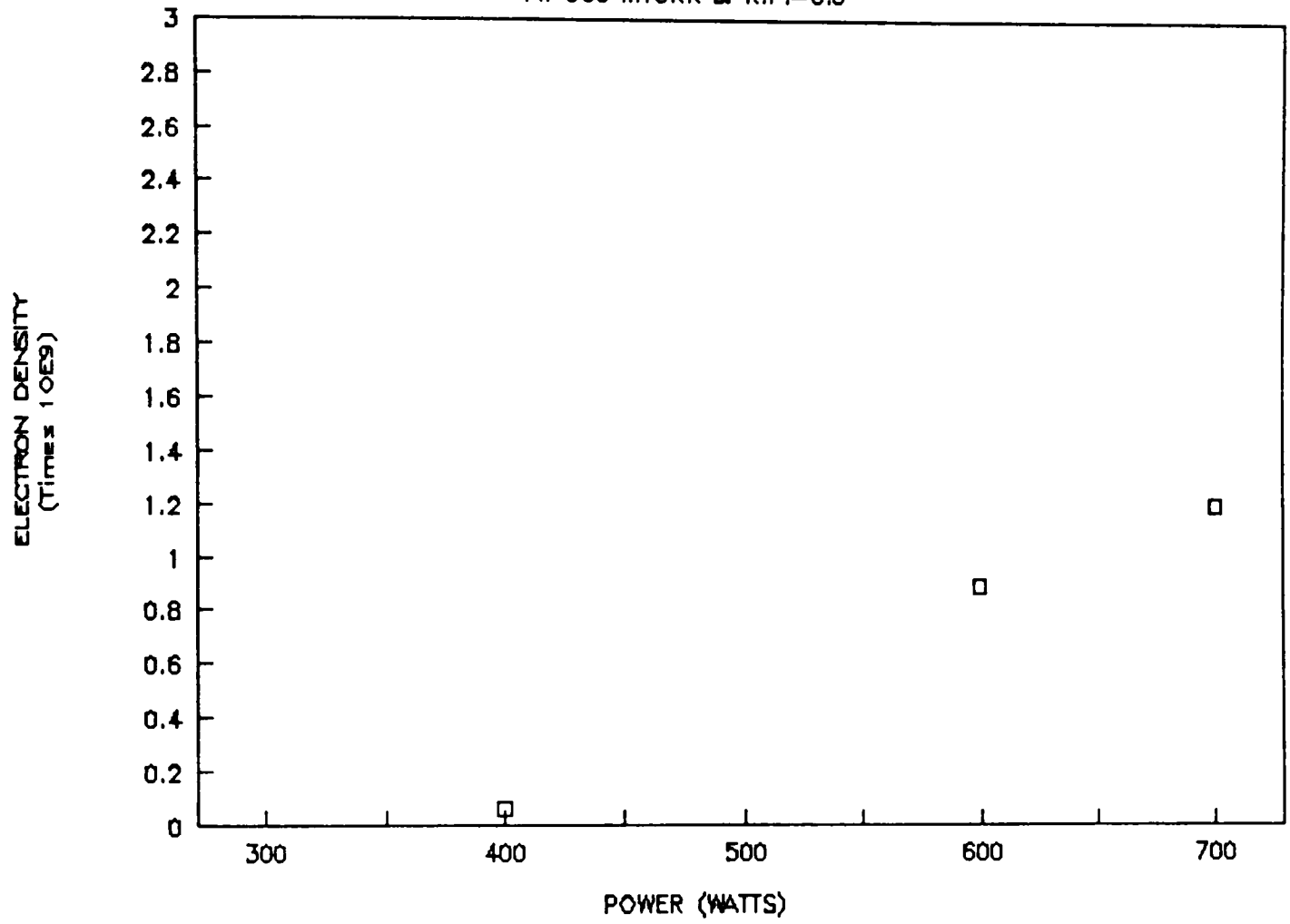
ELECTRON DENSITY VS. POWER

AT 500 MTORR & R.P.=6.6"



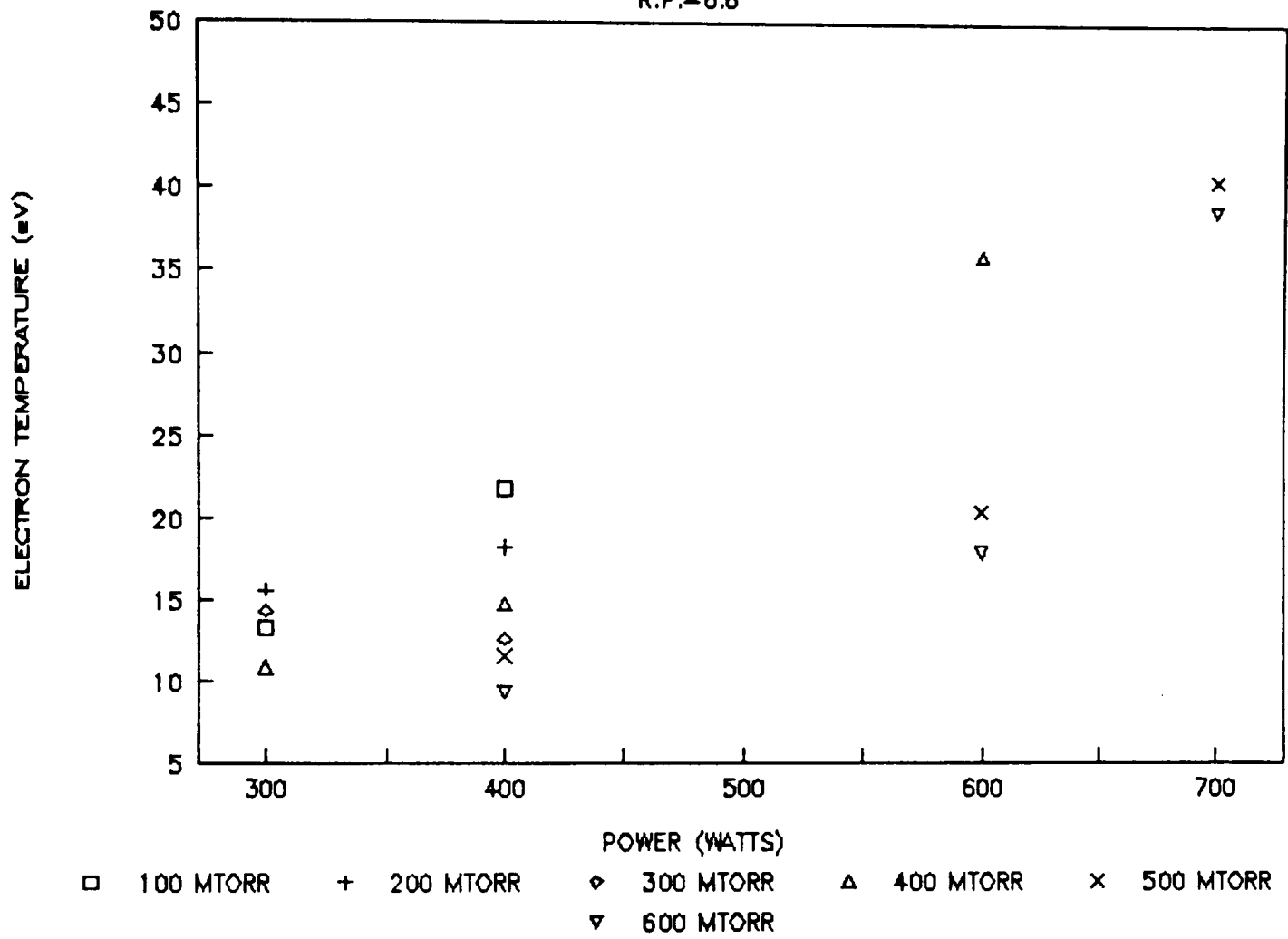
ELECTRON DENSITY VS. POWER

AT 600 MTORR & R.P.=6.6"



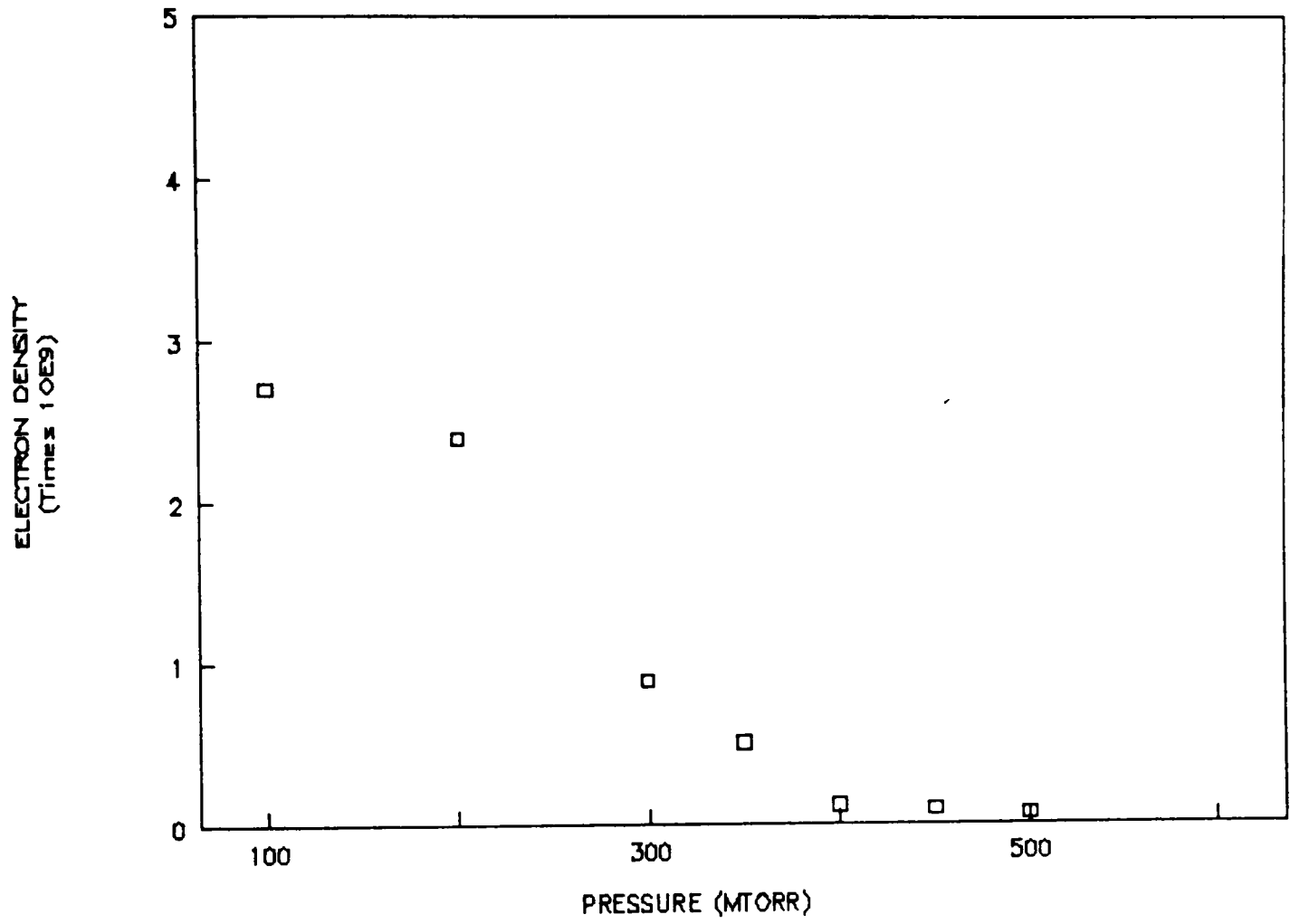
ELECTRON TEMP. VS. POWER

R.P.=6.6"



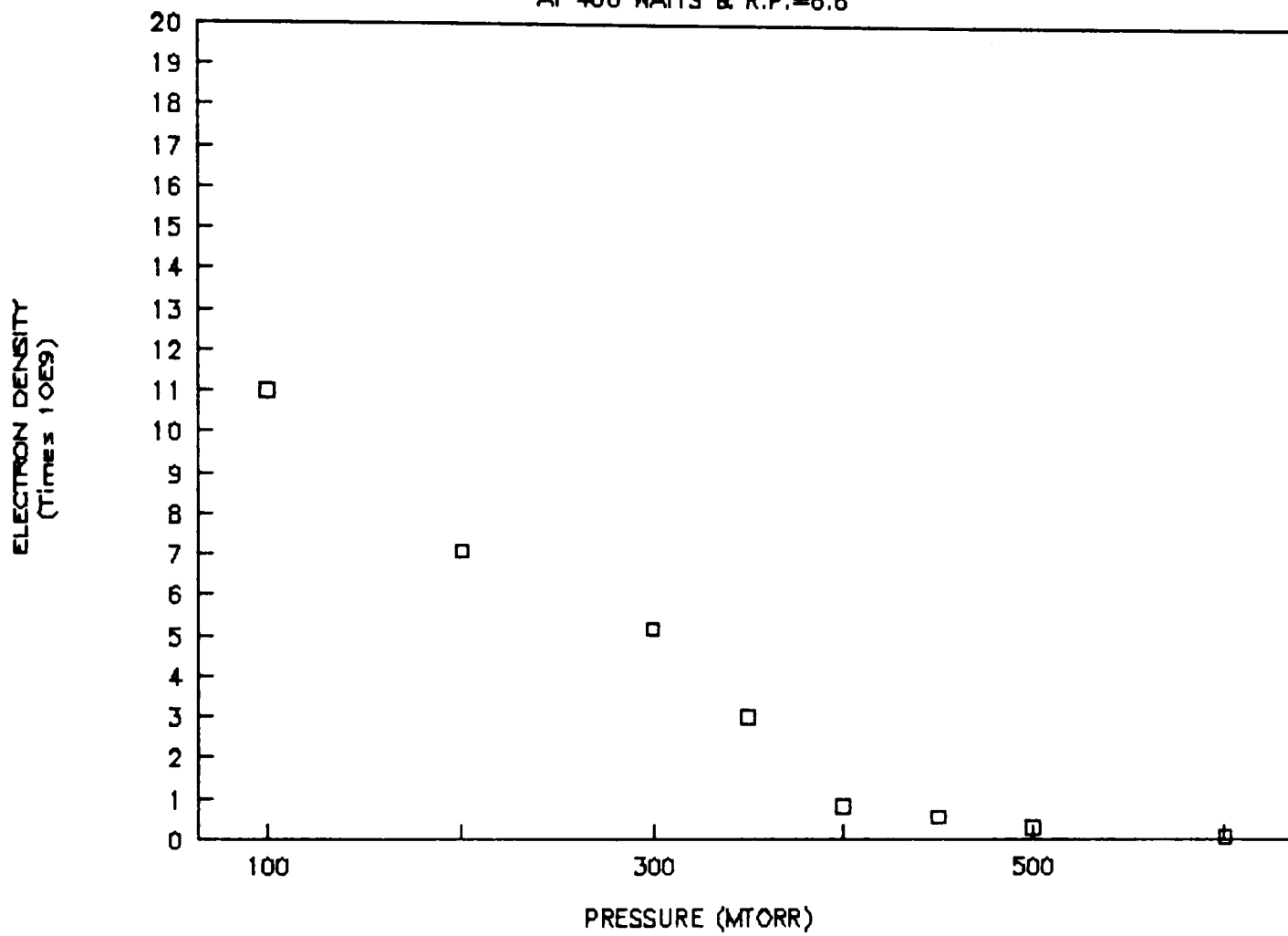
ELECTRON DENSITY VS. PRESSURE

AT 300 WATTS & R.P.=6.6"



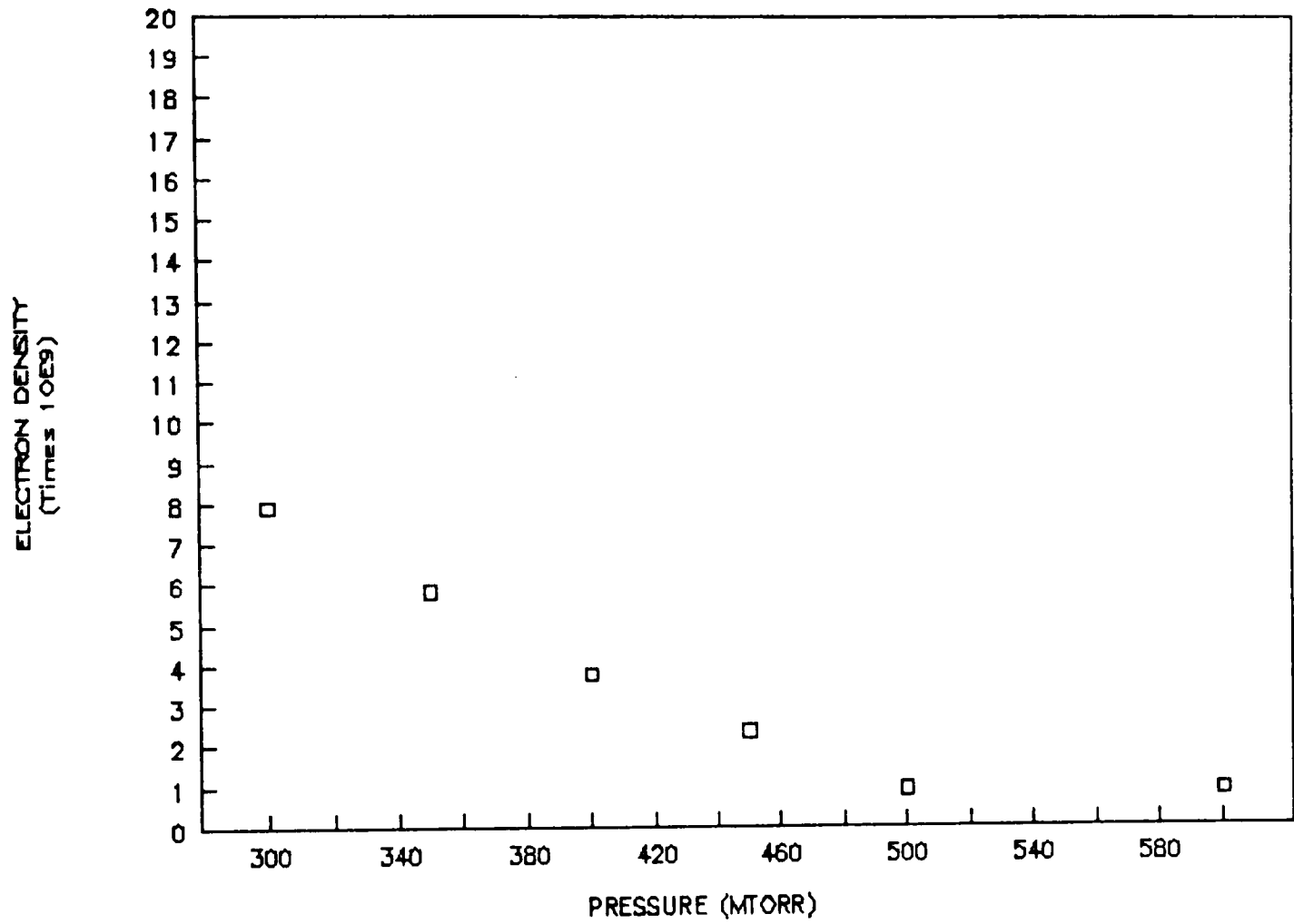
ELECTRON DENSITY VS. PRESSURE

AT 400 WATTS & R.P.=6.6"



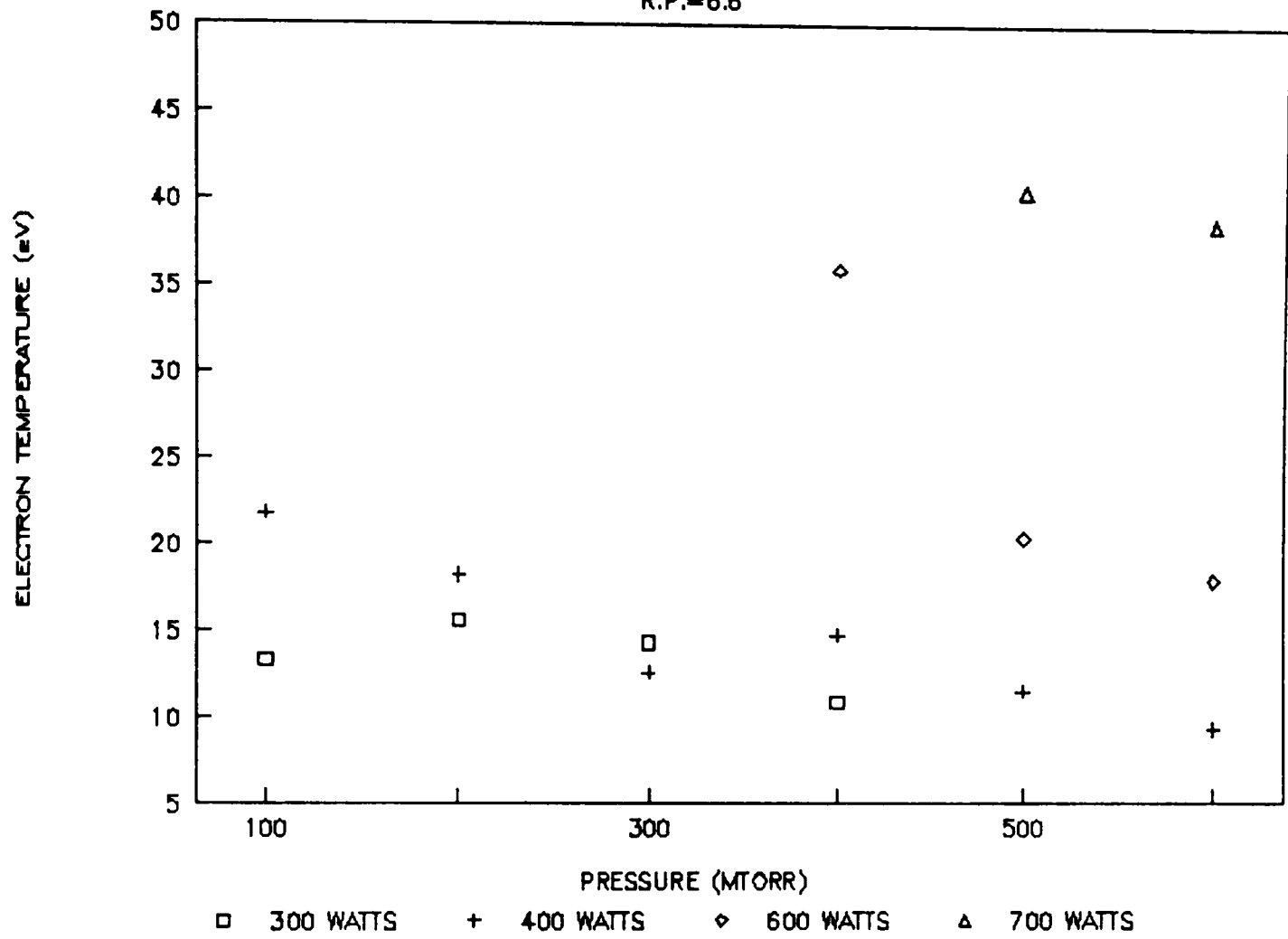
ELECTRON DENSITY VS. PRESSURE

AT 600 WATTS & R.P.=6.6"



ELECTRON TEMP. VS. PRESSURE

R.P.=6.6"



APPENDIX H

EMPIRICAL MODEL FOR ELECTRON

DENSITY DISTRIBUTION

The empirical model for electron density distribution was developed based on the experimental data presented in section one of Chapter 7. The model developed predicts the radial distribution of electron density at any power and pressure given the electron density at that power, pressure and 6.6" from the center of the reactor. This radial position selected, represents the region of maximum electron density in the reactor, for any set of operating conditions.

A fourth order polynomial was found to fit the experimental data fairly well, and the form of empirical model is as follows:

$$[EL] |_{r} = [EL] |_{r=6.6} // [A+B r+C r^2+D r^3] . \quad (G.1)$$

Here electron density is represented by [EL] whereas the radial position in the reactor is represented by r. A, B, C and D are the curve fit constants. The data presented in Appendix G for electron density at various powers and radial position at 200 mTorr pressure was used to evaluate the model constants. The values of these constants obtained at different powers using SAS are presented in Table 6.

The generalized model was obtained by taking the average of each constant value at different power. The

Table 6: Model Constants at 200 mTorr Pressure and at Various Powers.

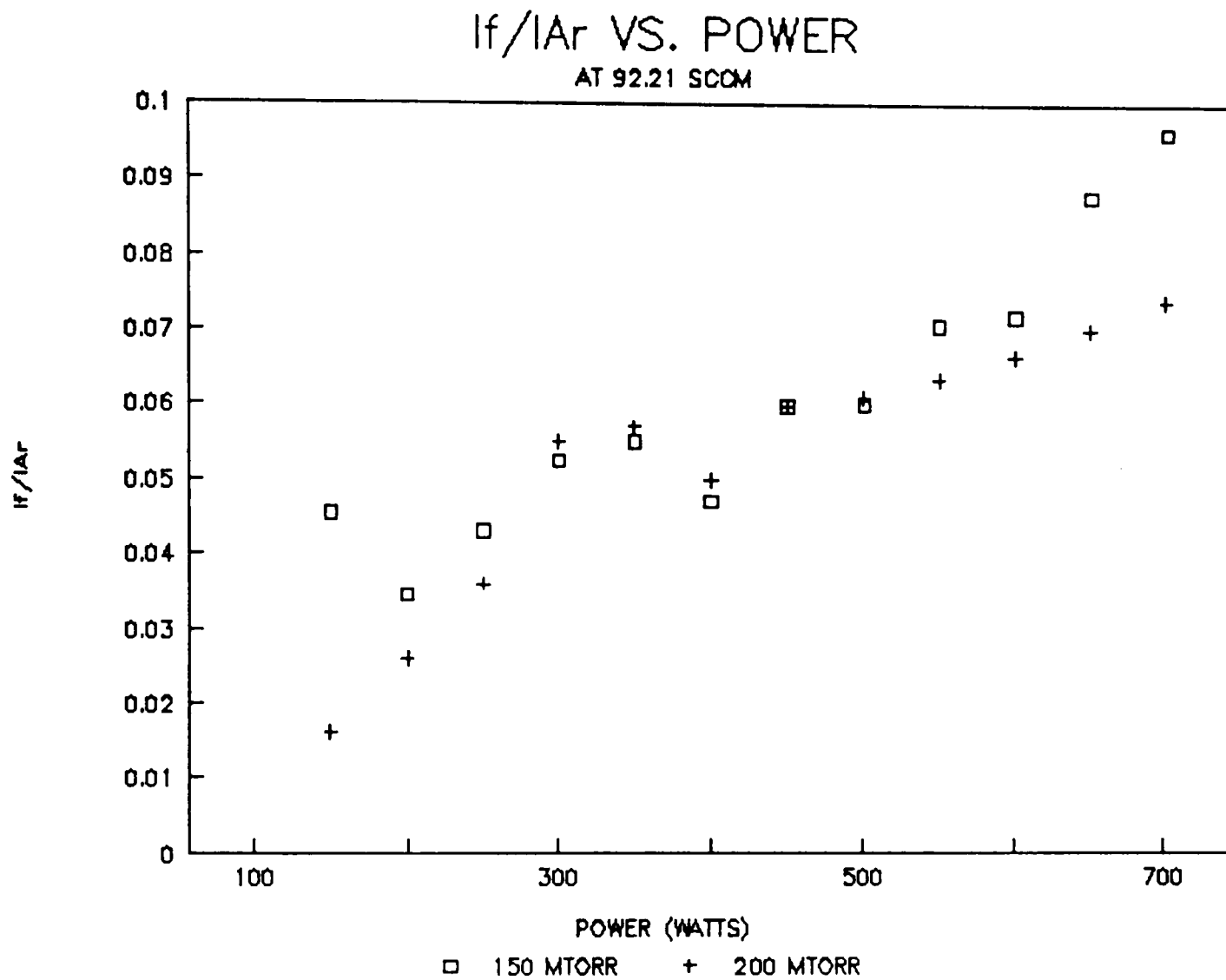
S.No.	Power	A	B	C	D
1.	100	0.4535	10.697	-71.436	124.81
2.	200	0.1228	7.359	-5.932	-47.17
3.	300	0.1986	10.806	-38.455	24.60
4.	400	0.1476	7.528	-7.539	-50.46
5.	500	0.0912	14.155	-72.024	120.15

final model developed is as follows:

$$\frac{[EL]}{[EL]_{6.6}} = [.2025+10.109r-39.076r^2+30.786r^3]. \quad (G.2)$$

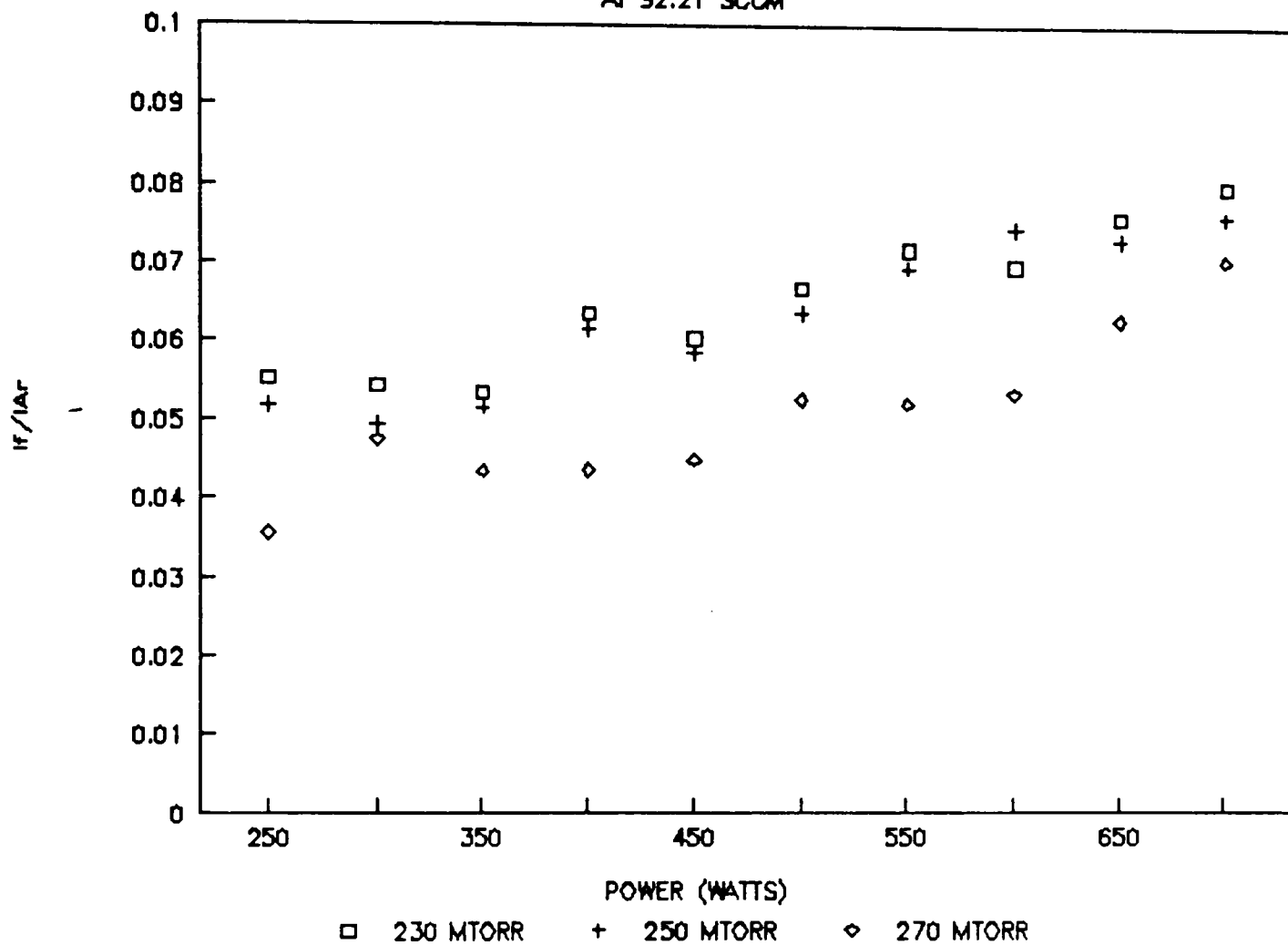
The comparison of model results with the experimentally obtained electron density distribution is presented and discussed in Chapter 9.

APPENDIX I
UNLOADED REACTOR RUNS DATA



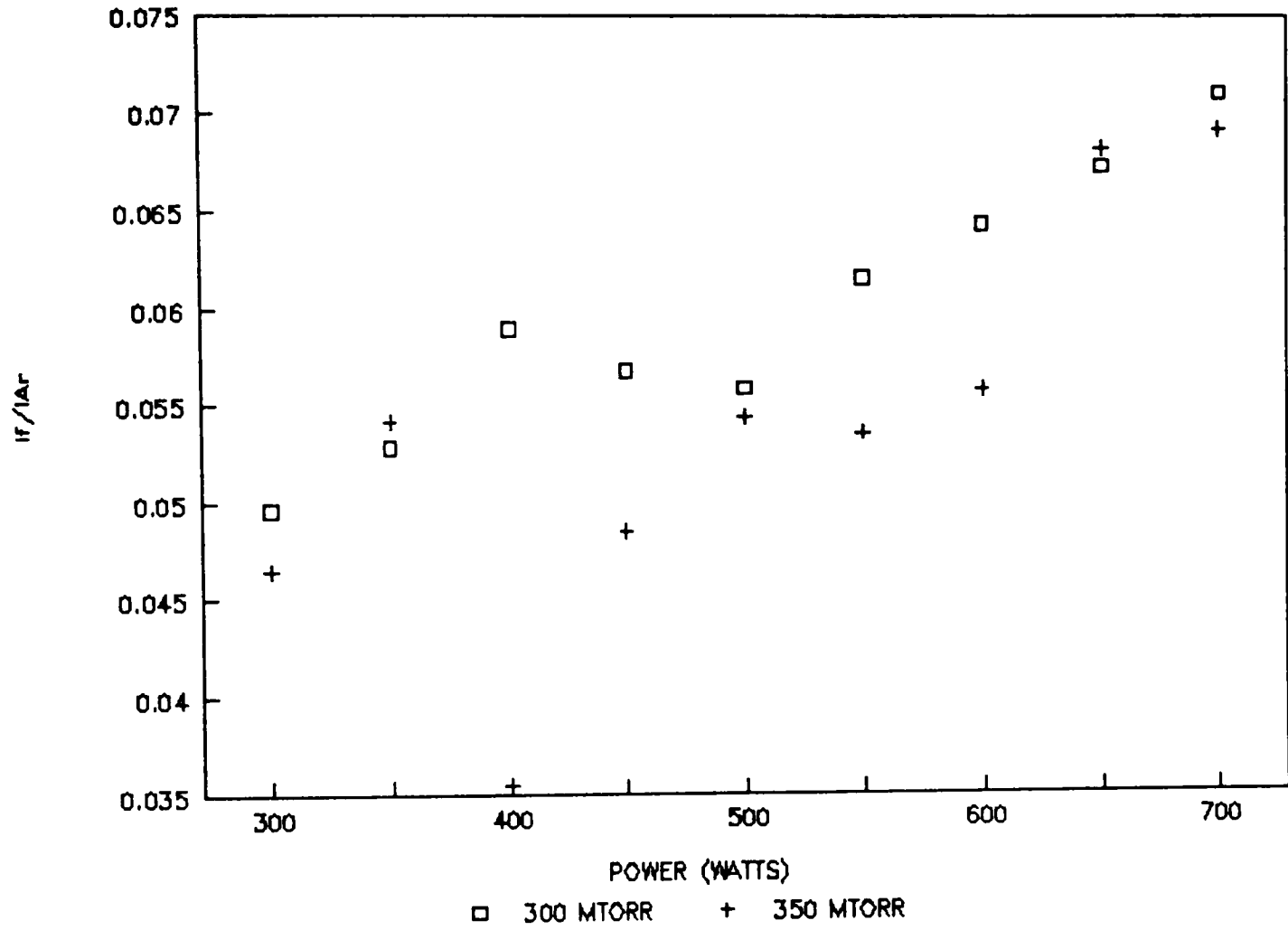
If/I_{Ar} VS. POWER

AT 92.21 SCOM



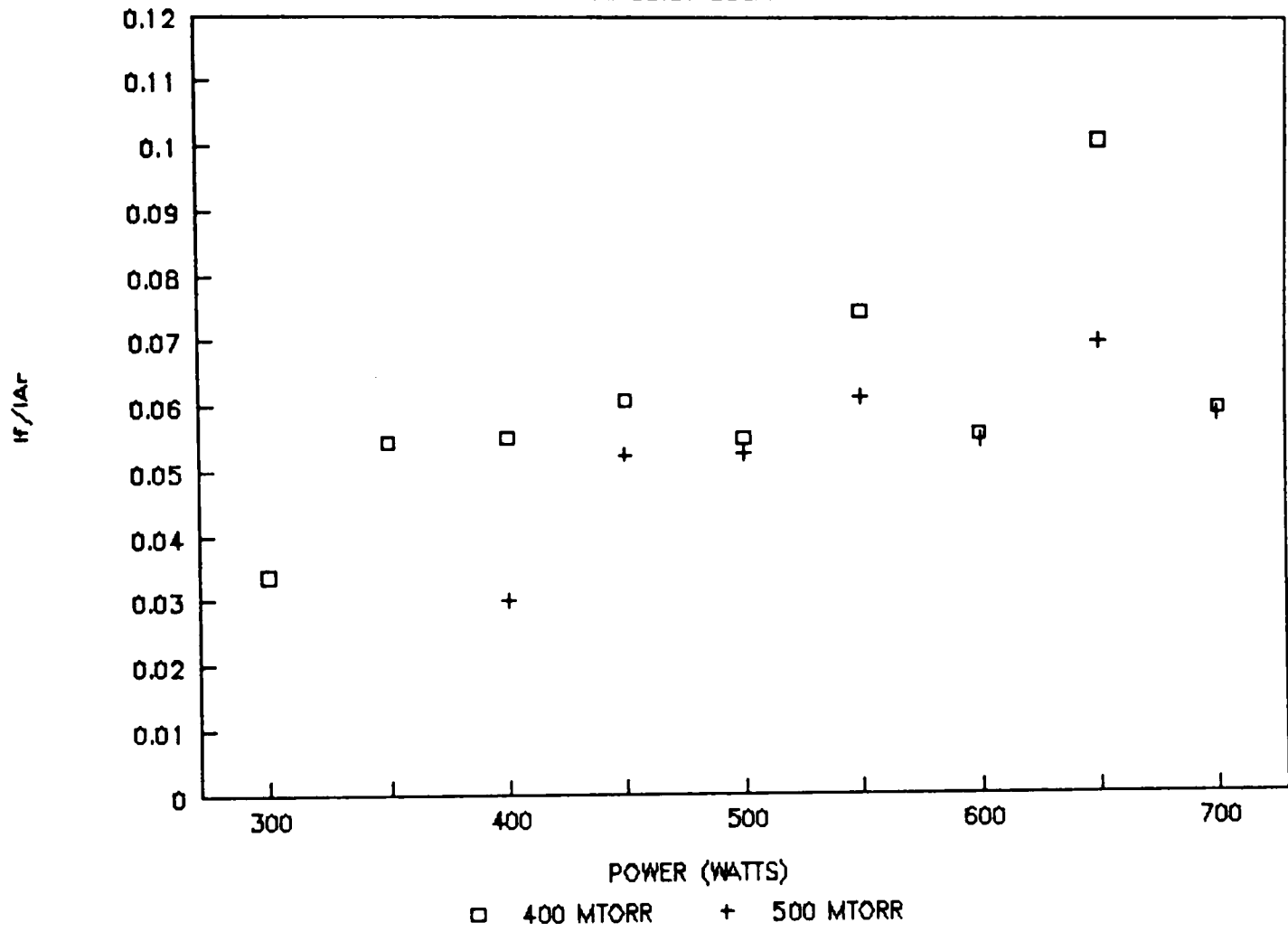
If/I_{Ar} VS. POWER

AT 92.21 SCOM



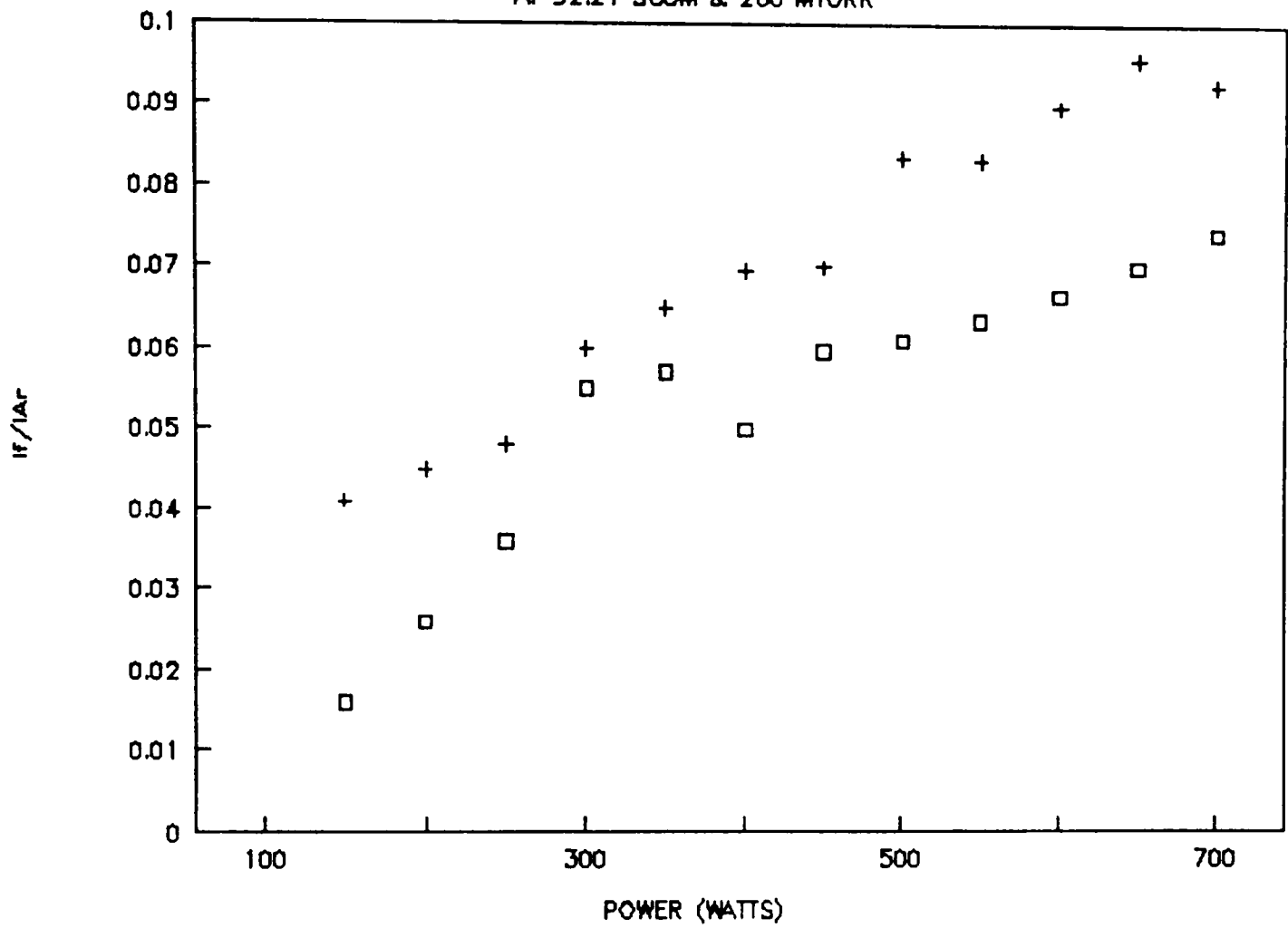
If/I_{Ar} VS. POWER

AT 92.21 SCOM



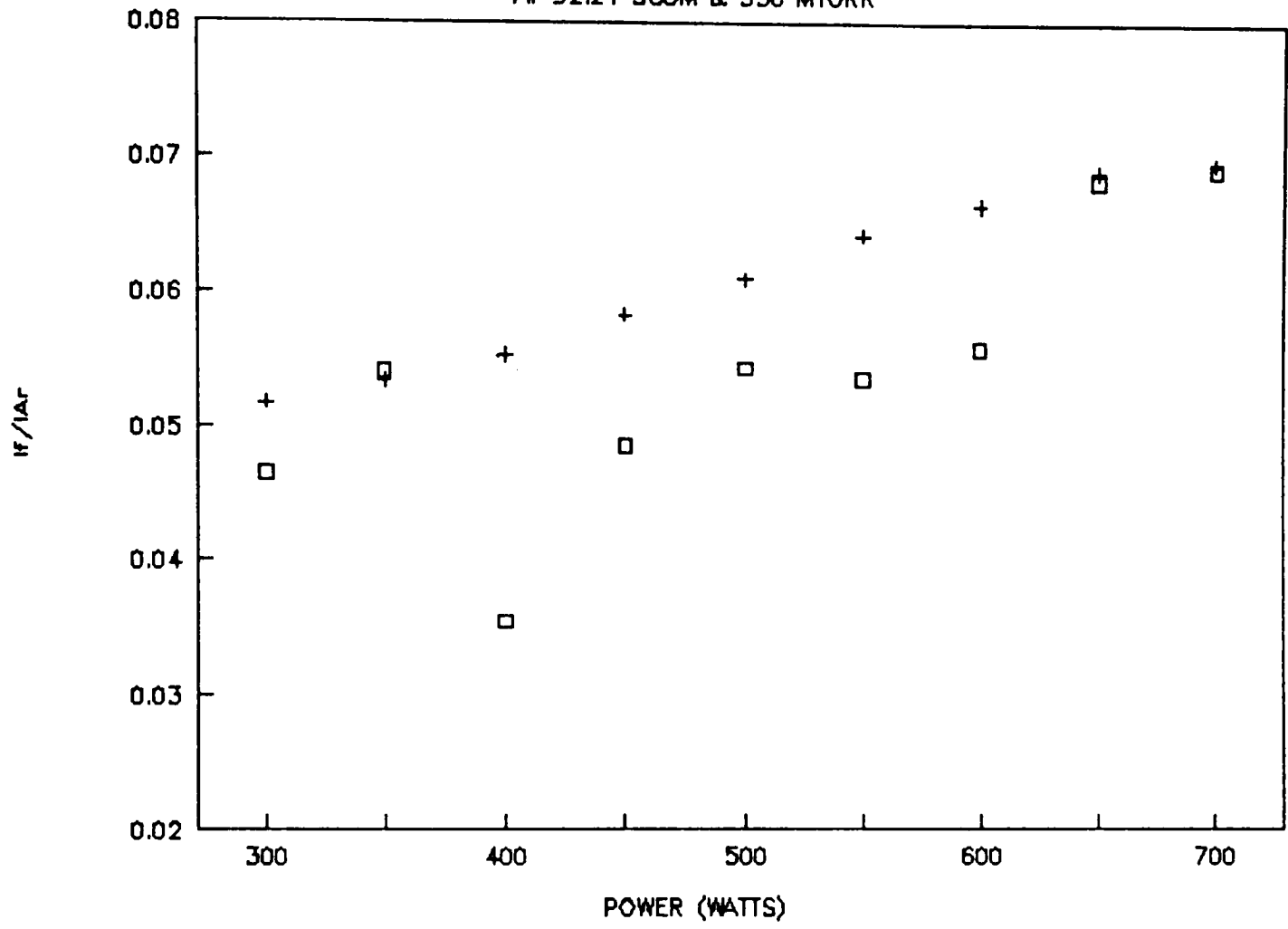
If/I_{Ar} VS. POWER

AT 92.21 SCCM & 200 MTORR



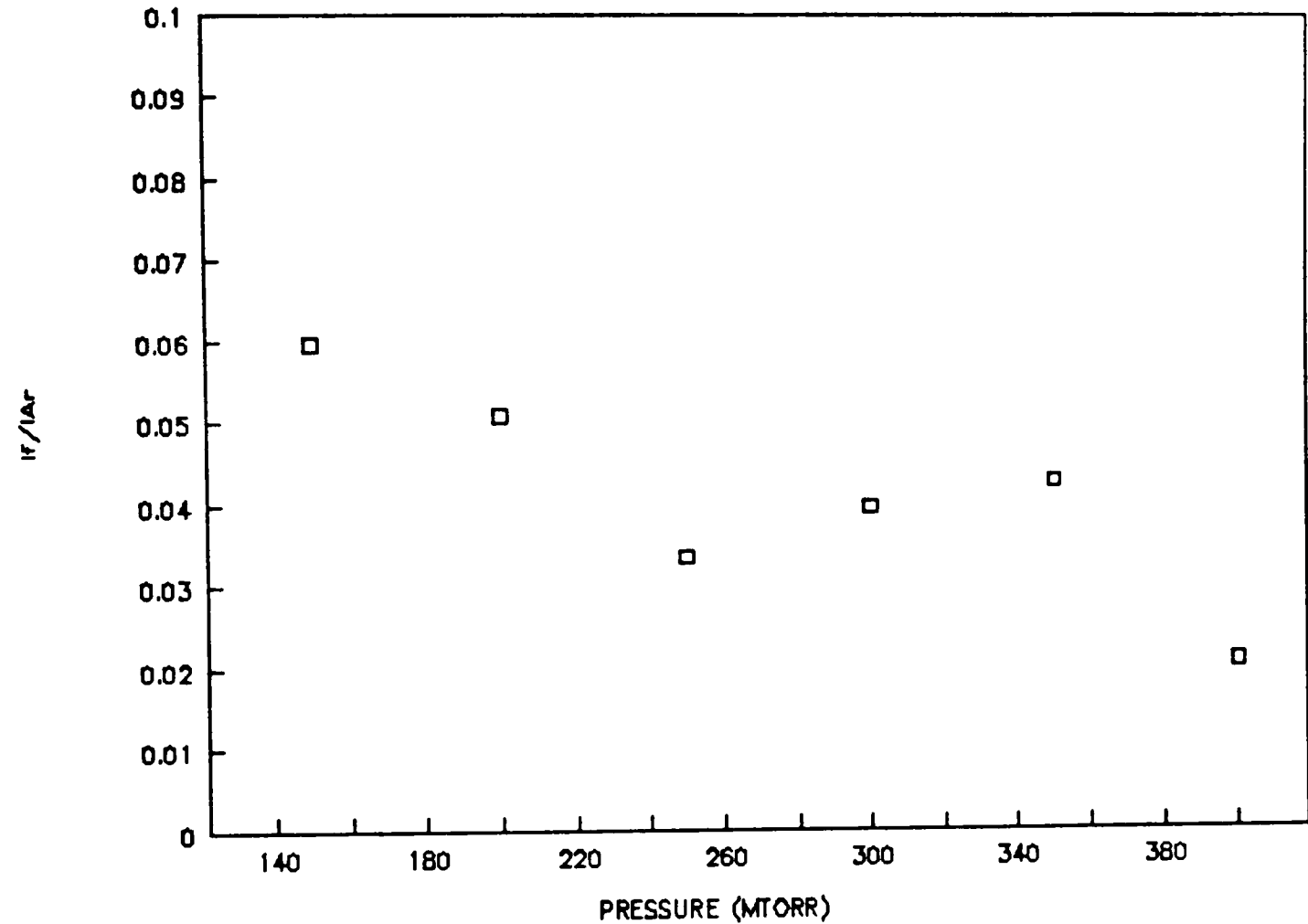
If/I_{Ar} VS. POWER

AT 92.21 SCCM & 350 MTORR



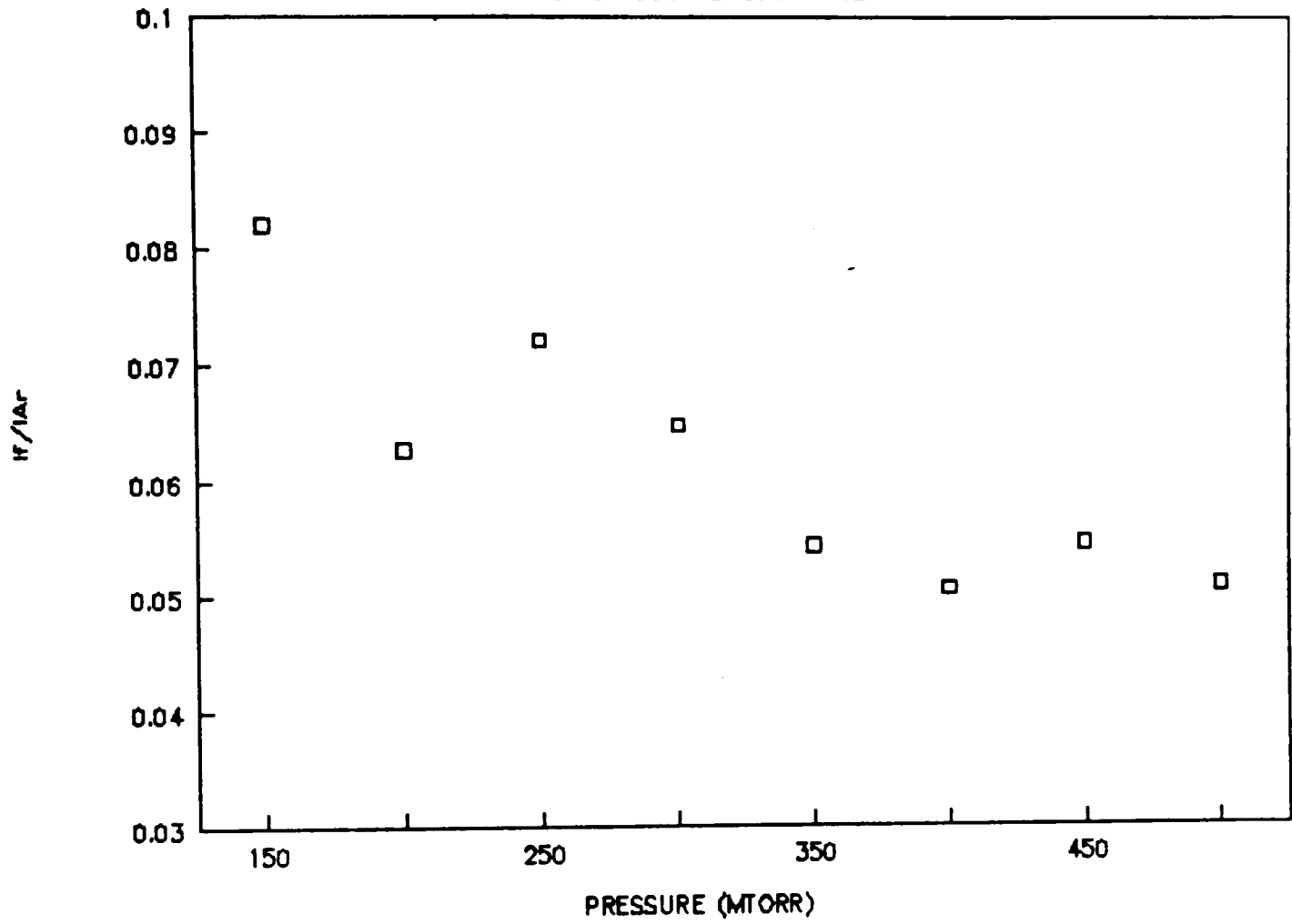
If/I_{Ar} VS. PRESSURE

AT 92.21 SCCM & 300 WATTS



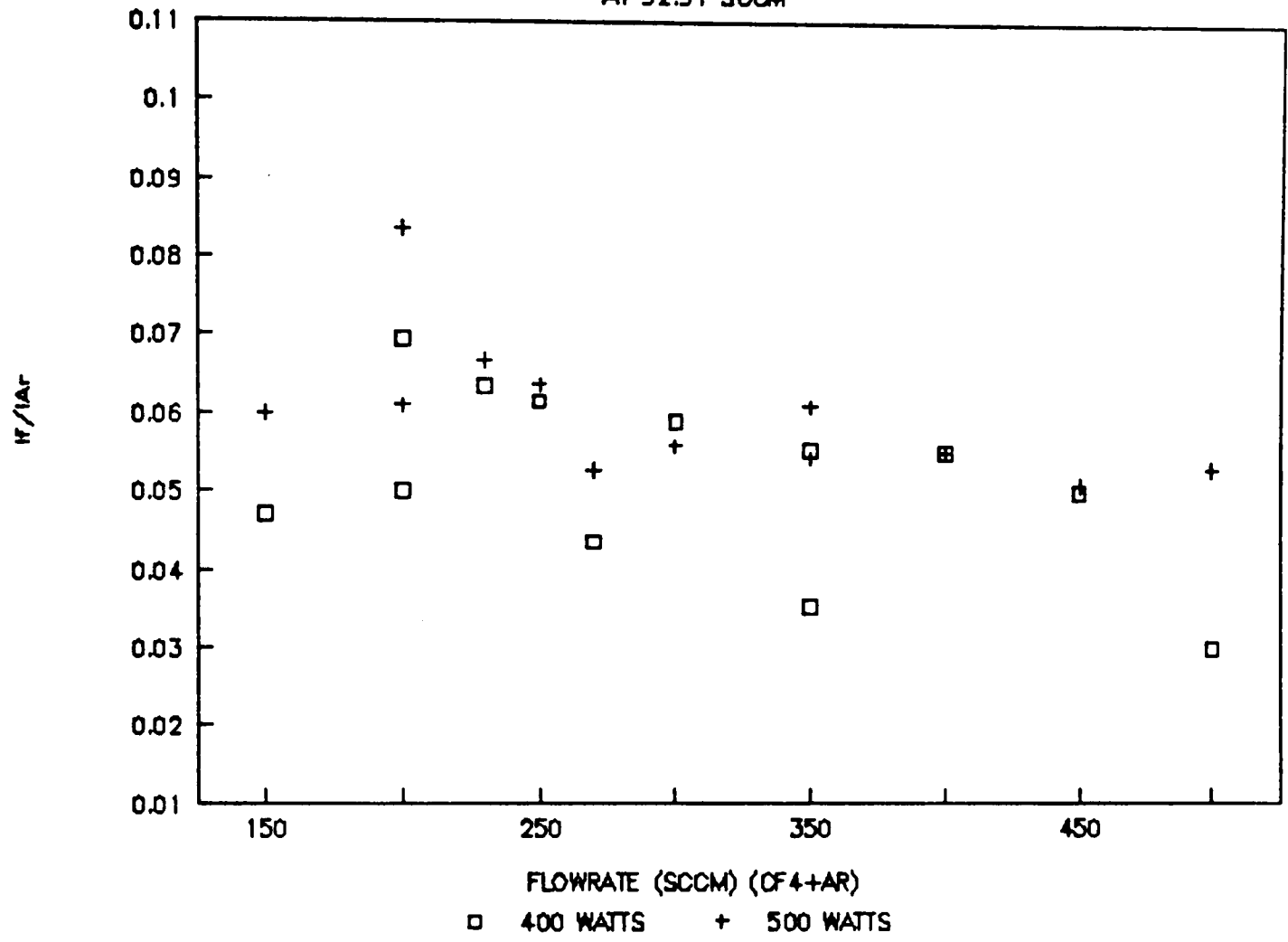
If/I_{Ar} VS. PRESSURE

AT 92.21 SCOM & 600 WATTS

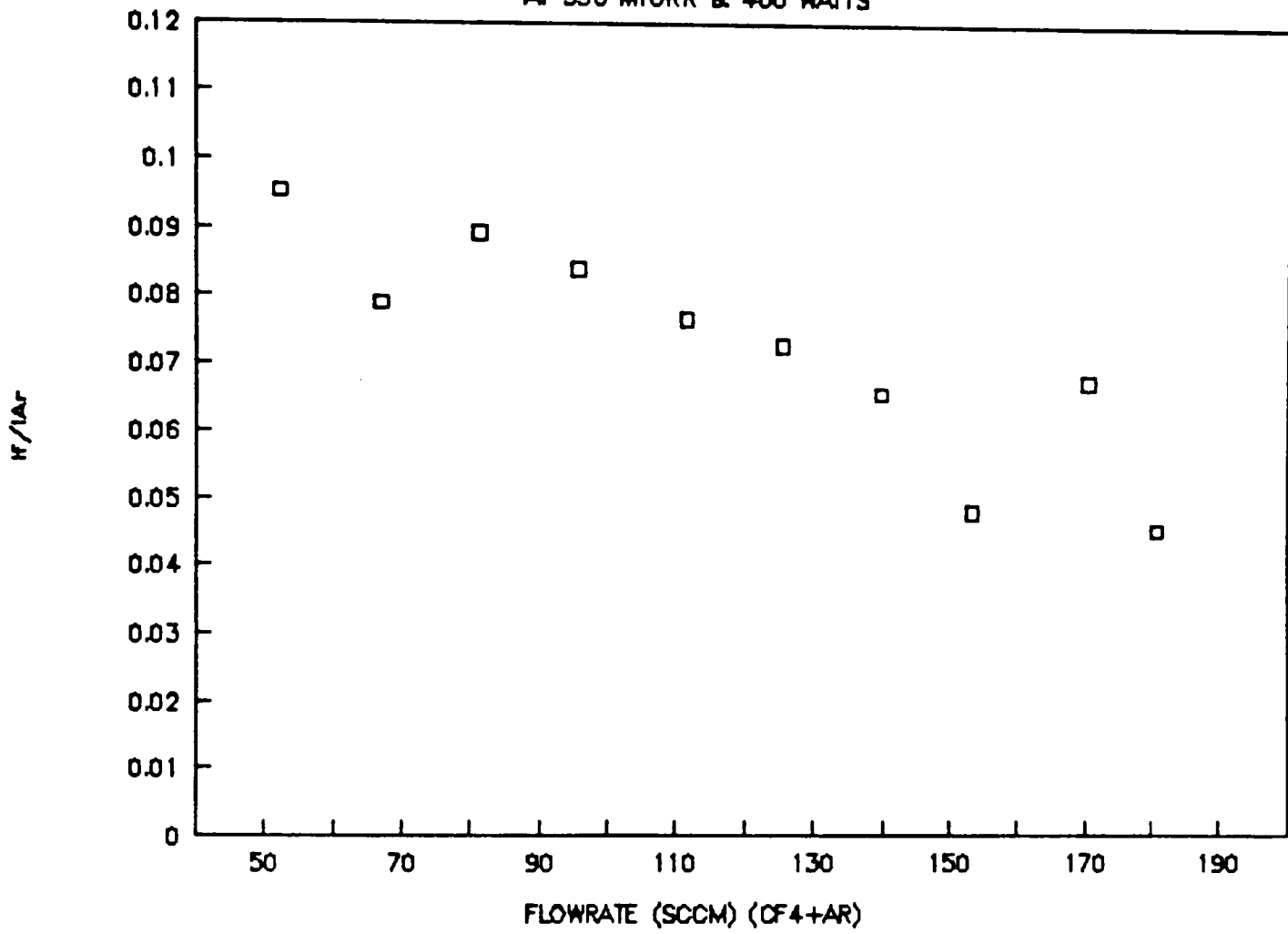


If/I_{Ar} VS. PRESSURE

AT 92.91 SCCM

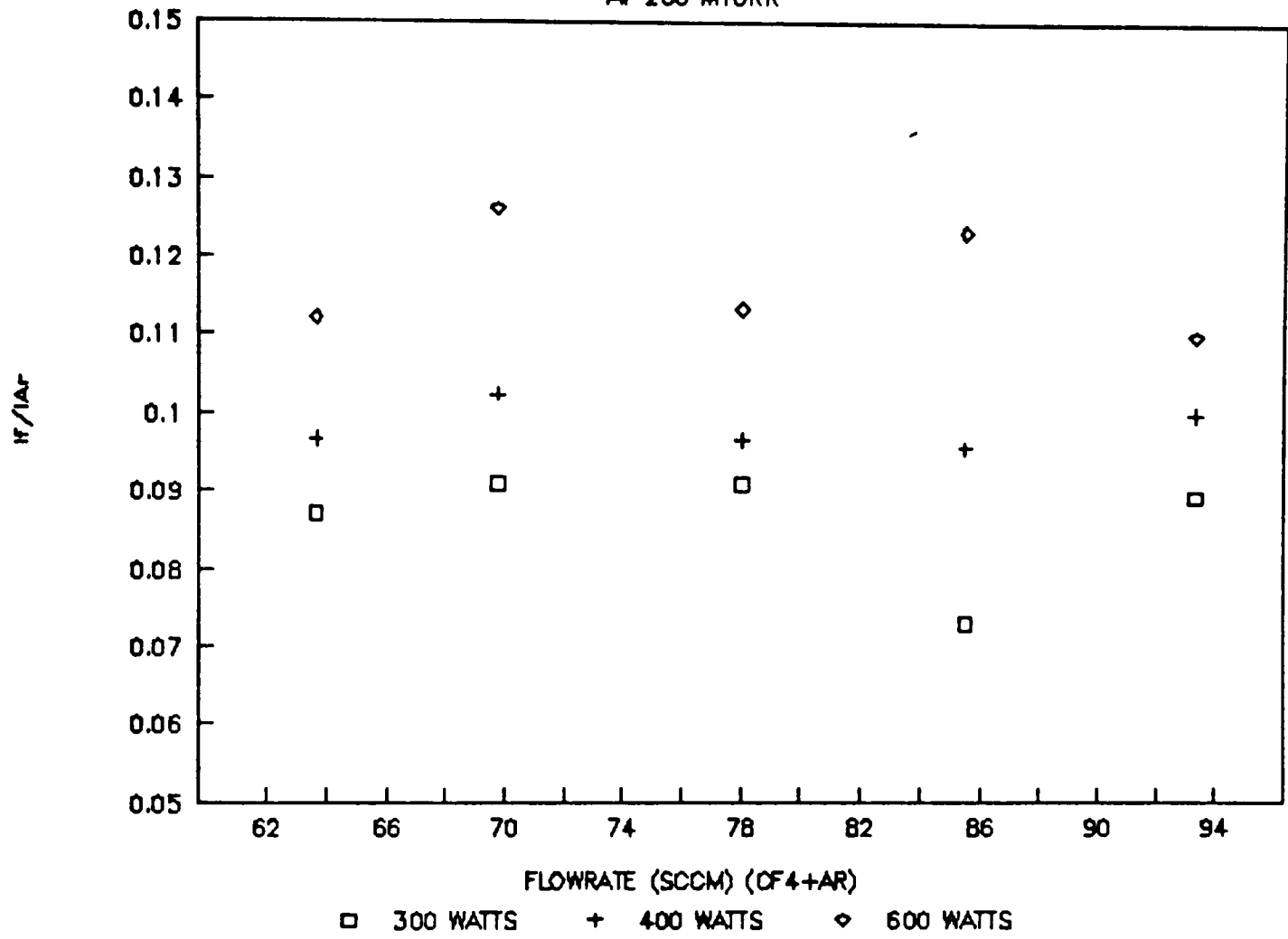


If/I_{Ar} VS. FLOWRATE
AT 350 MTORR & 400 WATTS



If/I_{Ar} VS. FLOWRATE

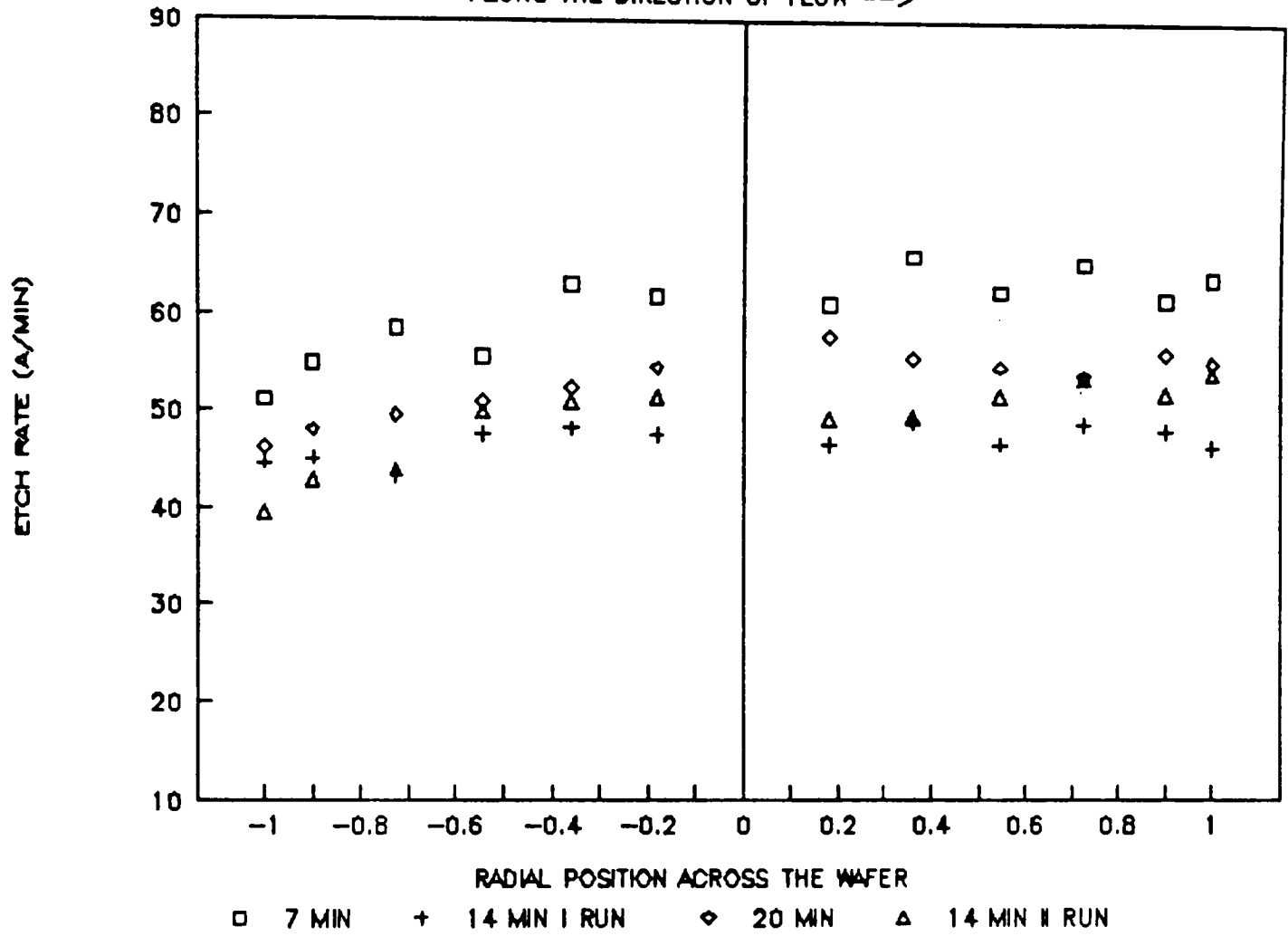
AT 200 MTORR



APPENDIX J

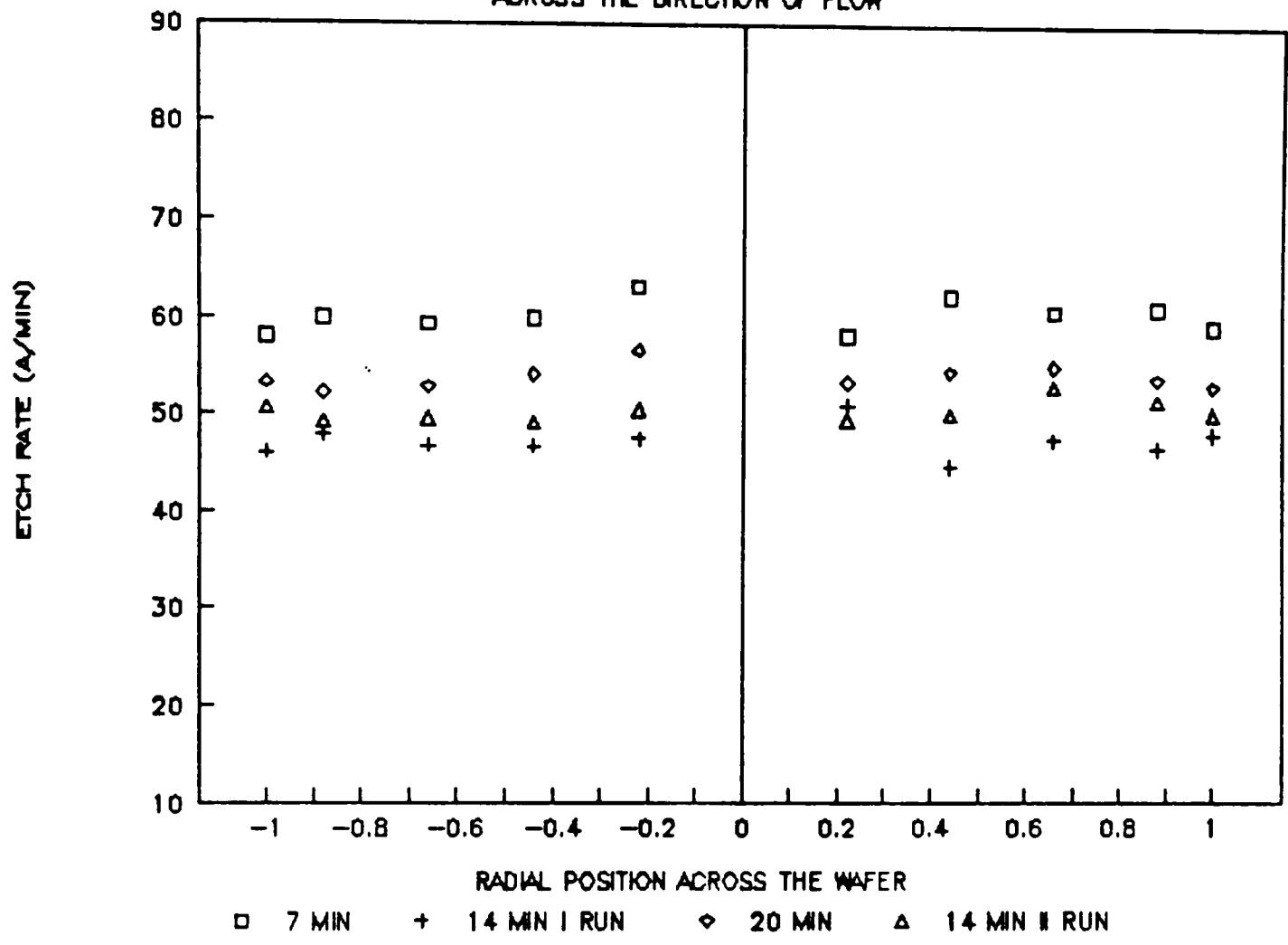
LOADED REACTOR RUNS DATA

ETCH RATE DATA (500 PO;300 PR;90 FL)
ALONG THE DIRECTION OF FLOW -->



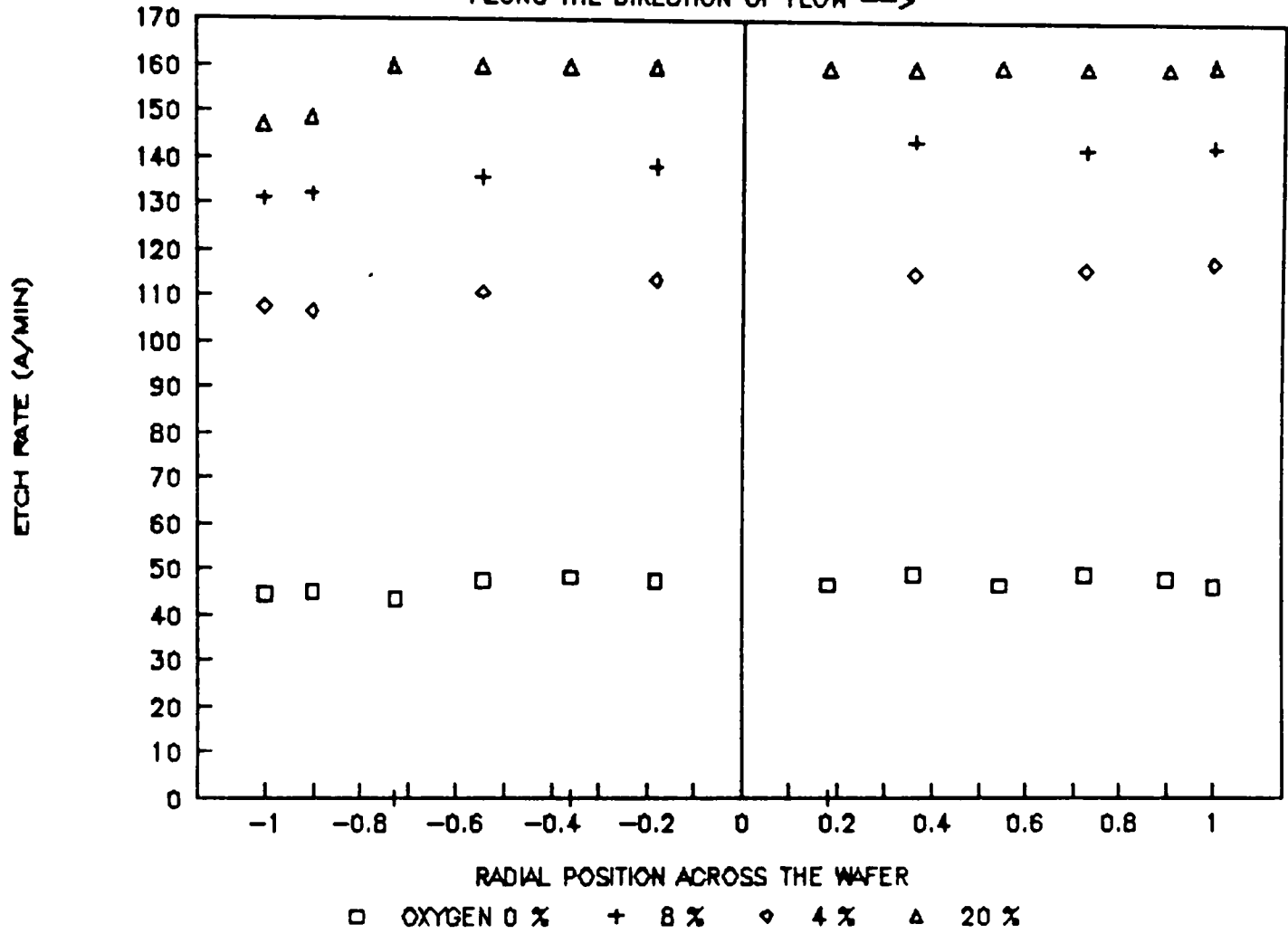
ETCH RATE DATA (500 PO;300 PR;90 FL)

ACROSS THE DIRECTION OF FLOW



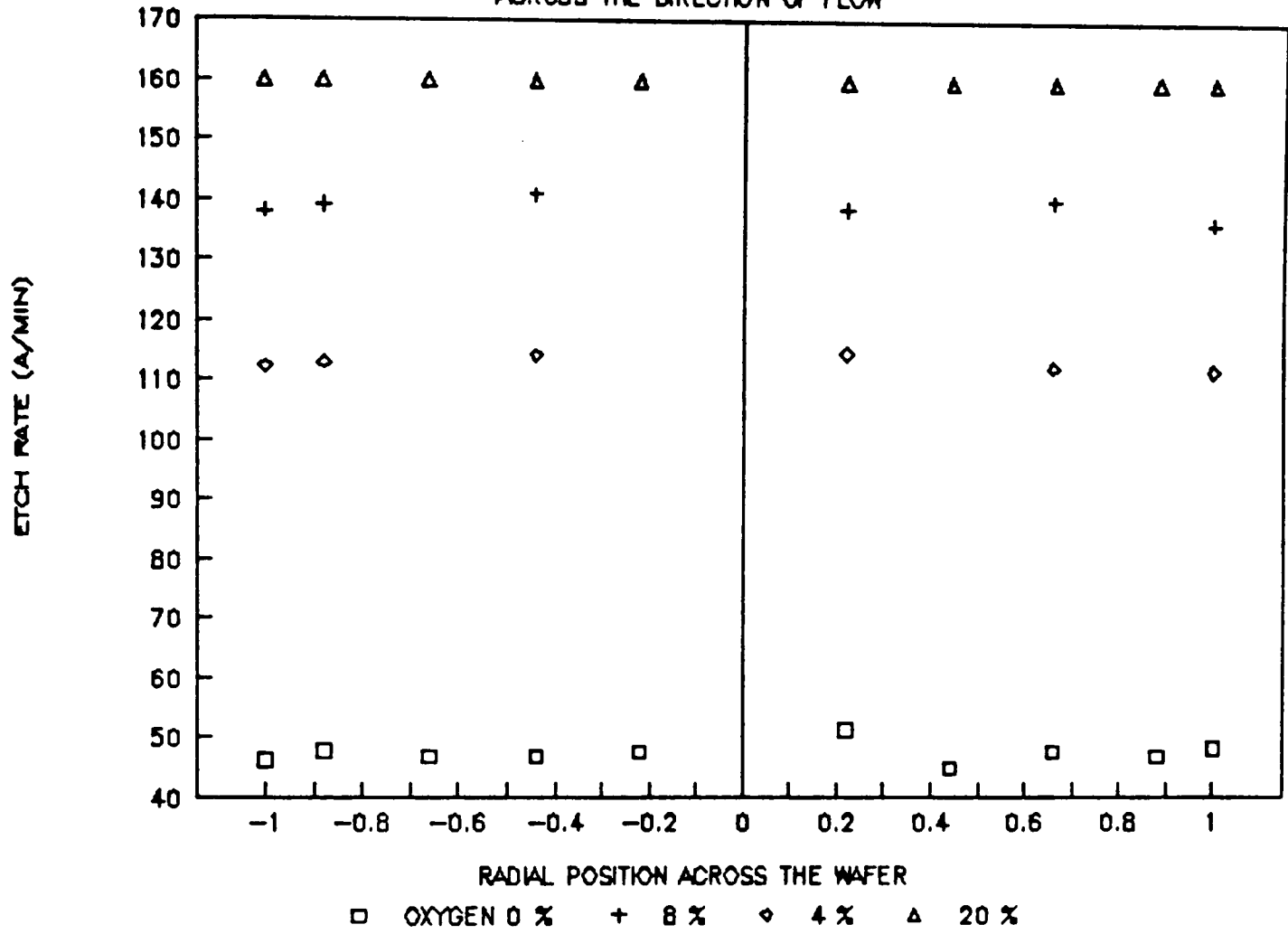
ETCH RATE DATA (500 PO;300 PR;90 FL)

ALONG THE DIRECTION OF FLOW →



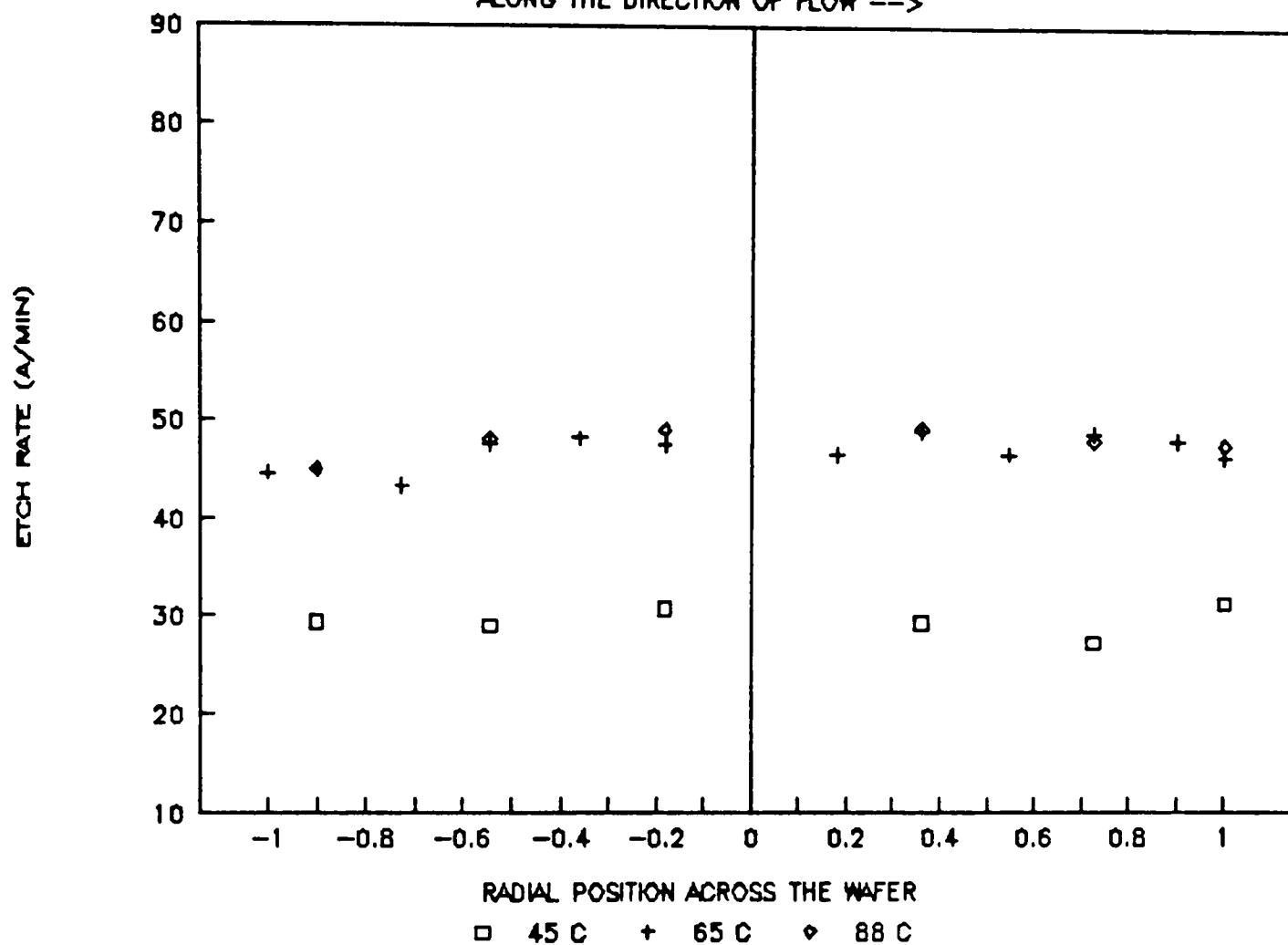
ETCH RATE DATA (500 PO;300 PR;90 FL)

ACROSS THE DIRECTION OF FLOW

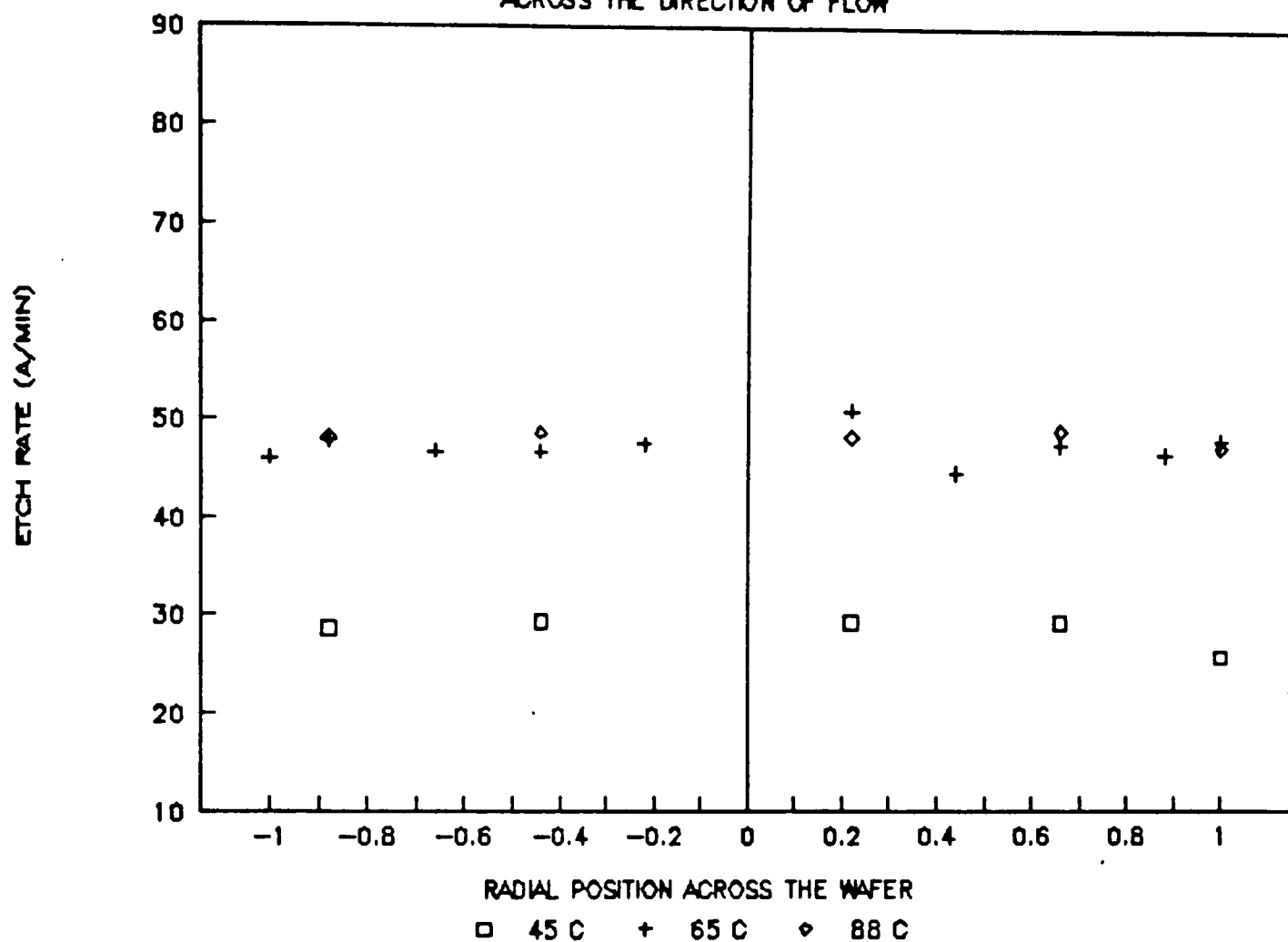


ETCH RATE DATA (500 PO;300 PR;90 FL)

ALONG THE DIRECTION OF FLOW -->

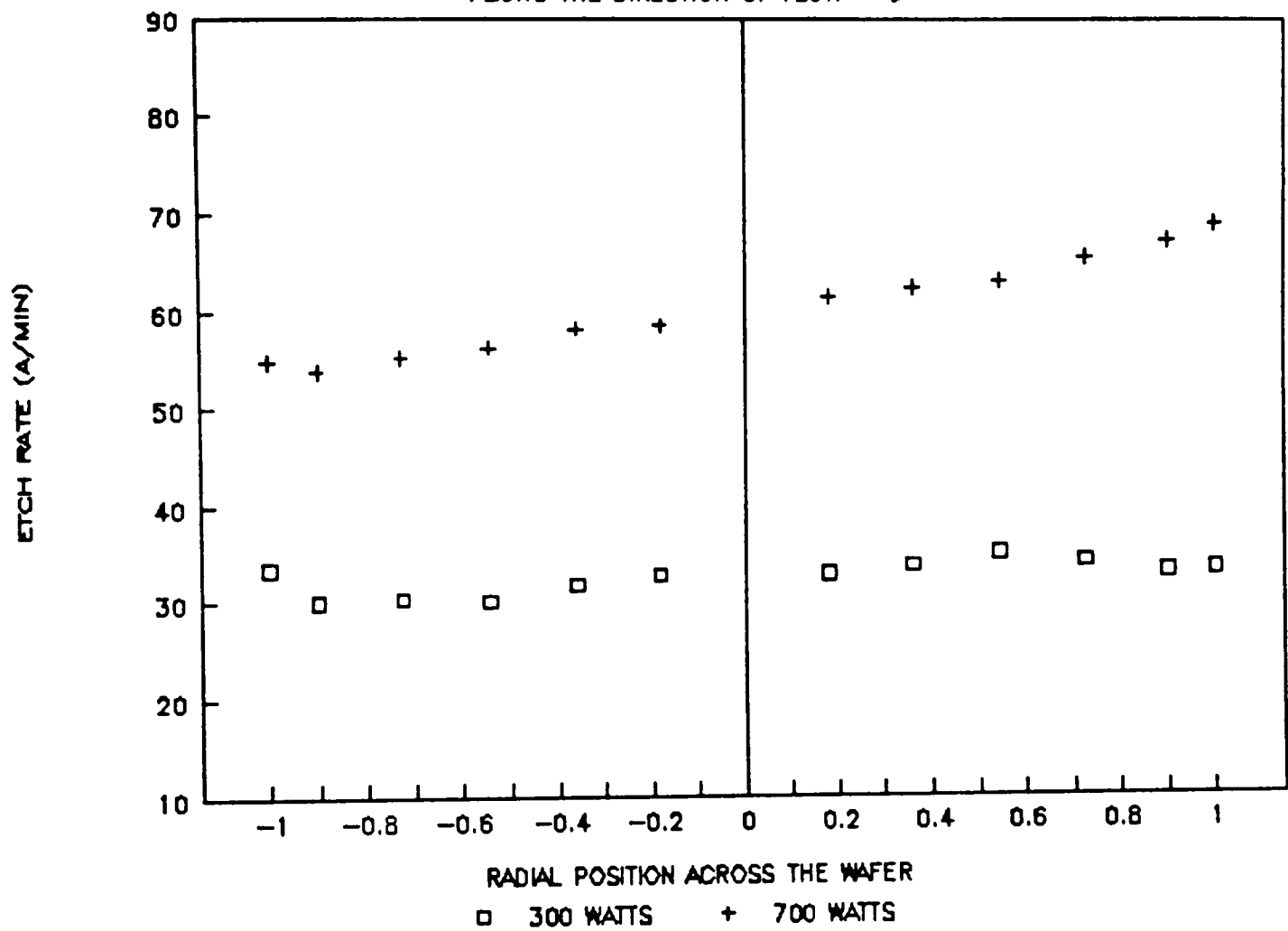


ETCH RATE DATA (500 PO;300 PR;90 FL) ACROSS THE DIRECTION OF FLOW

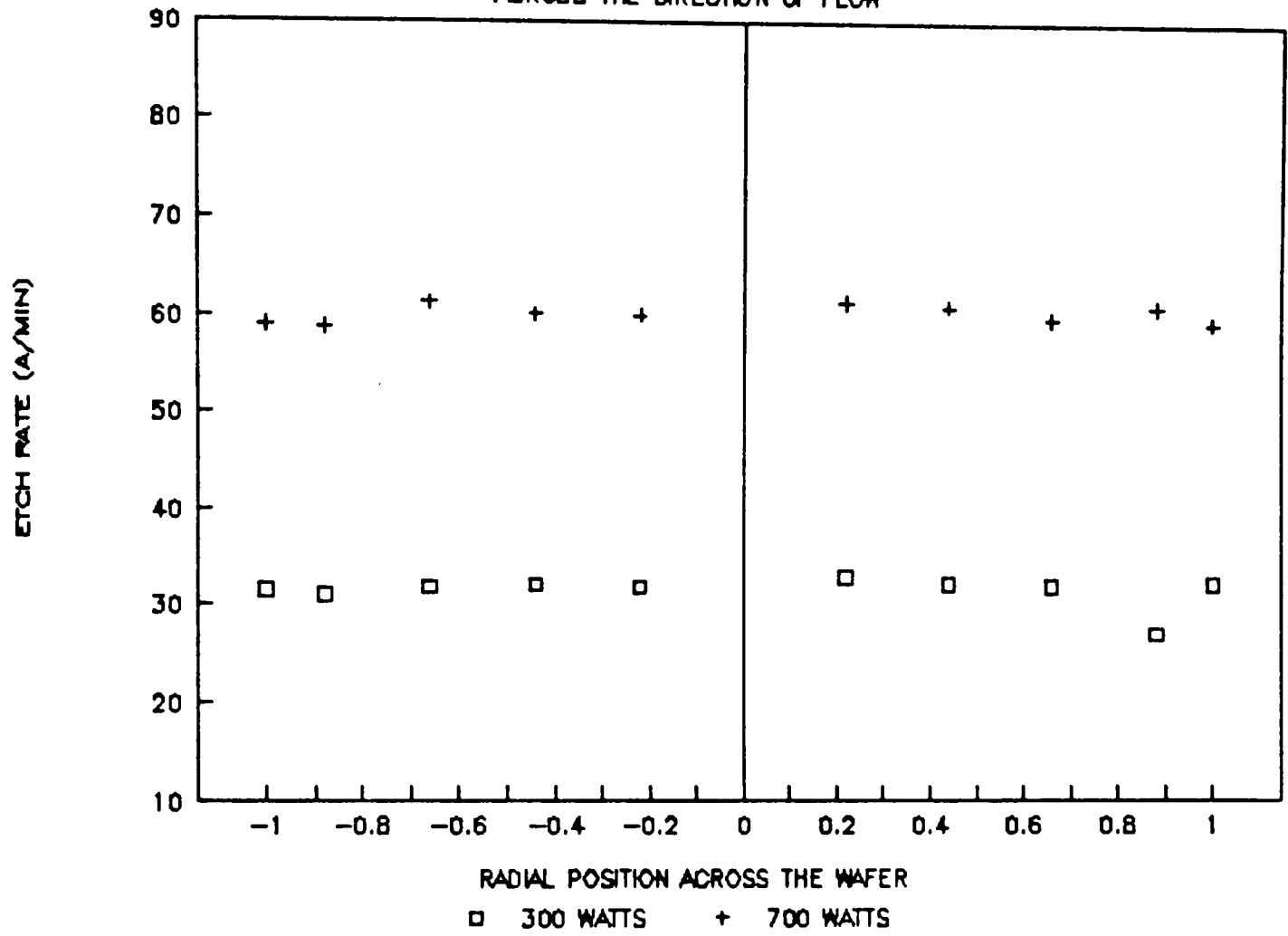


ETCH RATE DATA (200 MTORR;70 SCCM)

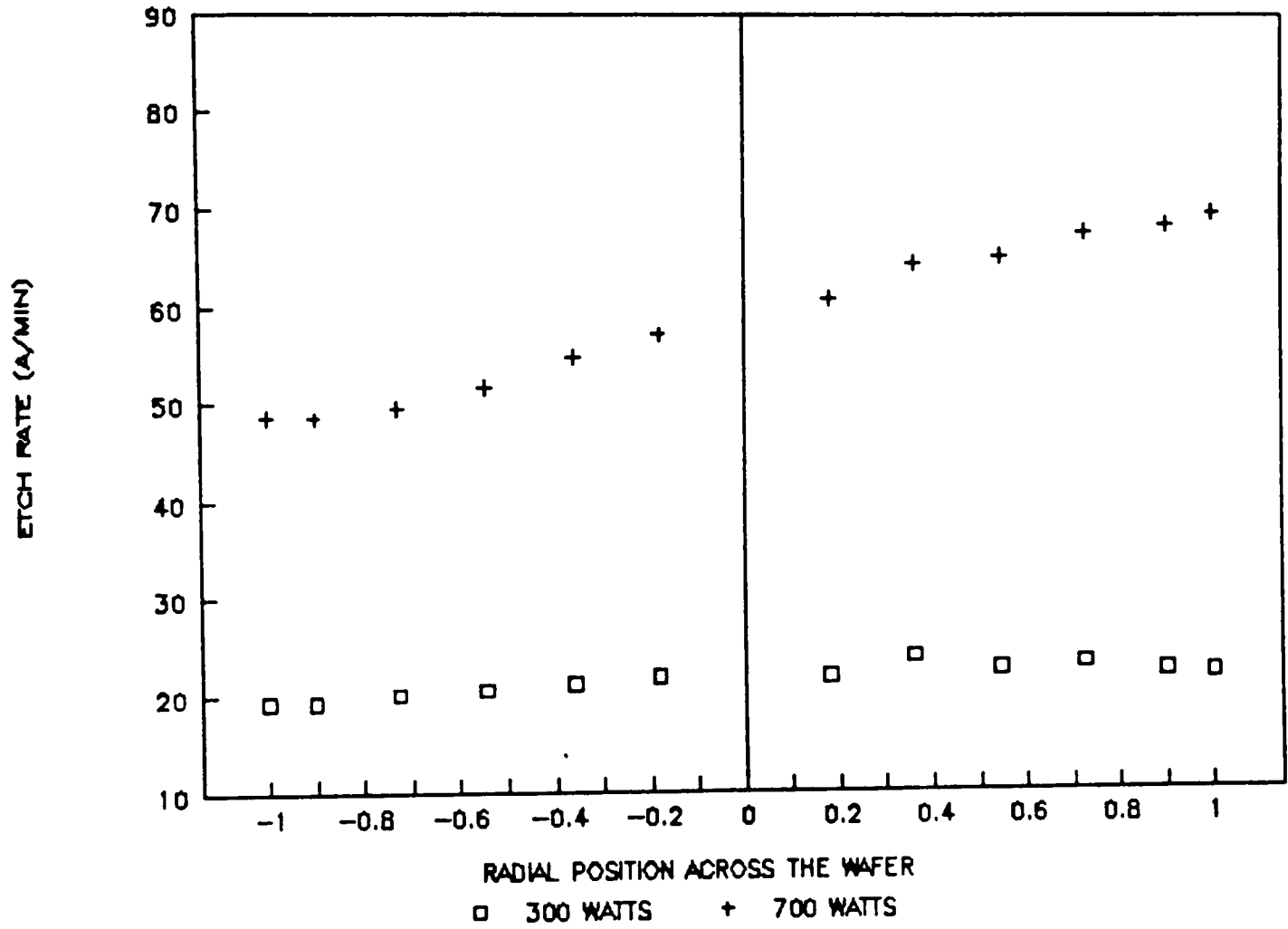
ALONG THE DIRECTION OF FLOW -->



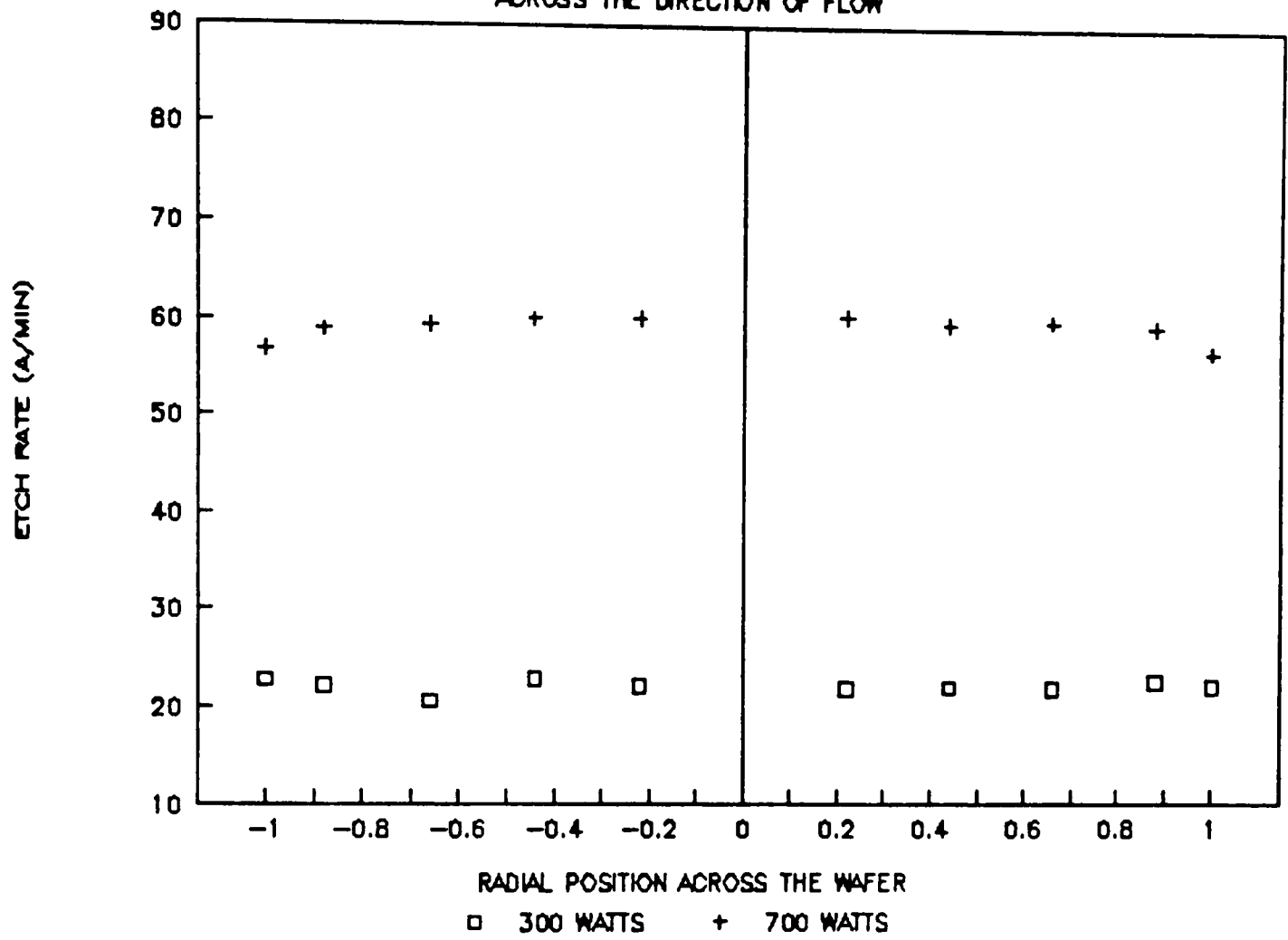
ETCH RATE DATA (200 MTORR;70 SCCM) ACROSS THE DIRECTION OF FLOW



ETCH RATE DATA (200 MTORR; 110 SCCM)
ALONG THE DIRECTION OF FLOW -->

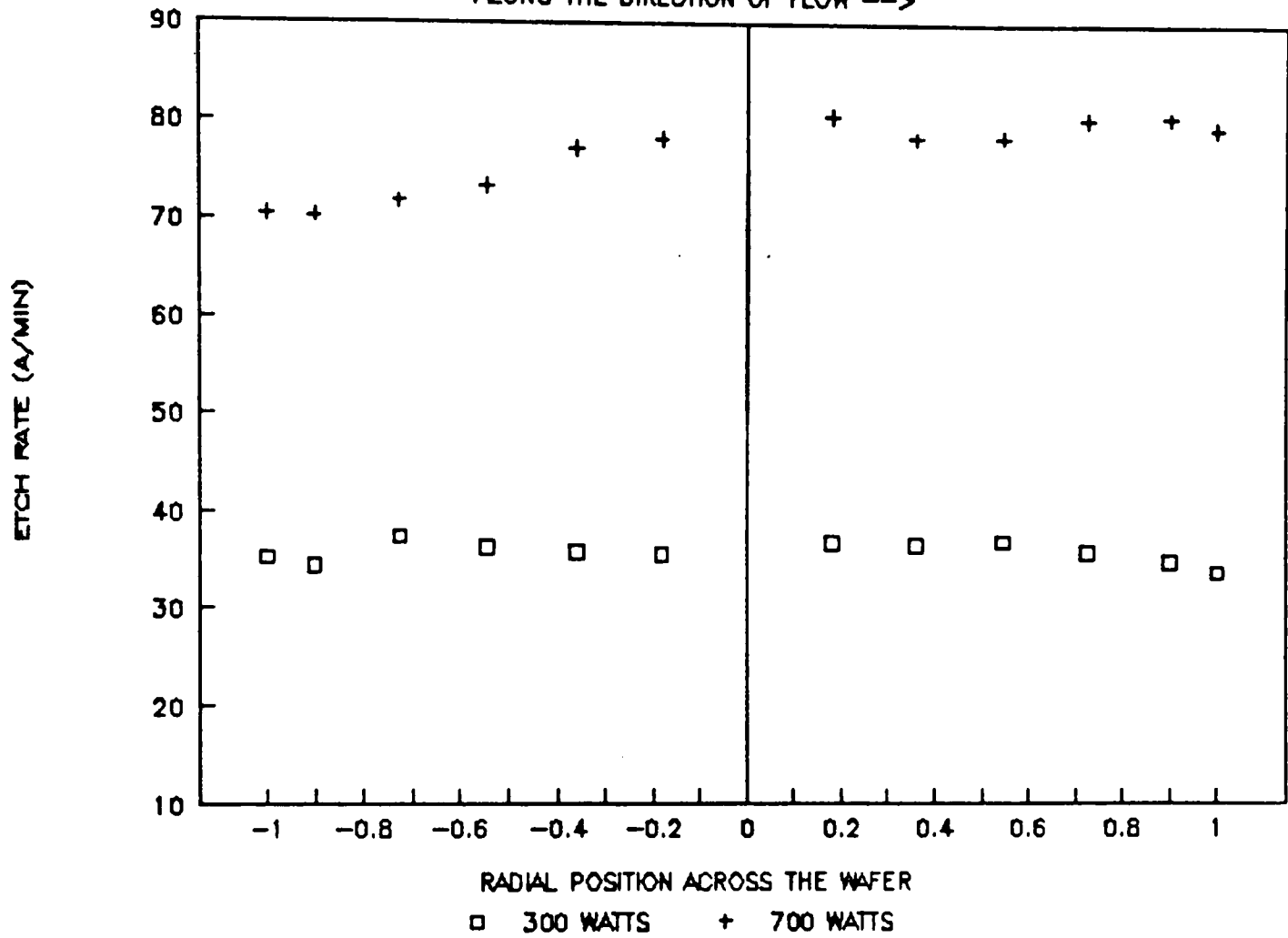


ETCH RATE DATA (200 MTORR; 110 SCCM) ACROSS THE DIRECTION OF FLOW

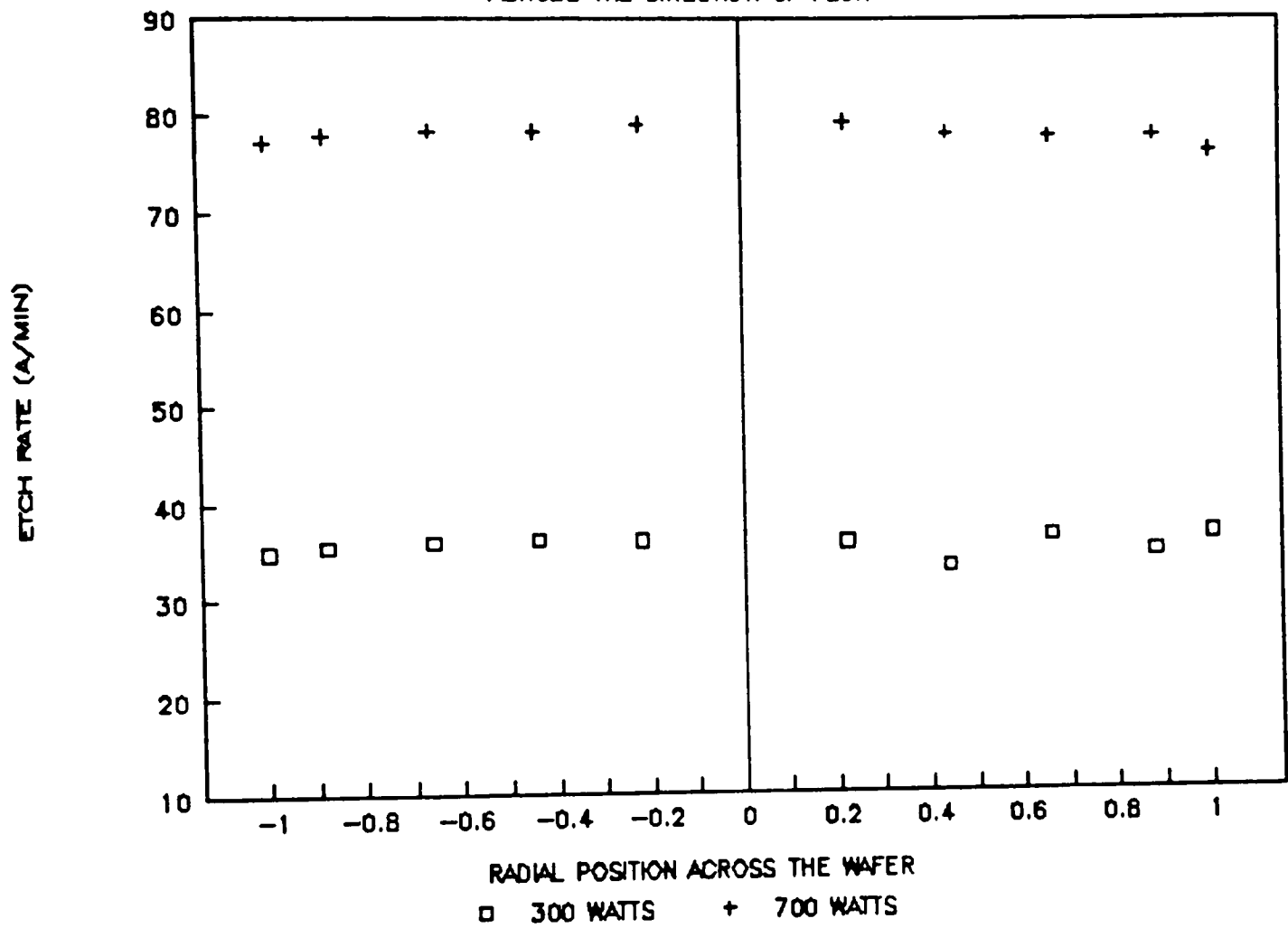


ETCH RATE DATA (400 MTORR; 70 SCCM)

ALONG THE DIRECTION OF FLOW -->

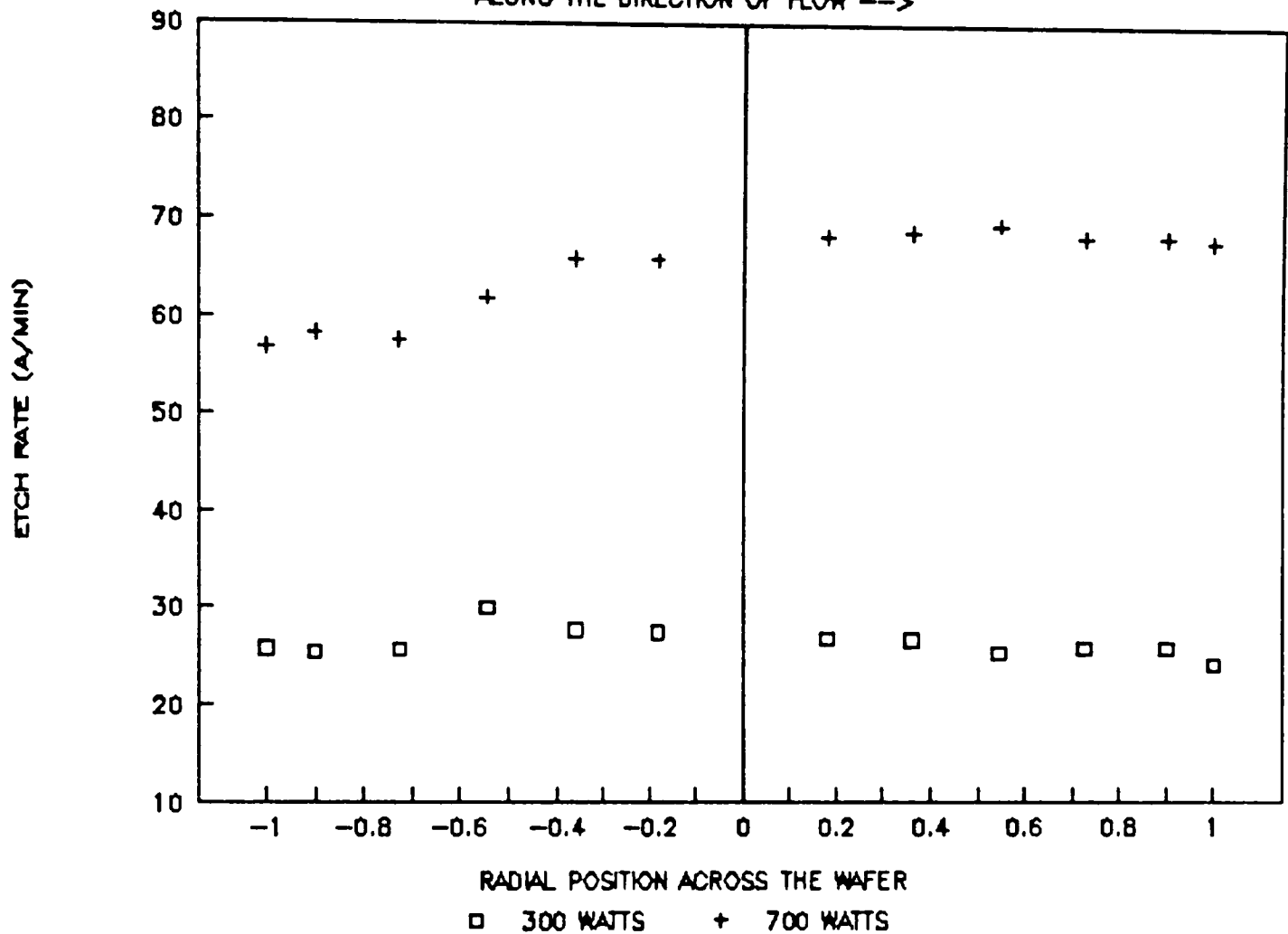


ETCH RATE DATA (400 MTORR; 70 SCCM) ACROSS THE DIRECTION OF FLOW

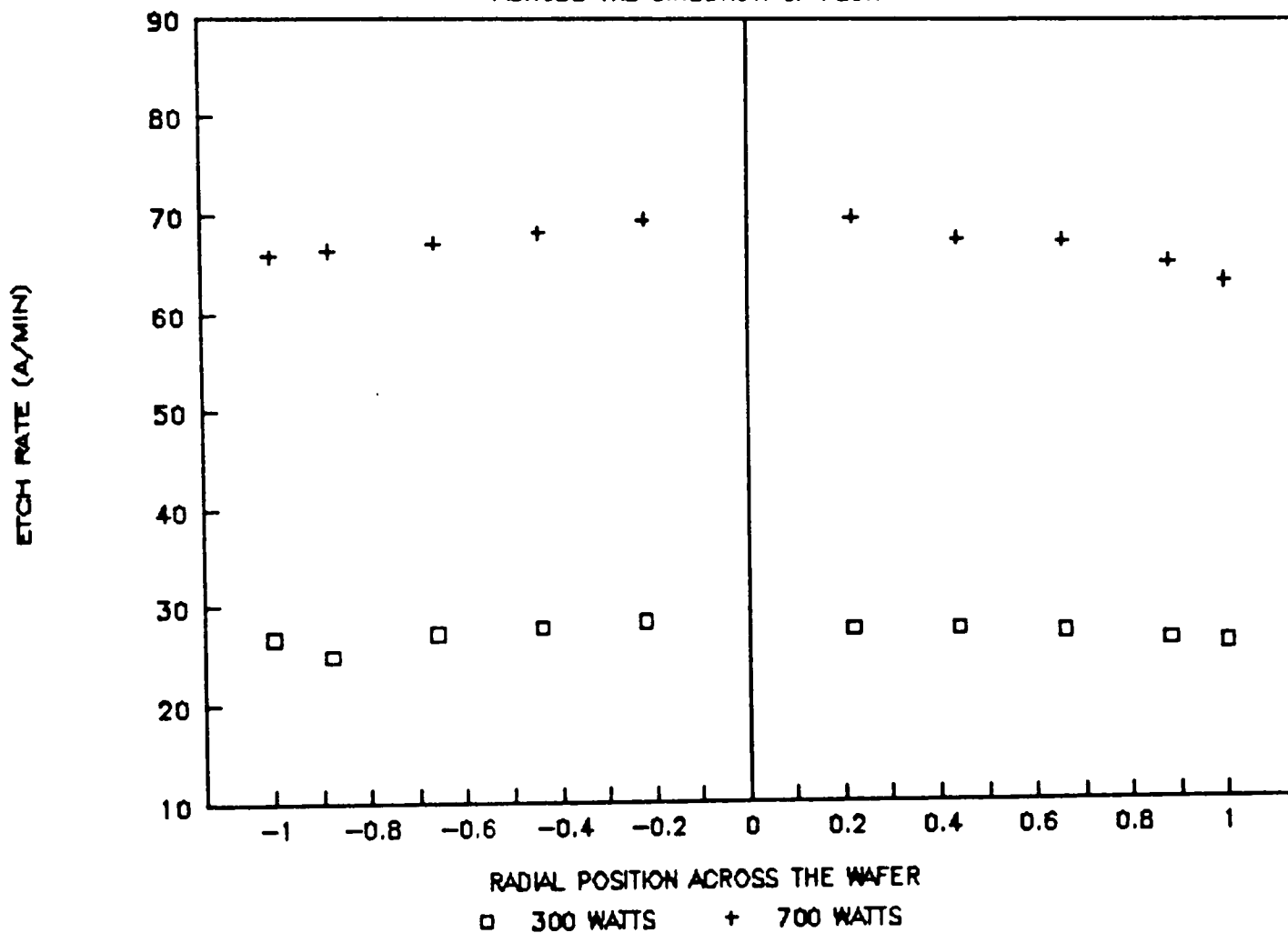


ETCH RATE DATA (400 MTORR; 110 SCCM)

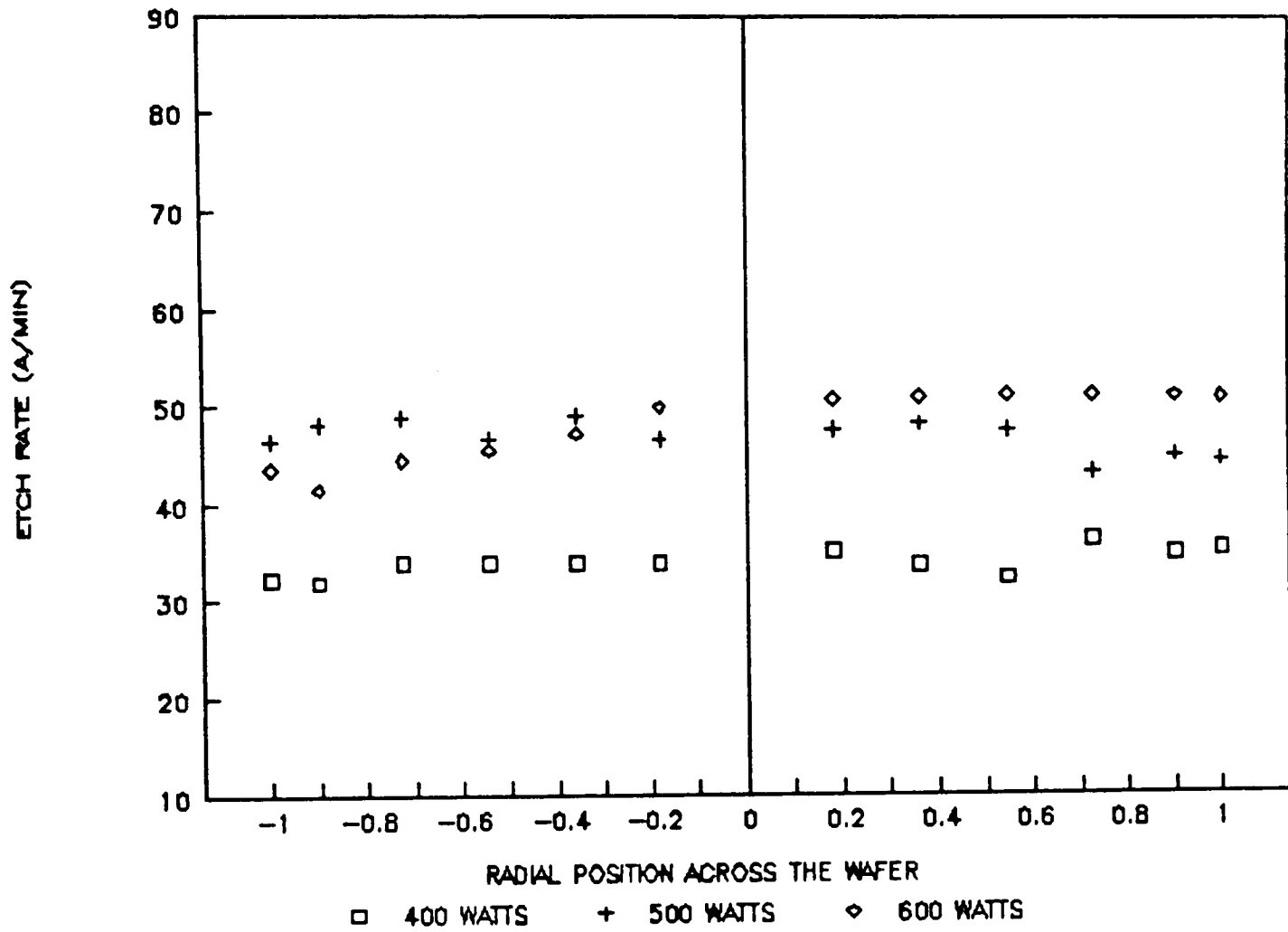
ALONG THE DIRECTION OF FLOW -->



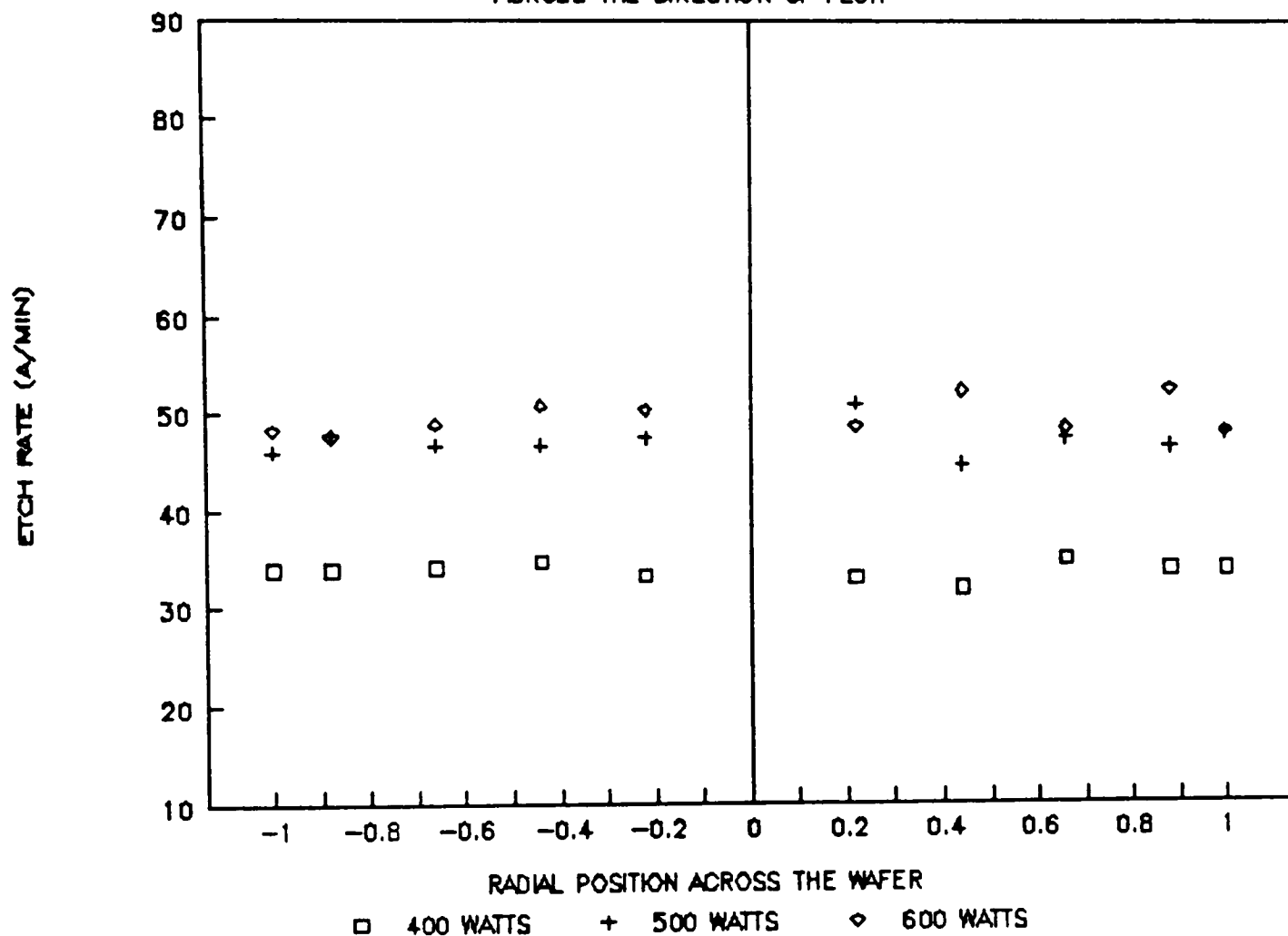
ETCH RATE DATA (400 MTORR; 110 SCCM) ACROSS THE DIRECTION OF FLOW



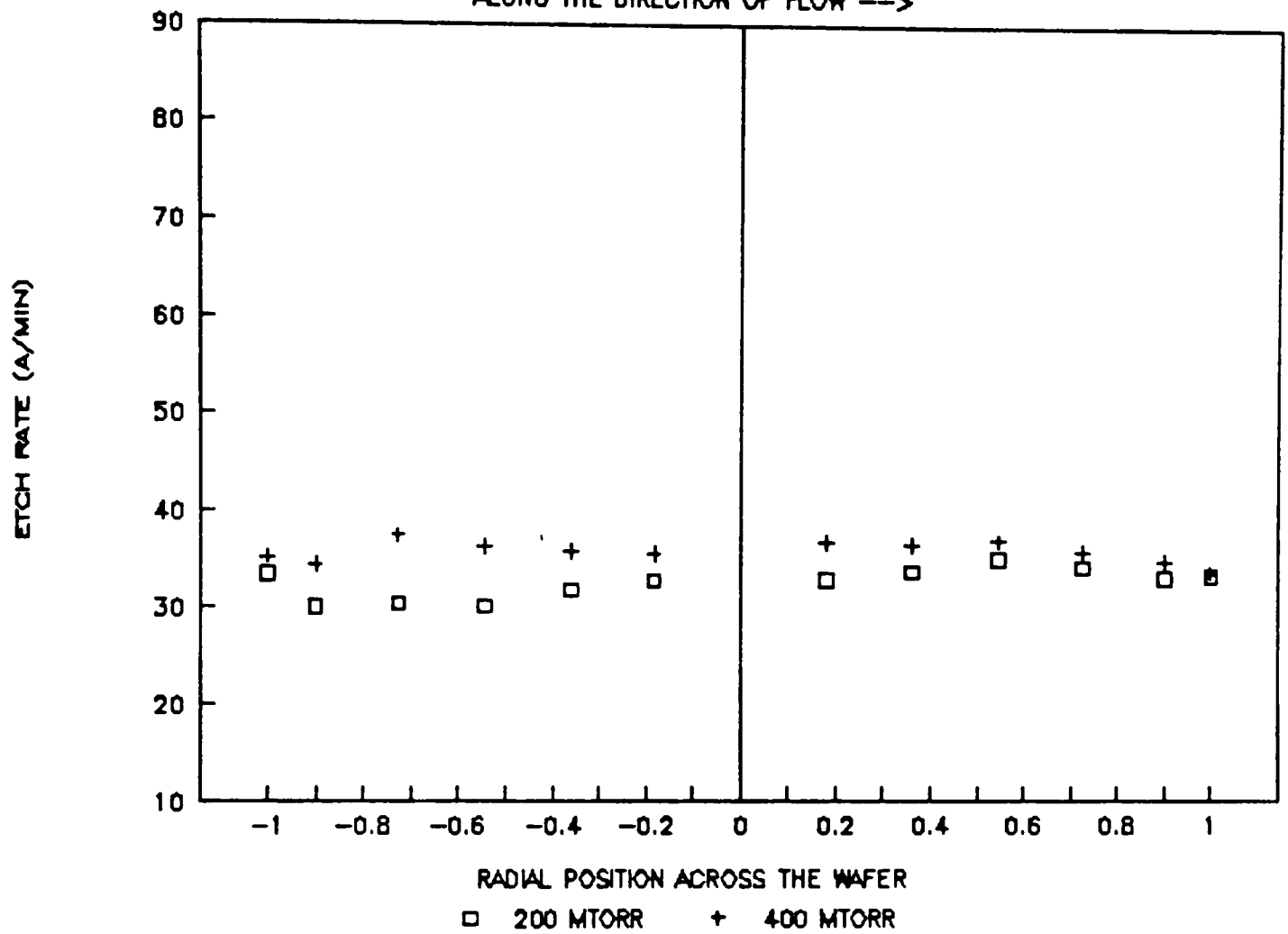
ETCH RATE DATA (300 MTORR;90 SCCM)
ALONG THE DIRECTION OF FLOW -->



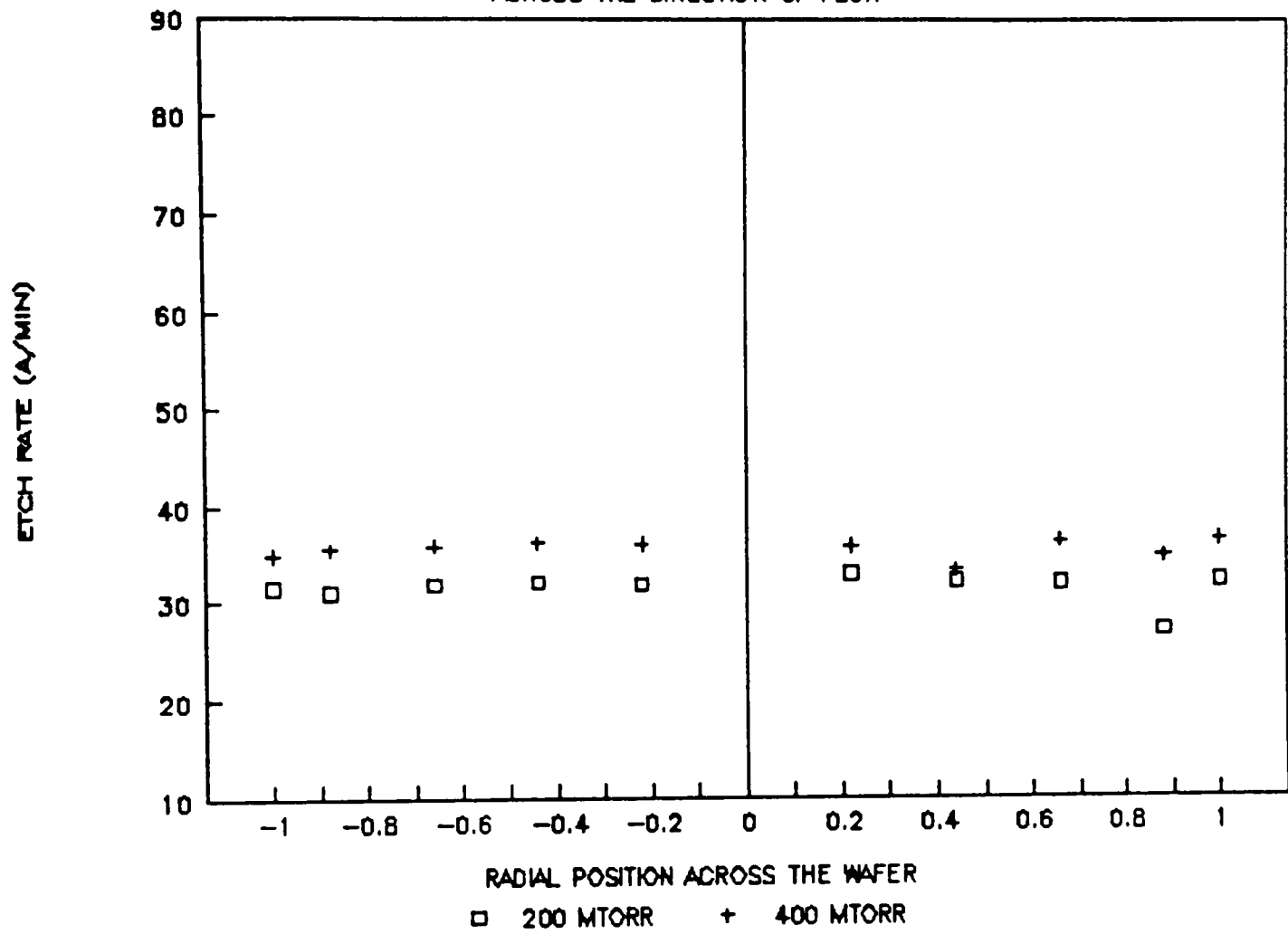
ETCH RATE DATA (300 MTORR;90 SCCM) ACROSS THE DIRECTION OF FLOW



ETCH RATE DATA (300 WATTS; 70 SCCM)
ALONG THE DIRECTION OF FLOW -->

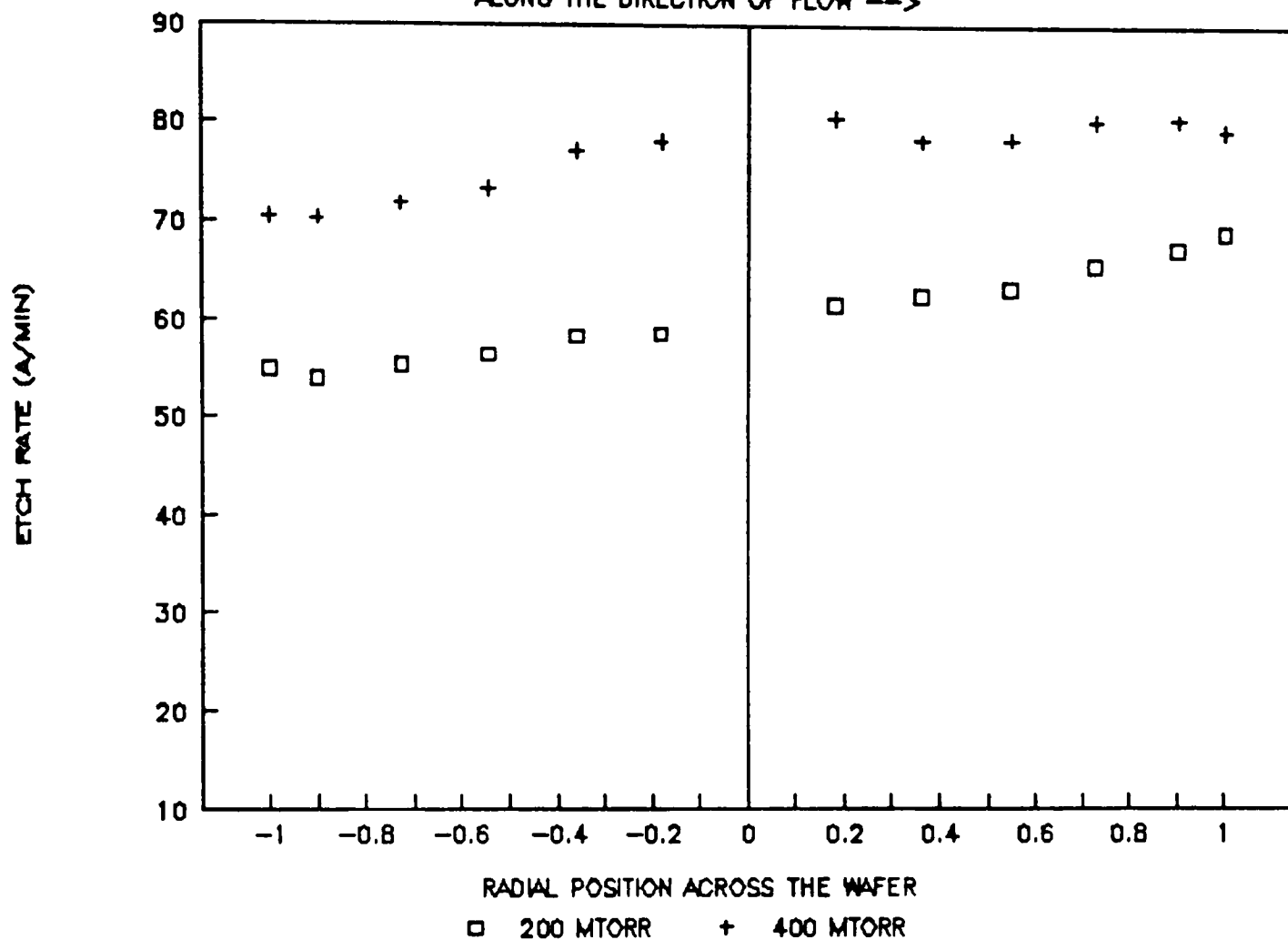


ETCH RATE DATA (300 WATTS; 70 SCCM) ACROSS THE DIRECTION OF FLOW

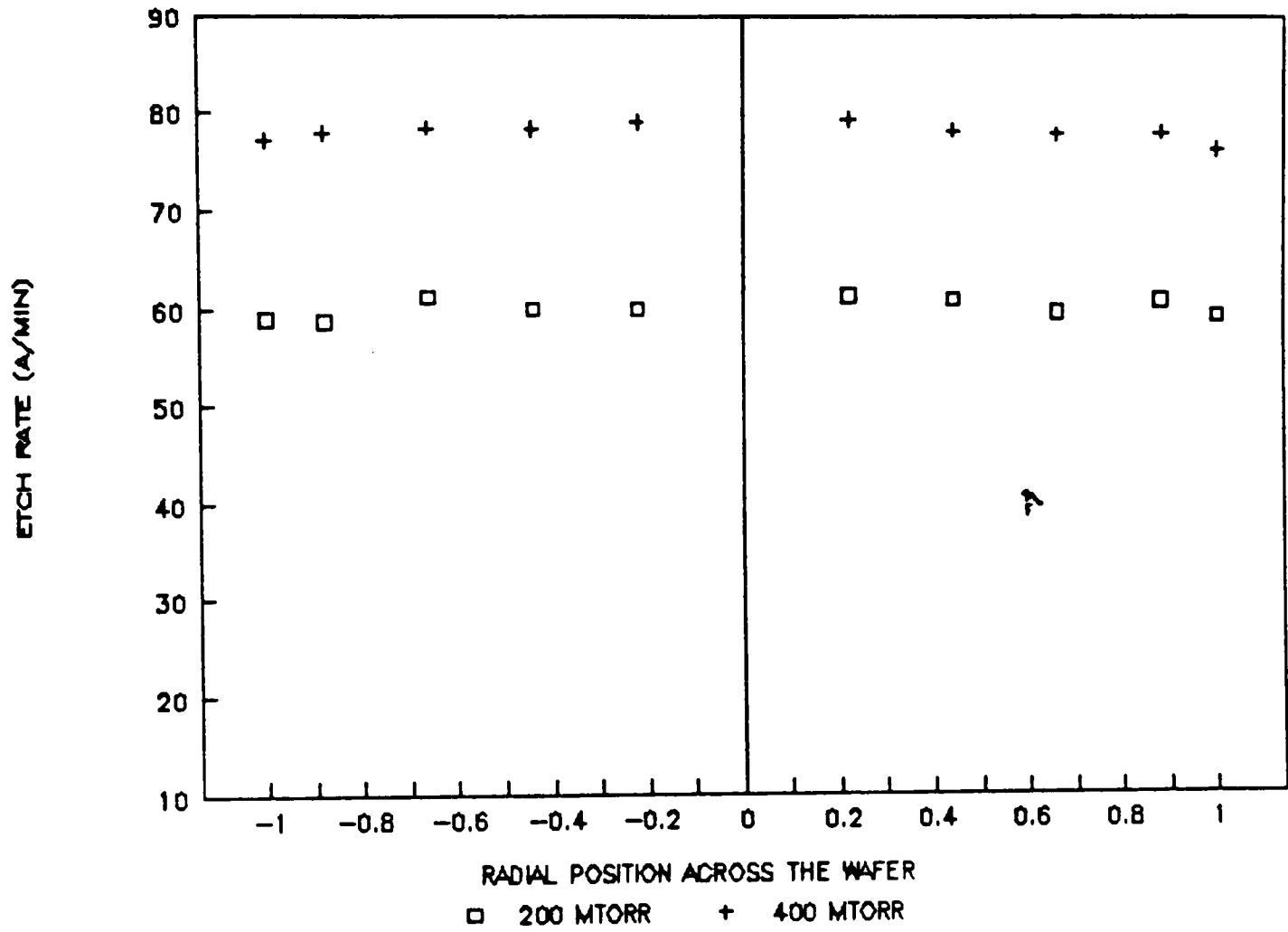


ETCH RATE DATA (700 WATTS; 70 SCCM)

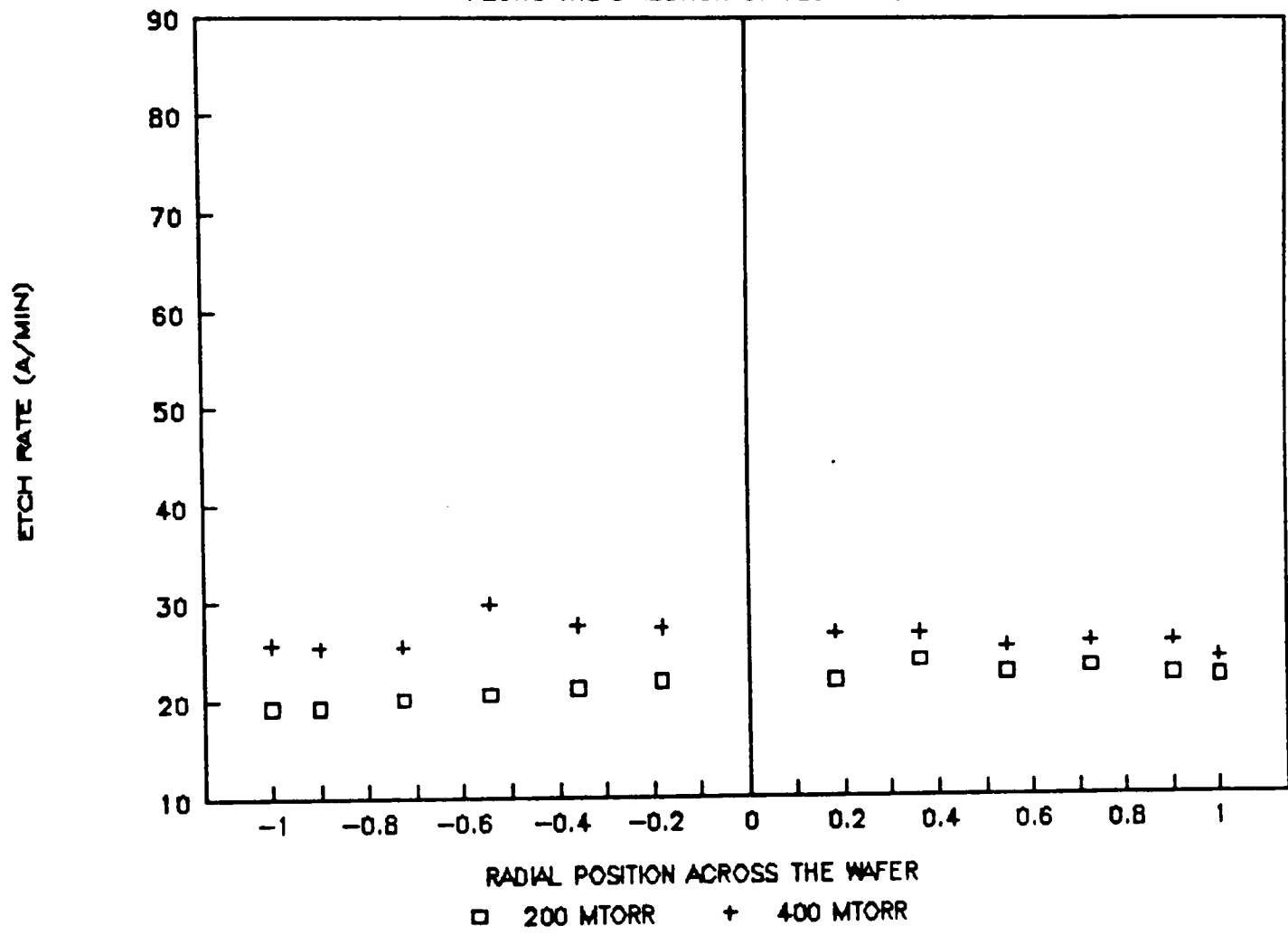
ALONG THE DIRECTION OF FLOW -->



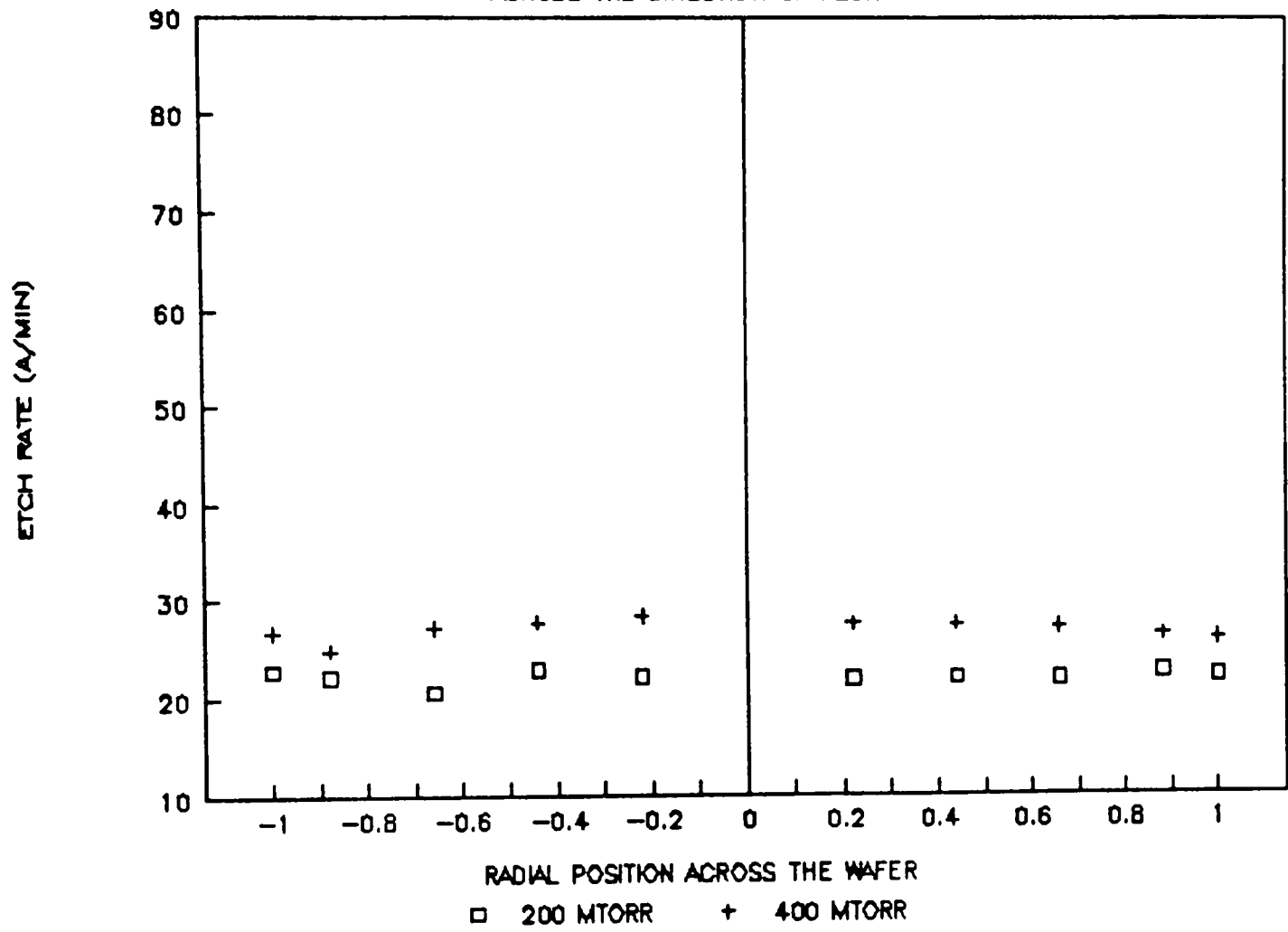
ETCH RATE DATA (700 WATTS; 70 SCCM) ACROSS THE DIRECTION OF FLOW



ETCH RATE DATA (300 WATTS; 110 SCCM)
ALONG THE DIRECTION OF FLOW -->

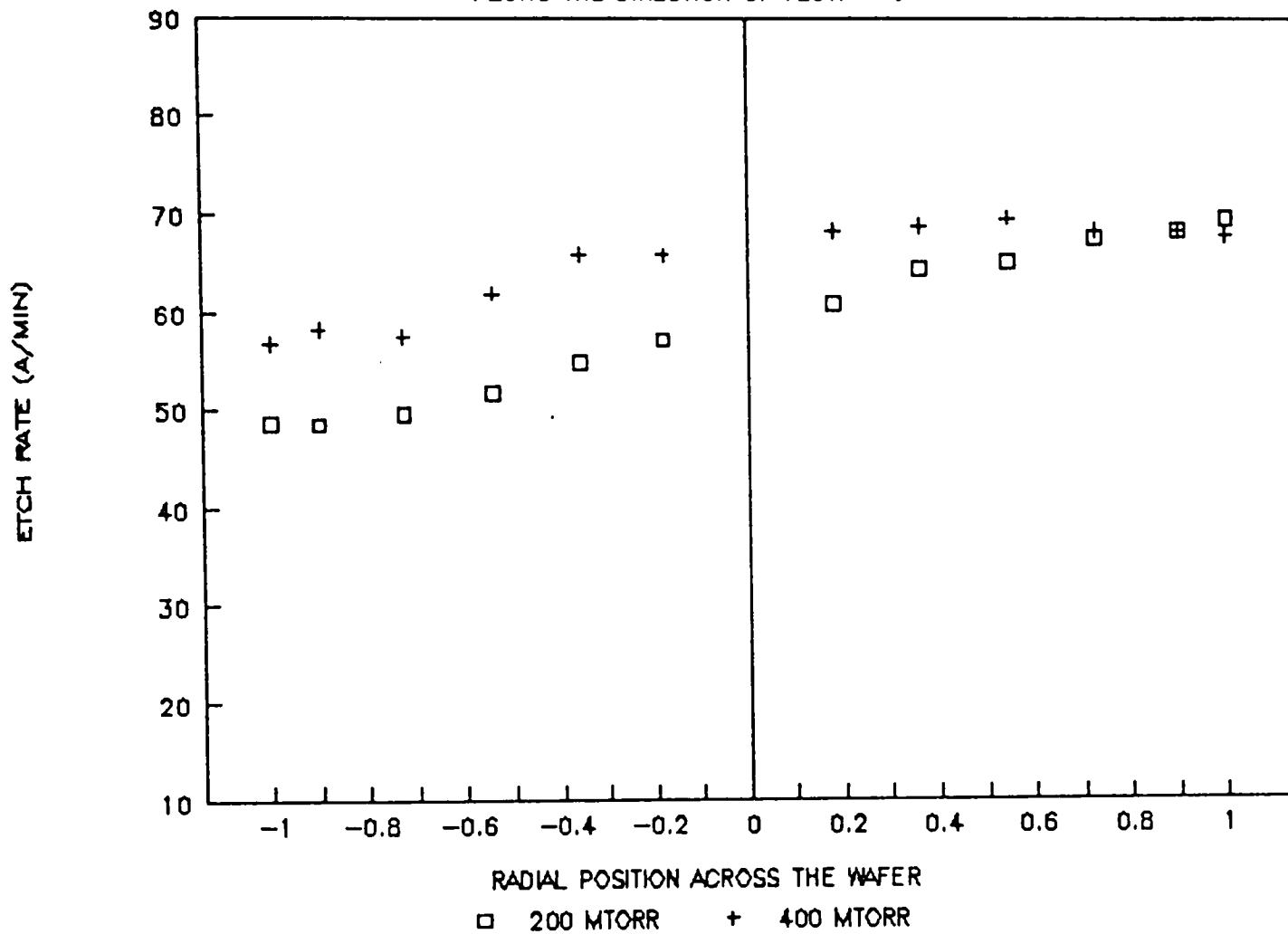


ETCH RATE DATA (300 WATTS; 110 SCCM) ACROSS THE DIRECTION OF FLOW

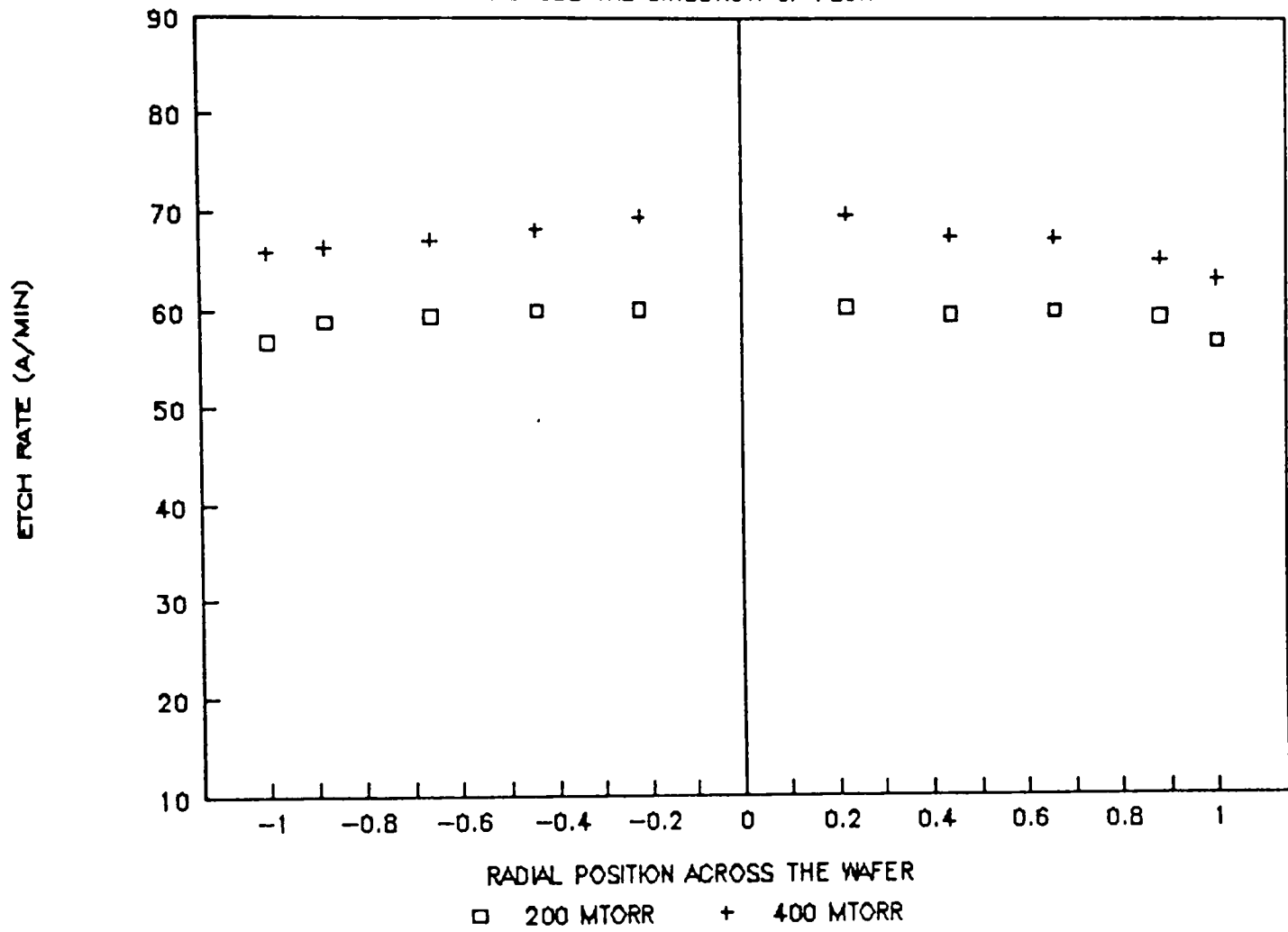


ETCH RATE DATA (700 WATTS; 110 SCCM)

ALONG THE DIRECTION OF FLOW -->

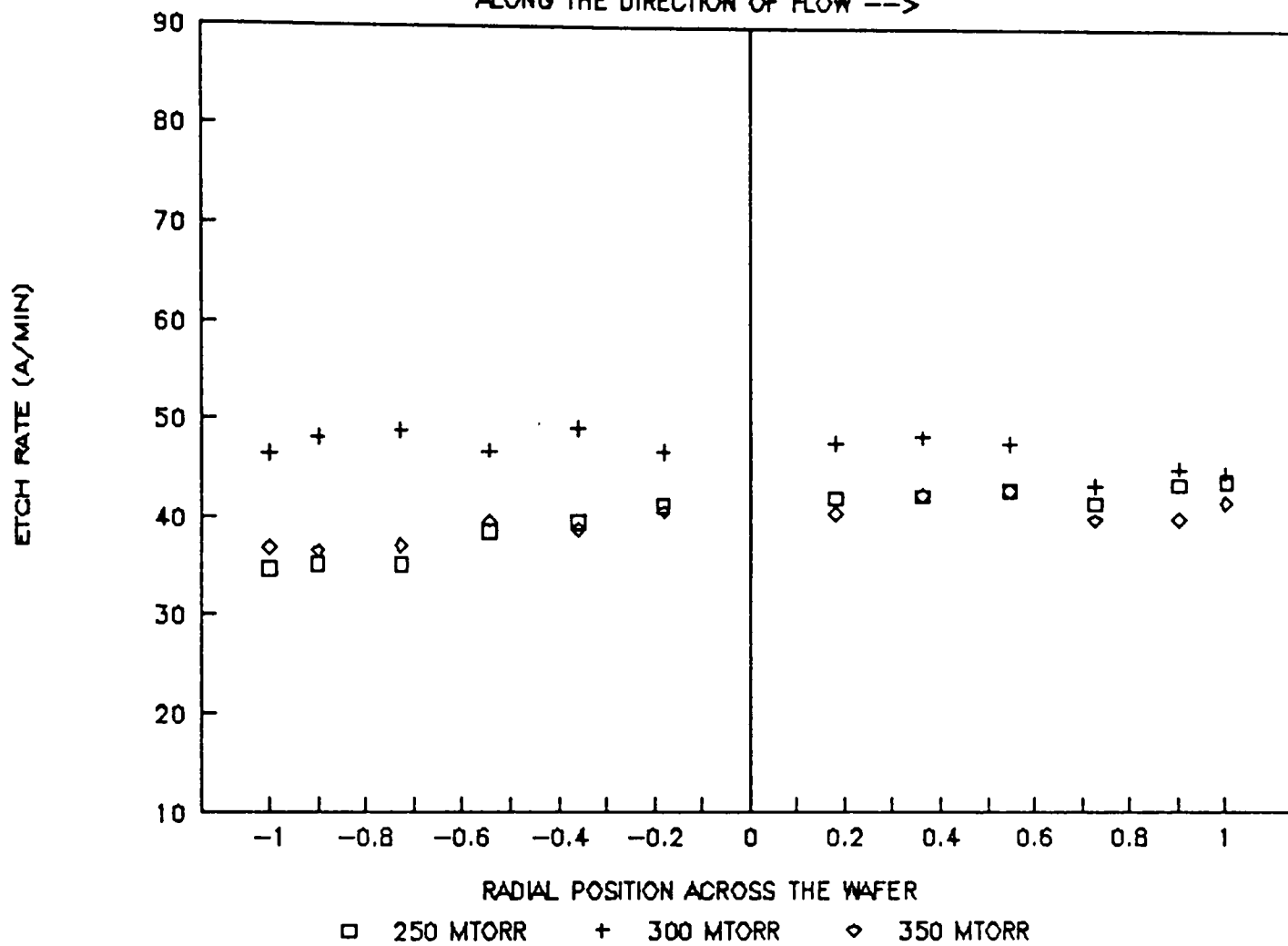


ETCH RATE DATA (700 WATTS; 110 SCCM) ACROSS THE DIRECTION OF FLOW

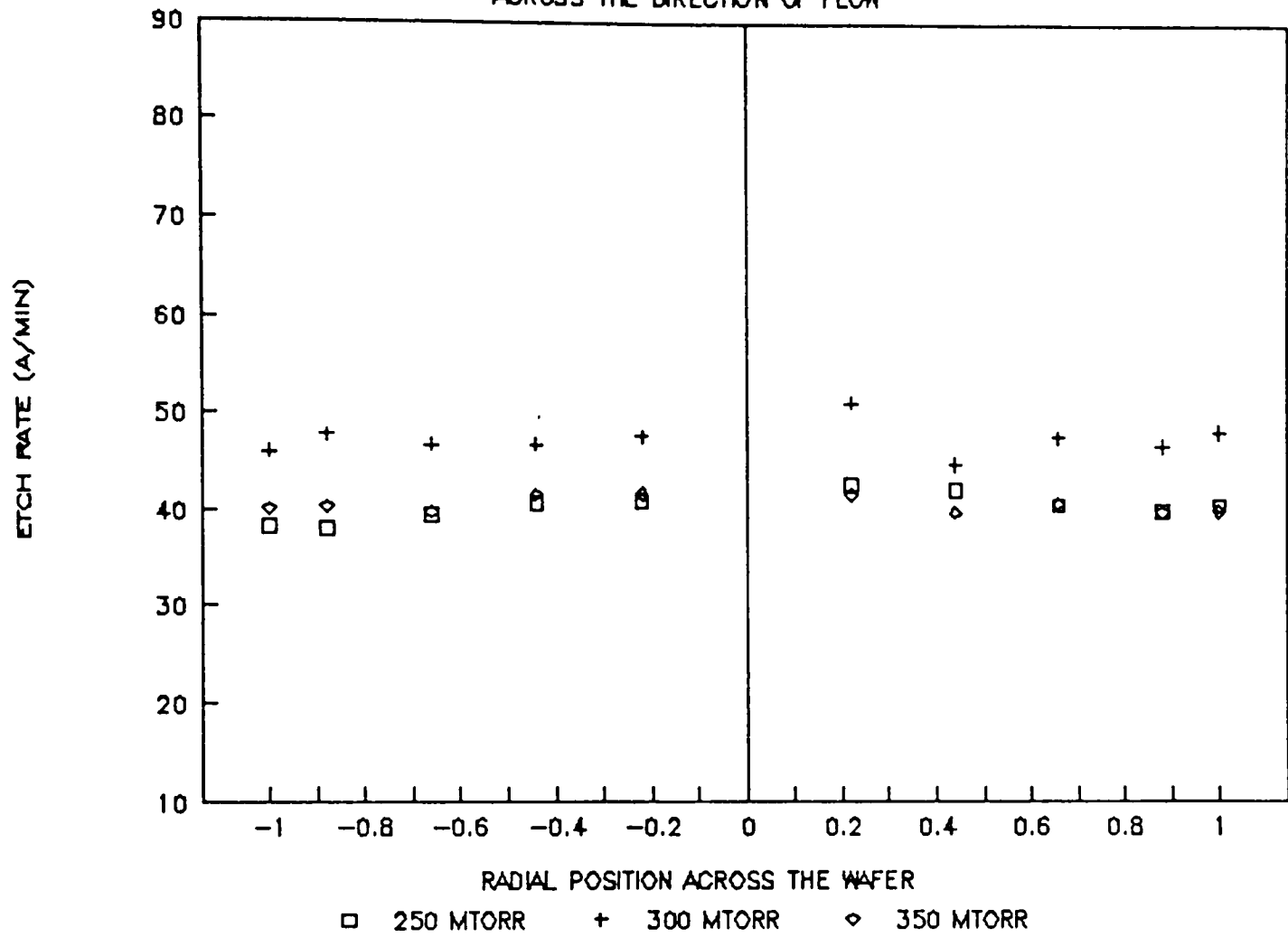


ETCH RATE DATA (500 WATTS; 90 SCCM)

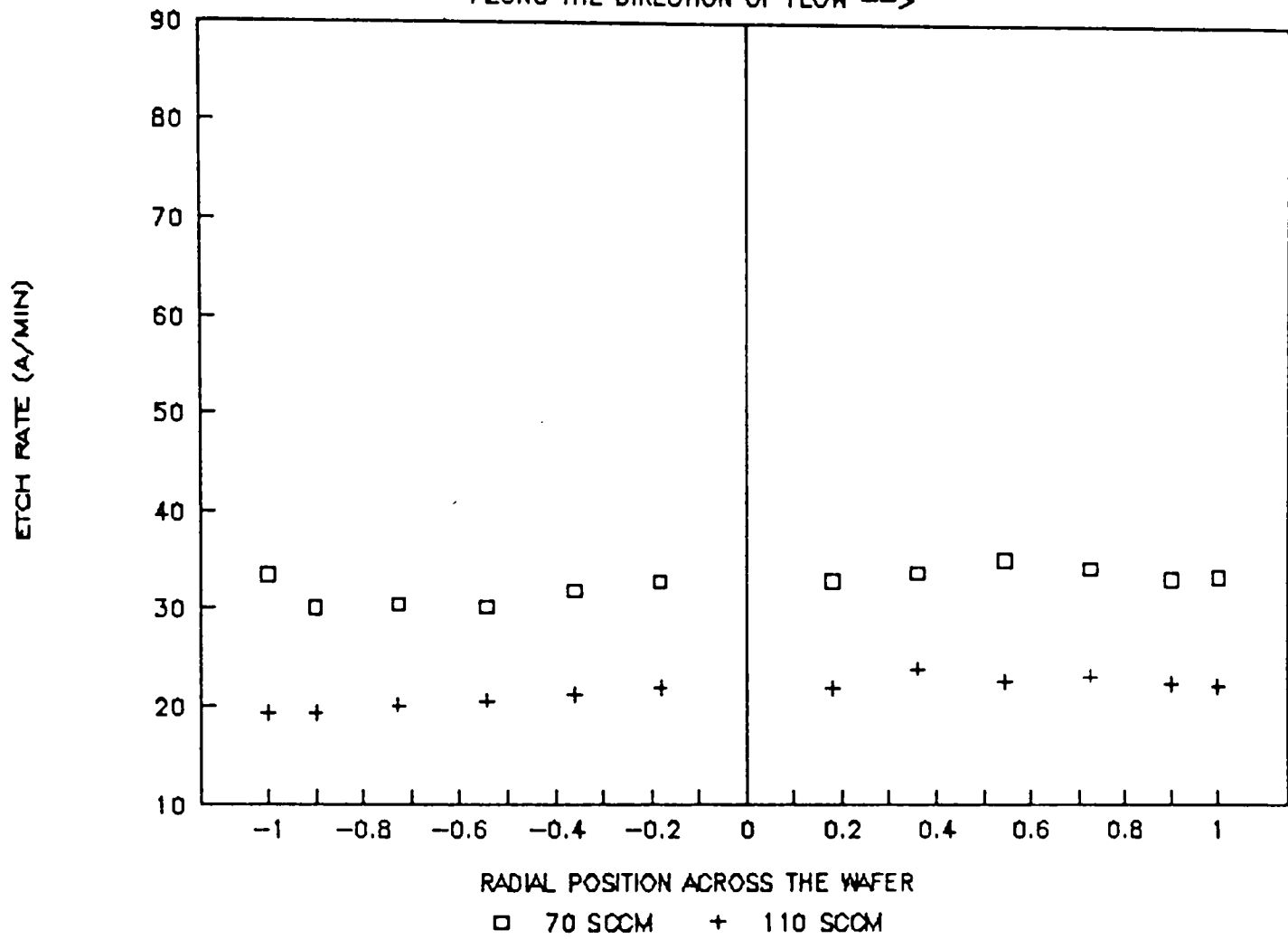
ALONG THE DIRECTION OF FLOW -->



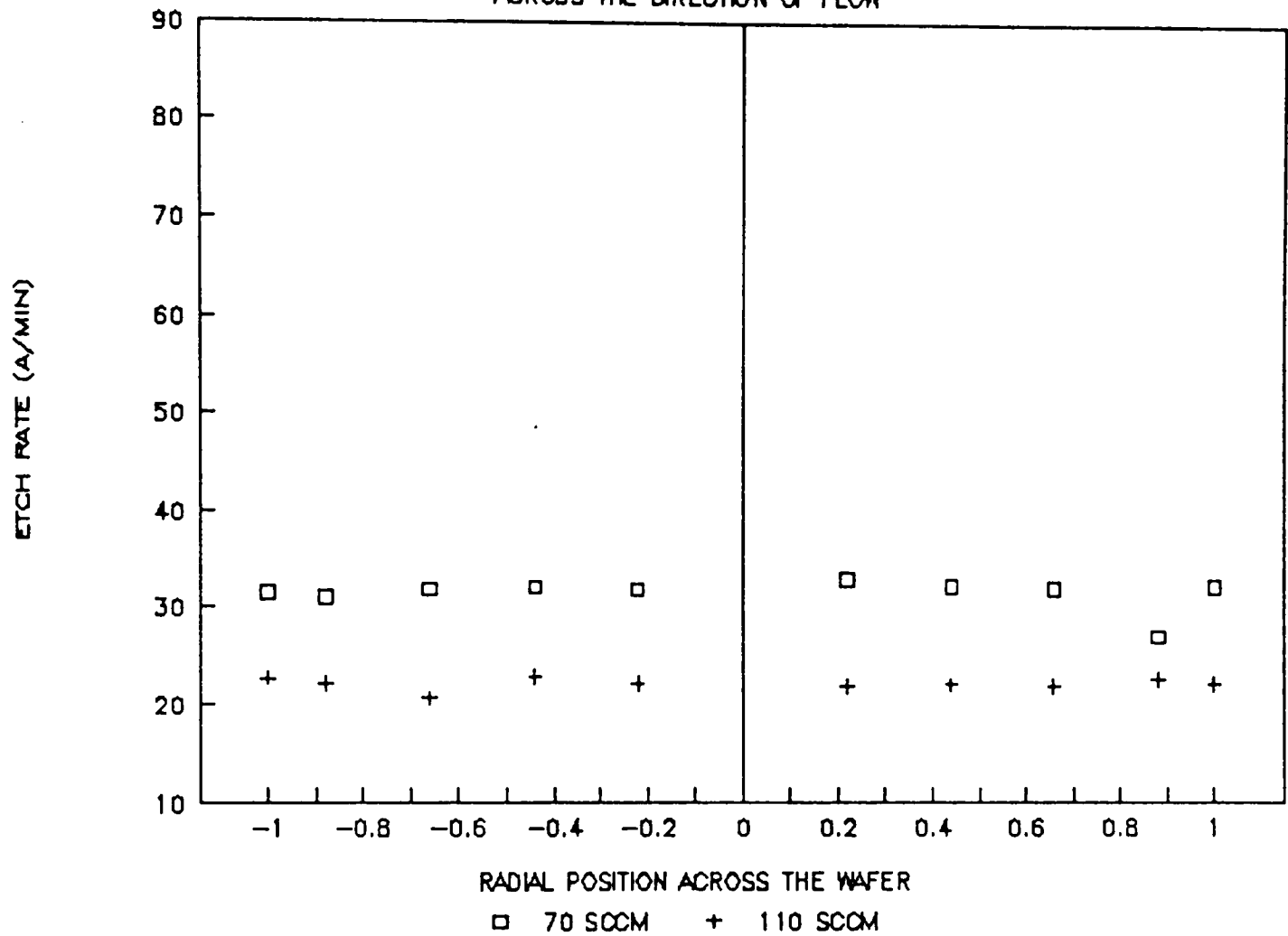
ETCH RATE DATA (500 WATTS; 90 SCCM) ACROSS THE DIRECTION OF FLOW



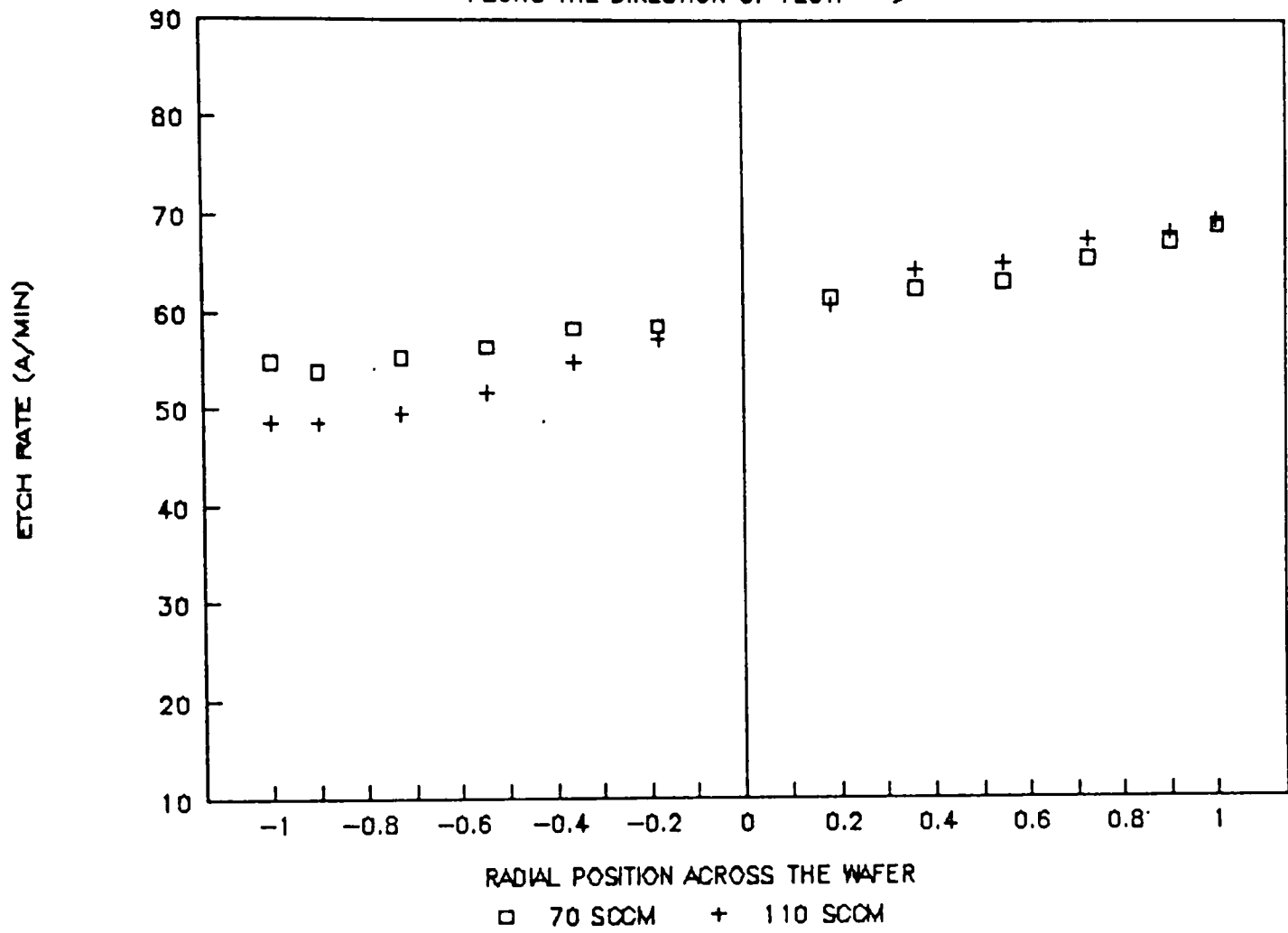
ETCH RATE DATA (300 WATTS; 200 MTORR) ALONG THE DIRECTION OF FLOW -->



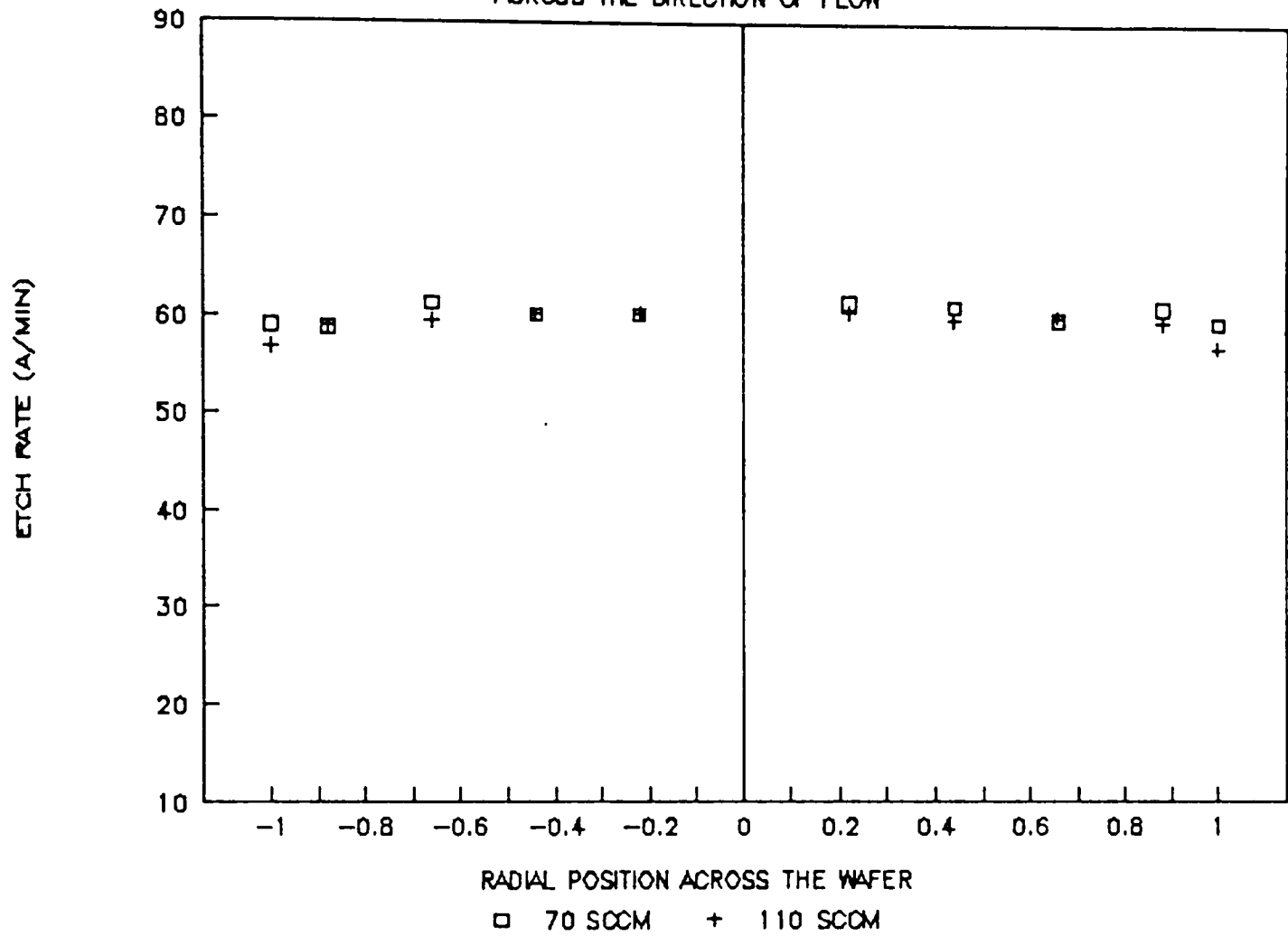
ETCH RATE DATA (300 WATTS; 200 MTORR)
ACROSS THE DIRECTION OF FLOW



ETCH RATE DATA (700 WATTS; 200 MTORR)
ALONG THE DIRECTION OF FLOW -->

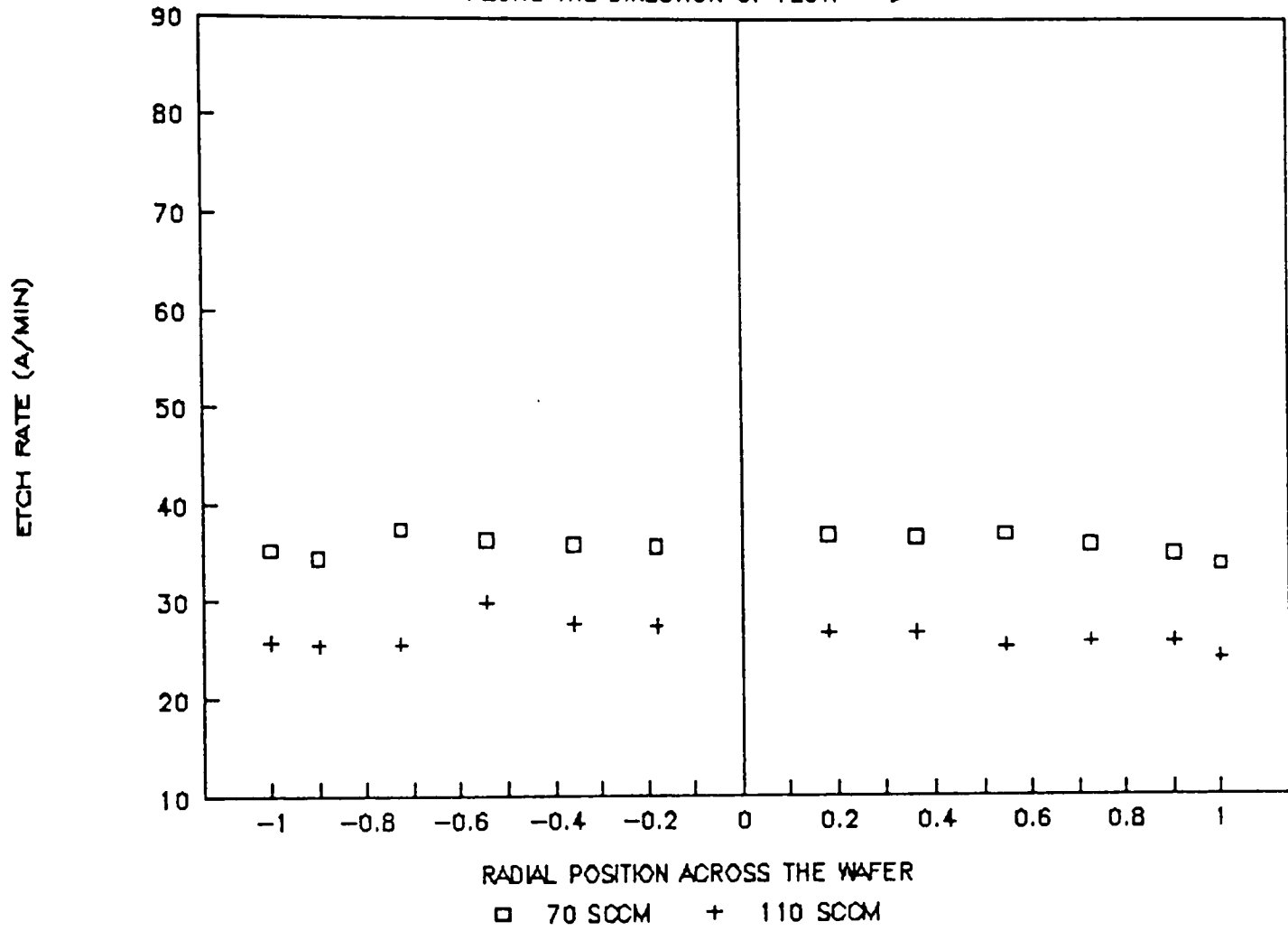


ETCH RATE DATA (700 WATTS; 200 MTORR) ACROSS THE DIRECTION OF FLOW

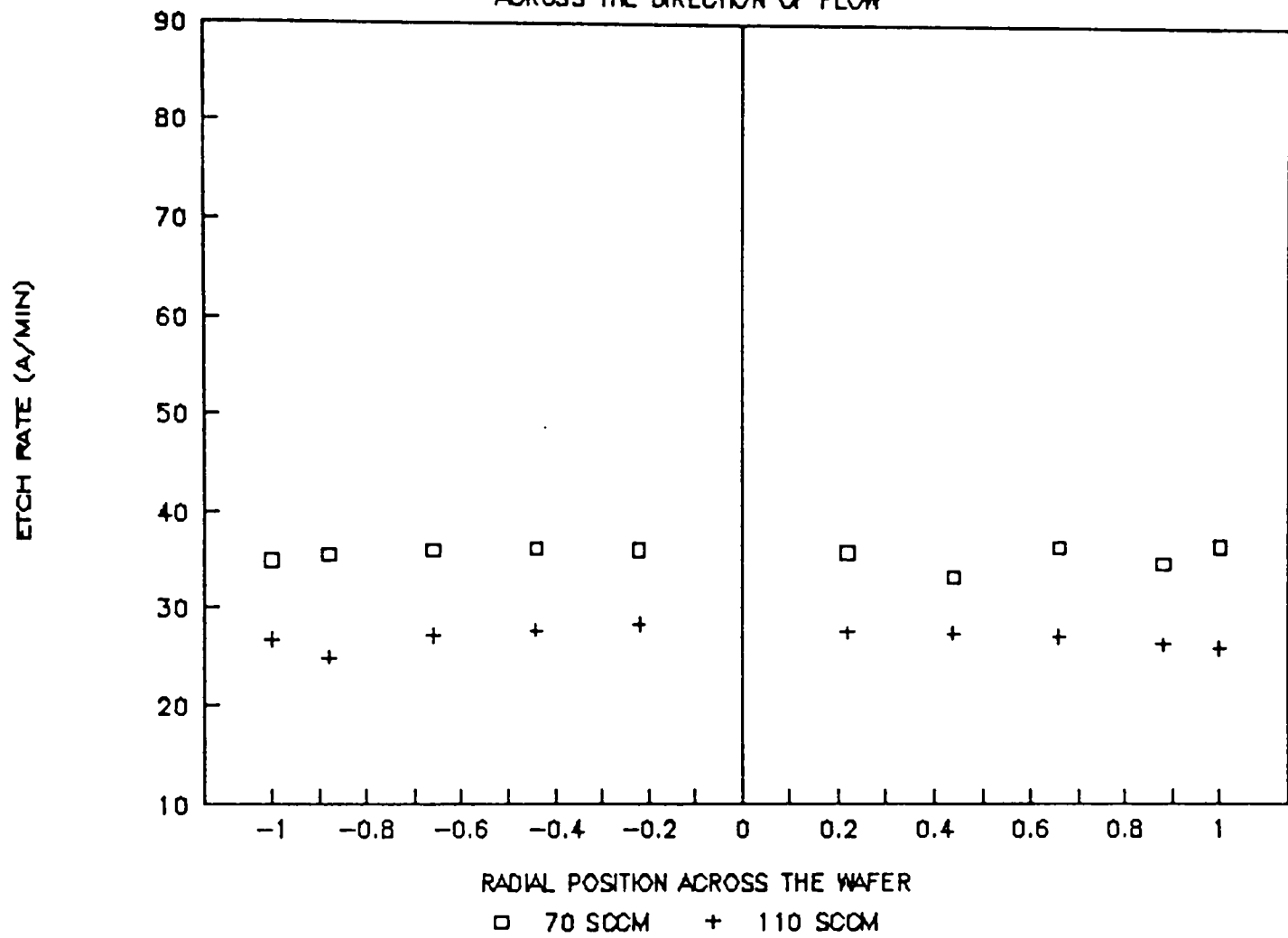


ETCH RATE DATA (400 WATTS; 300 MTORR)

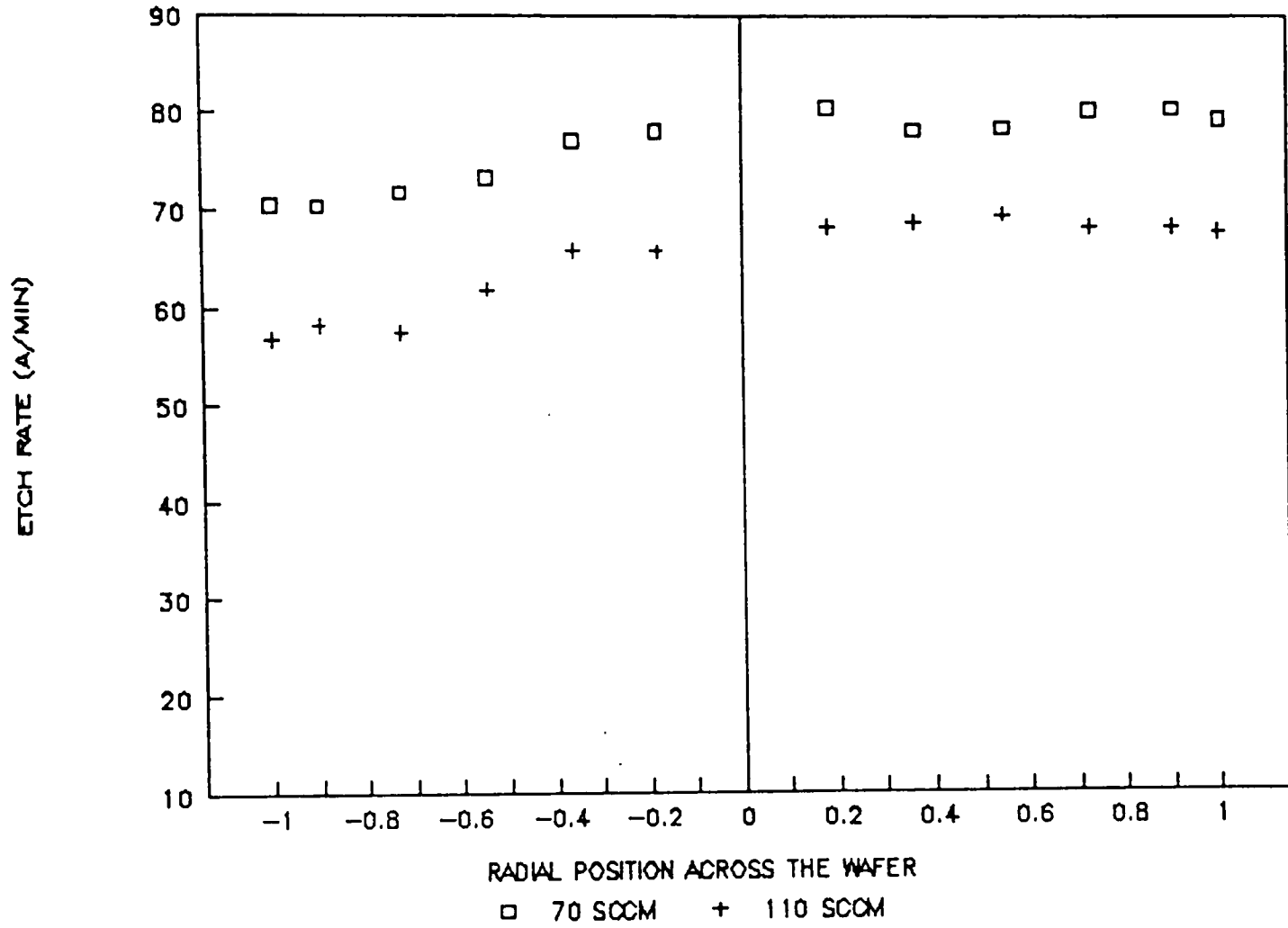
ALONG THE DIRECTION OF FLOW -->



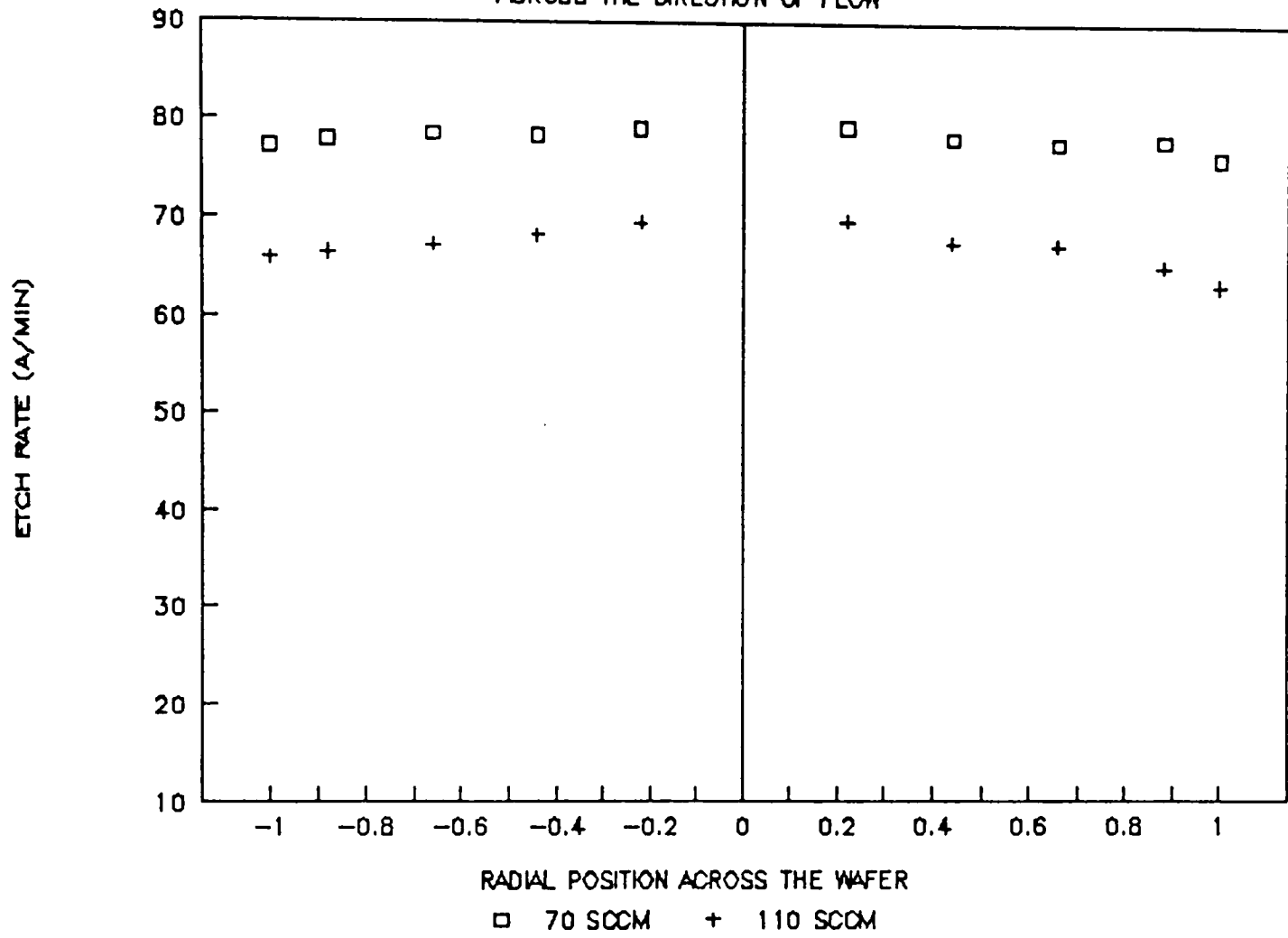
ETCH RATE DATA (400 WATTS; 300 MTORR) ACROSS THE DIRECTION OF FLOW



ETCH RATE DATA (700 WATTS; 400 MTORR)
ALONG THE DIRECTION OF FLOW -->

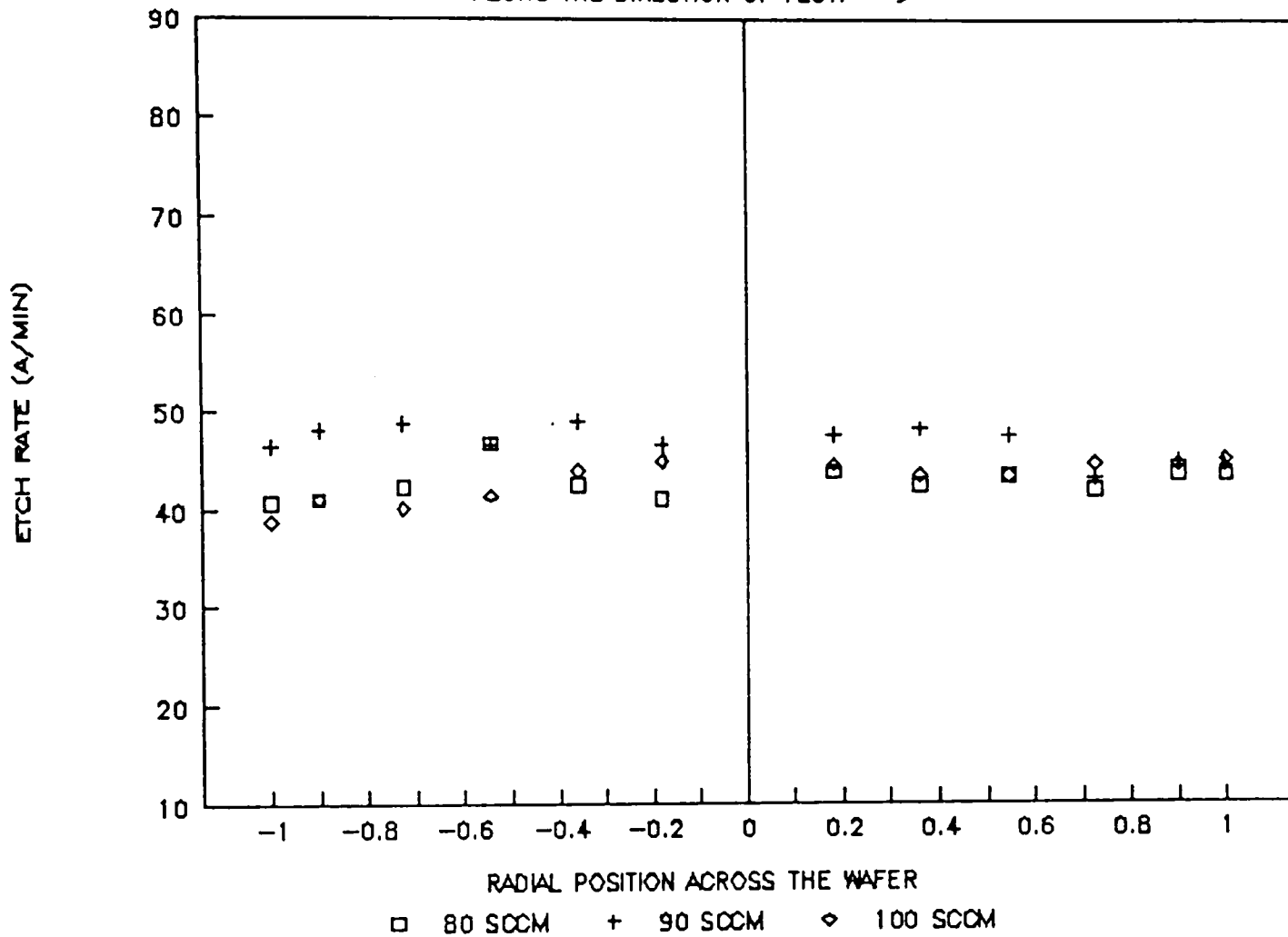


ETCH RATE DATA (700 WATTS; 400 MTORR) ACROSS THE DIRECTION OF FLOW

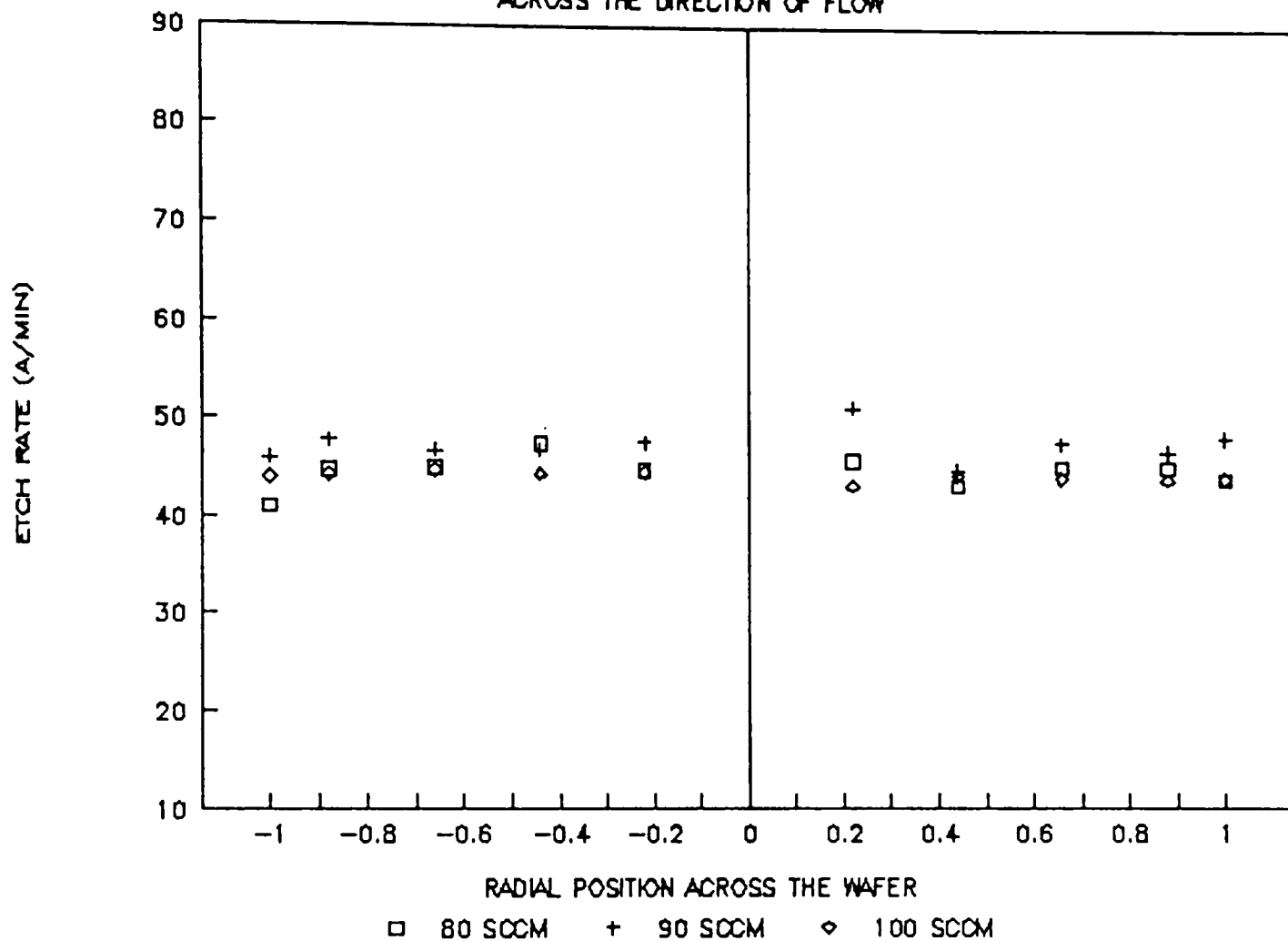


ETCH RATE DATA (500 WATTS; 300 MTORR)

ALONG THE DIRECTION OF FLOW -->

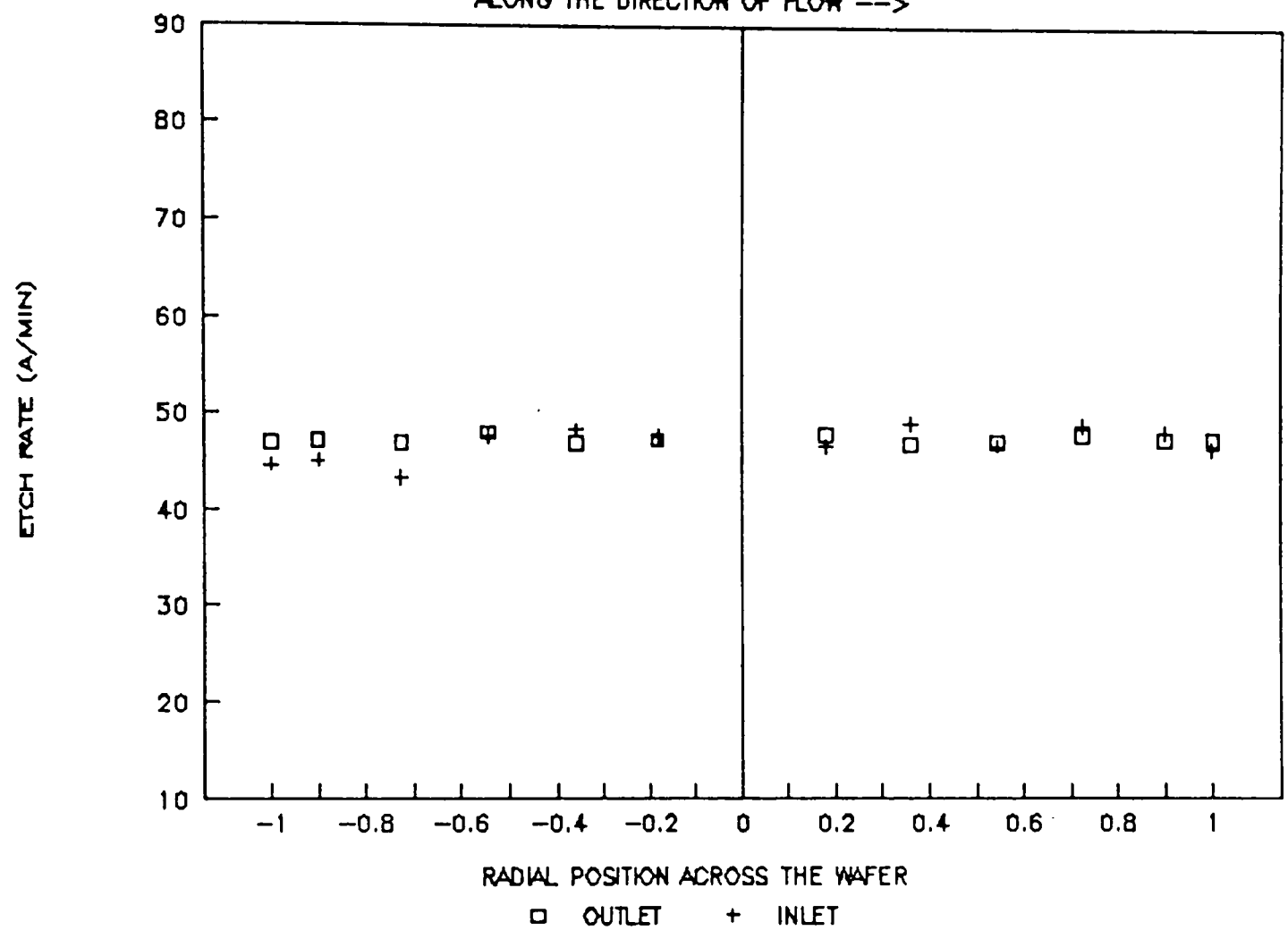


ETCH RATE DATA (500 WATTS; 300 MTORR) ACROSS THE DIRECTION OF FLOW

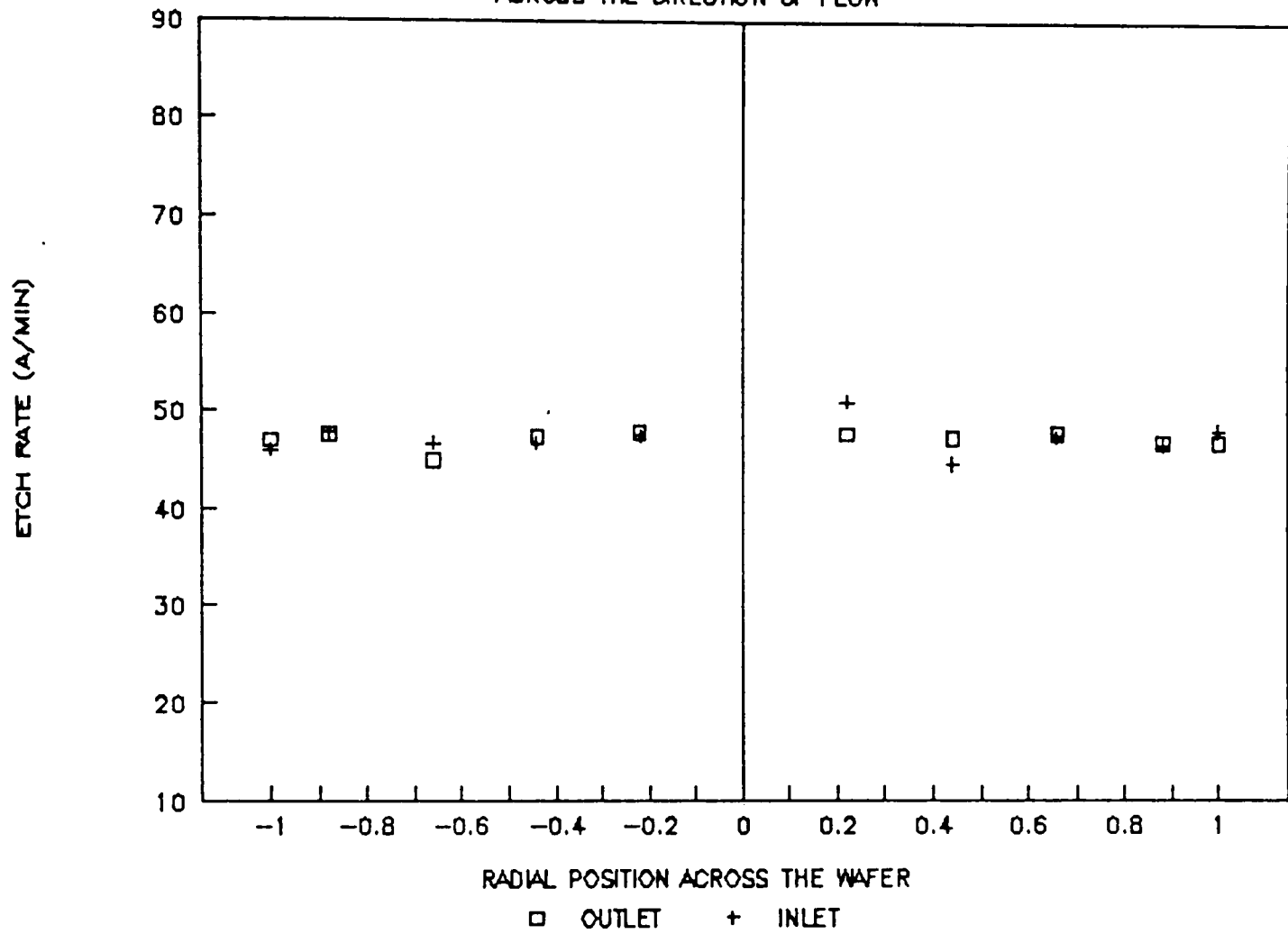


ETCH RATE DATA (500 PO;300 PR;90 FL)

ALONG THE DIRECTION OF FLOW -->



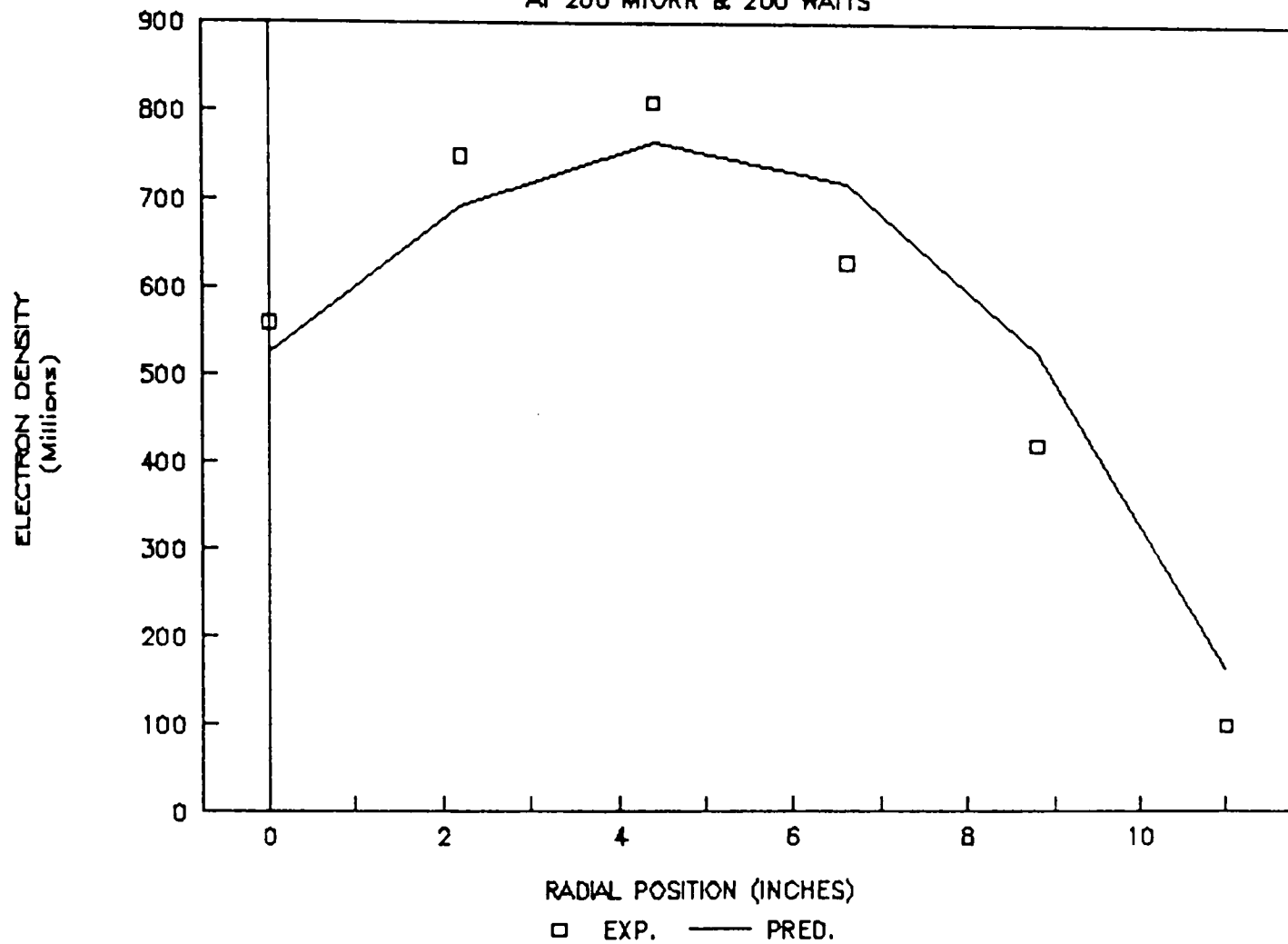
ETCH RATE DATA (500 PO;300 PR;90 FL)
ACROSS THE DIRECTION OF FLOW



APPENDIX K
MODEL VALIDATION RUNS

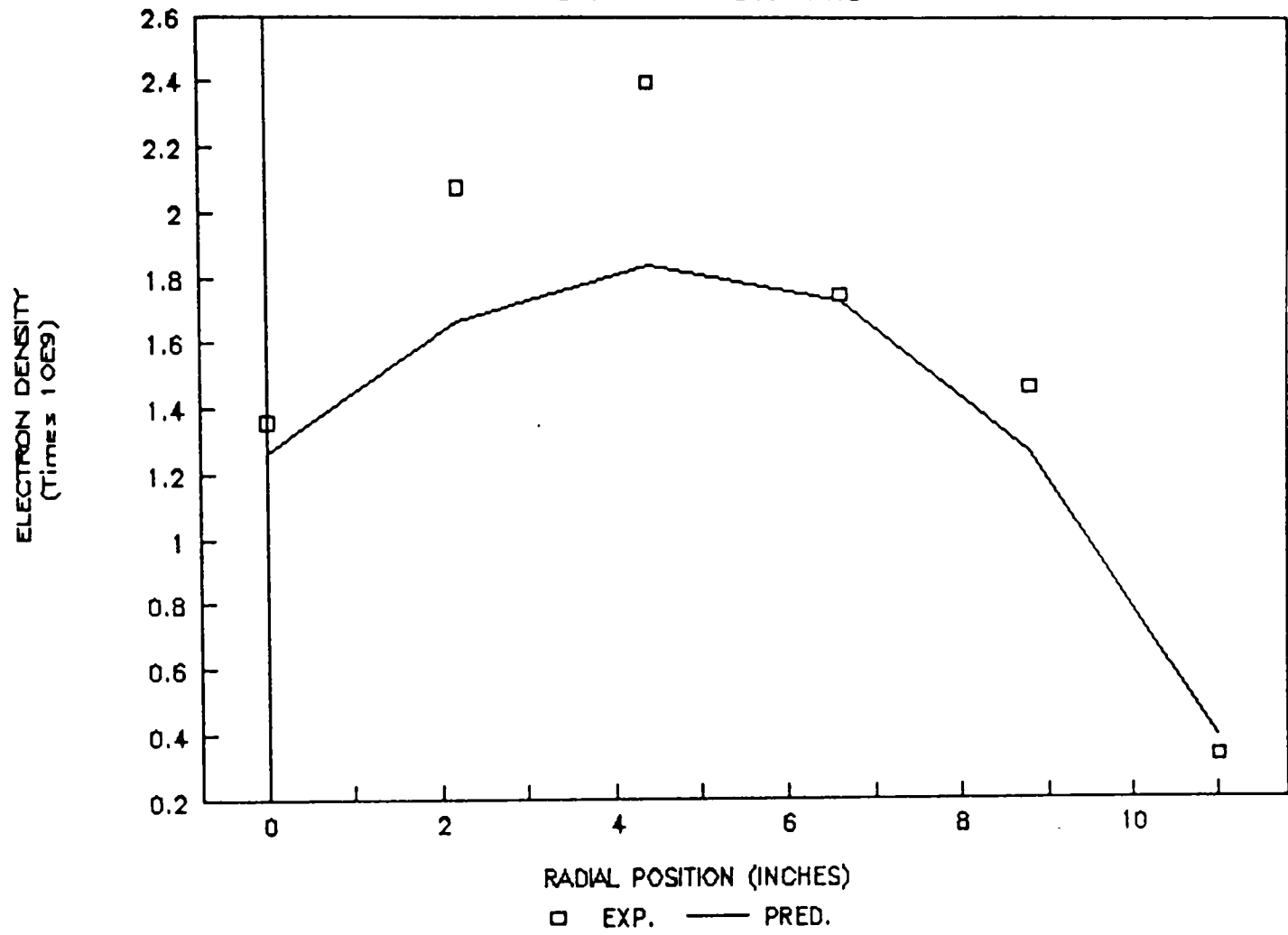
ELECTRON DENSITY VS. RADIAL POSITION

AT 200 MTORR & 200 WATTS



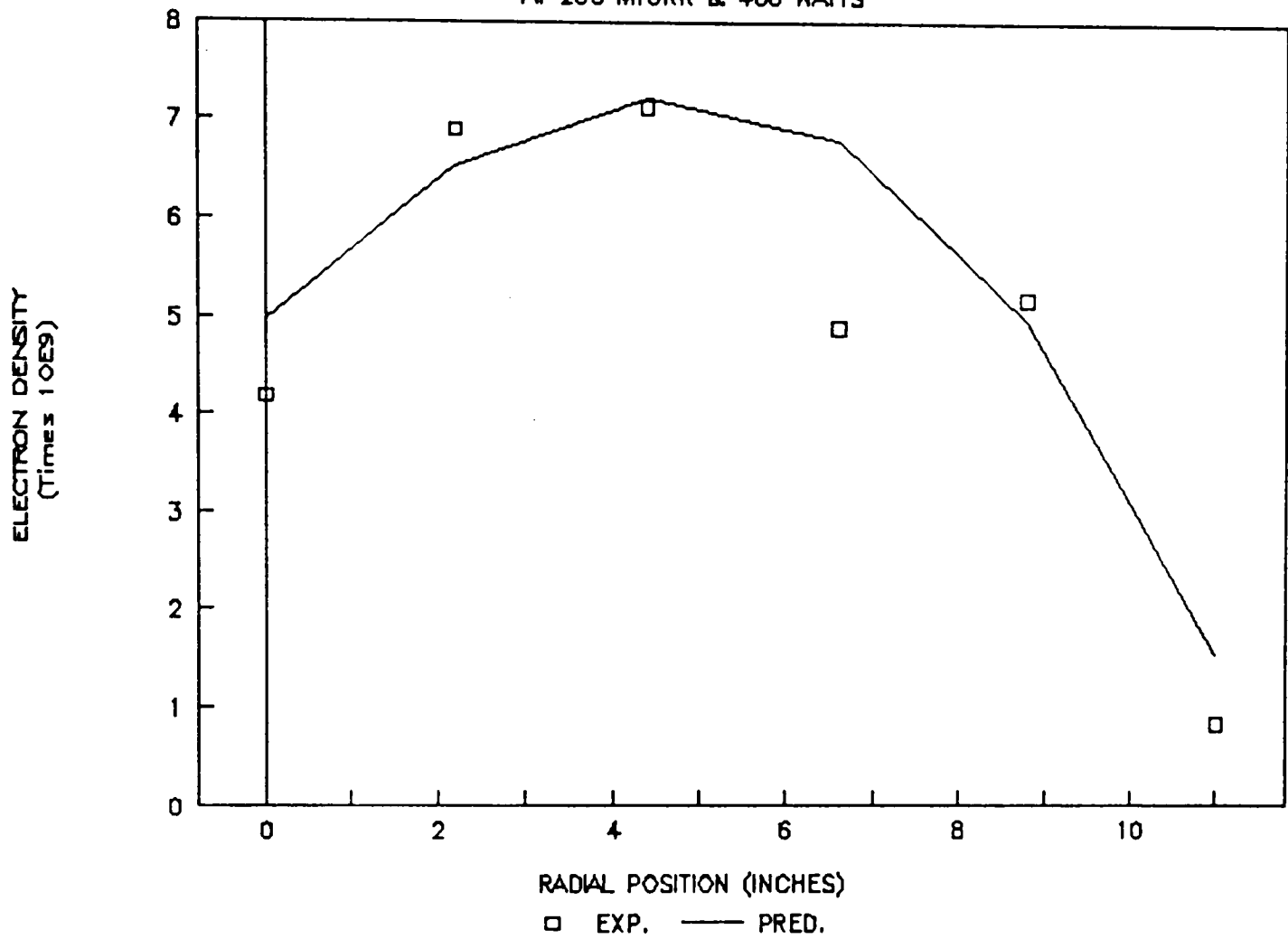
ELECTRON DENSITY VS. RADIAL POSITION

AT 200 MTORR & 300 WATTS



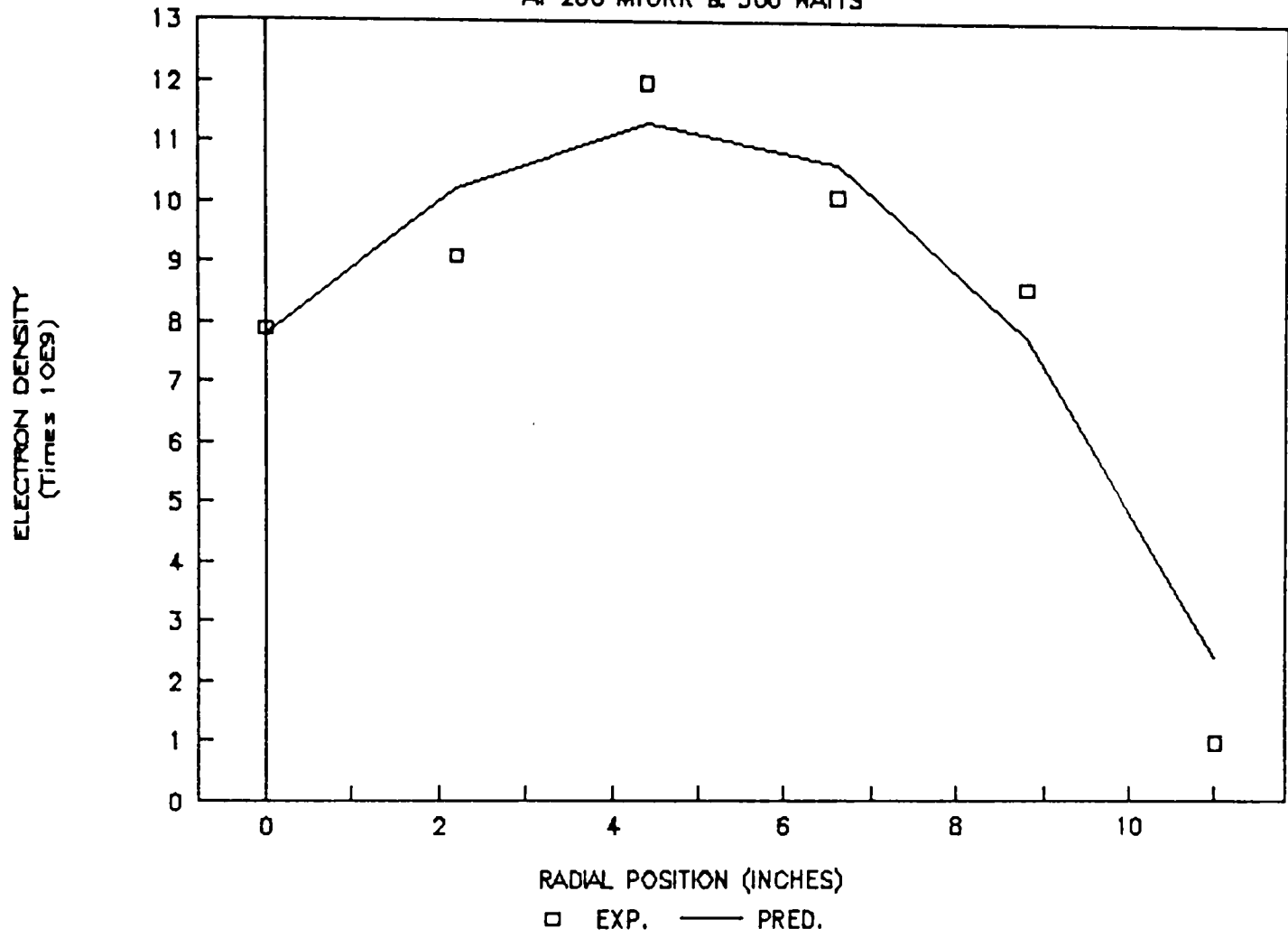
ELECTRON DENSITY VS. RADIAL POSITION

AT 200 MTORR & 400 WATTS



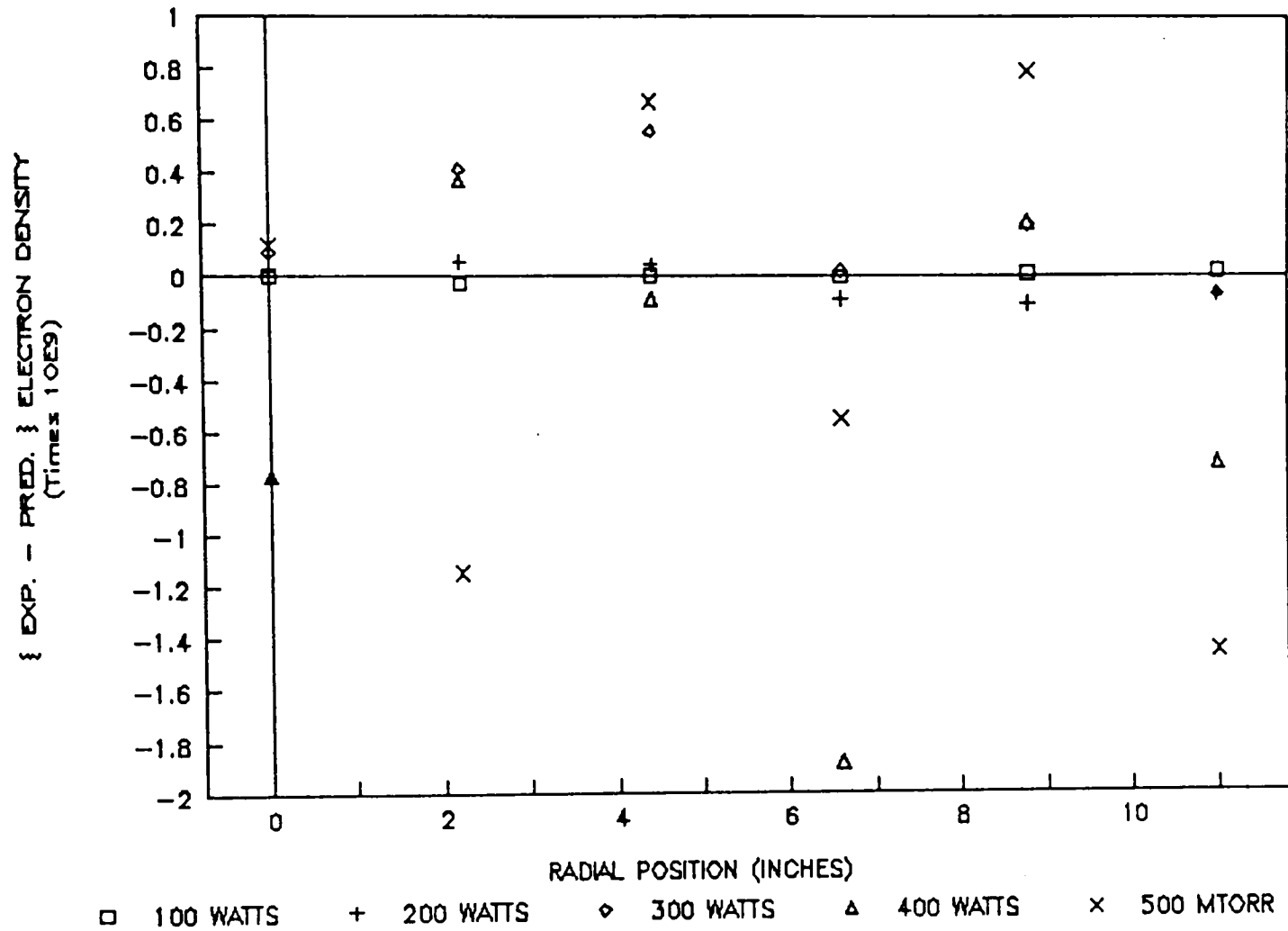
ELECTRON DENSITY VS. RADIAL POSITION

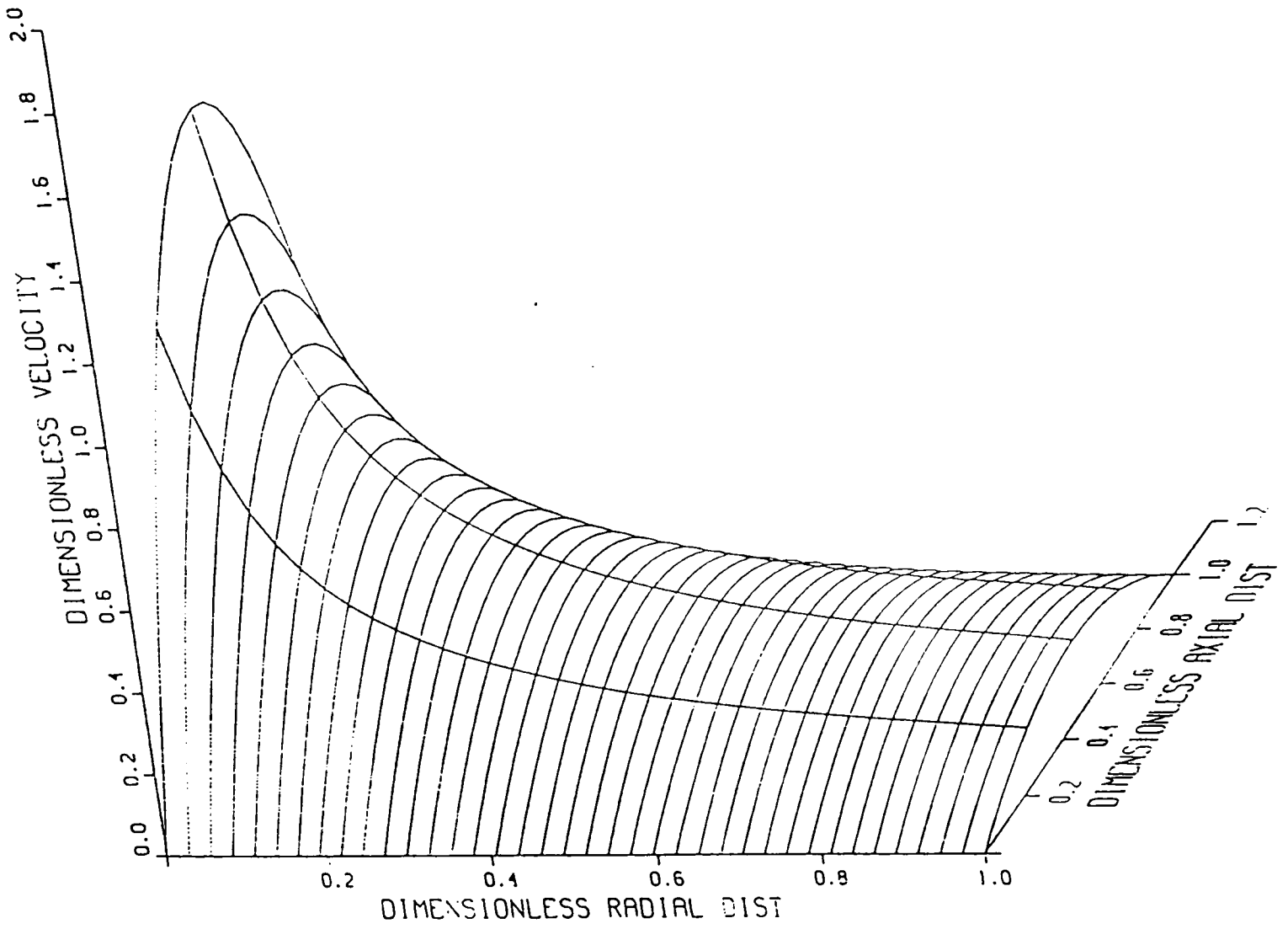
AT 200 MTORR & 500 WATTS



(EXP.-PRED.) [EL] VS. RADIAL POSITION

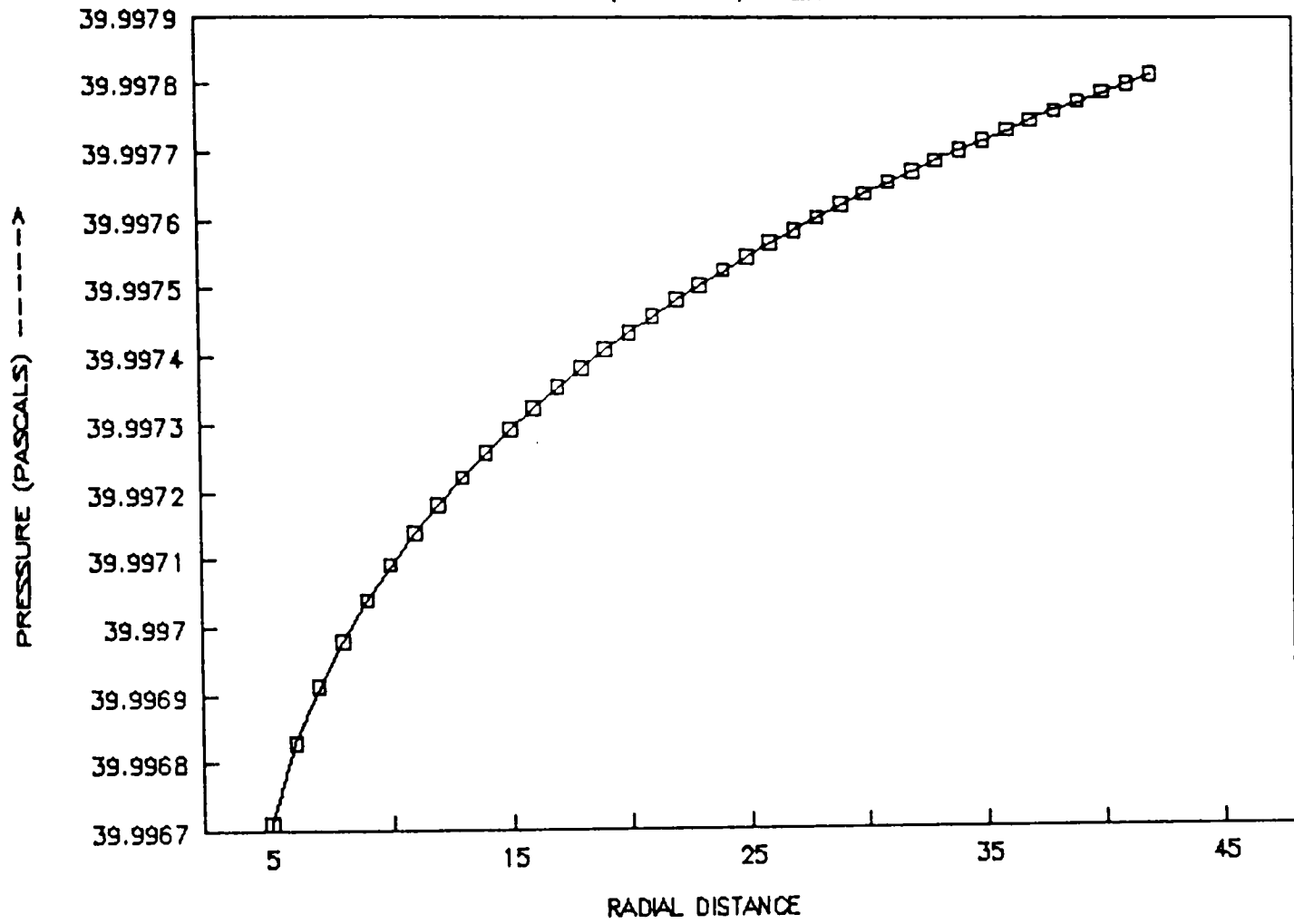
PRESSURE=200 MTORR

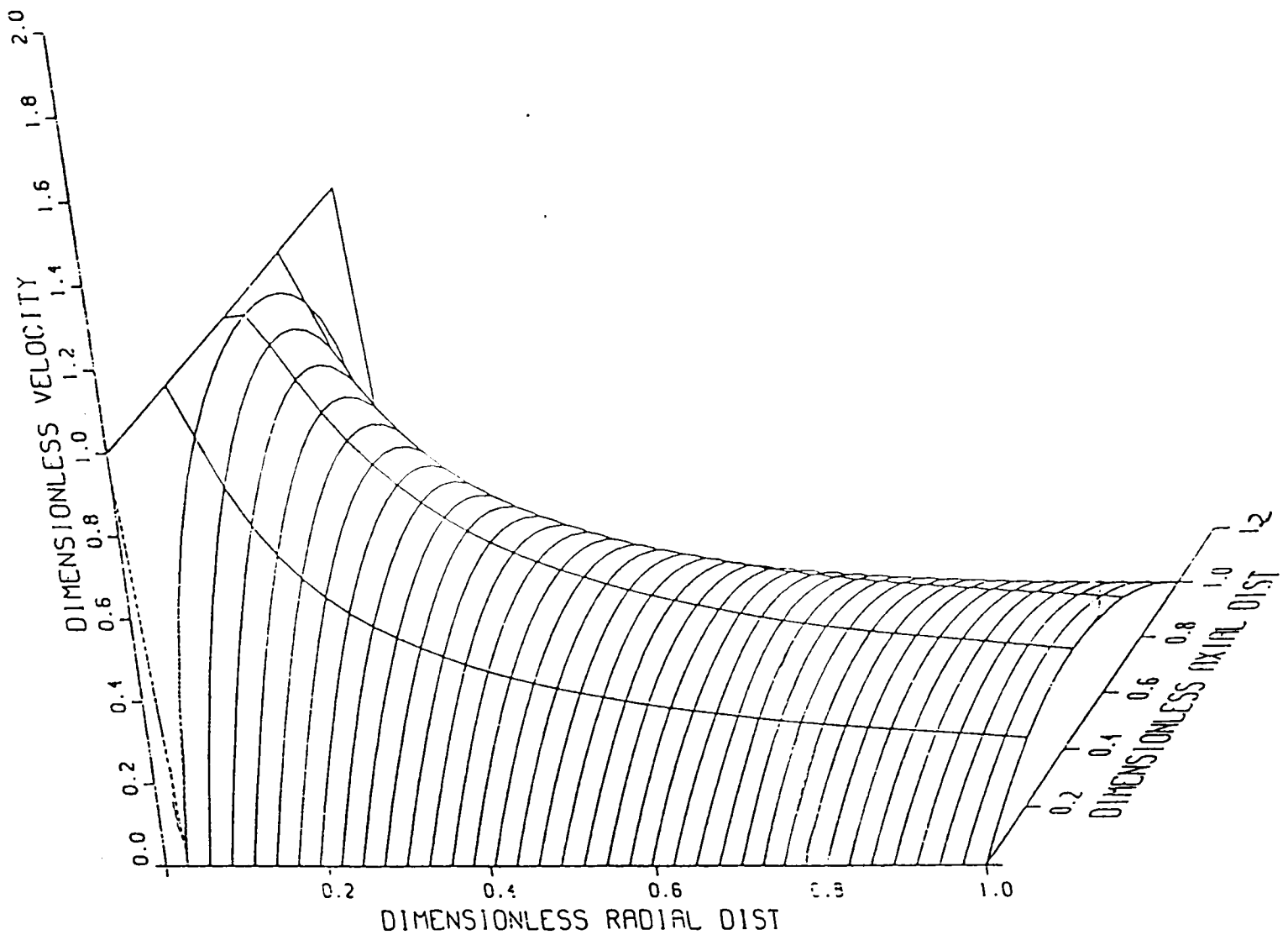




P (PASCALS) VS RADIAL DISTANCE

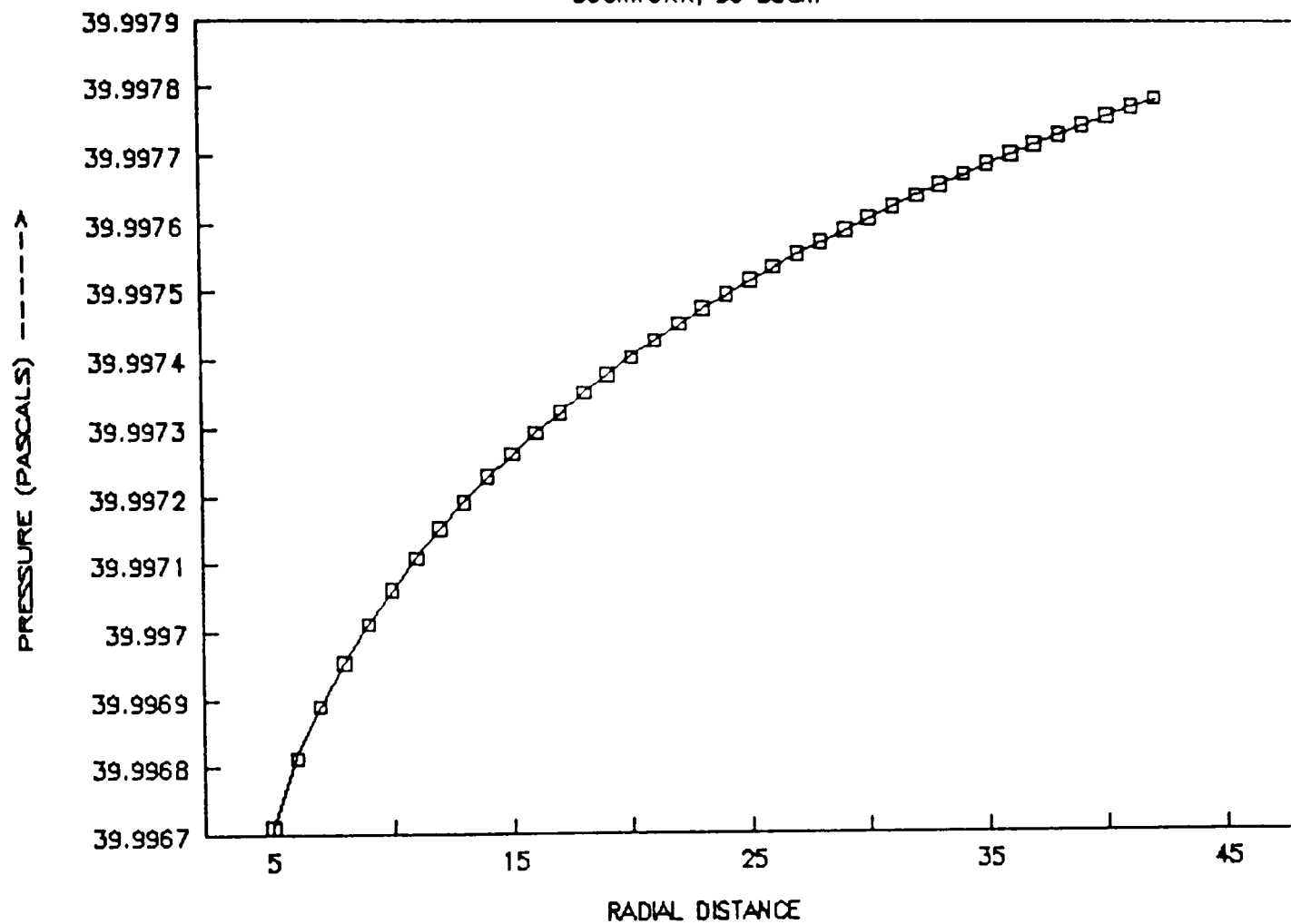
300MTORR; 90 SCCM; OUTLET PLUG

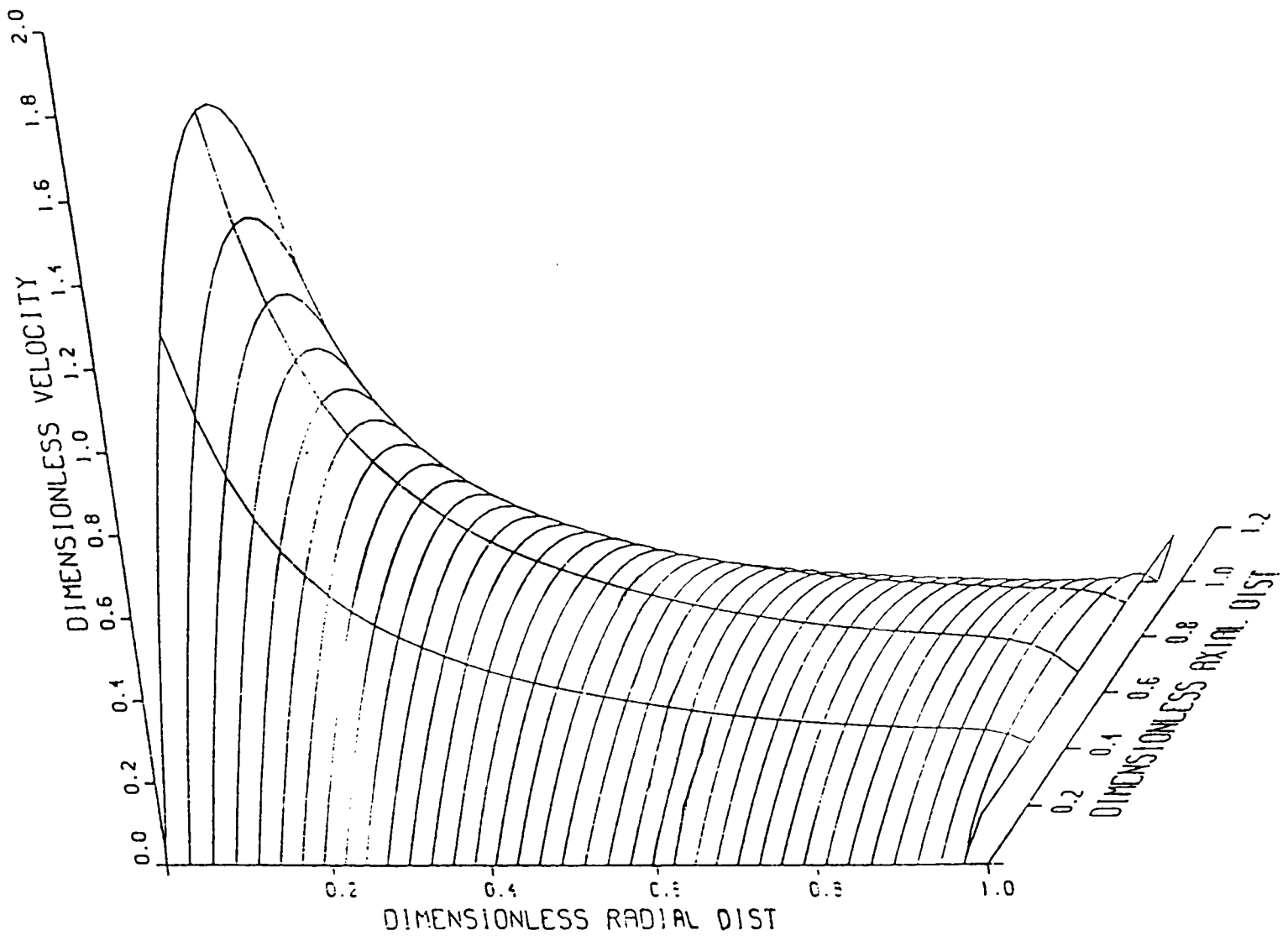




P (PASCALS) VS RADIAL DISTANCE

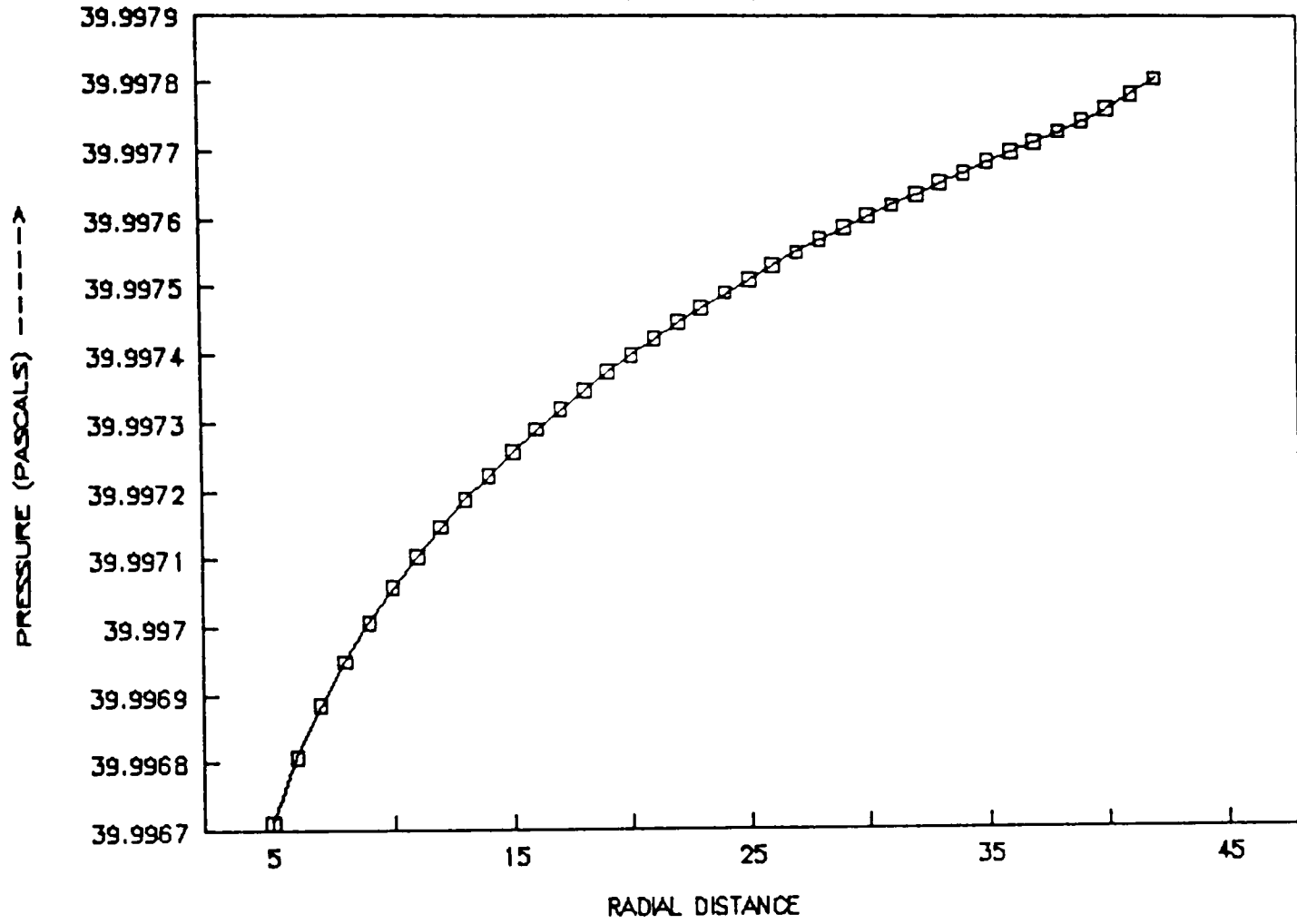
300MTORR; 90 SCOM





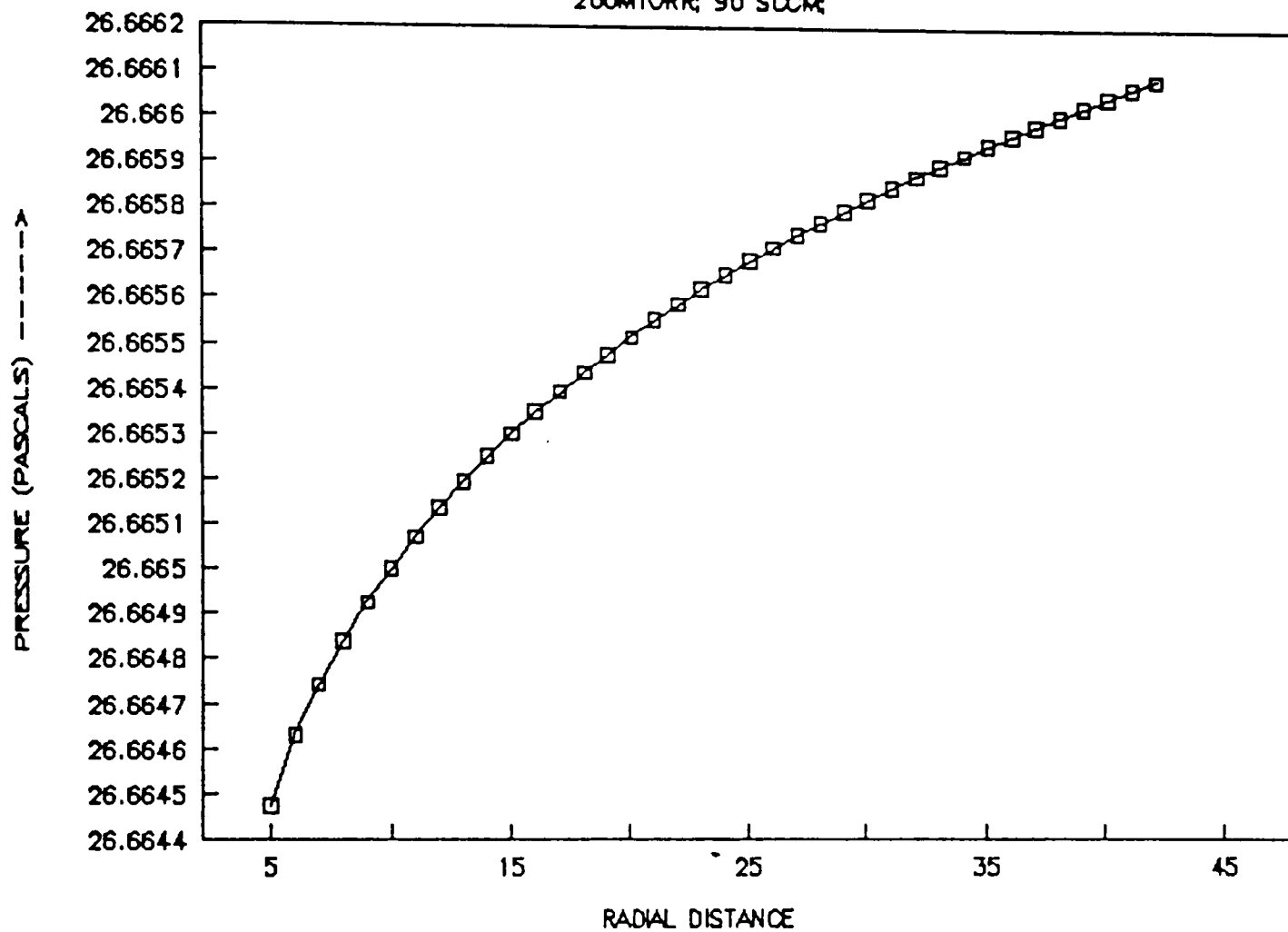
P (PASCALS) VS RADIAL DISTANCE

300MTORR; 90 SCCM; INLET PLUG



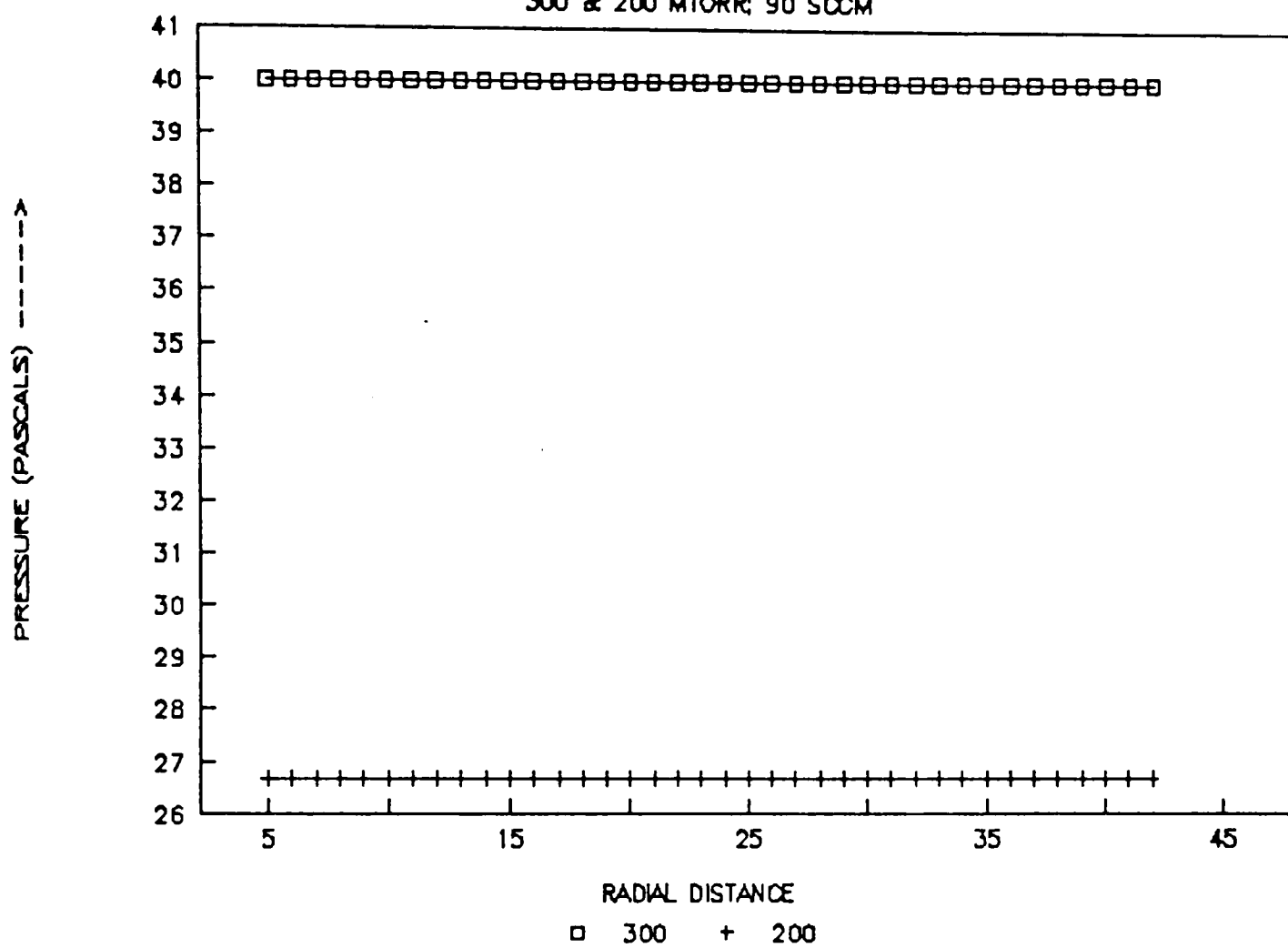
P (PASCALS) VS RADIAL DISTANCE

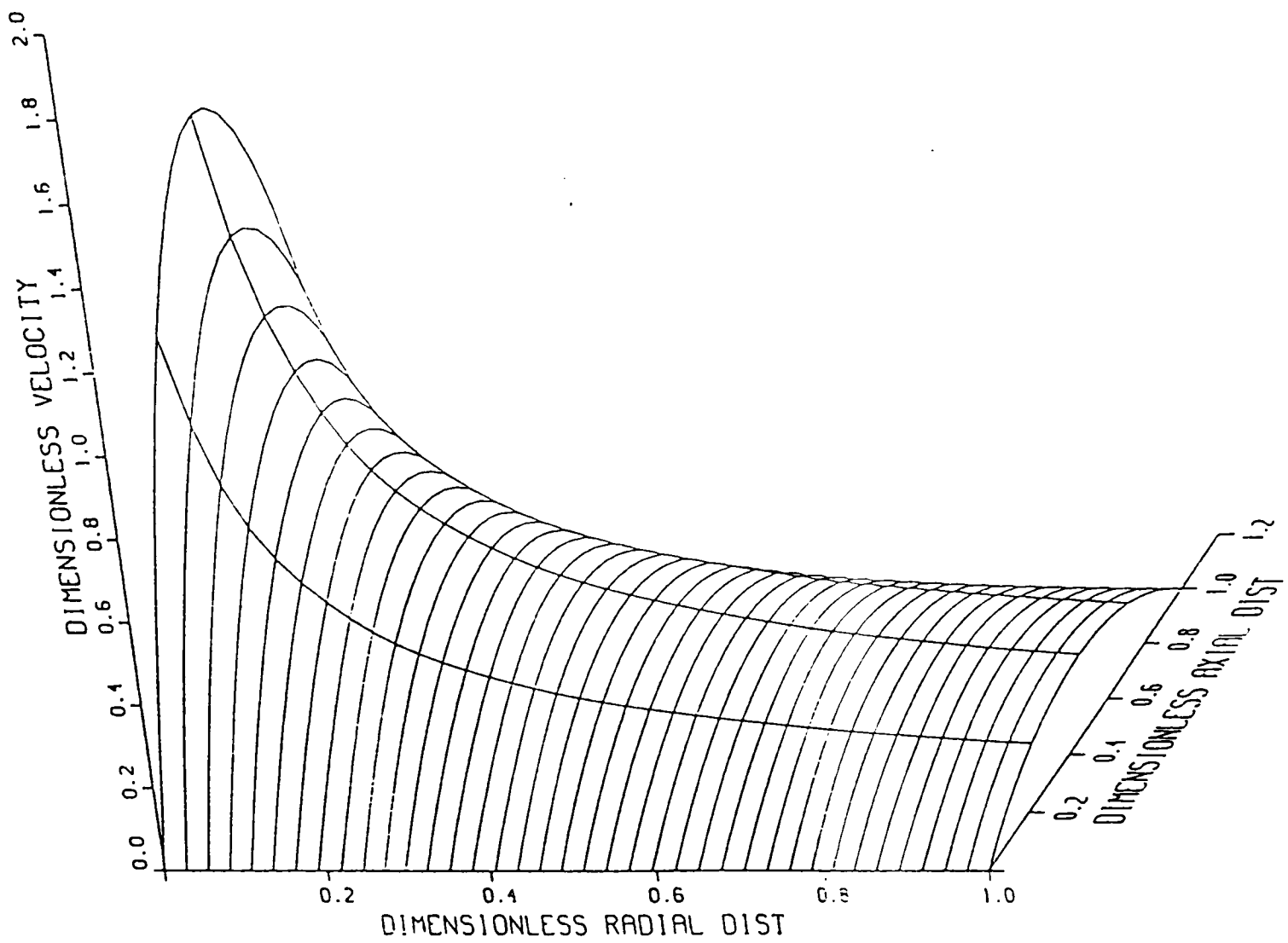
200MTORR; 90 SCCM



P (PASCALS) VS RADIAL DISTANCE

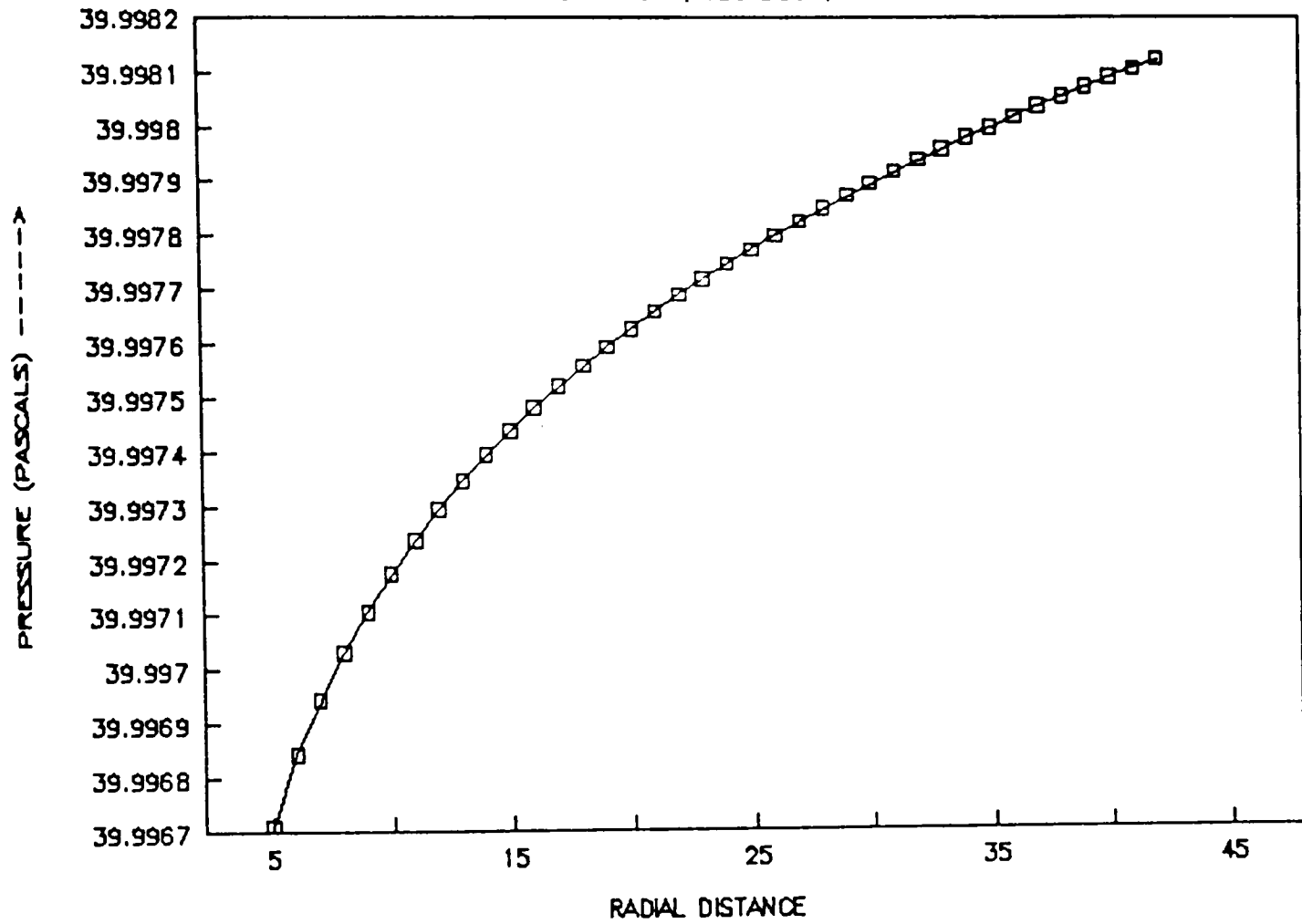
300 & 200 MTORR; 90 SCCM





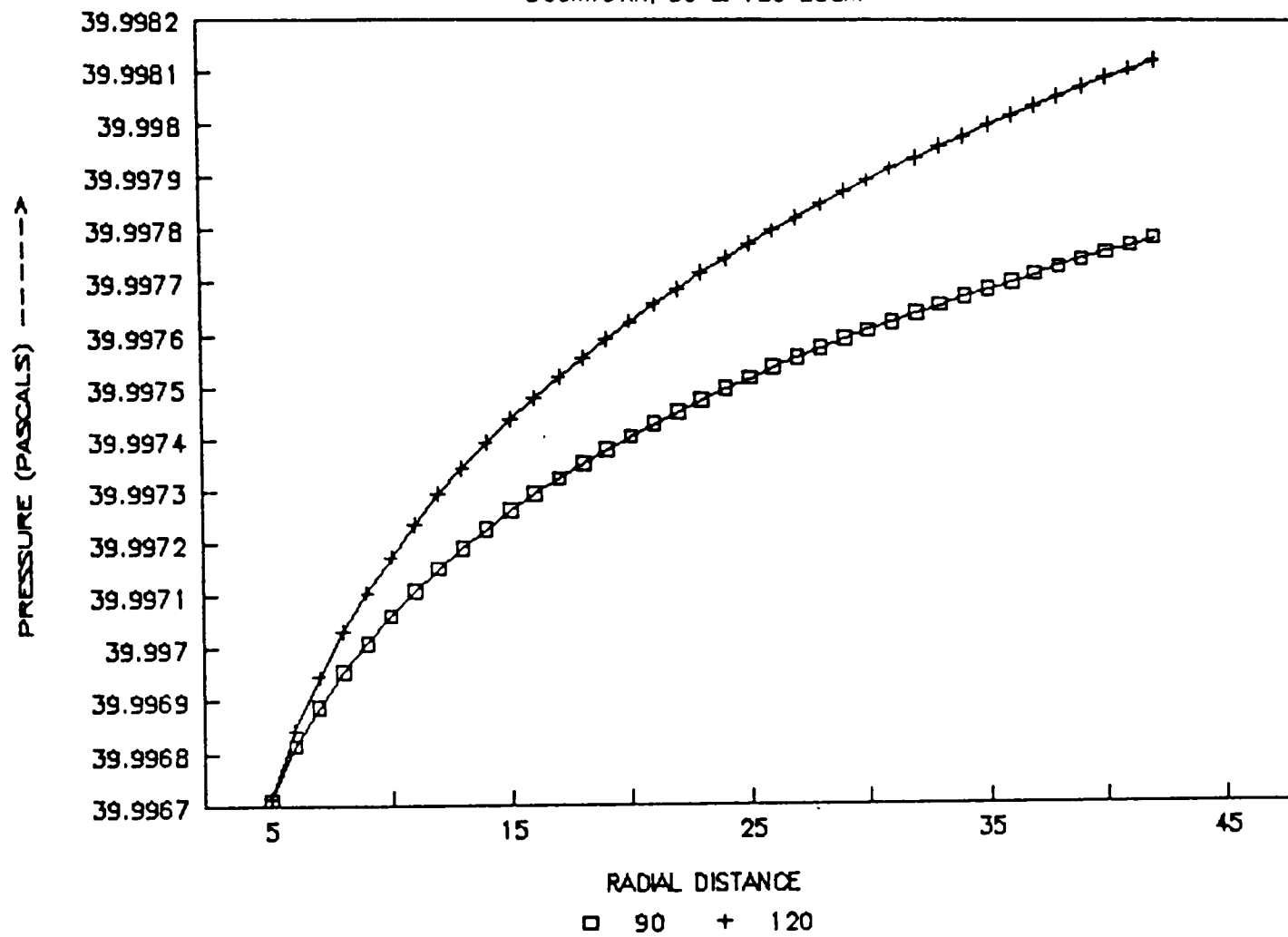
P (PASCALS) VS RADIAL DISTANCE

300MTORR; 120 SCOM



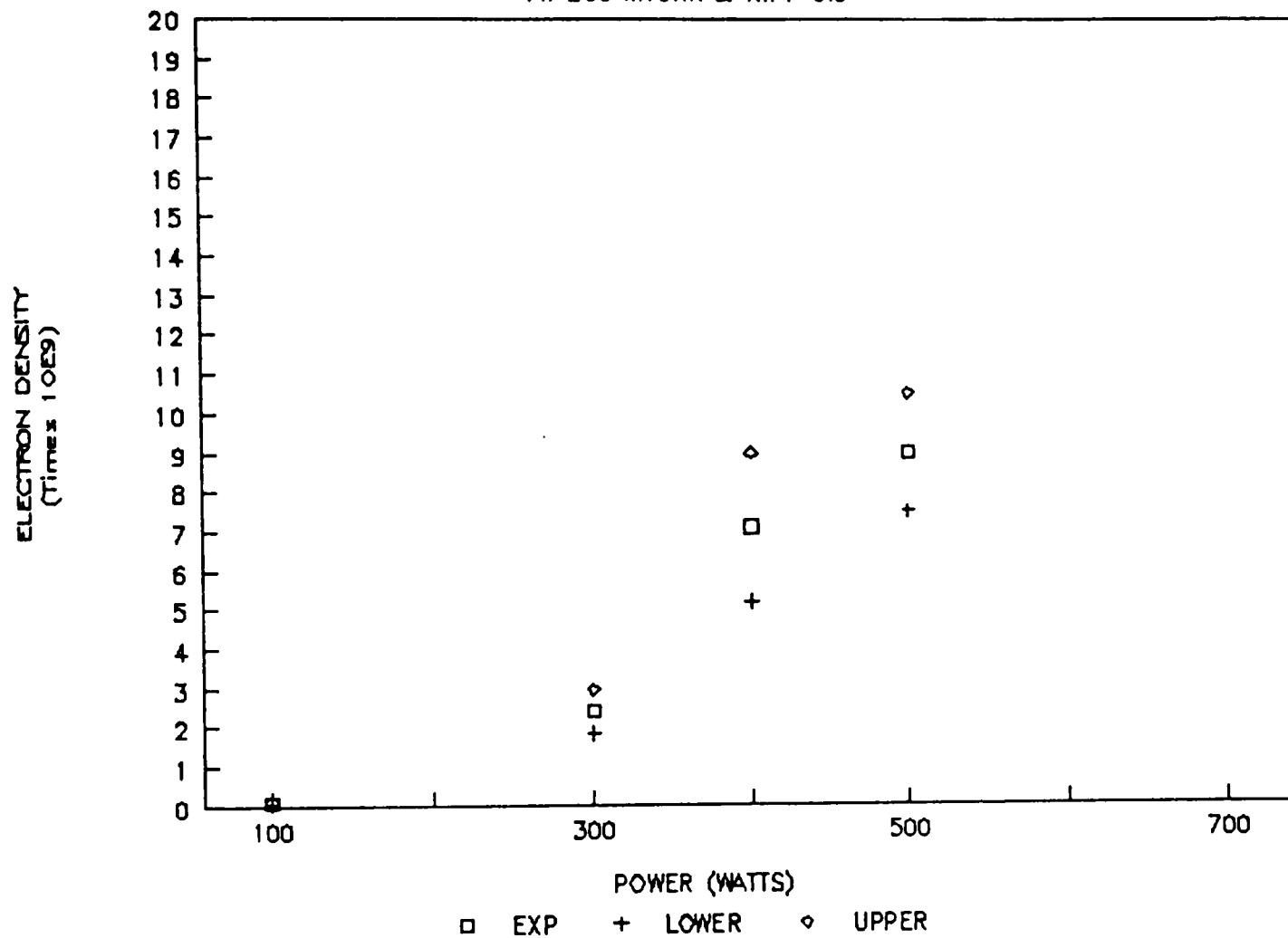
P (PASCALS) VS RADIAL DISTANCE

300MTORR; 90 & 120 SCCM



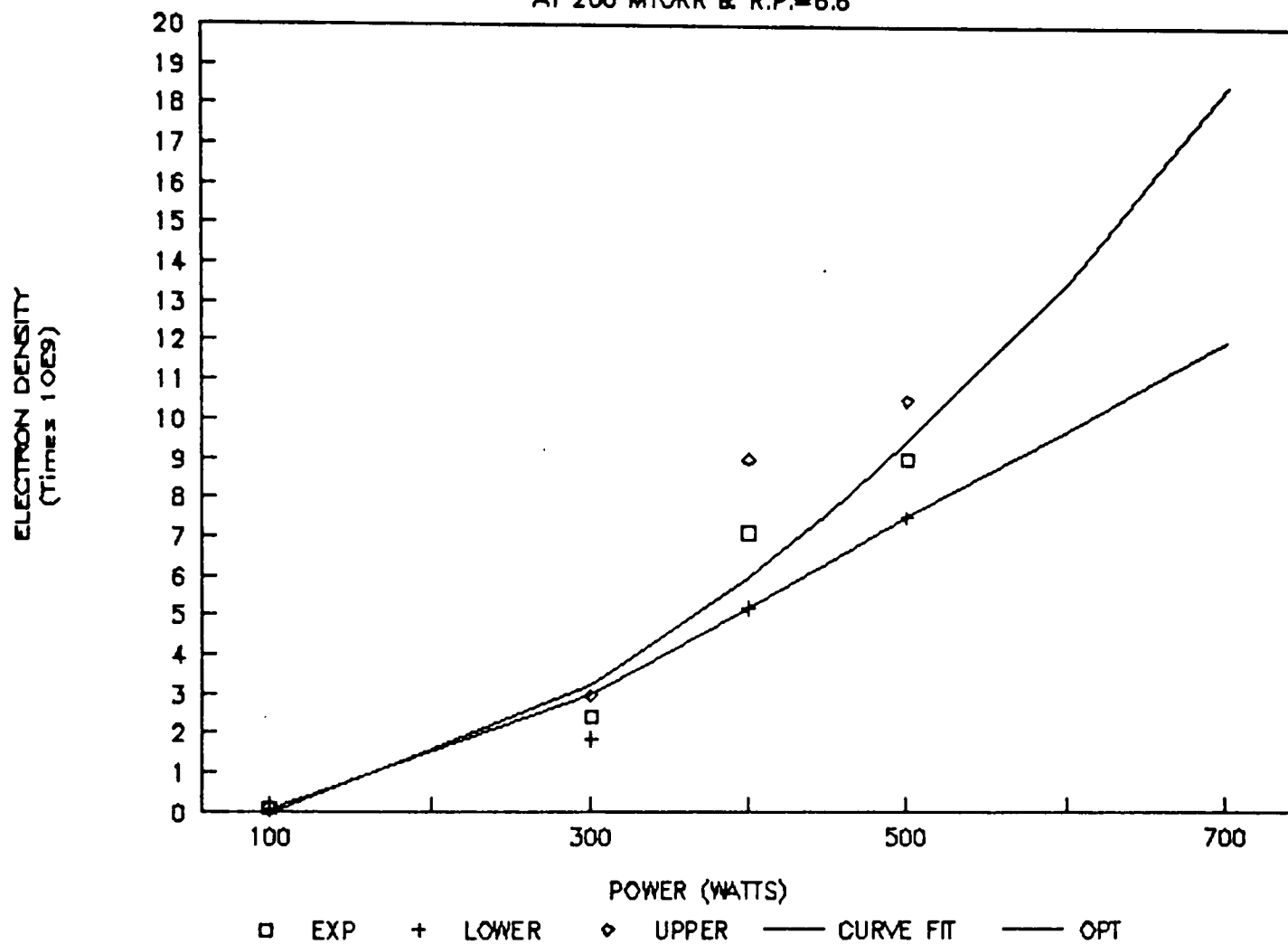
ELECTRON DENSITY VS. POWER

AT 200 MTORR & R.P.=6.6"



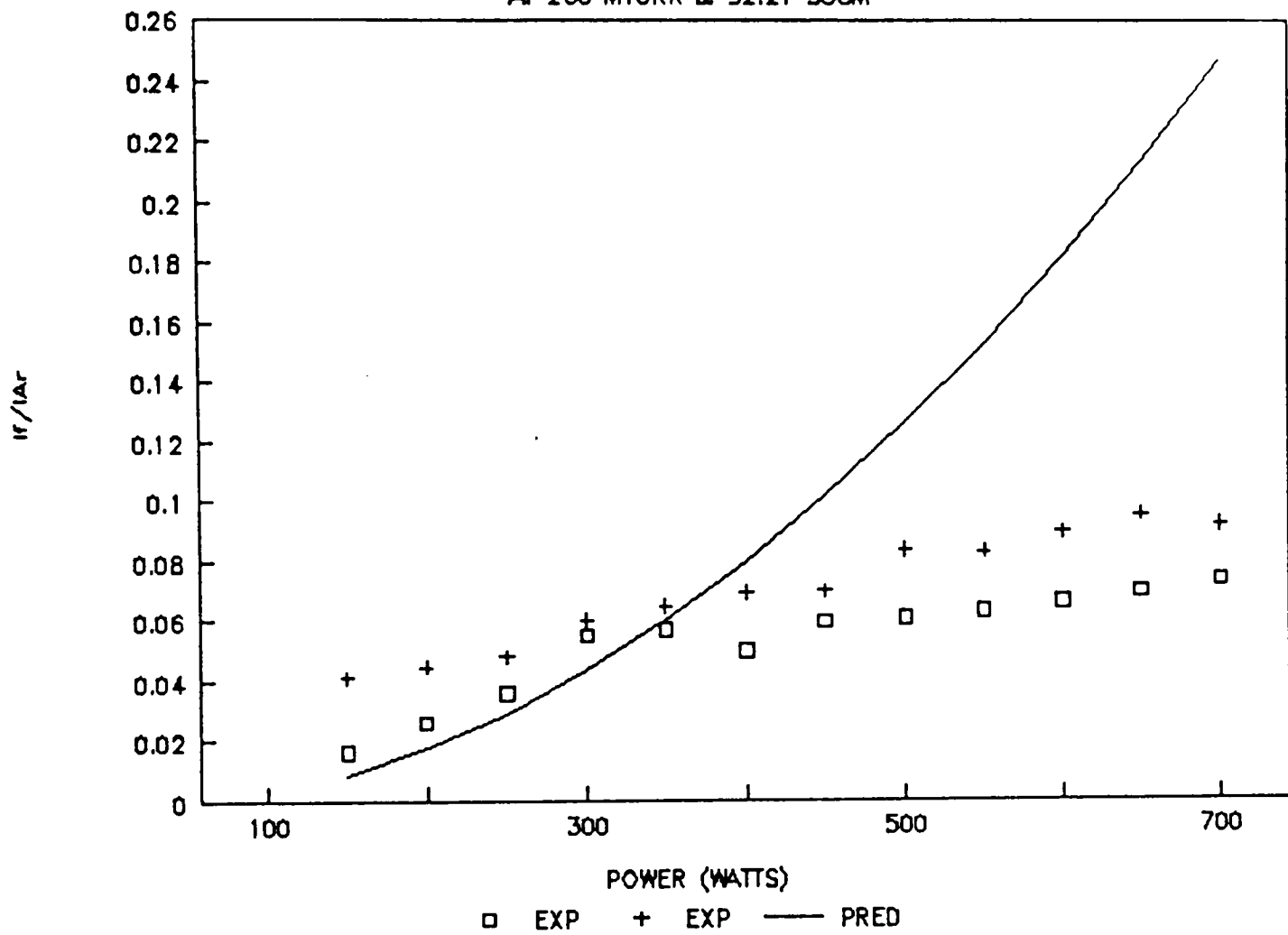
ELECTRON DENSITY VS. POWER

AT 200 MTORR & R.P.=6.6"



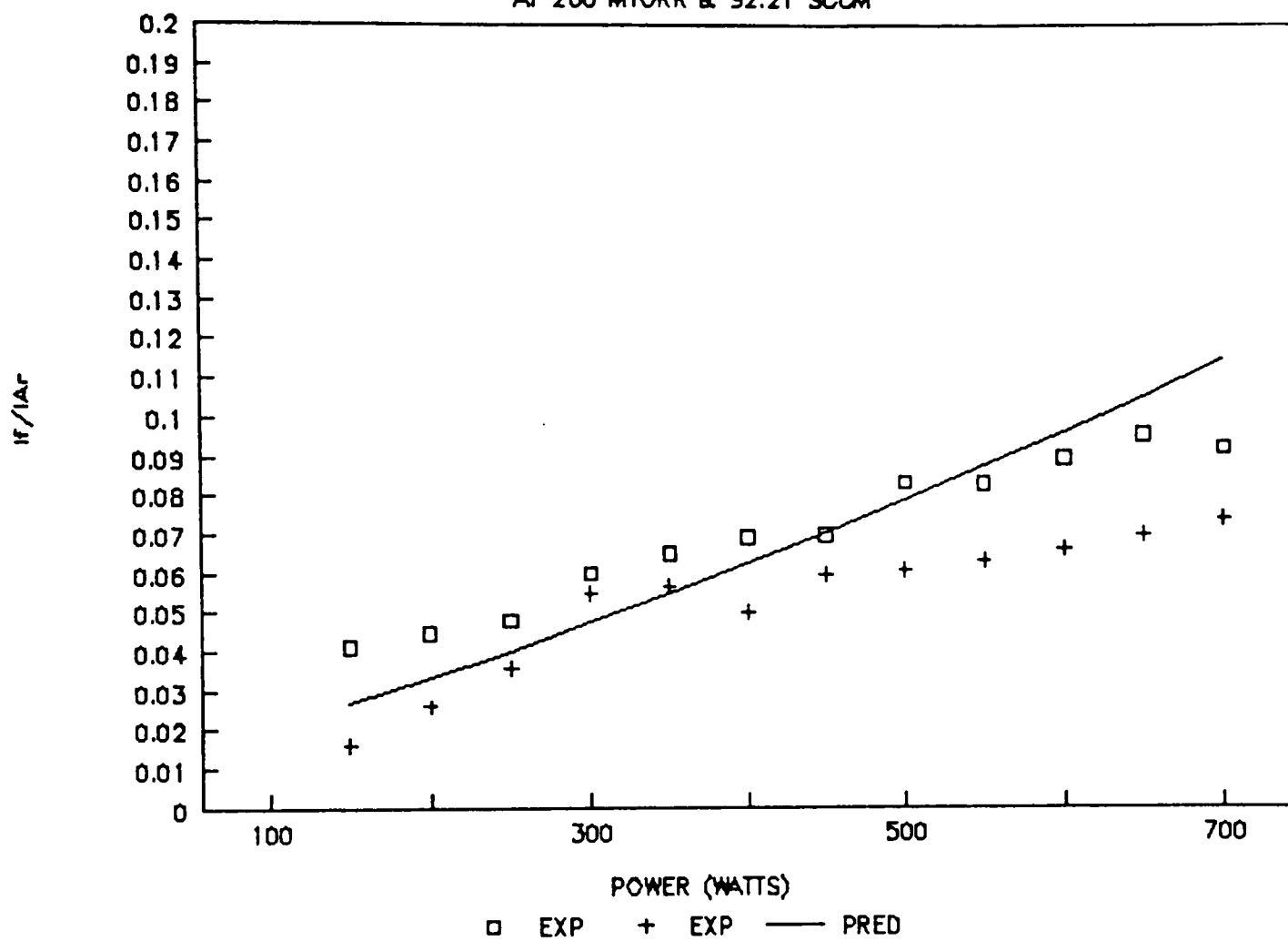
If/I_{Ar} VS. POWER

AT 200 MTORR & 92.21 SCCM



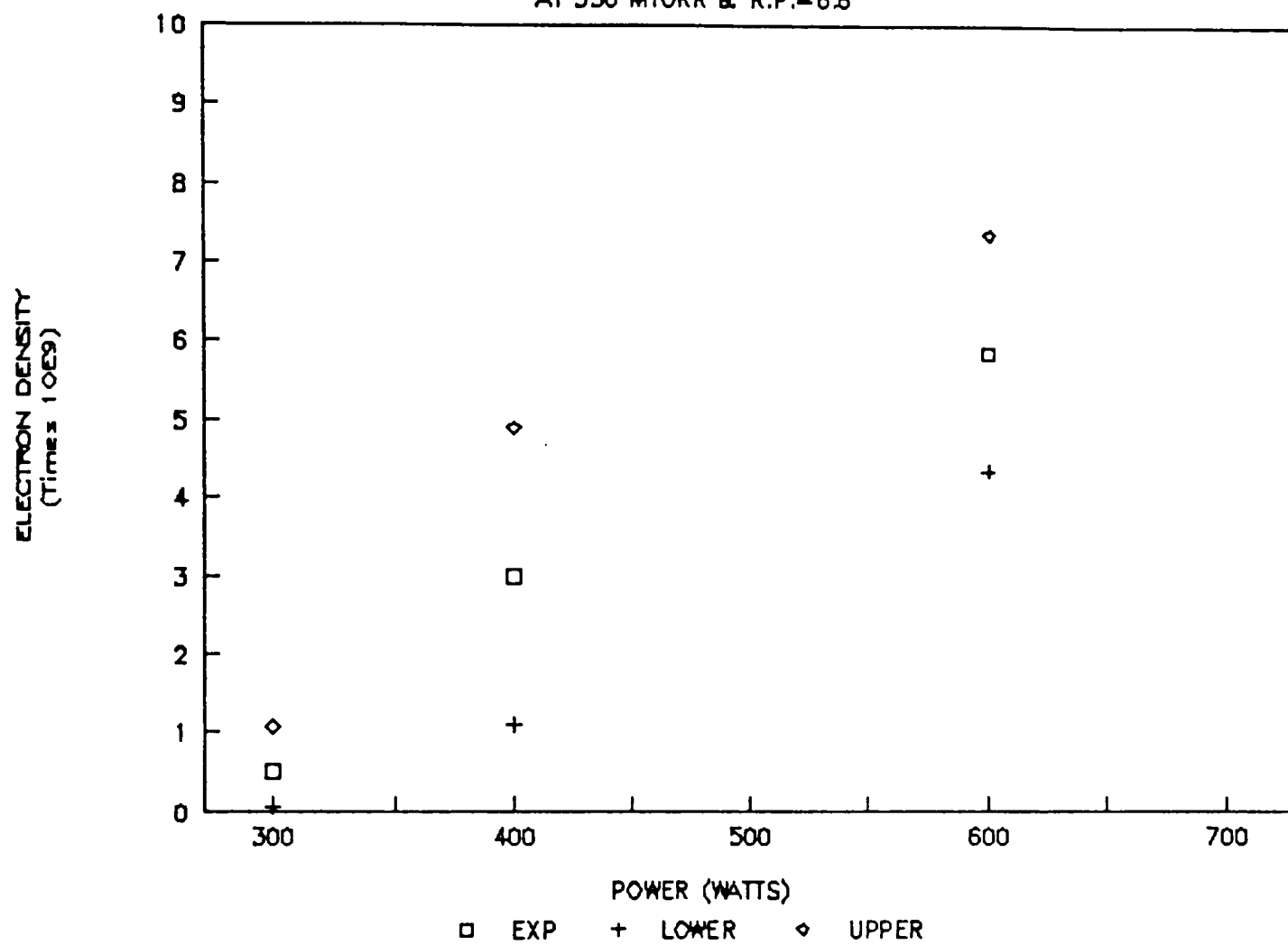
If/I_{Ar} VS. POWER

AT 200 MTORR & 92.21 SCOM



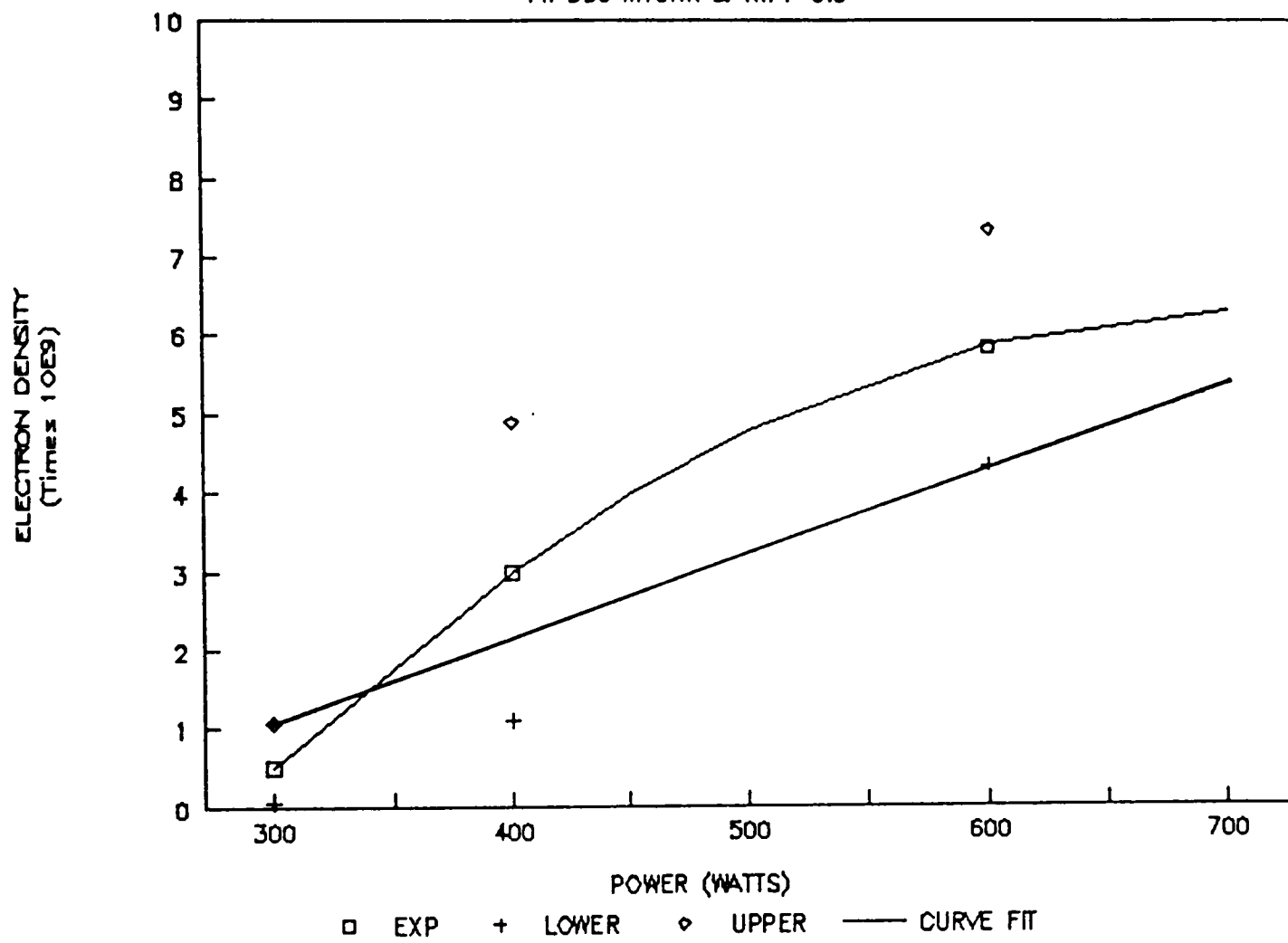
ELECTRON DENSITY VS. POWER

AT 350 MTORR & R.P.=6.6"



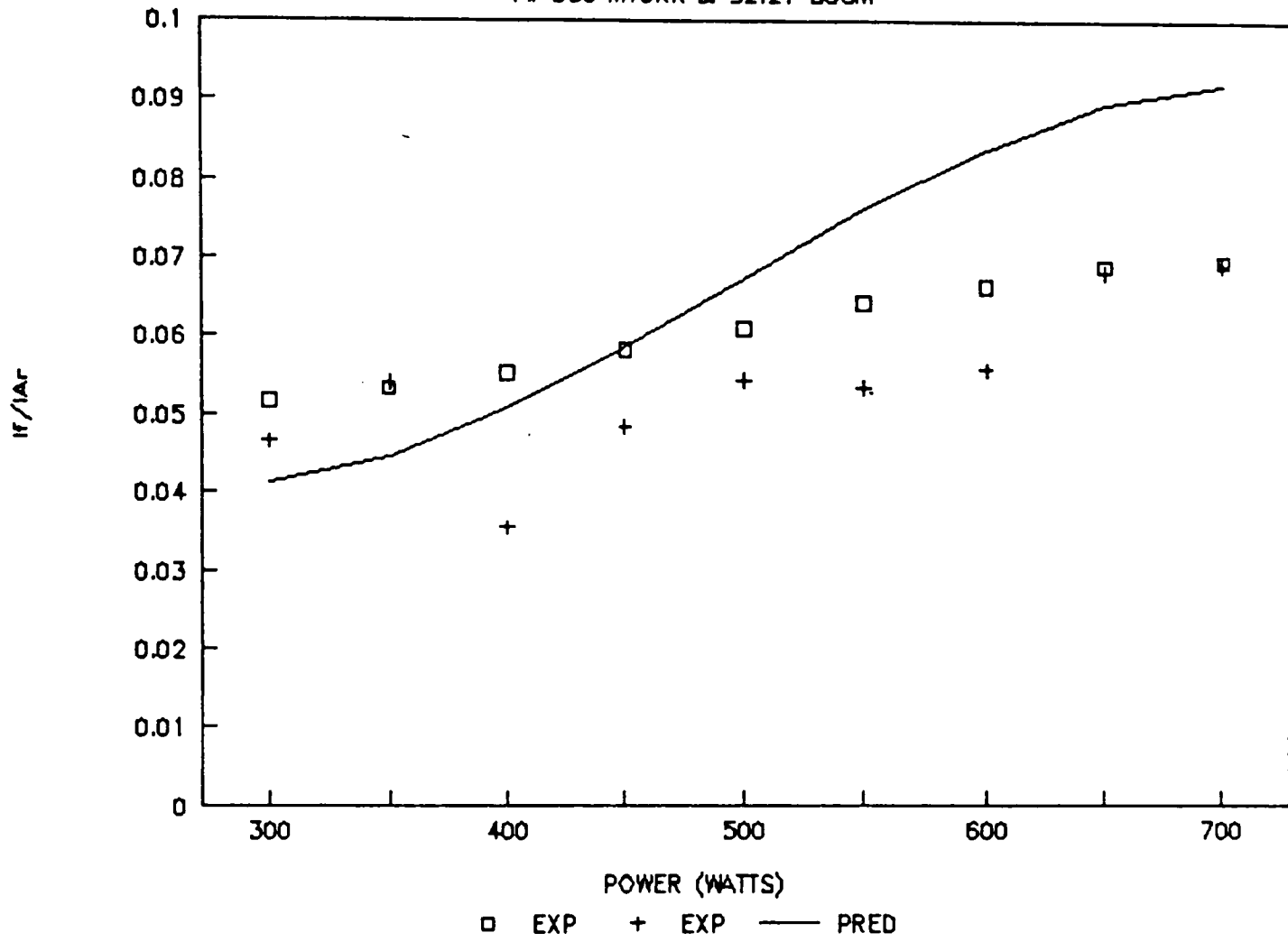
ELECTRON DENSITY VS. POWER

AT 350 MTORR & R.P.=6.6"



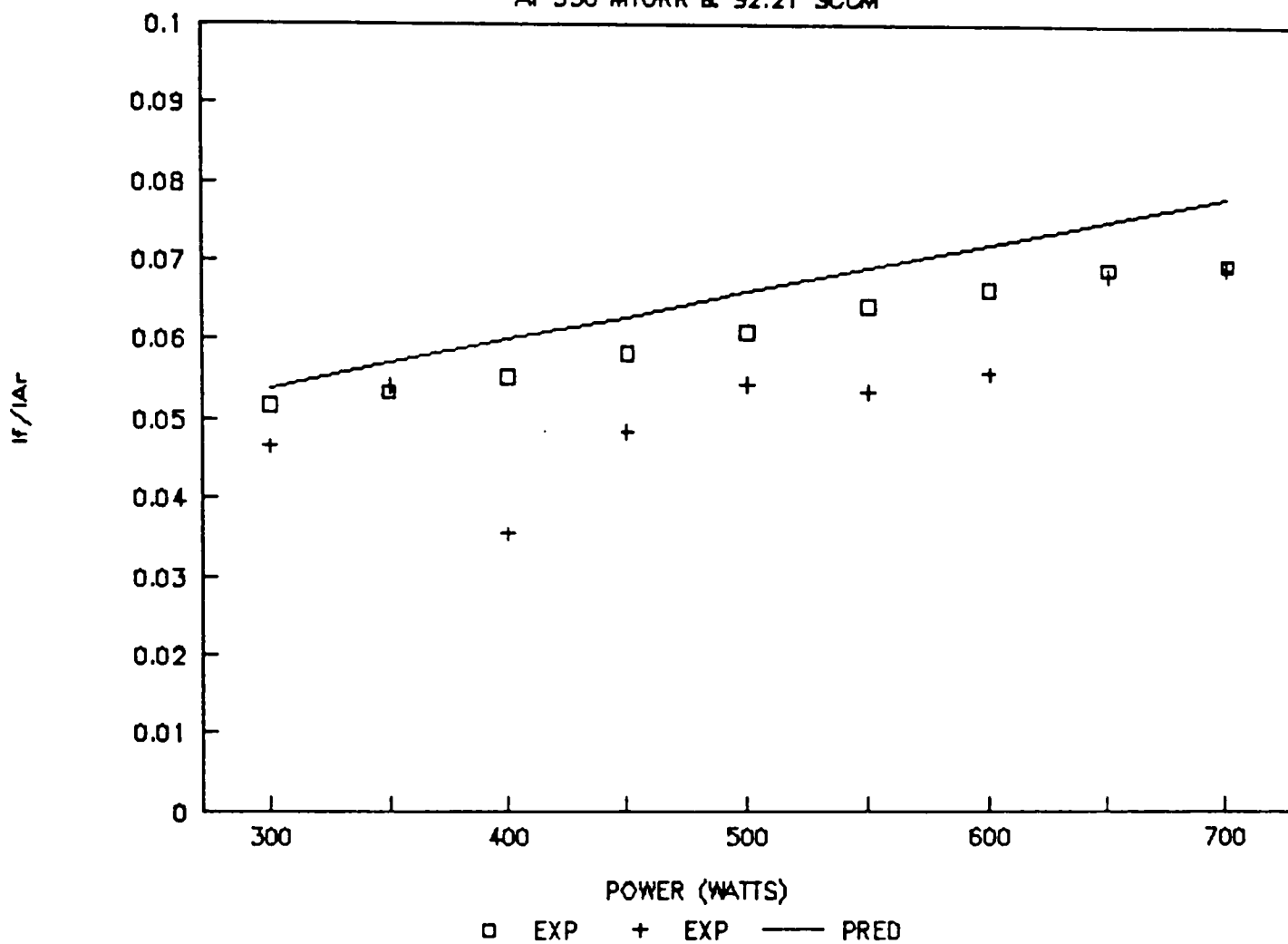
If/I_{Ar} VS. POWER

AT 350 MTORR & 92.21 SCOM



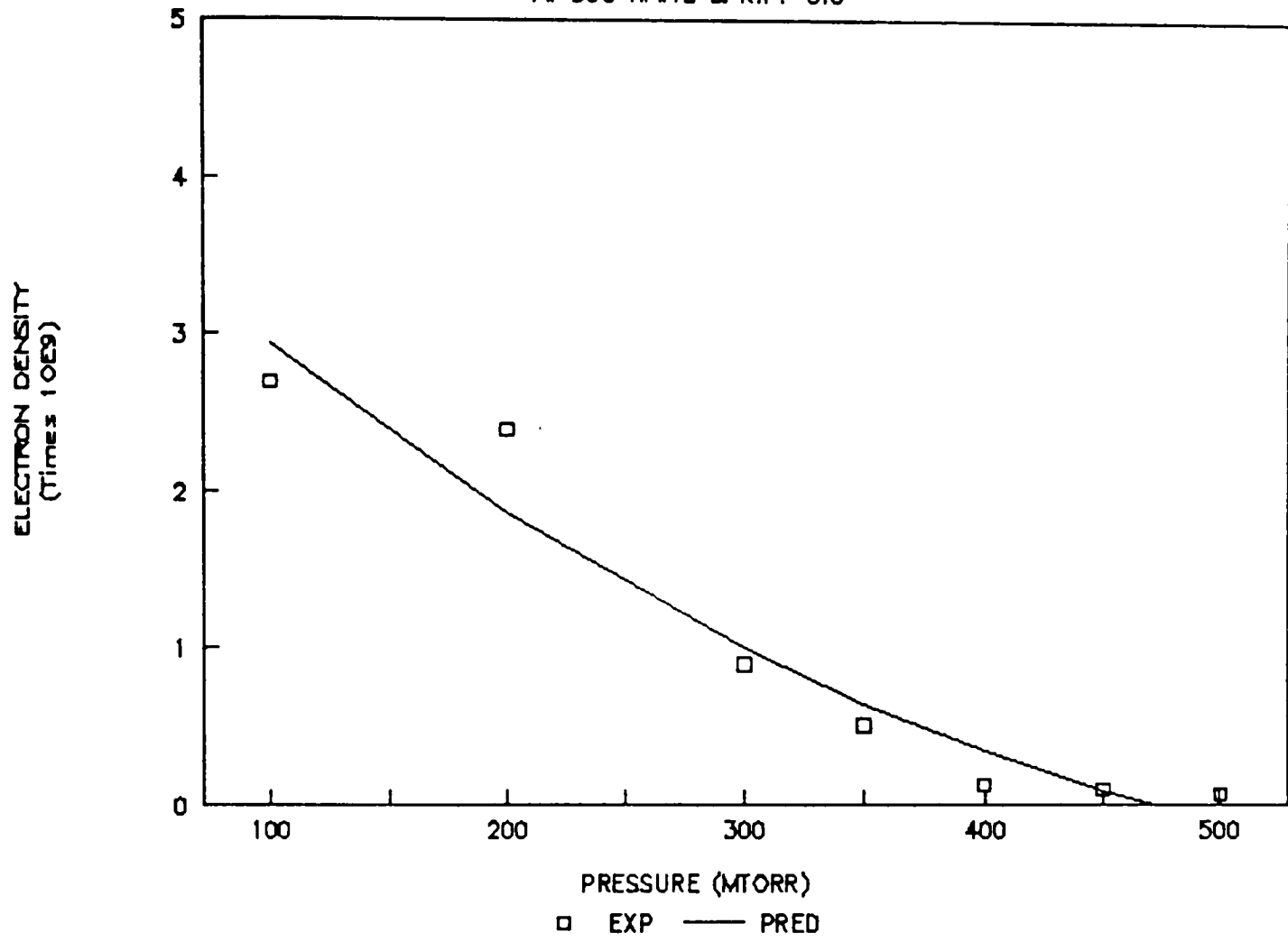
If/I_{Ar} VS. POWER

AT 350 MTORR & 92.21 SCOM



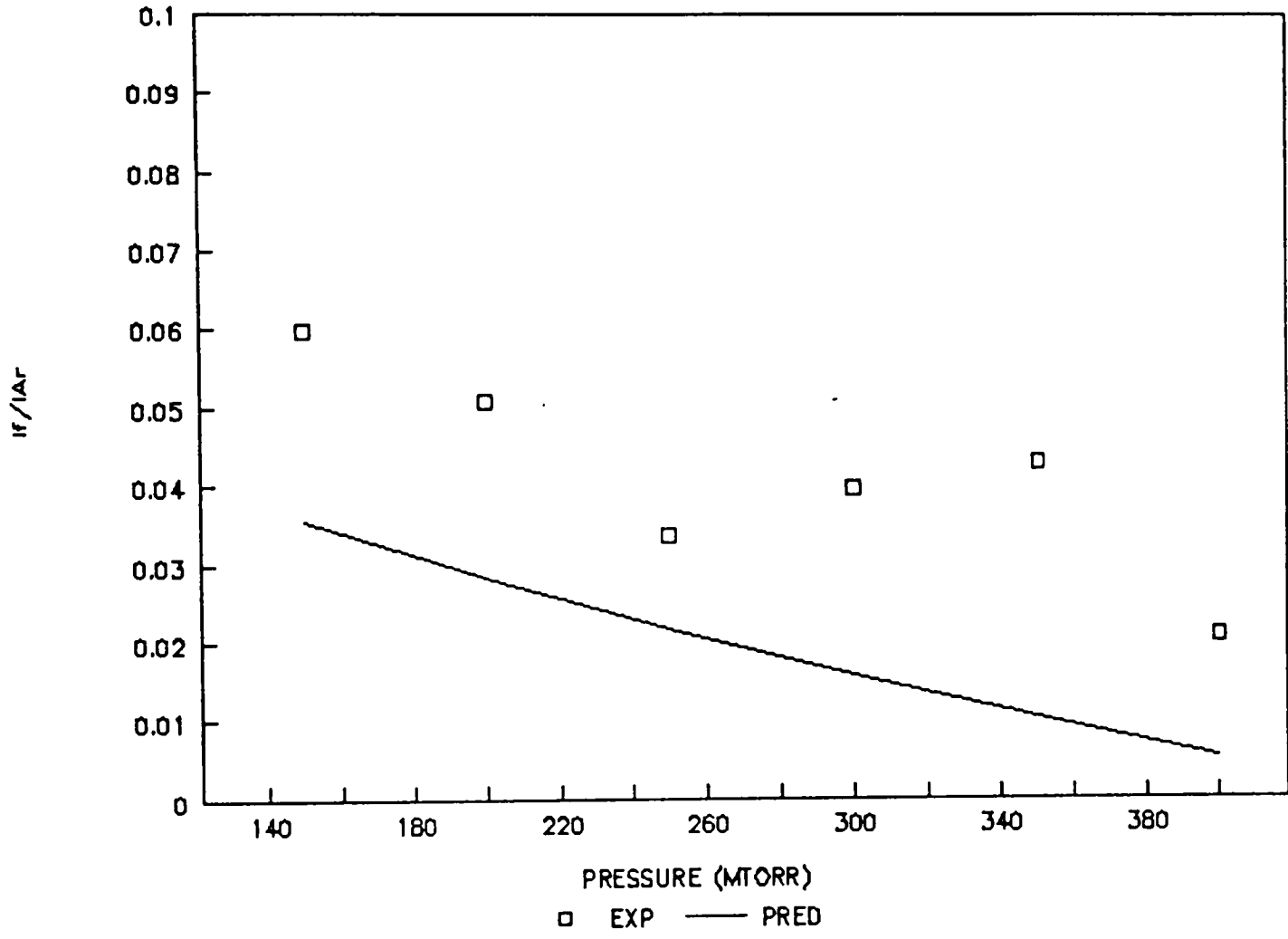
ELECTRON DENSITY VS. PRESSURE

AT 300 WATTS & R.P.=6.6"



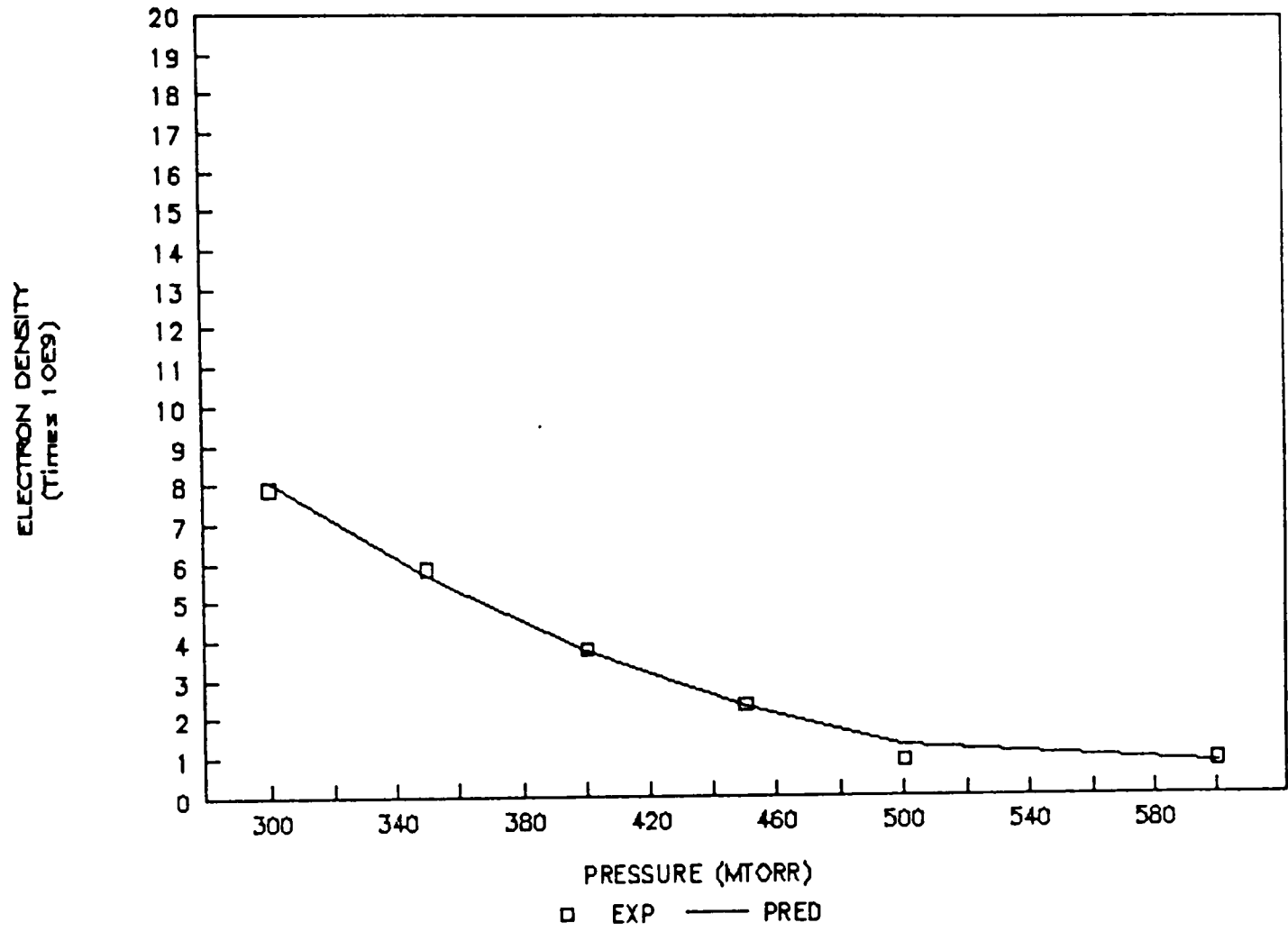
If/I_{Ar} VS. PRESSURE

AT 300 WATTS & 92.21 SCOM



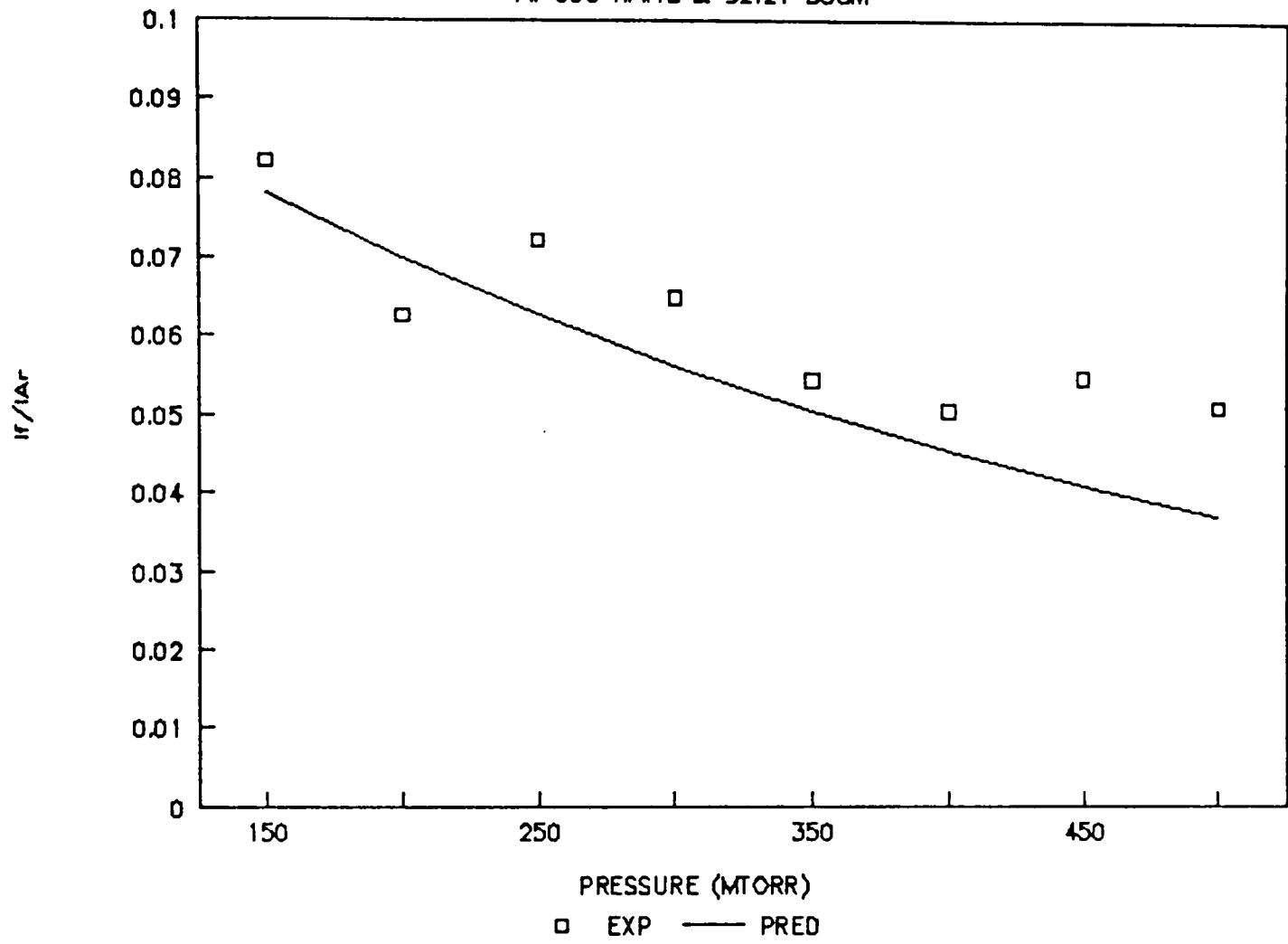
ELECTRON DENSITY VS. PRESSURE

AT 600 WATTS & R.P.=6.6"

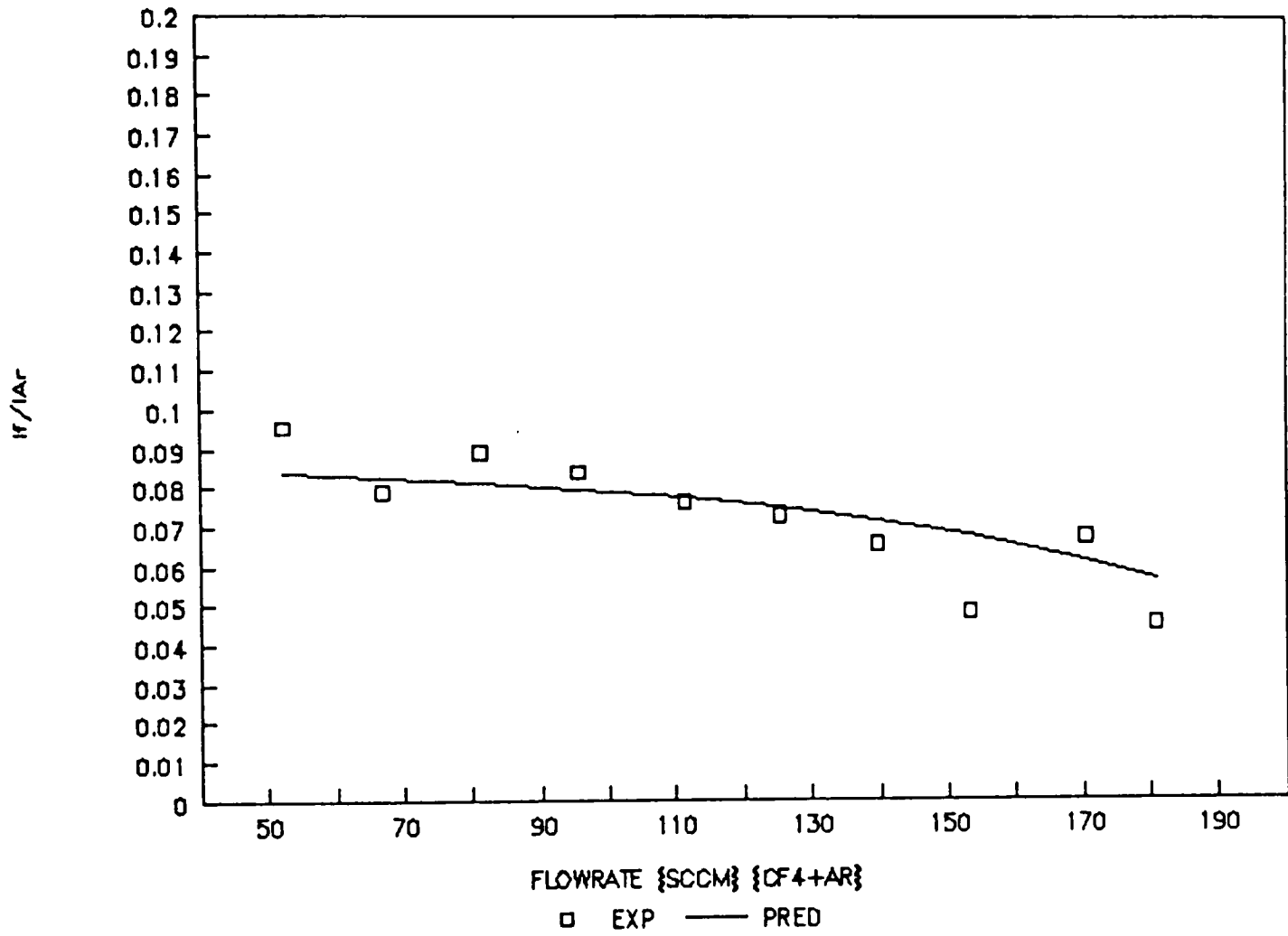


If/I_{Ar} VS. PRESSURE

AT 600 WATTS & 92.21 SCCM

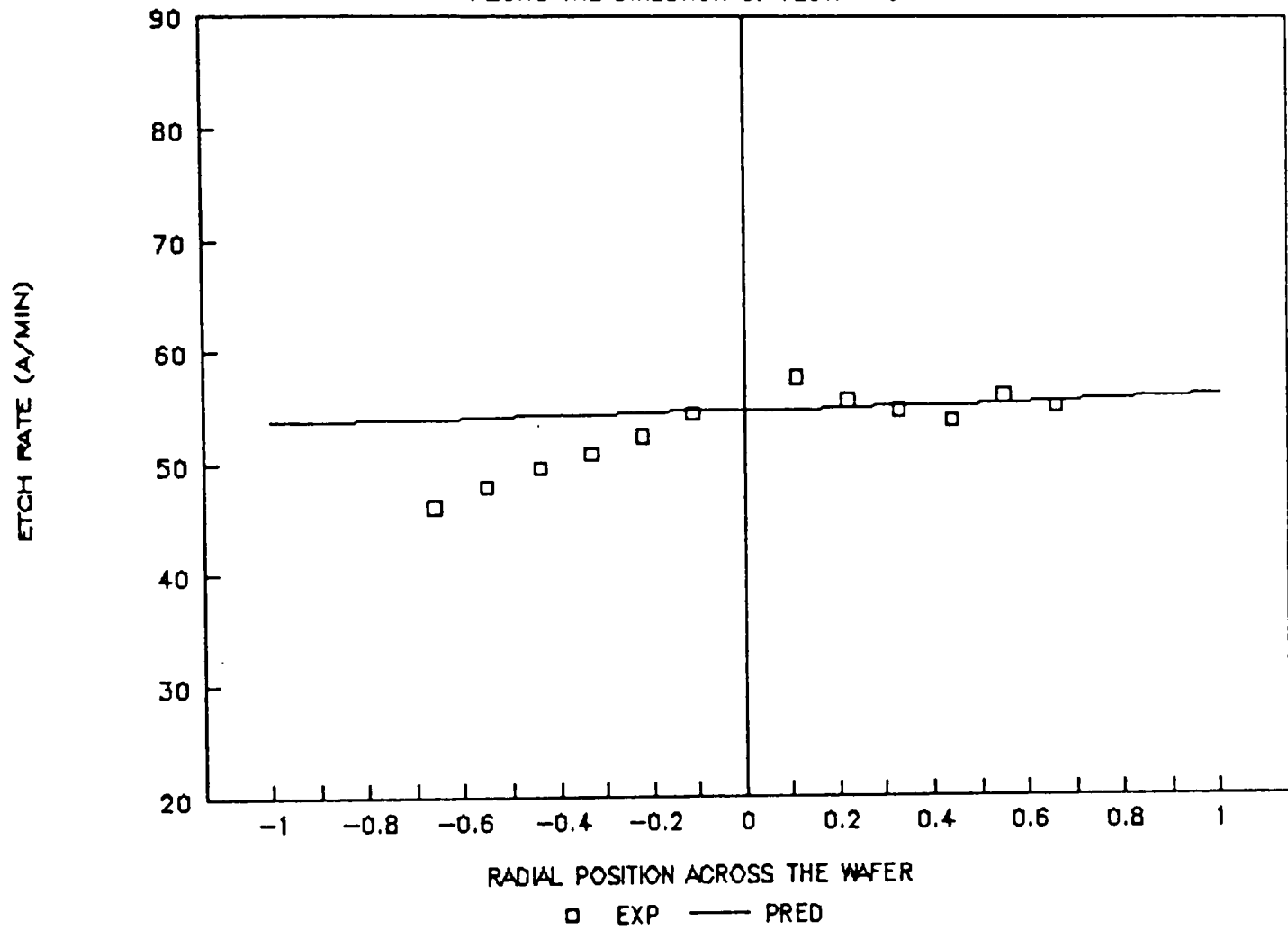


If/I_{Ar} VS. FLOWRATE
AT 400 WATTS & 350 MTORR

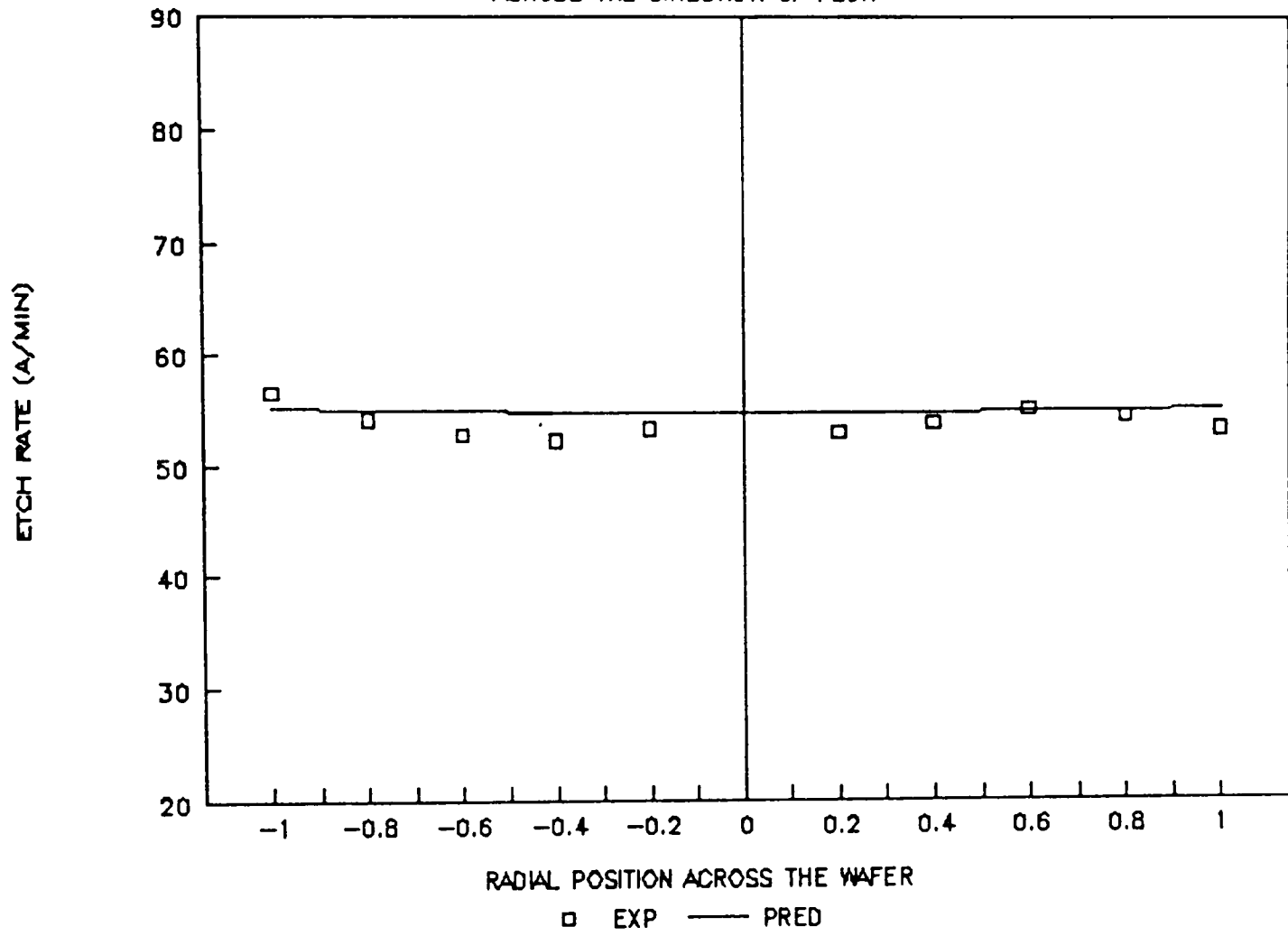


ETCH RATE DATA (Near Inlet)

ALONG THE DIRECTION OF FLOW -->

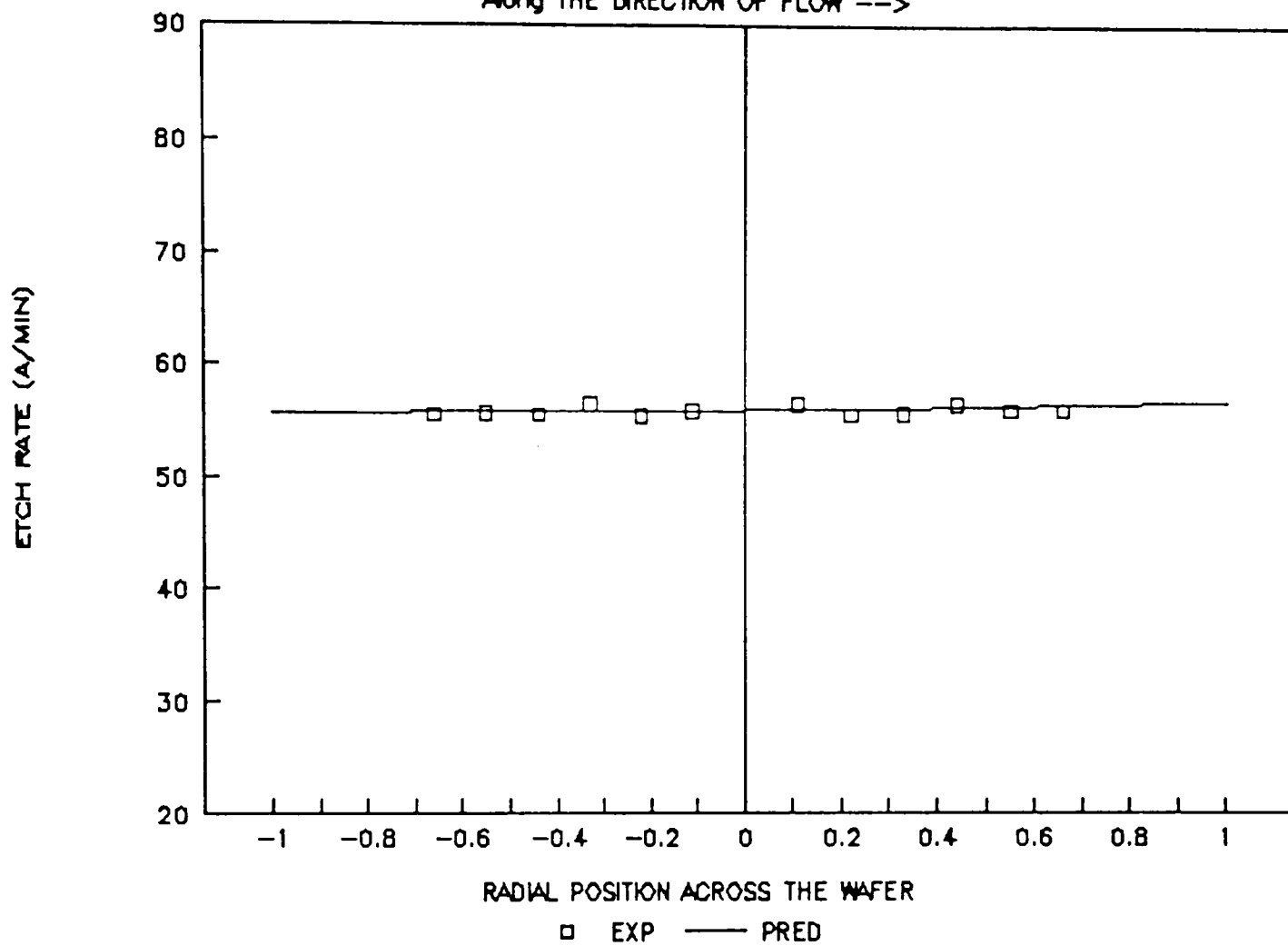


ETCH RATE DATA (Near Inlet) ACROSS THE DIRECTION OF FLOW

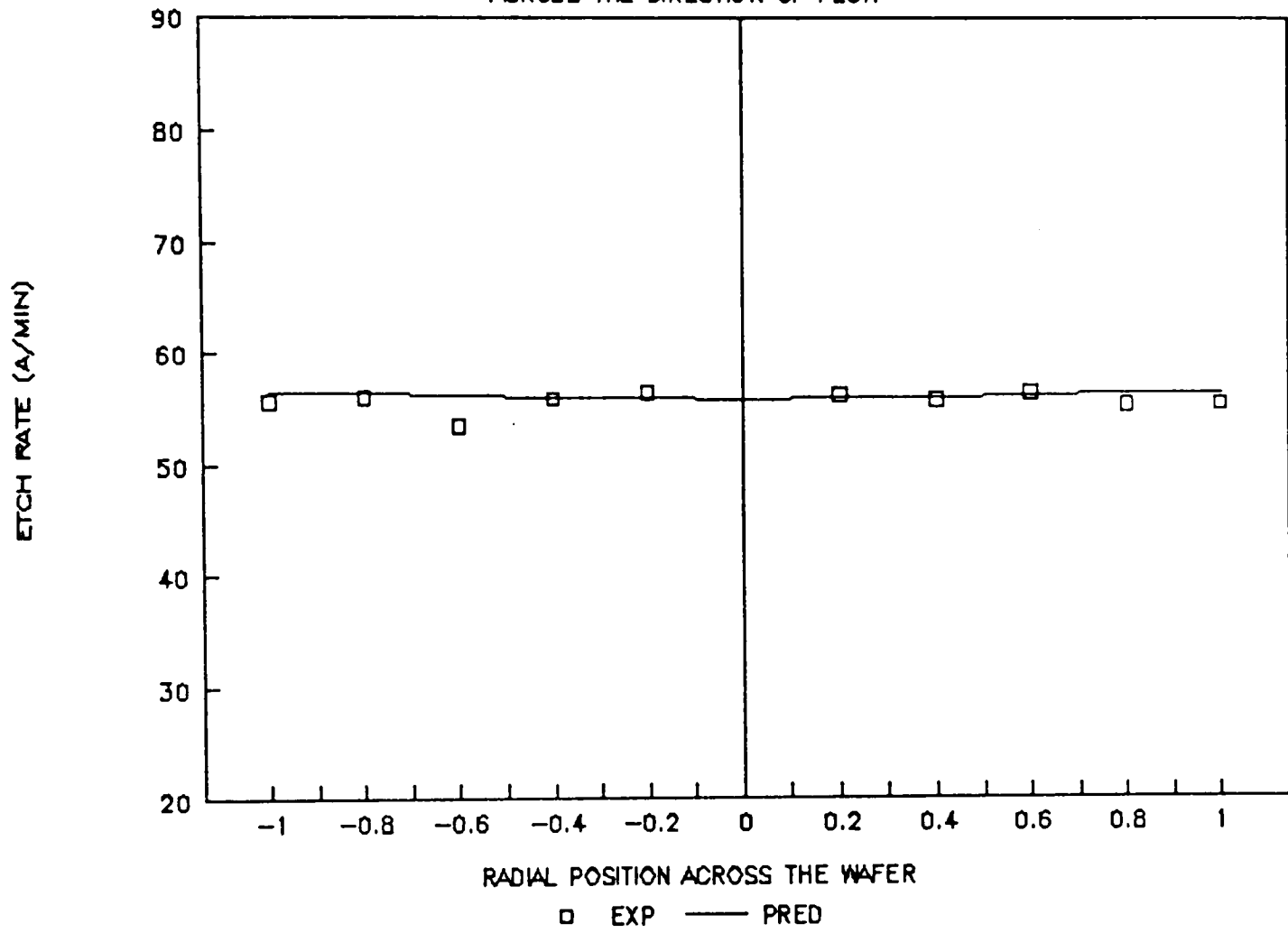


ETCH RATE DATA (Near Exit)

Along THE DIRECTION OF FLOW -->



ETCH RATE DATA (Near Exit) ACROSS THE DIRECTION OF FLOW



PERMISSION TO COPY

In presenting this thesis in partial fulfillment of the requirements for a master's degree at Texas Tech University, I agree that the Library and my major department shall make it freely available for research purposes. Permission to copy this thesis for scholarly purposes may be granted by the Director of the Library or my major professor. It is understood that any copying or publication of this thesis for financial gain shall not be allowed without my further written permission and that any user may be liable for copyright infringement.

Disagree (Permission not granted)

Agree (Permission granted)

Student's signature

Vikram Singh

Student's signature

Date

11-7-90

Date

